WAVE IMPACTS ON RECTANGULAR STRUCTURES

A thesis submitted for the degree of Doctor of Philosophy

by

Nor Aida Zuraimi Md Noar

Department of Mathematical Sciences, Brunel University

July 2012

ABSTRACT

There is a good deal of uncertainty and sensitivity in the results for wave impact. In a practical situation, many parameters such as the wave climate will not be known with any accuracy especially the frequency and severity of wave breaking. Even if the wave spectrum is known, this is usually recorded offshore, requiring same sort of (linear) transfer function to estimate the wave climate at the seawall. What is more, the higher spectral moments will generally be unknown. Wave breaking, according to linear wave theory, is known to depend on the wave spectrum, see Srokosz (1986) and Greenhow (1989). Not only is the wave climate unknown, but the aeration of the water will also be subject to uncertainty. This affects rather dramatically the speed of sound in the water/ bubble mixture and hence the value of the acoustic pressure that acts as a maximum cut-off for pressure calculated by any incompressible model. The results are also highly sensitive to the angle of alignment of the wave front and seawall. Here we consider the worst case scenario of perfect alignment.

Given the above, it seems sensible to exploit the simple pressure impulse model used in this thesis. Thus Cooker (1990) proposed using the pressure impulse $P(x, y)$ that is the time integral of the pressure over the duration of the impact. This results in a simplified, but much more stable, model of wave impact on the coastal structures, and forms the basis of this thesis, as follows:

Chapter 1 is an overview about this topic, a brief summary of the work which will follow and a summary of the contribution of this thesis.

Chapter 2 gives a literature review of wave impact, theoretically and experimentally. The topics covered include total impulse, moment impulse and overtopping. A summary of the present state of the theory and Cooker's model is also presented in Chapter 2.

In Chapter 3 and Chapter 4, we extend the work of Greenhow (2006). He studied the berm and ditch problems, see Chapter 3, and the missing block problem in Chapter 4, and solved the problems by using a basis function method. I solve these problems in nondimensionlised variables by using a hybrid collocation method in Chapter 3 and by using the same method as Greenhow (2006) in Chapter 4. The works are extended by calculating the total impulse and moment impulse, and the maximum pressure arising from the wave impact for each problem. These quantities will be very helpful from a practical point of view for engineers and designers of seawalls. The mathematical equations governing the fluid motion and its boundary conditions are presented.

The deck problem together with the mathematical formulation and boundary conditions for the problem is presented in Chapters 5 and 6 by using a hybrid collocation method. For this case, the basis function method fails due to hyperbolic terms in these formulations growing exponentially. The formulations also include a secular term, not present in Cooker's formulation. For Chapter 5, the wave hits the wall in a horizontal direction and for Chapter 6, the wave hits beneath the deck in a vertical direction. These problems are important for offshore structures where providing adequate freeboard for decks contributes very significantly to the cost of the structure.

Chapter 7 looks at what happens when we have a vertical baffle. The mathematical formulation and the boundary conditions for four cases of baffles which have different positions are presented in this chapter. We use a basis function method to solve the mathematical formulation, and total impulse and moment impulse are investigated for each problem. These problems are not, perhaps, very relevant to coastal structures. However, they are pertinent to wave impacts in sloshing tanks where baffles are used to detune the natural tank frequencies away from environmental driving frequencies (e.g ship roll due to wave action) and to damp the oscillations by shedding vortices. They also provide useful information for the design of oscillating water column wave energy devices.

Finally, conclusions from the research and recommendations for future work are presented in Chapter 8.

ACKNOWLEDGEMENTS

TABLE OF CONTENTS

LIST OF TABLES

.

LIST OF FIGURES

CHAPTER 1

INTRODUCTION

1.1   Overview

This thesis studies water wave impact on the vertical structures. This study is divided into eight chapters which cover various structures with rectangular geometries including the introduction of the pressure impulse theory and discussion. Each chapter has a separate literature review, but we will start with a brief summary of what will be covered in each chapter and some motivation for carrying out this work. For each type of structure, we will examine the pressure impulse on the vertical seawall, including the total impulse and overturning moments. In all the problems in this thesis we assume that the fluid is inviscid and incompressible. It is worth noting that the model does not require irrotationality, but that vorticity is conserved during the impact. Given that the impacting wave model before impact is irrotational, the motion afterwards will also be, but this is not a requirement of the pressure impulse model used throughout this thesis.

Ocean waves are caused by the wind blowing over the surface of the ocean. As the wind blows, it gives energy to the sea surface resulting in a spectrum of waves. When waves break onto a vertical structure they can cause a fast spray jet rising into the air. The pressure or forces that act on these structures under wave action are divided into two categories, pulsating (or quasi-static) and impulsive (or impact) (Allsop *et. al*, 1995). Pulsating pressures change relatively slowly while the impulsive pressures caused by breaking waves are large and much higher than pulsating pressures, but of shorter duration. We are especially interested in the highest pressures, which often cause damage to the vertical structures.

Seawalls are constructed to protect beaches and coastlines from being destroyed by erosion while breakwaters are constructed to provide a calm lagoon for ships and to protect the harbour facilities immediately behind them. For ports open to rough seas, breakwaters play a main role in port operations. Since sea waves have enormous power, the construction of the structures to eliminate most wave action is not easily accomplished. The history of breakwaters therefore can be said to be one of much damage and many failures, (Takahashi,1996).
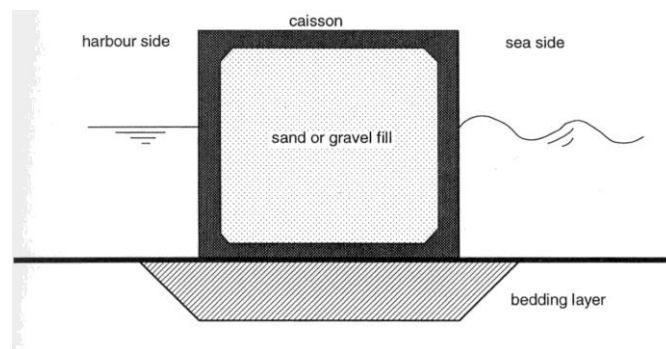
Figure 1.1: A simple example of a vertical caisson breakwater,
image taken from European Coast,
http://www.kennisbank-waterbouw.nl/EC/CLM01060002.html

It is important to understand the significance of wave impact for the design of seawalls and breakwaters. There are large peaks in pressure on the vertical structure, and the engineers should design breakwaters which can reduce these impacts as much as possible or else they may lead to structural failure. Poor designs also require constant maintenance as waves erode the base of the seawall. The first catastrophic failures of a series of large rubble mound breakwaters were recorded in the thirties, and reported by Oumeraci (1994). Since then, there are many developments which might enhance the stability of vertical breakwaters, for instance knowledge of wave breaking and impacts on structures has evolved theoretically and experimentally. There are several sophisticated facilities for investigating the dynamic, hydraulic and geotechnical aspect of waves which are available in model or large scales in the laboratory. The theory of pressure impulse for wave impact on vertical structures will be covered in Chapter 2 and also a literature review of experimental works by other researchers will be given.

A vertical breakwater is usually a composite breakwater consisting of a rubble foundation and a vertical wall. A rubble mound or berm can reduce the loads on a vertical wall. Using caissons as the vertical walls provides extremely stable structures in rough deep seas, see figure 1.1. We re-examine Greenhow's (2006) work on the effect of having a berm and a ditch on the pressure impulse on the wall and extend this model in Chapter 3. Figure 1.2 shows an example of a vertical seawall, having suffered damage.

Figure 1.2: Canvey's seawall in Essex, England is cracked due to high pressure arising from wave breaking on the wall. (image taken from http://www.echo-news.co.uk/)

The removal of blocks from the front of the seawall can cause further damage to a structure in failure mode. We carry out the analysis using pressure-impulse theory by consider the missing block region to be filled with fluid and always submerged below the impact region in Chapter 4.

In Chapter 5 and Chapter 6 we consider an application of relevance to an oil-rig or a pier. We have a small deck on the top of a seawall which is very close to the water level. We consider firstly a wave travelling from the right impacting against the wall in Chapter 5 and secondly the wave impact upwards on a horizontal surface in Chapter 6. We set up the problem in a similar manner to the previous chapters, and solve using pressure-impulse theory.

For an oscillating water column wave energy device with turbine valve open/closed, or sloshing impact in liquid carrier transport, violent wave motion can occur when the wave impacts on a vertical baffle. We are interested in studying the effect of having a baffle on the pressure impulse, with different baffle locations. A full description of this problem is given in Chapter 7.

A simple overtopping model is also covered but not in all chapters. Wave overtopping can occur when waves break against seawalls throwing water and spray over the top the structure. As a result, wave overtopping is an important parameter for the design of many coastal structures. Underestimates for this factor will cause the failure of seawalls to function properly. Functional failure also refers to cases where, for example, waves generated by storms run up the inclined face of a sea defence and cause large overtopping discharge, not only leading to flooding, but also building damage, disruption of infrastructures and loss of life. An example of the failure of a coastal defence during a storm was in the North Sea in 1953 and caused extensive flooding on Canvey Island, UK with the loss of 59 lives reported by Offord (2011). This run-up mechanism for overtopping is not considered in this thesis.
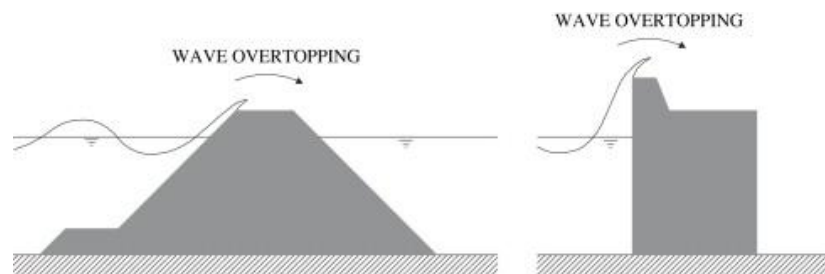
Figure 1.3 : Wave overtopping definition sketches of run up and impact generated overtopping. Images from J. Geeraerts *et al.* (2007), figure 1.

Wave overtopping cannot be completely avoided due to the random nature of the waves (or extreme events such as tsunami) and due to the high building costs of high seawalls and the possible damaging effects on the surrounding environment. For example in Japan, the effectiveness of building tsunami walls of up to 4.5 m (13.5 ft) high in front of populated coastal areas has been questioned. An earthquake triggered an extremely destructive tsunami in March 2011, and the seawalls failed catastrophically, as the tsunami was higher than the barrier. Building larger and stronger seawalls to protect

large areas would have been too costly. However, for successful protection of any area, the capacity to construct seawalls that can withstand the largest wave forces during storm conditions and build high enough to prevent overtopping is needed. Recent research programmes into wave overtopping of coastal structures include VOWS (Violent Overtopping of Waves at Seawalls, http://www.vows.ac.uk/) and CLASH (Crest Level Assessment of Coastal Structures By Full Scale Monitoring, Neural Network Prediction and Hazard Analysis on Permissible Wave Overtopping, http://www.clash-eu.org). The objectives of the VOWS project were to develop new or improved prediction formulae for overtopping discharges, while the CLASH project measured overtopping discharge at full-scale on a vertical seawall and produced a generic prediction method based on experiments at coastal sites such as at Samphire Hoe, UK and in the laboratory. The guidelines and prediction method will be used for design, safety assessment for coastal structures, risk assessment of coastal areas, and all works where crest height of coastal structures play an important role.

Figure 1.4 : Violent wave overtopping at the Samphire Hoe seawall, UK, taken from CLASH project, http://www.clash-eu.org .

There is also a group called Eurotop Team, who produced an Assessment Manual for Wave Overtopping of Sea Defenses and Related Structures (http://www.overtopping-manual.com/). Their manual gives guidance on analysis and prediction of wave overtopping for flood defences attacked by wave action. The main contributions to this manual have been derived from many researchers, included VOWS and CLASH.

Oumeraci (1994) has conducted a review and analysis of vertical breakwater failures. He suggested that the three main categories of reasons for failures are (a) inherent to the

structure itself, (b) the hydraulic conditions and loads, and (c) the morphology of the base of the seawall and the seabed. The major reasons for the failures are recorded as being due to the overtopping and, erosion of rubble mound foundations, seabed scour and breaking waves. This forms a strong motivation for undertaking the present work.

a) sliding   b) overturning   c) erosion beneath seaward and shoreward edges

d) seabed scour and toe erosion
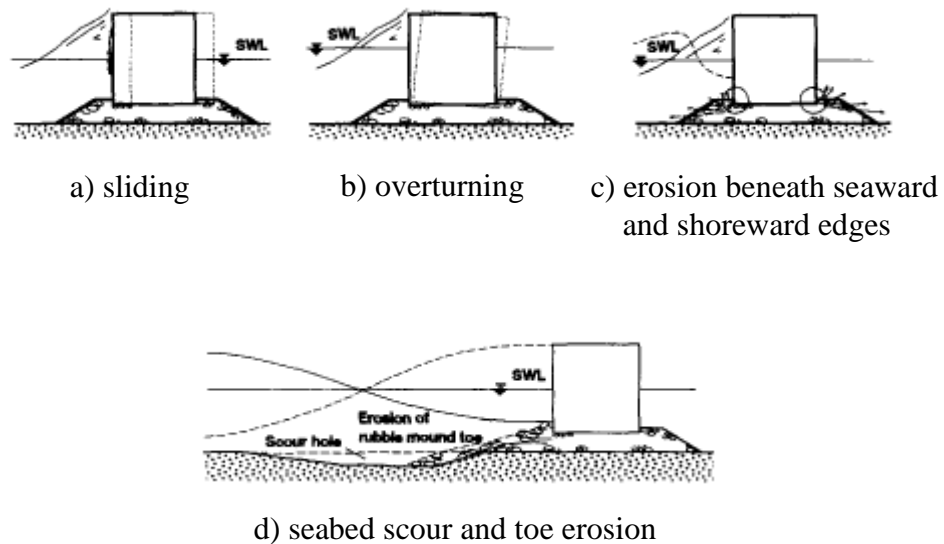
Figure 1.5: Failure modes of vertical breakwaters, images from Oumeraci (1994), figure 10.

In the UK, a large proportion of the coast is currently suffering from erosion, as reported by Masselink and Russell, in the Marine Climate Change Impacts Partnership (MCCIP), Scientific Review, (2007-2008). Of the 17,281 km length of the UK coastline, 3,008 km are currently experiencing erosion. The highest coast length eroding is reported in Yorkshire and Humber which is 56.2% of its coast length. Erosion is also reported on almost two-thirds of the intertidal profiles in England and Wales. Both coastal erosion and steepening of the intertidal profiles are expected due to climate change, potentially causing sea-level rise and changes to the wave conditions. This will provide a significant challenge for coastal engineers to protect the coastlines.

The main objective of this study is to contribute to the understanding of vertical breakwaters by theoretical studies that might help engineers to estimate the pressure impulse on the wall for certain geometries. Development of simple mathematical

models for the impact and overtopping, and the development and study of detailed numerical models of impulse and overturning moments are undertaken. It is also hoped that this study will be considered by engineers and designers to predict the design wave load conditions, to help ensure the stability of the structures.

In this study the influence of how different geometries of rectangular structures affect the pressure impulses on the wall have been investigated. This has been achieved through extending studies from the existing literature, especially the pressure impulse theory used by Cooker (1990).

The formulation for each problem is solving by using a basis function integral method and a hybrid collocation method. Then we truncate the Fourier series and find the Fourier coefficients by solving a matrix system using MATLAB.

1.2   Contributions to knowledge

In this section the contributions of this thesis to knowledge are summarised into theoretical and engineering significance as follows:

- The pressure impulse has been extended to a range of geometries.
- A secular term in pressure impulse solution is needed for some problems.
- The work of Wood and Peregrine (1997) is confirmed by using hybrid collocation method.
- Difficulties with using the Fourier method encountered by Greenhow (2006) have been largely resolved by using a collocation method.
- The total impulse and moment impulse for berm, ditch and missing block problems are given theoretically.
- The pressure impulse for vertical structures with a horizontal deck is given theoretically for different impact regions.
- The calculations of pressure impulse, total impulse and moment impulse for several baffle problems are given theoretically.

CHAPTER 2

WAVE IMPACTS ON A VERTICAL SEAWALL

2.1　Introduction –A Literature Review

The engineering importance and intrinsic interest of wave impact on coastal structures has attracted many researchers and experimenters for many years. Among the earliest is Bagnold (1939) and his colleagues who formed a committee to investigate the nature of the shock pressure exerted on the vertical seawall when a wave strikes it. The research in this area then evolved theoretically and experimentally, both at model and full scale and generally confirmed Bagnold's observations.

The results of laboratory (e.g. Bagnold, 1939; Chan and Melville, 1988; Kirkgöz, 1991; Chan, 1994; Hattori et al., 1994; Chiu et al., 2007) and full-scale experiments (e.g. Blackmore and Hewson, 1984; Bullock et al., 2001, 2007; Hofland et al., 2010) have made further contributions to the knowledge of pressures occurring during wave impact and its effects on coastal structures. This is important for improving the design of coastal structures such as breakwaters and seawalls. This previous work is divided into three categories as described below.

2.1.1 Model scale/laboratory tests

The laboratory and field tests brought new insights into the wave impact phenomenon both in terms of pressure magnitudes and durations. The researchers and experimenters provided us with new information and improved our understanding of the physics and the characteristics of impact pressures. From these studies and experiments, it becomes clear that when waves break directly onto a vertical seawall, they are likely to yield high shock pressures of very short duration compared with the pressures caused by non-breaking waves.

Bagnold (1939) investigated the problem of wave pressures on coastal structures using wave-tank models. He suggested that a pressure rises to a high peak value, p_{pk}, of very short duration, Δt, which is normally 1-10ms, with the larger pressure peaks having shorter duration. He showed that the product $p_{pk} \Delta t$ is a more consistent measure of impact and led him to consider the integral of pressure over the impact time, called the pressure impulse, *P,* as used in this thesis.

Chan and Melville (1988) conducted laboratory experiments on the impact pressures due to deep-water breaking on a surface-piercing flat plate. They claimed that the dynamics of trapped air during impact may contribute to both higher pressures and pressure oscillations. The characteristics and distributions of impact pressures depend on wave-breaking location. The results are confirmed by Chan (1994) who also conducted experiments on deep-water plunging-wave impacts on vertical structures. The distribution of peak pressures obtained from his experiments is examined and compared with theoretical pressure-impulse used by Cooker and Peregrine (1990) in Chan (1994) and good agreement was found.

Breaking wave impact on vertical walls was studied experimentally by Kirkgöz (1982). He found that a breaking wave having its front face parallel to the wall produces the greatest shock pressures. He further indicates that the maximum impact pressures occur when the wave breaks directly on the wall rather than breaking in front of the wall or not quite breaking. Based on his experiments Kirkgöz (1991) then claimed that backward-sloping walls (inclined up to 45^0 to the vertical) can experience higher impact

pressure than vertical walls. In Hattori et al.'s, (1994) experiments, they observed after the peak of the impact pressure, pressure oscillations may be observed due to the air pocket trapped between the wall and the water surface. Among such impacts the highest impact pressures, of very short duration, occurred when the smallest air pocket was trapped between wall and the vertical wave face during impact.

2.1.2 Full-scale measurement

Blackmore and Hewson (1984) carried out full-scale measurements of wave impacts on seawalls in the South and West England using modern measuring and recording techniques. They investigated four seawalls of different profiles ranging from curved to flat to stepped and different types of foreshores, but the report is confined to the data from curved seawalls due to limited data from the other three sites. Here relatively small impact pressures were measured, compared to those measured by other full-scale experiments, mainly due to the high percentage of air entrained in the wave crests.

Bullock et al. (2001) conducted experiments on the influence of air and scale on wave impact pressures. The field measurements were performed at the Admiralty Breakwater, Alderney. In their study, Bullock et al., (2001) found that the volume fraction of aeration is higher in seawater than freshwater. They also found that the peak impact pressures tended to be higher with freshwater waves than seawater waves and concluded that entrained air reduces the maximum impact pressure. This is broadly compatible with Lundgren's (1969) ideas concerning the sound velocity, c_s decreasing rapidly as a function of increasing aeration in bubbly fluid resulting to the decreasing of peak pressure for water hammer pressure, $p \propto \rho c_w c_s$ where c_w is wave impact velocity and ρ is the density. c_s can decrease from 1500m/s to 20 m/s with increasing air fraction up to 10% by volume.

The characteristics of impacting waves were again investigated by Bullock et al. (2007) in their large-scale regular wave tests on vertical and sloping walls. They proposed that the wave impacts depend on the breaker conditions. They also suggest that the high level of aeration does not always reduce the peak pressure but can also increase both the

force and impulse on the structure in some cases. The pressures, forces and impulses on the sloping wall were found to be lower than those on the vertical seawall.

Recently Hofland et al., (2010) have conducted large scale measurements of pressure fields on a vertical seawall under wave impacts. These measurements were done in collaboration with Joint Industry Project Sloshel on sloshing in LNG tanks using high spatial and temporal resolution. They found that the 'flip-through' impacts created the largest peak pressures and peak forces but this occurred very rarely in a random wave field. The 'flip-through' is caused by violent pressures on the roof of the LNG tank which occur without impact of liquid on the wall and is independent of the global geometry and dynamics, being a local phenomenon (Peregrine, 2003). A theoretical model has been given by Cooker (2010). Large forces created by air pocket impact were also observed.

Recent studies have been made by Cuomo et. al., (2010, 2011). Within the VOWS (Violent Overtopping by Waves at Seawalls) project (Cuomo, 2010), a series of large scale physical model tests have been carried out. A new prediction formula was introduced and compared with previous measurements from physical model tests, giving satisfactory results. Cuomo et. al., (2011) then presented a new approach to the definition of loads for use in performance design of vertical structures subject to breaking wave impacts.

2.1.3   Theory

Now, we will look at previous theoretical studies of wave impacts on coastal structures. Weggel and Maxwell (1970) and Partenscky and Tounsi (1989) have modelled the wave impact on vertical walls by solving the wave equation in a compressible fluid. In this thesis, we assume that the fluid is incompressible so we take the fluid velocities to be much less than the speed of sound, c_s. However compressibility is important in wave impacts where air is trapped in the water, see Cooker and Peregrine (1995).

Cooker and Peregrine (1990) modelled the wave as a rectangular region which is filled by fluid as in figure 2.4.1. We will discuss this theory more in the next section as we use

this theory and compare our results with Cooker and Peregrine (1990) throughout our work in this thesis. Their theory has been compared with experimental works such as Weggel and Maxwell (1970) and Partenscky and Tounsi (1989) by Cooker and Peregrine (1990). The shape distributions of peak pressure have been compared using the chosen value of μ (see §2.4) by the experimenters in their own mathematical model and the agreement has been found. Cooker and Peregrine (1995) use the theory for studies of impact of deep water waves, impact in a container, the impact of a water sheet on still water and a triangular wave. They concluded that pressure impulse field is insensitive to variations of the wave's shape at distances greater than half the water depth from the impact region.

Mamak and Kirkgöz (2004) developed a theoretical approach for the pressure impulse on a vertical wall using boundary element methods and the results show good agreement with experimental data. They concluded that if the impact pressure rise time is known, the pressure impulse model can be used to predict the wave impact pressures on vertical seawalls.

Okamura (1993) presented theoretical work on wave impacts on an inclined plane wall. He indicated that the largest pressure impulse on a wall occurred when the wall is near to vertical, in contrast to the results of Kirkgöz (1991). The application of pressure impulse theory has been used to show that the impulsive force due to a wave can move a large object near a seawall. Cooker and Peregrine (1992), considered a hemispherical boulder on the bed, and Cox and Cooker (1999), considered a spherical boulder. They found that the impulse is directly proportional to the boulder volume and indicated that the impulse on a long thin body is larger compared to low wide ones and that such shapes will move the farthest. Another application on pressure impulse theory was for impact in containers by Topliss, (1994) and impacts under a deck by Wood and Peregrine, (1996) which we will discuss more in Chapter 6. Wood and Peregrine (1998) studied three-dimensional examples for wave impact on a vertical seawall. They suggested that the three-dimensional model should be included if waves have a crest width less than twice the water depth.

Clearly there is a good deal of uncertainty and sensitivity in the results for wave impact. In a practical situation, many parameters such as the wave climate will not be known with any accuracy. Even if the wave spectrum is known, this is usually recorded offshore, requiring same sort of (linear) transfer function to estimate the wave climate at the seawall. What is more, the higher spectral moments, $m_n = \int_0^\infty w^n S(w)\,dw$ where w is the radian frequency and $S(w)$ the frequency spectrum, will generally be unknown. Wave breaking, according to linear wave theory, is known to depend on m_4 which is sensitive to the cut-off frequency of the spectrum, see Srokosz (1986) and Greenhow (1989). Not only is the wave climate unknown, but the aeration of the water will also be subject to uncertainty. This affects rather dramatically the speed of sound in the water/ bubble mixture and hence the value of the acoustic pressure that acts as a maximum cut-off for pressure calculated by any incompressible model. Given the above, it seems sensible to exploit the simple pressure impulse model used in this thesis. Naturally, fully non-linear calculations, such as theory of Cooker (1990), give more accurate calculation of pressure for a given wave, but, as noted above, waves are far from being "given" in the real situation. Ultimately what is need is a balanced reduction of all the uncertainties; this would then justify the use of more sophisticated hydrodynamic models, to calibrate the pressure impulse model and justify its use. For now we note that comparisons between different geometries can be made on a rational basis. Moreover, using a typical water depth of say $H = 2m$, and the corresponding shallow water wave speed $\sqrt{gH}$ as the impact velocity, and an impact time of 0.1s, the present results for pressure impulse P roughly agree with design specification for impact peak pressures of $4 \times 10^5\,Nm^{-2}$ (i.e $4 \times$ atmospheric pressure) as calculated by equation 2.2.3 below.

2.2   Pressure Impulse Theory

Cooker and Peregrine (1990, 1995) proposed that the pressure impulse P is defined as the integral of pressure with respect to time

$$P(x, y) = \int_{t_b}^{t_a} p(x, y, t)\,dt \tag{2.2.1}$$

where t_b and t_a are the times just before and just after the impact, x, y are Cartesian coordinates of position (this could be x, y, z for three-dimensional situations not considered here) and p is measured relative to atmospheric pressure. The pressure impulse idea removes time from the equations of motions, but p_{pk} (peak pressure) can be estimated from a calculated value P by assuming the pressure as a function of time during impact is approximately triangular, and $\Delta t = t_a - t_b$ is known, see figure 2.2.1 below.
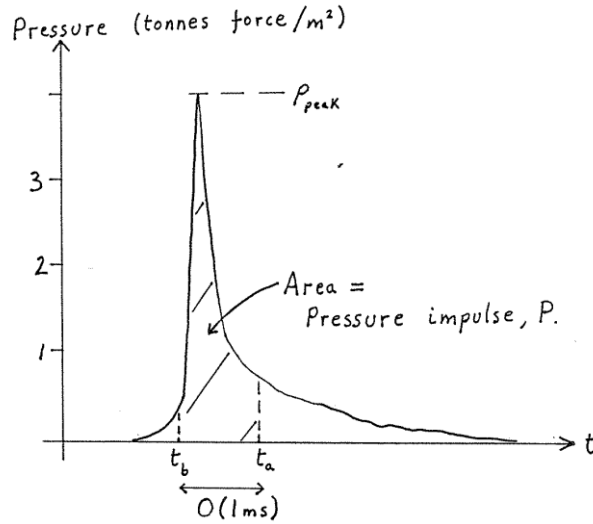
Figure 2.2.1: The sketch of pressure against time, image taken from Cooker (1990) figure 8.1.

Bagnold (1939) and Cooker and Peregrine (1990) pointed out that, despite the wide scatter in peak pressure, the product of $p_{pk}\Delta t$ remains approximately constant, thus;

$$P = p_{pk}\frac{\Delta t}{2} \tag{2.2.2}$$

So that

$$p_{pk} \approx \frac{2P}{\Delta t} \tag{2.2.3}$$

Since Δt is prone to uncertainty, any estimate of p_{pk} is also uncertain. For extreme impact p_{pk} may be very large and Δt very small, but the product given in (2.2.2) will remain finite and approximately constant for wave impacts from similar waves. From comparisons of their result with some experimental measurements, they justified that this simple theory using simple boundary conditions gives approximate solutions for various wave shapes. Here we refer throughout to the Cooker and Peregrine (1990)

14

model, a two-dimensional model for water wave impact on a vertical wall which is the base case used in this thesis. It is assumed that *P* is insensitive to the shape of the wave away from the impact region. This shape is therefore taken to be rectangular throughout. On the other hand the maximum impact pressure is sensitive to the alignment of the wave front with the impacted part of the wall. We assume a worst case scenario here of perfect alignment. However, since the impacts are of shorter duration than those wave oblique impacts, the pressure impulse should be less sensitive to the angle of alignment than maximum pressure.

2.3   Cooker's Model

Cooker and Peregrine (1990, 1995) proposed a mathematical model for pressure-impulse theory for impact between a region of incompressible and inviscid liquid and either a rigid surface or a second liquid region. The boundary conditions are defined below and the theory gives information on the peak pressure distribution and the velocity after impact as well. The use of 'impact pressure' as the generic term instead of 'shock pressure' to describe the large brief pressure of wave impact is suggested. The hydrostatic pressure is $\rho g H$, where ρ is density of water, *g* is gravity and *H* is height of the top of the wave above the bed is assumed to be very much smaller than the impact pressures. The 'impact zone' refers to the rigid surface area which is impacted by the moving liquid.

Figure 2.3.1 shows the basic model in the form of two-dimensional vertical cross-section of the coastline. The dotted line represents the incoming waves, and the full line represents wave after the impact. The interval between dotted line and full line on the rigid structure shows the area the location of the wave impact along the coastal structure and is known as the 'impact zone'.
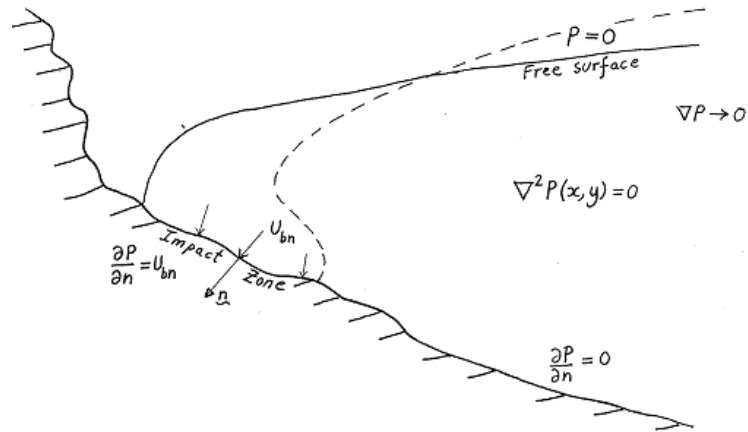
Figure 2.3.1: The sketch of realistic wave impact, image taken from Cooker (1990), figure 8.2.

Cooker (1990) then modelled the wave impact on a rigid structure as a rectangular region which is filled by fluid as figure (2.4.1). He assumed the rectangular region contained an ideal fluid and neglected any cushion of air. Bagnold (1939) proposed that the greatest pressure-impulse occurs due to adiabatic compression over a large area of the thin air cushion and the wave front must be almost plane and parallel to the wall at the moment of impact. This is not considered here but theoretical models for this have been developed by Faltinsen and Timokha (2009).

2.4   The Governing Equations

From the mathematical model proposed by Cooker and Peregrine (1990, 1995), the governing equations for the problem can be stated as below. The boundary conditions are shown in figure 2.4.2. The fluid is assumed to be incompressible and inviscid. However the fluid does not have to be irrotational for the pressure impulse model, see equation (2.4.5).

1. Let U_0, $L_0, \Delta t$, and p_s be velocity, length, time and pressure scales for the incident wave. Euler's equations, made dimensionless with respect to these scaling are:

$$\frac{\partial u}{\partial t} + \underbrace{\left[\frac{U_0 \Delta t}{L_0}\right]}_{G_1} (u.\nabla) u = -\underbrace{\left[\frac{\Delta t p_s}{\rho U_0 L_0}\right]}_{G_2} \nabla p - \underbrace{\left[\frac{g \Delta t}{U_0}\right]}_{G_3} j \qquad (2.4.1)$$

16

where j is a unit vector pointing upwards. Cooker's (1990) terms G_1, G_2, and G_3 are

discussed as below:

For a sudden impact, the impact time is much less than the time scale of the

evolution of the wave as a whole, i.e. $\Delta t \ll L_0 / U_0$. So, in (2.4.1), $G_1 = \dfrac{U_0 \Delta t}{L_0} \ll 1$,

and so this nonlinear term can be neglected. Furthermore, $G_3 = \dfrac{g \Delta t}{U_0} \ll 1$, so the

last term in (2.4.1) is also small and can be neglected. If $G_2 = \dfrac{\Delta t p_s}{\rho U_0 L_0} \sim 1$, then we

have a balance between the first and third term in (2.4.1) and Cooker has a proof this

is consistent with the statement:

"Impulse exerted on the wall~ Incident wave momentum."

By neglecting the small terms in (2.4.1), during the impact we have:

$$\frac{\partial u}{\partial t} = - \left[\frac{\Delta t p_s}{\rho U_0 L_0} \right] \nabla p \qquad\qquad (2.4.2)$$

We choose units so that $\Delta t p_s = |U_0| = L_0 = 1$, i.e. $p_s = \dfrac{\rho U_0 L_0}{\Delta t}$. In this cases

considered here we can choose to non-dimensionalise the problem by the

characteristic length, time and velocity being the water depth, duration of impact

and velocity of impact respectively. Then equation (2.4.2) shows that the pressure

impulse is scaled by $\rho U_0 L_0$. Equation (2.4.2) then becomes:

$$\frac{\partial u}{\partial t} = - \frac{1}{\rho} \nabla p \qquad\qquad (2.4.3)$$

2. From equation (2.4.3), integrating this with respect to time through the impact
   interval $[t_b, t_a]$, gives us

$$\int_{t_b}^{t_a} \frac{\partial u}{\partial t} dt = - \frac{1}{\rho} \nabla \left\{ \int_{t_b}^{t_a} p dt \right\} \qquad\qquad (2.4.4)$$

Using definition (2.2.1) for the pressure impulse P, (2.4.4) reduces to

$$u_a - u_b = - \frac{1}{\rho} \nabla P, \qquad\qquad (2.4.5)$$

where $\underset{\sim b}{u}$ and $\underset{\sim a}{u}$ are the fluid velocities at times immediately before and after impact, respectively. Taking the curl of the equation shows that the vorticity is conserved during the impact. For models of water waves we usually assume this flow is irrotational before the impact so it will also be irrotational after the impact. We assume that the flow is incompressible, by excluding the presence of bubbles in the fluids, so that $\nabla . \underset{\sim b}{u}$ and $\nabla . \underset{\sim a}{u}$ both vanish. Taking divergence of (2.4.5) shows that the pressure impulse satisfies Laplace's equation

$$\nabla^2 P(x, y) = 0. \tag{2.4.6}$$

Note that (2.4.6) does not involve time so we can solve boundary-value problems in a fixed domain which is a mean position for the fluid during impact.

3. The boundary conditions to be applied to Laplace's equation are readily found to be as follows:

(a) At a free surface, the pressure is constant and taken to be the zero reference pressure. Hence (2.2.1) gives

$$P = 0 \text{ on } y = 0 \tag{2.4.7}$$

(b) At a stationary (or even moving) rigid boundary, in contact with the liquid before and after the impulse, the normal velocity is unchanged so equation (2.4.1) gives

$$\partial P / \partial n = 0 \tag{2.4.8}$$

(c) Where liquid meets a solid boundary during impact, the change in normal velocity gives the normal derivative of pressure impulse. For the simplest case of a stationary or moving rigid boundary

$$u_{nb} = \frac{1}{\rho} \frac{\partial P}{\partial n}, \tag{2.4.9}$$

where u_{nb} is the normal component of the approach velocity of the liquid.

(d) Although not considered in this thesis, when liquid meets liquid two boundary conditions are needed on the common interface. One is that the pressure impulse is continuous:

$$P_1 = P_2 \tag{2.4.10}$$

18

Consideration of the change in velocity on each side of the interface gives

$$u_{1nb} - u_{2nb} = \frac{1}{\rho_1}\frac{\partial P_1}{\partial n} - \frac{1}{\rho_2}\frac{\partial P_2}{\partial n}, \qquad (2.4.11)$$

where subscript n denotes the components normal to the boundary and subscript b denotes the liquid velocities immediately before the impact. In all the above cases, an inelastic impact is assumed.
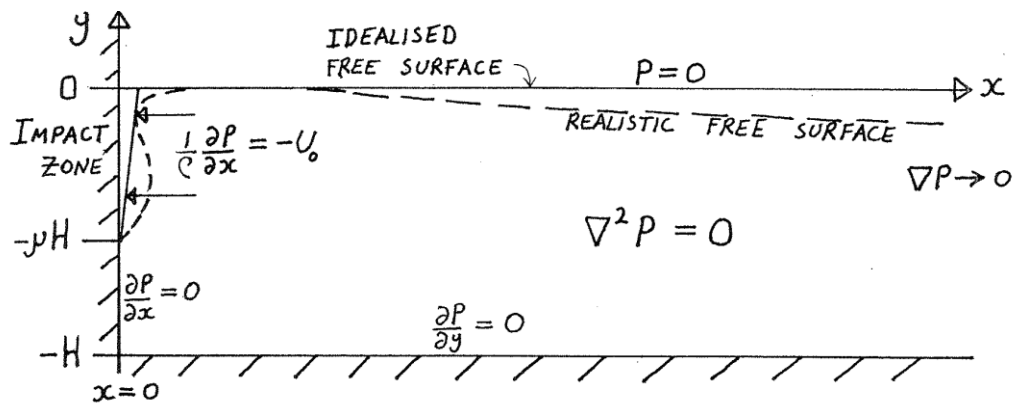
Figure 2.4.1: Governing equation and boundary conditions of theoretical model proposed by Cooker (1990), image taken from Cooker (1990) figure 8.3.

Since *P* is harmonic it satisfies the maximum principle, see Zauderer (1989). Hence *P* must take its maximum value on the boundary of the fluid region. Since *P = 0* on the free surface and distant boundary, then its maximum value must occur on one of the solid surfaces. This general result is respected by all calculations in this thesis.

A proof of the existence of a solution of boundary-value problems in general are difficult; here, however, since we construct a solution, that guarantees existence, assuming that the series of eigenfunctions actually converge throughout the fluid region. This is known to be the case for the seawall, see section 2.4.1, and is assumed for all other problems considered. For an elementary proof of uniqueness of the solution based on energy integrals, see for example Wright (2002). Although this proof is set up in terms of a Dirichlet condition on the boundary, it works without modification in the

present case of Dirichlet condition on part of the boundary and a Neumann condition on the rest. This leaves the issue of whether or not the problem is well-posed i.e. does the solution depend continuously on the boundary data? This is in fact the case, as follows easily from the maximum principle, see Frey (2008). This is important to underpin any numerical solution technique since it asserts that small errors in the boundary conditions will only cause small errors in the solution elsewhere in the fluid domain. The matching procedures used in this theses can also be justified by noting that, since the same boundary conditions are used for the fluid region and its two (or more) matching regions, the solution from matching will be the same throughout the fluid because of the uniqueness of the problem.

2.4.1 Impact on a seawall (Cooker model)

The solution of Laplace's equation, $\nabla^2 P = 0$, is given by separating variables, followed by imposing the mixed boundary conditions as below:

a) at free surface, air motion is ignored, hence the atmospheric pressure is constant and taken to be the zero reference pressure. This gives the Dirichlet boundary condition, *P = 0* as in equation (2.4.7).

b) At a stationary rigid boundary, in contact with the liquid before and after the impulse, the normal velocity must be zero before and after impact, so that gives the Neumann boundary condition $\partial P / \partial n = 0$, where;

- $n = x$, on the seawall, for $y \in [-H, -\mu H)$

- $n = y$, on the seabed, for $x \in [0, \infty)$

c) At the wall, at $x = 0$ and in the impact region we have a Neumann boundary condition

$$\frac{\partial P}{\partial x} = -\rho U_0 \qquad \text{for } y \in [-\mu H, 0) \tag{2.4.12}$$

where:

$0 \leq \mu \leq 1$: dimensionless constant indicating how much of the wall is hit

$H > 0$: total water depth at time impact, from seabed to top of wave

U_0 : impact speed (taken as negative as it is travelling along the *x*-axis in the negative direction.)

d) As $x \to \infty$, $P \to 0$: this is consistent with Cooker's $\nabla P \to 0$ statement in figure (2.4.1) since $P = 0$ on the free surface $y = 0$.

The solution for the boundary-value problem of figure 2.3 which satisfies the bed, free-surface and infinity boundary conditions is

$$P(x, y; \mu) = \sum_{n=1}^{\infty} a_n \sin\left(\frac{\lambda_n y}{H}\right) \exp\left(\frac{-\lambda_n x}{H}\right) \qquad (2.4.13)$$

where $\lambda_n = \left(n - \frac{1}{2}\right)\pi$ and the constants a_n are determined by solving the boundary conditions with given $\partial P / \partial x$ at $x = 0$, the wall

$$\left.\frac{\partial P}{\partial x}\right|_{x=0} = \sum_{n=1}^{\infty} -a_n \lambda_n \sin \lambda_n y$$

$$= \begin{cases} -\rho U_0 & \text{for } -\mu H \leq y \leq 0 \\ 0 & \text{for } -H \leq y < -\mu H \end{cases} \qquad (2.4.14)$$

Applying $\int_0^{-H} \dots \sin\left(\frac{\lambda_m y}{H}\right) dy$ to equation (2.4.14) and using orthogonality of the basis functions in the usual way gives

$$a_n = 2\rho U_0 H \{\cos(\mu \lambda_n) - 1\} / \lambda_n^2. \qquad (2.4.15)$$

so that the pressure impulse at $x = 0$ is given by

$$P(0, y; \mu) = 2\rho U_0 H \sum_{n=1}^{\infty} \{\cos(\mu \lambda_n) - 1\} \lambda_n^{-2} \sin\left(\frac{\lambda_n y}{H}\right) \qquad (2.4.16)$$

This analytic solution gives quantitative predictions of the pressure impulse on the wall. The series in (2.4.16) is rapidly convergent because of squared term in the denominator.

2.4.2   Alternative model

Cooker and Peregrine (1995) modified Cooker's model by using hyperbolic terms instead of exponential terms in the Fourier series. They suggested that the exponential decay as $x \to \infty$ in Cooker (1990) can be changed to $P = 0$ at a finite boundary $x = B$ instead of as $x \to \infty$. This change still satisfies the Laplace's equations $\nabla^2 P = 0$ as the

solution for the mixed boundary-value problem and the model can be illustrated as in figure 2.4.2.
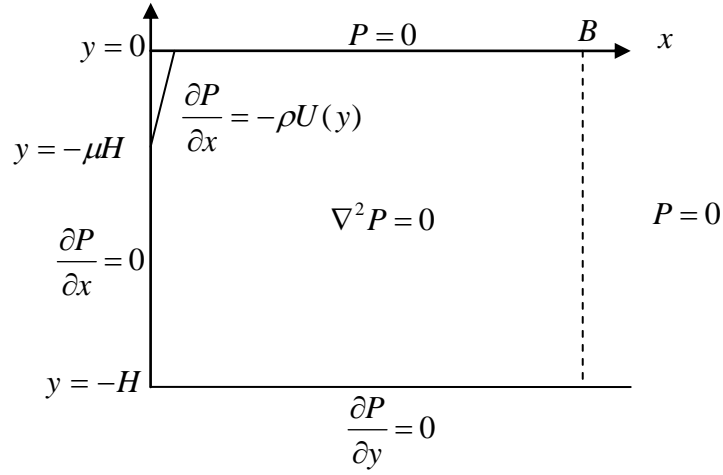
Figure 2.4.2: The boundary-value problem for pressure impulse

The solution of Laplace's equation in the Fourier series form can be written as

$$P(x, y; \mu) = \sum_{n=1}^{\infty} a_n \sin\left(\frac{\lambda_n y}{H}\right) \frac{\sinh(\lambda_n(x - B)/H)}{\cosh(\lambda_n B/H)} \qquad (2.4.17)$$

with $a_n = 2\rho U_0 H\{\cos(\mu\lambda_n) - 1\}/\lambda_n^2$ where $\lambda_n = \left(n - \frac{1}{2}\right)\pi$.

Here U is a function of y. Cooker (1990) uses several forms for this impact speed profile, but the present thesis assumes it is of the form $\frac{\partial P}{\partial x} = -\rho U_0$ as in the original Cooker (1990) model, giving the Fourier coefficients of equations (2.4.15). The standard results for Cooker's model shown as figure 2.4.3 and pressure impulse on the wall for Cooker's model shown as figure 2.4.4

	3-D plot	Contour plot
$\mu = 0.1$		
$\mu = 0.5$		
$\mu = 0.8$		

23
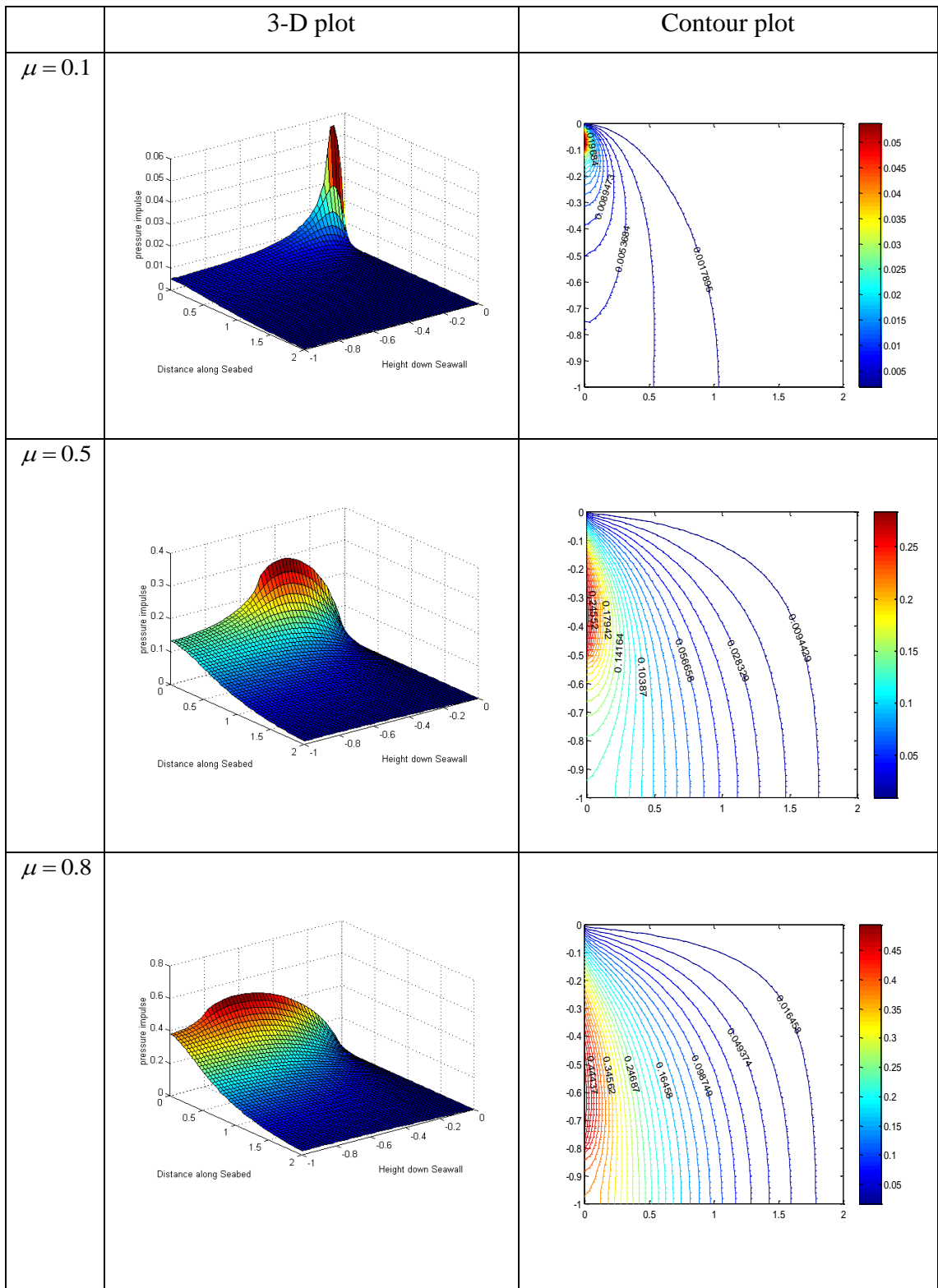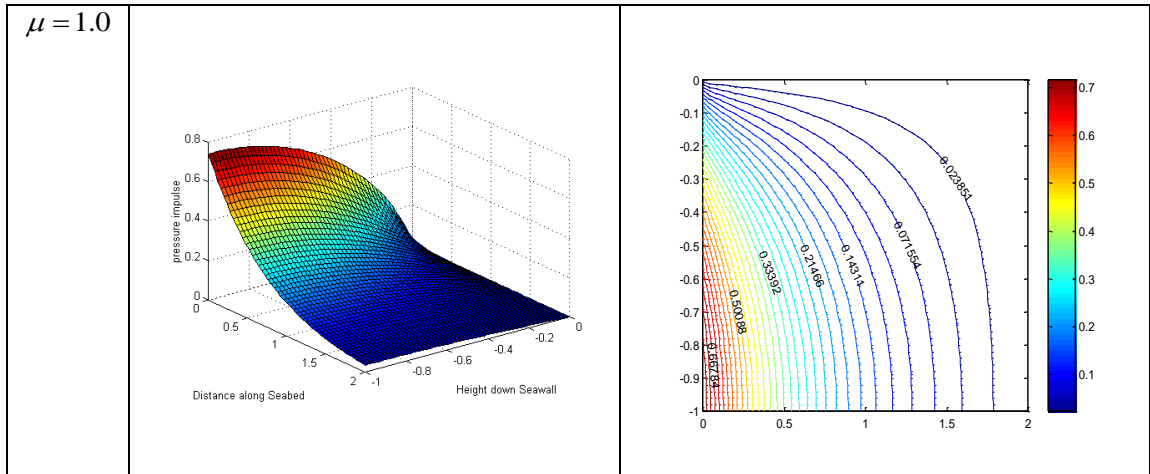
Figure 2.4.3: Standard result for non-dimensional pressure impulse Cooker's model for varying μ with $B = 2, H = 1, N = 50$. Note the vertical scales in 3-D plots.

For the next chapter, we will use the pressure impulse solution in hyperbolic terms in Fourier series for our next problem. The trigonometric and the hyperbolic terms will depend on the modelling of the problem. We also will use Cooker and Peregrine (1995) solution for comparison with our result.

Peregrine (2003) indicated that the pressures measured from experiment are much greater than would be expected. On the other hand the pressure impulse, which is pressure integrated with respect to time, shows greater consistency. He also suggested that there are a few important parameters that influence the impact of a wave at a wall that need to be considered. The parameters are: the mean water depth at the wall, the geometry of the wall, the shape of the wave as it meets the wall, and the water depth at the wall. The assumptions that we have made to model this theory are that the wall is vertical and the seabed is horizontal immediately in front of the wall.
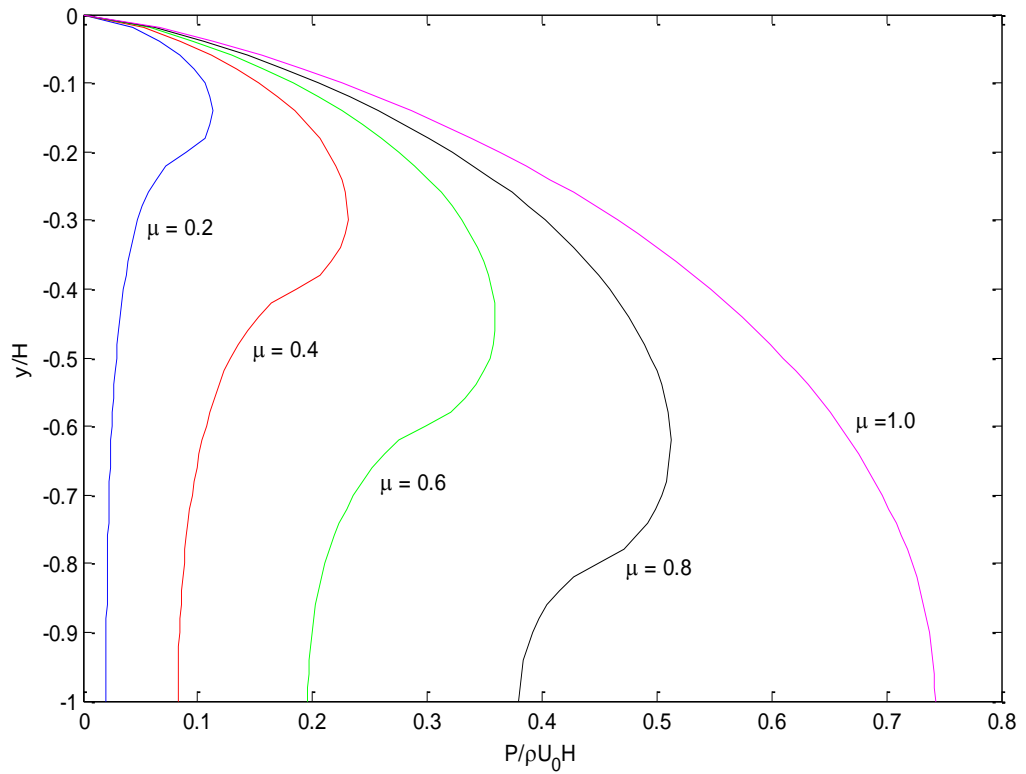
Figure 2.4.4: The pressure impulse on the wall, $P(0, y)$, for $\mu = 0.2$, 0.4, 0.6, 0.8 and 1.0. The maximum pressure is $0.742\,\rho U_0 H$ when $\mu = 1.0$ and occurs at $y = -1$.

Whilst the impulse on the wall has obvious engineering significance, the impulse on the seabed is also of interest. It can instantaneously liquify any sand by driving water into it. This can lead to destablisation of the foundation. Results for the seabed impulse are given in figure 2.4.5.
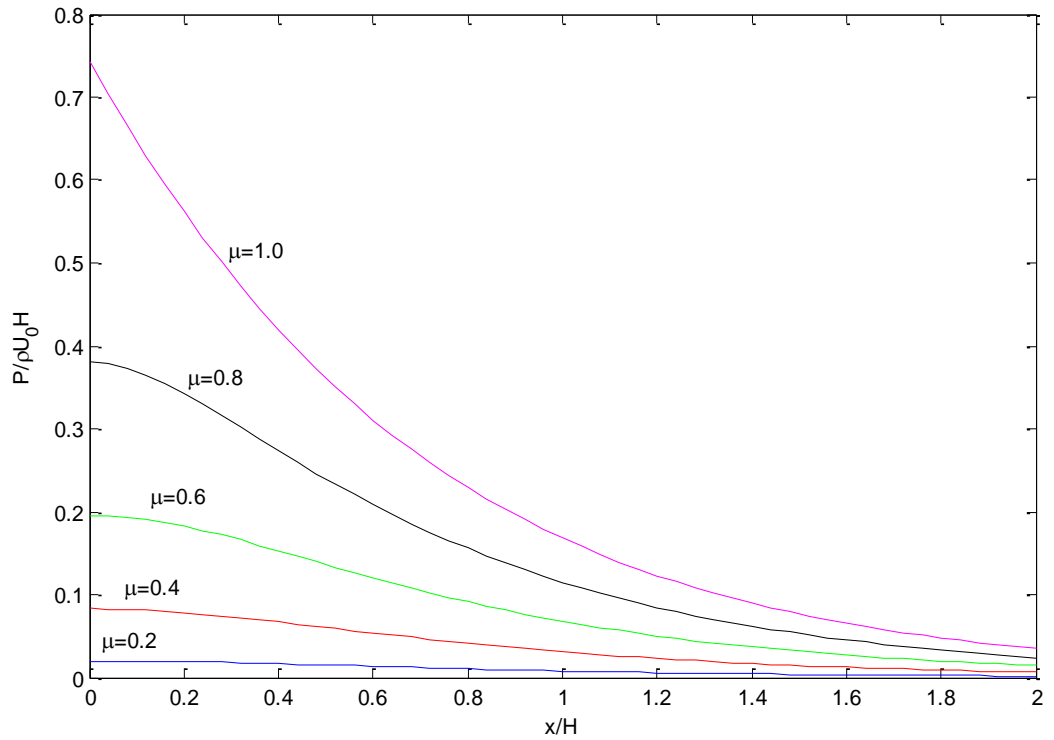
Figure 2.4.5: The pressure impulse on the seabed, $P(x,-1)$, for $\mu = 0.2$, 0.4, 0.6, 0.8 and 1.0.

2.5   Total impulse and moment impulse

Other quantities of engineering significance, the total impulse and moment impulse, are given by Cooker (1990). These quantities are important to help engineers avoid seawall failures due to seabed scour, wave loads on structures, and overturning. A large impulse on the seabed can lead to excavation which can contribute to failure, for example the failure of Algiers Mustapha Breakwater recorded by Oumeraci (1994). The total impulse I_w on the wall is the integral of the pressure impulse (2.4.17) at $x = 0$ over the wall, that is

$$I_w = \int_{-H}^{0} P(0, y)\,dy \tag{2.5.1}$$

This gives

$$I_w = 2\rho U_0 H^2 \sum_{n=1}^{\infty} \{1 - \cos(\mu\lambda_n)\} / \lambda_n^{\,3} \tag{2.5.2}$$

The same calculation for the total impulse on the seabed is the integral of pressure impulse (2.4.17) at $y = -H = -1$ with respect to x.

$$I_s = \int_0^B P(x, -H)dx \tag{2.5.3}$$

We take the left/down direction as positive total impulse as in figure 2.5.1.
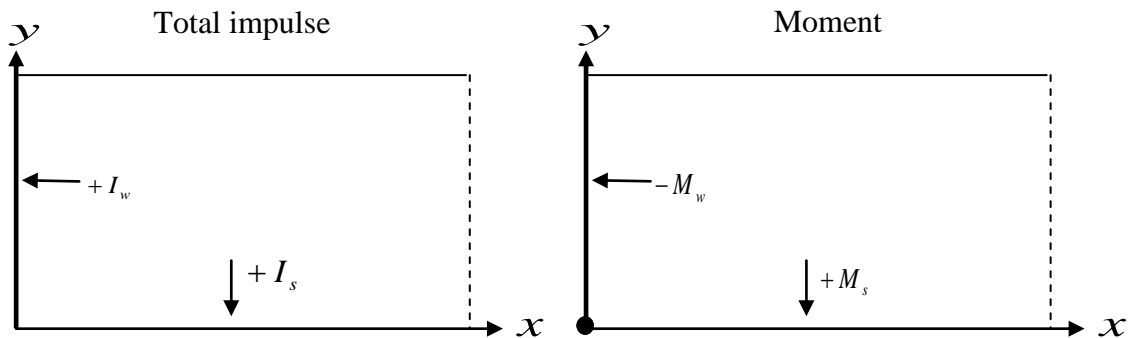
Figure 2.5.1: The direction of the total impulse and moment impulse.

The results for total impulse on the wall and on the seabed for Cooker's model are given in the figure (2.5.2). As more of the seawall is impacted (increasing μ) the total impulse also increases. The unit for total impulse is $\rho U_0 H^2$.
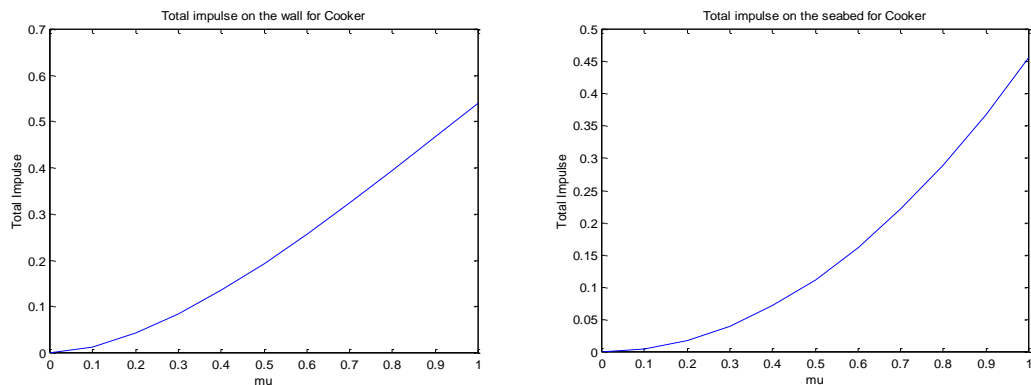
Figure 2.5.2: On the left, total impulse on the seawall (from equation (2.5.2)) and on the right, total impulse on the seabed (from equation (2.5.3)) for Cooker's model.

The pressure impulse acting on the coastal structure generates a moment about the base of the wall that can, to a certain extent, move or even topple it. The moment impulse on the wall M_w, about an axis at its bottom (see figure 2.5.1), due to pressure impulse on the wall, is given by

$$M_w(\mu) = -\int_{-H}^{0}(y + H)P(0, y)dy \tag{2.5.4}$$

This gives us

$$M_w(\mu) = 2\rho U_0 H^3 \sum_{n=1}^{\infty}\{1 - \cos(\mu\lambda_n)\}\left(1 - [-1]^n / \lambda_n\right)/ \lambda_n^3 \tag{2.5.5}$$

M_w is negative for forces directed in a clockwise sense about the foot of the wall. The same calculation is done for calculating moment impulse on the seabed, M_s.

$$M_s(\mu) = \int_{0}^{B} xP(x, -H)dx \tag{2.5.6}$$

which gives us

$$M_s(\mu) = 2\rho U_0 H^3 \sum_{n=1}^{\infty}\{1 - \cos(\mu\lambda_n)\}/ \lambda_n^4 \tag{2.5.7}$$

The following graph shows the variation of the moment impulse on the seawall and the seabed for Cooker's model. The unit for moment impulse is $\rho U_0 H^3$.
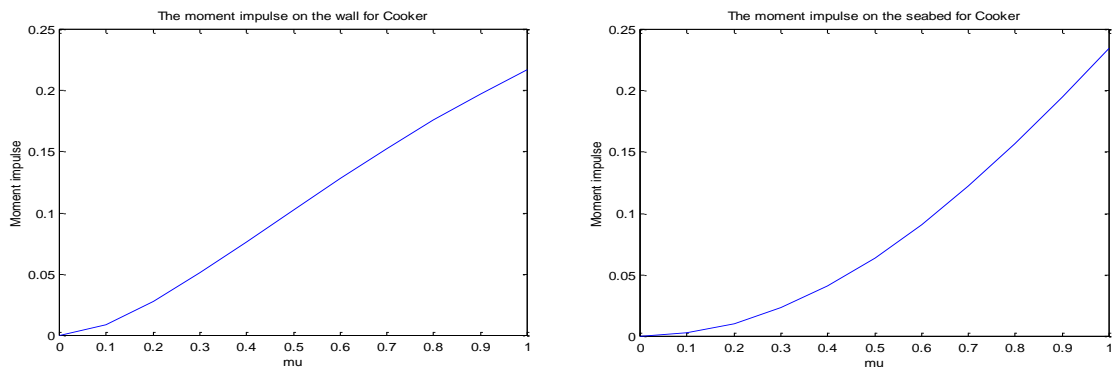
Figure 2.5.3: On the left, moment impulse on the wall (from equation (2.5.5)), and on the right, moment impulse on the seabed (from equation (2.5.7)) for Cooker's model.

2.6   Nondimensionalisation

We have nondimensionalised our calculations for all problems in this thesis. Taking the Cooker's Model (figure 2.4.2) as example, the boundary conditions have been nondimensionalised by choosing a new set of nondimensional variables based on the variables that naturally appear in the problem. Dashed variables denote nondimensionalised quantities.

$$x = x' H, \ y = y' H, \ B = B' H, \text{and} \ P' = \frac{P}{\rho U_0 H} \tag{2.6.1}$$

Derivatives are correspondingly

$$\partial x = \partial x' H, \ \partial y = \partial y' H, \text{and} \ \partial P' = \frac{\partial P}{\rho U_0 H} \tag{2.6.2}$$

At the wall, substituting the non-dimensional variables into (2.4.17) gives

$$\frac{\partial P}{H \partial x'} = -\rho U(y) = -\rho U_0 \tag{2.6.3}$$

So that

$$\frac{\partial P}{\partial x'} = -\rho U_0 H$$

$$\frac{\partial P'}{\partial x'} = -1 \tag{2.6.4}$$

The same steps are done to the other boundary conditions and the solution; rather than introduce a new notation for all variables, we drop the prime notation giving us the dimensionless boundary-value problem for pressure impulse as figure 2.6.1. The dimensionless solution for the Fourier series becomes

$$P'(x, y; \mu) = \sum_{n=1}^{\infty} a_n \sin(\lambda_n y) \frac{\sinh(\lambda_n (x - B))}{\cosh(\lambda_n B)} \tag{2.6.5}$$

with $a_n = \int_{-\mu}^{0} \frac{-2}{\lambda_n} \sin(\lambda_n y) dy$ where $\lambda_n = \left(n - \frac{1}{2} \right) \pi$

resulting in

$$P'(x, y; \mu) = \sum_{n=1}^{\infty} \frac{2}{\lambda_n^2} (1 - \cos(\mu \lambda_n)) \sin(\lambda_n y) \frac{\sinh(\lambda_n (x - B))}{\cosh(\lambda_n B)} \tag{2.6.6}$$

The dimensionless boundary conditions are given in the figure (2.6.1).
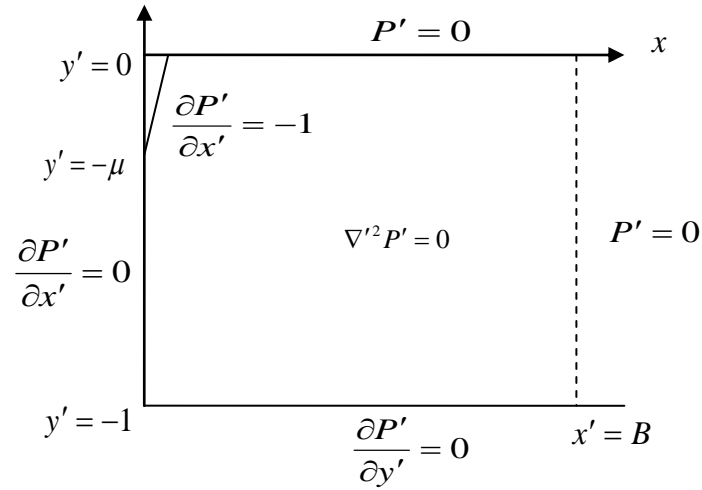
Figure 2.6.1: The dimensionless boundary-value problem for pressure impulse, showing μ, B are the dimensionless parameters.

We can find the physical parameters involved in the problems and the quantity units and dimensions in the next table. We can show that P is a dimensionless quantity given that

$$P = \int_{t_b}^{t_a} p \ dt = \frac{[T][M][L][T^{-2}]}{[L^2]} = [M][L^{-1}][T^{-1}] \tag{2.6.7}$$

has the same dimensions as

$$\rho U_0 H = [M][L^{-3}][L][T^{-1}][L] = [M][L^{-1}][T^{-1}] \tag{2.6.8}$$

The scaling pressure for pressure impulse, P total impulse, I and moment impulse, M are respectively given as below:

$$P = \frac{P^{'}}{\rho U_0 H}, I = \frac{I^{'}}{\rho U_0 H^2}, \text{ and } M = \frac{M^{'}}{\rho U_0 H^3} \tag{2.6.9}$$

Table 2.6.1 below shows the physical parameters involved in this thesis.

Table 2.6.1: The physical quantities.

Physical Quantity	Symbol for the Quantity	SI Unit	Dimensions
density	ρ	kgm^{-3}	$[M][L^{-3}]$
velocity	U_0	ms^{-1}	$[L][T^{-1}]$
depth	H	m	$[L]$
force	F	N	$[M][L][T^{-2}]$
Impact time	t	t	$[T]$
area	A	m^2	$[L^2]$
Pressure Impulse	P'	Nsm^{-2}	$[M][L^{-1}][T^{-1}]$
Total Impulse	I'	Nsm^{-1}	$[M][T^{-1}]$
Moment Impulse	M'	Ns	$[M][L][T^{-1}]$

2.7 Overtopping

Violent wave overtopping occurs when waves break against sea walls throwing water and spray over the top, see VOWS. Oumeraci (1994) has reported that observations show that all vertical structures were heavily overtopped by the waves. So the volume of water per unit length of seawall (here called overtopping) is very important to estimate, and the design of coastal structures should include a specification of freeboard that allows an acceptable amount of overtopping. Designing structures with sufficient freeboard should provide safety for people and vehicles on and behind the structure and limit damage to the structure itself as well as damage to properties behind the structure. It should include a safety factor to guarantee that economic activities on and behind the structures can be assured during bad weather conditions, Geeraerts *et al.* (2007).

A theoretical study of overtopping of waves at a wall was undertaken by Jervis and Peregrine (1996). The results show the overtopping volume per wave is roughly exponentially decaying with the height of wall above the still water level i.e. freeboard.

They computed the waves with an accurate irrotational flow solver. They also took the effects of surface tension into account to study the possibility of errors in scaling experimental results to prototype scales.

Figure 2.7.1: Overtopping at Whitby, UK, image taken from
http://www.scmdt.mmu.ac.uk/cmmfa/projects/overtopping.html

A prediction tool and hazard analysis of wave overtopping was given by Geeraerts *et al.*(2007). They show that seawalls reduce wave overtopping but do not stop it. Building a seawall with no overtopping is extremely expensive, so an acceptable amount of overtopping should be specified. They have suggested limits for overtopping mean discharges and peak volumes for public safety and agreed with Franco *et al.* (1994), the upper limit for mean discharge of overtopping for unaware pedestrians is 0.03 (litres/s per m) and 0.01-0.05 (litres/s per m) for moderate or high speed vehicles. They also have established a generic prediction method of wave overtopping using the technique of neural network modelling which can be found at http://www.clash-eu.org.

Allsop *et al.* (2005) presented a summary of prediction methods for wave overtopping from a number of UK and European research projects spanning 10 years. The prediction methods for overtopping on slopes, vertical walls, battered seawalls, composite walls and broken waves are well discussed. They also have highlighted two conditions of waves: 'pulsating' conditions occur when waves are small with regard to the local water

depth, and 'impulsive' conditions occur when waves are large with regard to local water depth. These two conditions need to use different prediction tools.

Franco *et al.* (1994) conducted laboratory tests to analyse the overtopping volumes for a variety of sloping and vertical structures. They focused on cases where waves do not break in pulsating or impulsive conditions. Mean overtopping discharges for functional safety (vehicles, pedestrians and buildings) and structural safety (embankment seawall and revetment seawalls) were also proposed. However the engulfment mechanism of these experiments is different to the impact cases considered in this thesis, so the overtopping results of Franco *et al.* will not apply.

Pullen *et al.* (2004) conducted a full-scale measurement to identify mean and peak overtopping discharge during three storms on a vertical seawall at Samphire Hoe, England. They designed and implemented an overtopping hazard warning system based on a forecast of wind speed and direction. They observed the overtopping discharged hourly, recorded by on-site personnel using field monitoring equipment, see Pullen *et al*. The missing data between the tank compartments are estimated using a trapezoidal distribution to approximate the total overtopping discharge. They found that behaviour of overtopping was in agreement with predictions by Besley's (1999) using empirical overtopping prediction methods. The mean overtopping discharge for the three storms is considered hazardous (compared to the tolerable discharge rate for public safety) when it is around 0.031 (litres/s per m) as suggested by Franco *et al.* (1994).

Pearson *et al.* (2002) have performed a series of experiments under the VOWS collaborative research project. Overtopping measurements results from small-scale and large-scale tests of 10:1 battered seawalls are compared with predictions for overtopping on vertical walls by Besley (1999), see Allsop *et al.* (2005). From their experiments they concluded that the small-scale and the large-scale experiments give a good agreement with the prediction method of Besley (1999), showing that scale effects are not significant. Clearly the above is empirical, based on fitting the known data. We here give a theoretical, but highly simplified, model.

2.7.1 Simplified model of wave overtopping calculation

This section gives a simplified model of wave overtopping calculation for a vertical seawall. Here freeboard refers to vertical distance between still water level and top of the seawall. The wave overtopping discharge is defined as overtopping volume [m^3] per time [s] and structure width [m]. In this section, we use Cooker's model (see figure 2.4.2) for calculating the overtopping discharge for the model. This gives an estimate of the maximum quantity of water that could possibly move over the seawall, perhaps under the action of onshore wind.
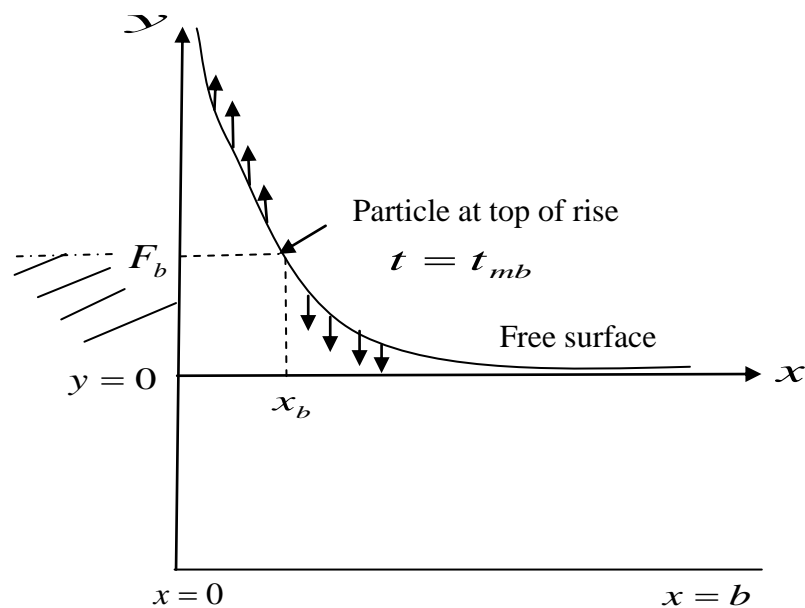
Figure 2.7.2: Overtopping definition sketch.

The parameters of this situation are:

F_b = the height of freeboard from the free surface
x_b = distance at which predicted free surface is at F_b
b = distant boundary
y_{max} = the highest vertical height of overtopping of free surface particles. This is a function of x.

Given that the jet of fluid is thin and the pressure gradients are low in the jet, we assume the jet particles move as free projectiles. Hence the maximum height achieved by the jet is given by:

$$mgh' = \frac{1}{2}mv_y^{'2} \tag{2.7.1}$$

i.e.
$$h' = y_{max} = \frac{v_y^{'2}}{2g}$$

Clearly the maximum height occurs at different times for different particles. Here dashed variables are dimensional. Non-dimensionalising gives

$$y_{max} = \frac{y_{max}'}{H} = \frac{U_0^2 v_y^2}{2gH}$$

$$y_{max} = \frac{1}{2}F_r v_y^2 \qquad \text{where } F_r = \frac{U_0^2}{gH} \text{ is the Froude number}$$

Since the initial upwards velocity (before impact) is zero the velocity afterwards is simply given by equation (2.4.17)

$$v_y = \frac{\partial P}{\partial y} = \sum_{n=1}^{\infty} a_n \lambda_n \cos(\lambda_n y) \frac{\sinh(\lambda_n(x-b))}{\cosh(\lambda_n b)} \tag{2.7.2}$$

So that the initial velocity upward when $y = 0$ gives

$$v_y = \lambda_n \frac{\sinh(\lambda_n(x-b))}{\cosh(\lambda_n b)} \tag{2.7.3}$$

Hence the maximum vertical height of jet is

$$y_{max} = \frac{1}{2}F_r\left(\sum_{n=1}^{\infty} a_n \lambda_n \frac{\sinh(\lambda_n(x-b))}{\cosh(\lambda_n b)}\right)^2 \tag{2.7.4}$$

For freeboard, F_b we have

$$F_b = \frac{1}{2}F_r\left(\sum_{n=1}^{\infty} a_n \lambda_n \frac{\sinh(\lambda_n(x_b-b))}{\cosh(\lambda_n b)}\right)^2 \tag{2.7.5}$$

where a_n is Fourier coefficient from equation (2.4.17). So we can find F_b in terms of a parameter x_b, the distance at which F_b is achieved. The series for F_b diverges at $x = 0$ but for $x > 0$ the series converges, see appendix A.2.1.

Calculating the overtopping discharge, V

$$V = \int_0^{x_b} \left(y_{max} - F_b \right) dx$$

i.e.

$$V = \int_0^{x_b} y_{max} \, dx - x_f F_b \qquad (2.7.6)$$

where y_{max} comes from (2.7.4) and F_b from (2.7.5).

Assuming shallow water theory and taking the impact velocity U_0 to be the wave speed $\sqrt{gH}$ gives $F_r = 1$.

The integral of y_{max} from $x = 0$ to $x = x_b$, can be found numerically by the trapezoidal rule:

$$\int_a^b f(x) dx \approx \frac{\Delta x}{2} \left(y_0 + 2y_1 + 2y_2 + \cdots + 2y_{n-1} + y_n \right) \qquad (2.7.7)$$

where $\Delta x = \dfrac{b-a}{n}$ which easily calculated by using MATLAB. The result for the volume of overtopping subject to the height of freeboard is shown in figure (2.7.2). Given the assumption that particles in the jet move as free projectiles, the model will not be valid for very low freeboard since the pressure impulse gradients will be appreciable for region above F_b and away from the wall.
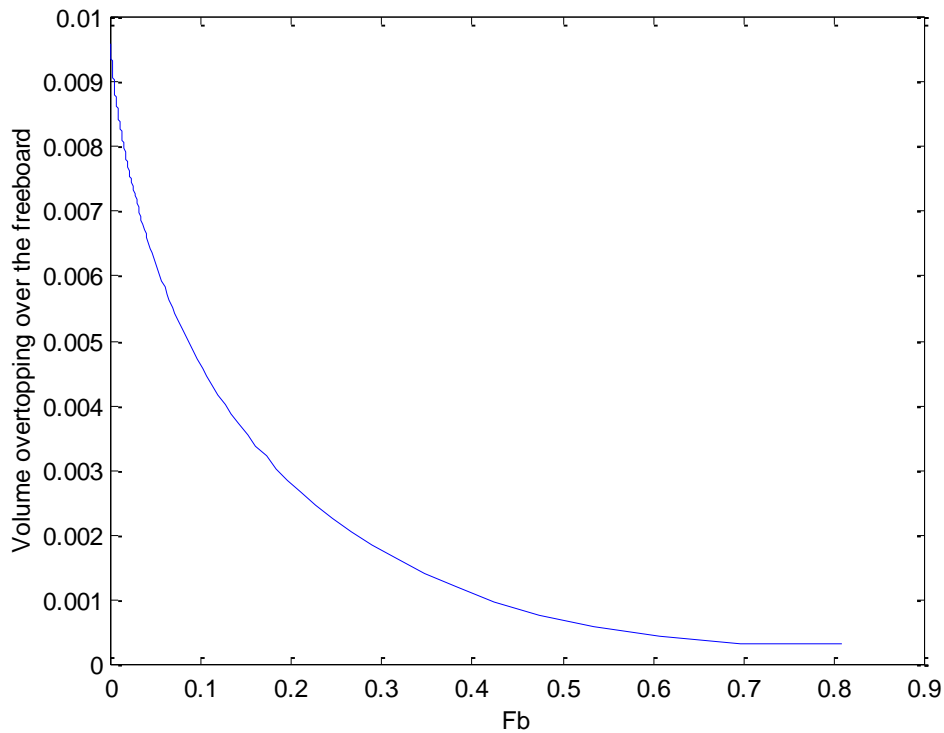
Figure 2.7.3: Overtopping discharge for Cooker's Model for $\mu = 0.1$. Give the units here i.e. F_b is the dimensionless freeboard reference to depth H and V is volume overtopping per unit length of seawall divided by H^2.

From the figure (2.7.3), we can see that increasing the height of the seawall will reduce the overtopping discharge.

It is instructive to translate this result for engineering purposes. Firstly we need to convert the freeboard and volume of overtopping per unit seawall length to dimensional quantities by multiplying by the length scale H and H^2 respectively.

With, $H = 2m$, $\mu = 0.1$ and $F_b = 0.5$, we have volume of overtopping, $V = 0.001H^2$ per impact, gives us

$0.001(2)^2 = 0.004m^2$ each wave impact.

1 impact in 10 waves of 10 sec ~ 100 sec. This gives:

$V = 4 \times 10^{-5} m^3 s^{-1}$ per metre frontage.

$V \approx 0.04 ls^{-1}$ per metre frontage.

This is comparable with the rules given by Franco *et al.* (1994). Unfortunately comparison with the VOWS model (Allsop *et al.* (2005)) is not possible because some of the necessary parameters were not published.

2.8   Convergence Check

The sums in the Fourier Series have to be truncated at $n = N$, where N is an integer large enough for accuracy. The convergence itself can be looked at numerically and analytically.

To see that the infinite sum converges analytically, we use the Integral Test to prove the series is converges, (Stewart,2009).

Take the infinite sum (2.4.10) as example, we have:

$$P(x, y; \mu) = \sum_{n=1}^{\infty} \frac{(\cos(\mu\lambda_n) - 1)}{\lambda_n^2} \sin\left(\frac{\lambda_n y}{H}\right) \exp\left(\frac{-\lambda_n x}{H}\right) \qquad (2.8.1)$$

where $\lambda_n = \left(n - \frac{1}{2}\right)\pi$.

Let $\alpha_n = \frac{(\cos(\mu\lambda_n) - 1)}{\lambda_n^2} \sin\left(\frac{\lambda_n y}{H}\right) \exp\left(\frac{-\lambda_n x}{H}\right)$.

The most slowly convergent case occurs when $x = 0, y = H$ and $\mu = 1$. Then the summation is $\sum_{n=1}^{\infty} \alpha_n \approx \sum_{n=1}^{\infty} \frac{1}{\lambda_n^2}$ and since $\lambda_n = \frac{1}{\left(n - \frac{1}{2}\right)^2 \pi^2} = O(n^{-2})$

This converges by the Integral Test.

The effects of the truncation of the Fourier series should be considered. To illustrate this, computations were performed with truncation of the Fourier series at $N = 10$ to $N = 100$ for $y = -0.125$ which is the position of the pressure maximum when $\mu = 1.0$. We calculated the percentage of difference (pressure) for each result with results which truncate at $N = 100$ assumed to have converged. From table 2.8.1, we can see that the Fourier series can be truncated at $N = 50$ as there is only 0.061% difference compare to $N = 100$ in the pressure output. These results show that acceptable accuracy of less than 0.1% relative error can be obtained even though truncation of the Fourier series is at 50-100.

Table 2.8.1: Pressure changes for values of N.

N	Pressure at $y = -0.125$, and $\mu = 1.0$	% Difference from $N=100$
10	0.26772	1.56
20	0.26332	0.11
30	0.26327	0.125
40	0.26392	0.12
50	0.26344	0.061
60	0.26361	0.0038
70	0.26367	0.03
80	0.26352	0.03
90	0.26365	0.02
100	0.26360	0

The following graph shows the convergence of the peak pressure impulse numerically for different values of *N* up to 100. The pressure impulse for Cooker model clearly converges as the value of *N* increases. These results provide a guide to the more complicated cases considered in this thesis where we generally truncate at $N = 40$.
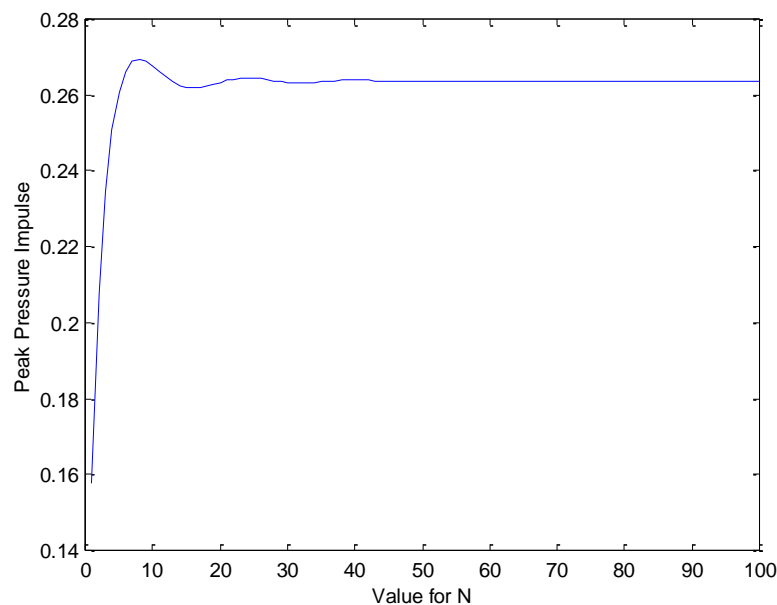
Figure 2.8.1: Convergence of series for the maximum of *P*, equation (2.7.6), at $x = 0$, $y = -0.125$ and $\mu = 1.0$.

CHAPTER 3

BERM AND DITCH

3.1   Introduction

In this chapter, we will extend the two-dimensional work of Greenhow (2006) who has applied Cooker's model to the:

    i.   Berm problem

    ii.   Ditch problem

These two problems were solved using a basis function method. Here we solve these problems again by using hybrid collocation method (a collocation method at the matching area and integral method on the wall) to validate that this method can be used to solve other problems in this thesis. Comparison of the results has been made and the results will be discussed in this chapter. Greenhow's results are extended by calculating the total impulse, moment impulse and overtopping for both problems above.

3.2   Literature Review

Greenhow (2006) extended Cooker's model to the berm and ditch problems. These models have an unchanged seabed, but the seawall is altered, to incorporate a foundation attached to the base of the wall. Greenhow formulated each problem into two regions in his model. The inner region labelled as region 1, is the altered seawall

geometry and the outer region labelled as region 2, is simply uniform depth, see figure 3.3.1. He has found that ditches can double the pressure impulse, while having a berm in front of the vertical seawall can reduce the wave impact on the wall.

The wave impact on a wall with a berm has also been studied by Wood (1997) and further work has been made by Wood and Peregrine (2000). They extended Cooker and Peregrine (1990, 1995) model for impact on a wall by including a region of porous material in front of the wall. They split the problem into two regions where the top half, labelled as region 1, is simply water and the bottom half, labelled as region 2, is a rubble berm. They found that having a porous berm can reduce the pressure impulse by up to 20%.

3.3   Mathematical modelling

3.3.1   Berm Problem

We take our length scale L to be the depth of water in region 2 and work in dimensionless parameters. The origin is taken to be on the wall at the still water level with x taken in the direction perpendicular to the wall, and y vertically. Let P_1 and P_2 be the solutions in the respective regions. In the inner region we have similar conditions to those of impact on the wall, with the exception that the seabed is higher than the seabed in the outer region because of the presence of the berm. The boundary conditions are as shown in figure 3.3.1, and the parameters of this situation are:

H_b = Distance down seawall from free surface to the top of the berm

B_1 = Width of the berm

B_2 = Total width of fluid domain

μ = parameter of impact region
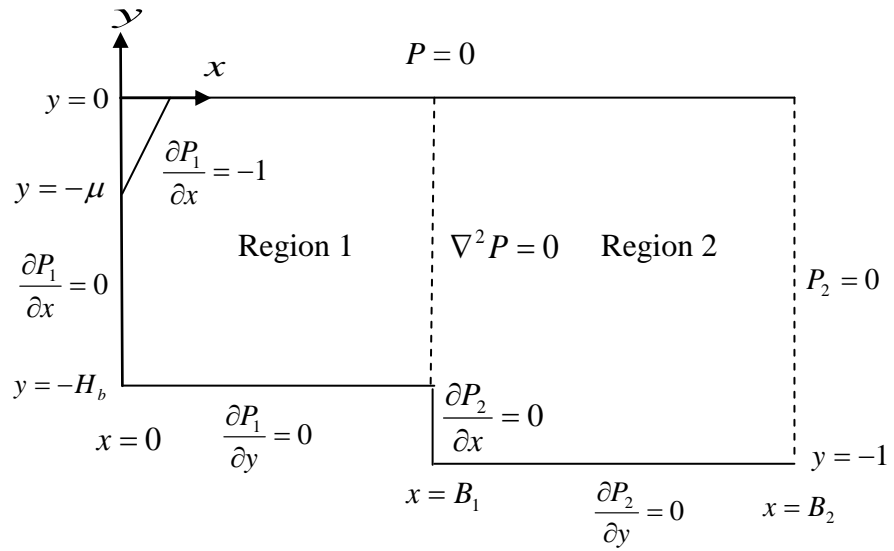
Figure 3.3.1: Boundary conditions for the pressure impulse for wave impact on vertical wall with a berm.

The solution for regions 1 and 2 are given by the following eigenfunction expansions:

$$
P_1(x,y) = \sum_{n=1}^{\infty} \frac{\sin\left(\dfrac{\lambda_n y}{H_b}\right)}{\cosh\left(\dfrac{\lambda_n B_1}{H_b}\right)} \left\{ \alpha_n \sinh\left[\frac{\lambda_n(x-B_1)}{H_b}\right] + \beta_n \cosh\left[\frac{\lambda_n(x-B_1)}{H_b}\right] \right\};
\tag{3.3.1}
$$

for the inner region and the outer region is given by

$$
P_2(x,y) = \sum_{n=1}^{\infty} c_n \frac{\sin(\lambda_n y)}{\cosh(\lambda_n B_2)} \sinh(\lambda_n(x-B_2))
\tag{3.3.2}
$$

where $\lambda_n = (n-\frac{1}{2})\pi$. Here we are free to normalise the coefficients c_n by a different factor than in equation (3.3.2). These Fourier series are obtained using separation of variables on Laplace's equation, the exact forms being chosen to satisfy the free surface and seabed boundary conditions. The exact sum is from $n=1$ to ∞, so we must truncate it. For most cases in this thesis inclusion of $N = 30$ to 50 is sufficient to give an accuracy of at least 4 decimal places as described in §2.8.

The equation above satisfies all the boundary conditions for the problem shown in figure 3.3.1 except on the wall and the matching line at $x = B_1$. Along the line $x = B_1$ we require the pressure, and hence the pressure impulse to be continuous, so along the boundary $x = B_1$, for $-H_b \leq y \leq 0$ we require

$$P_1 = P_2 \tag{3.3.3}$$

and also we need

$$\frac{\partial P_2}{\partial x} = \begin{cases} \dfrac{\partial P_1}{\partial x} & \text{for} \quad -H_b \le y \le 0 \\[2mm] 0 & \text{for} \quad -1 \le y < H_b \end{cases} \tag{3.3.4}$$

On the wall at $x = 0$ we have

$$\frac{\partial P_1}{\partial x} = \begin{cases} -1 & \text{for} \quad -\mu \le y \le 0 \\ 0 & \text{otherwise} \end{cases} \tag{3.3.5}$$

Multiplying (3.3.5) by the basis function $\sin\left(\dfrac{\lambda_l y}{H_b}\right)$ and integrating from $y = -H_b$ to 0

gives:

$$\alpha_l - \beta_l \tanh\left(\frac{\lambda_l B_1}{H_b}\right) = \frac{2H_b}{\lambda_l^2}\left[1 - \cos\left(\frac{\lambda_l \mu}{H_b}\right)\right] \tag{3.3.6}$$

for $l = 1$ to N. We need to solve equations (3.3.3) and (3.3.4) together with (3.3.6).

Matching at $x = B_1$ for $-H_b \le y \le 0$ for (3.3.5) gives us:

$$\sum_{n=1}^{\infty} \beta_n \frac{\sin\left(\dfrac{\lambda_n y}{H_b}\right)}{\cosh\left(\dfrac{\lambda_n B_1}{H_b}\right)} - \sum_{n=1}^{\infty} c_n \frac{\sin(\lambda_n y)}{\cosh(\lambda_n B_2)} \sinh(\lambda_n(B_1 - B_2)) = 0 \tag{3.3.7}$$

Matching at $x = B_1$ for (3.3.4) for $-H_b \le y \le 0$ gives:

$$\sum_{n=1}^{\infty} \alpha_n \frac{\lambda_n}{H_b} \frac{\sin\left(\dfrac{\lambda_n y}{H_b}\right)}{\cosh\left(\dfrac{\lambda_n B_1}{H_b}\right)} - \sum_{n=1}^{\infty} c_n \lambda_n \frac{\sin(\lambda_n y)}{\cosh(\lambda_n B_2)} \cosh(\lambda_n(B_1 - B_2)) = 0 \tag{3.3.8}$$

and for $-1 \le y < -H_b$ gives:

$$\sum_{n=1}^{\infty} c_n \lambda_n \frac{\sin(\lambda_n y)}{\cosh(\lambda_n B_2)} \cosh(\lambda_n(B_1 - B_2)) = 0 \tag{3.3.9}$$

To solve equations (3.3.6), (3.3.7), (3.3.8) and (3.3.9) we choose different values of y i.e. collocation points, to give the system of equations shown in figure 3.3.2. From here we have $3M$ conditions for the M collocation points and the equations involving three Fourier coefficients (α_n, β_n, c_n). This requires $3M = 3N$ so that $M = N$ which is a square matrix system that needs to be solved, see figure (3.3.2). More specifically, the collocation points for (3.3.7) are chosen to be separated by a distance $L = \dfrac{H_b}{M}$ and collocation points for (3.3.8) and (3.3.9) are separated by a distance $L = \dfrac{1}{M}$, i.e. evenly spaced out. In accordance with the convergence shown in §2.8, the pressure impulse can be calculated by evaluating the Fourier series after truncation at $N = 30$. Test with other values of N show that $N = 30$ converges to within 1% of the peak pressure values. The results for this problem will be discussed in §3.4.

$$
\left(\begin{array}{ccc:ccc:ccc}
 & \vdots & & & \vdots & & & \vdots & \\
 & diagonal & & & diagonal & & & zero & \\
 & \vdots & & & \vdots & & & \vdots & \\
\hdashline
- & - & - & - & - & - & - & - & - \\
 & \vdots & & & \vdots & & & \vdots & \\
 & zero & & & full & & & full & \\
 & \vdots & & & \vdots & & & \vdots & \\
\hdashline
- & - & - & - & - & - & - & - & - \\
 & full & & & zero & & & full & \\
\cdots & \cdots & \cdots & \cdots & \cdots & \cdots & \cdots & \cdots & \cdots \\
 & zero & & & zero & & & full &
\end{array}\right)
\left(\begin{array}{c}
\alpha_1 \\ \vdots \\ \alpha_N \\ \hdashline \beta_1 \\ \vdots \\ \beta_N \\ \hdashline c_1 \\ \vdots \\ c_N
\end{array}\right)
=
\left(\begin{array}{c}
\dfrac{2H_b}{\lambda_1^2}\left[1-\cos\left(\dfrac{\lambda_1\mu}{H_b}\right)\right] \\ \vdots \\ \dfrac{2H_b}{\lambda_N^2}\left[1-\cos\left(\dfrac{\lambda_N\mu}{H_b}\right)\right] \\ \hdashline 0 \\ \vdots \\ 0 \\ \hdashline 0 \\ \vdots \\ 0
\end{array}\right)
$$

Figure 3.3.2: Matrix system of equations for berm problem. The first M rows come from (3.3.6), the next from (3.3.7) and the last from (3.3.8) and (3.3.9).

3.3.2 Ditch Problem

Now we look at the ditch problem, which we also split into two regions. The inner region is the altered seawall with a ditch. The ditch problem is almost same with the berm problem except that the seabed in the inner region is lower than the seabed in the outer region. The parameters of this situation are the same as before and the boundary conditions are as shown in figure 3.3.3.
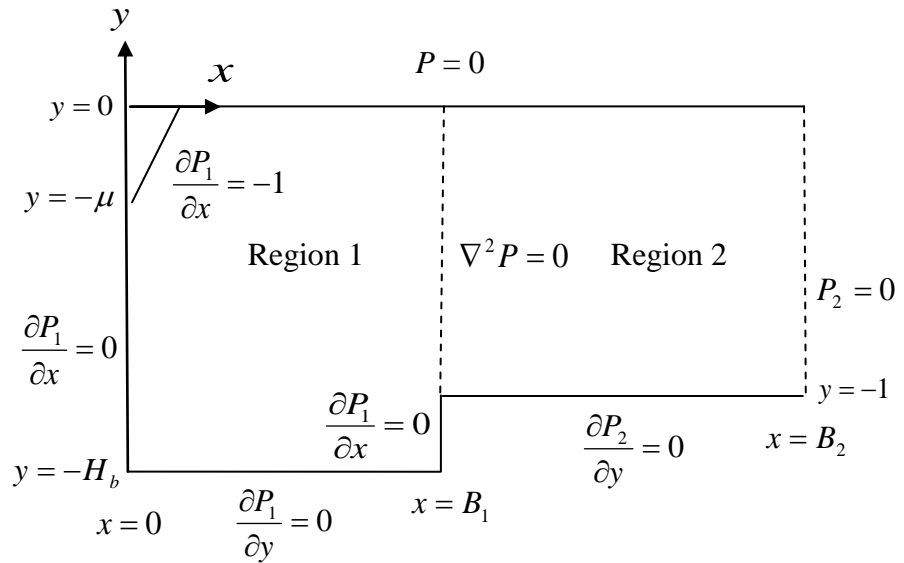
Figure 3.3.3: Boundary conditions for the pressure impulse for wave impact on a vertical wall with a ditch.

For the problem given in the figure 3.3.3, we have the same solution for regions 1 and 2 as in equations (3.3.1) and (3.3.2) respectively, which satisfy all the boundary conditions for the problem shown in figure 3.3.3 except on the wall and the matching line at $x = B_1$. As in the berm problem, we have 3 conditions which need to be solved: on the wall we need to solve equation (3.3.5) and matching line at $x = B_1$ we need to solve equation (3.3.3) and for derivatives we need to solve

$$\frac{\partial P_1}{\partial x} = \begin{cases} \dfrac{\partial P_2}{\partial x} & \text{for} \quad -1 \le y \le 0 \\ \\ 0 & \text{for} \quad -H_b \le y < -1 \end{cases} \qquad (3.3.10)$$

Multiplying (3.3.5) with the same basis function as in berm problem, gives us (3.3.6). Matching line at $x = B_1$ gives us (3.3.7) for $P_1 = P_2$ and (3.3.8) for derivatives for $-1 \leq y \leq 0$ and

$$\sum_{n=1}^{\infty} a_n \frac{\lambda_n}{H_b} \frac{\sin\left(\dfrac{\lambda_n y}{H_b}\right)}{\cosh\left(\dfrac{\lambda_n B_1}{H_b}\right)} = 0 \tag{3.3.11}$$

for $-H_b \leq y < -1$.

Greenhow (2006) originally solved this using a Fourier method but this fails due to poor-conditioning for some situations. Hence we again apply the collocation method, as follows.

From equation (3.3.6), (3.3.7), (3.3.8) and (3.3.11) we can create the system of equations as shown in figure 3.3.4. This also gives us $3M = 3N$ equations so that $M = N$ resulting in a square matrix system that needs to be solved, see figure 3.3.4. The collocation points in this problem are also evenly spaced out. Thus pressure impulse can be calculated by evaluating the Fourier series after truncation at $N = 50$. The results for this problem will be discussed in §3.4 where we will make comparisons of results for ditch and berm problems.

$$\begin{pmatrix} diagonal & \vdots & diagonal & \vdots & zero \\ - \quad - \quad - & \vdots & - \quad - \quad - & \vdots & - \quad - \quad - \\ zero & \vdots & full & \vdots & full \\ - \quad - \quad - & \vdots & - \quad - \quad - & \vdots & - \quad - \quad - \\ full & \vdots & zero & \vdots & full \\ \cdots \quad \cdots \quad \cdots & \vdots & \cdots \quad \cdots \quad \cdots & \vdots & \cdots \quad \cdots \quad \cdots \\ full & \vdots & zero & \vdots & zero \end{pmatrix} \begin{pmatrix} \alpha_1 \\ \vdots \\ \alpha_N \\ - - - - \\ \beta_1 \\ \vdots \\ \beta_N \\ - - - - \\ c_1 \\ \vdots \\ c_N \end{pmatrix} = \begin{pmatrix} \frac{2H_b}{\lambda_1^2}\left[1-\cos\left(\frac{\lambda_1\mu}{H_b}\right)\right] \\ \vdots \\ \frac{2H_b}{\lambda_N^2}\left[1-\cos\left(\frac{\lambda_N\mu}{H_b}\right)\right] \\ - - - - - - - - - - \\ 0 \\ \vdots \\ 0 \\ - - - - - - - - - - \\ 0 \\ \vdots \\ 0 \end{pmatrix}$$

Figure 3.3.4: Matrix system of equations for ditch problem. The first M rows come from (3.3.6), the next from (3.3.7) and the last from (3.3.8) and (3.3.11).

3.4   Pressure Impulse

We compare the pressure impulse result for the present hybrid collocation method with the results from the basis function method used by Greenhow (2006). Then we will compare the berm and ditch problems with Cooker's model results. The Fourier coefficients (α_n, β_n, c_n) and the pressure impulse will be calculated using MATLAB. The results obtained are given as three-dimensional surface plots. The plots show us how the pressure impulse is distributed over the surface of the seawall. The red zone on the graph indicates the maximum pressure impulse, and the blue zone indicates minimum pressure impulse. The result are made dimensionless by choosing units for which $H = 1$ and the pressure impulse is in the form of $P/\rho U_0 H$.

3.4.1 Comparison results between hybrid collocation method and basis function method used by Greenhow (2006) for berm and ditch problem

	Hybrid collocation method	Basis function method
$\mu = 0.1$		
$\mu = 0.5$		
$\mu = 0.8$		
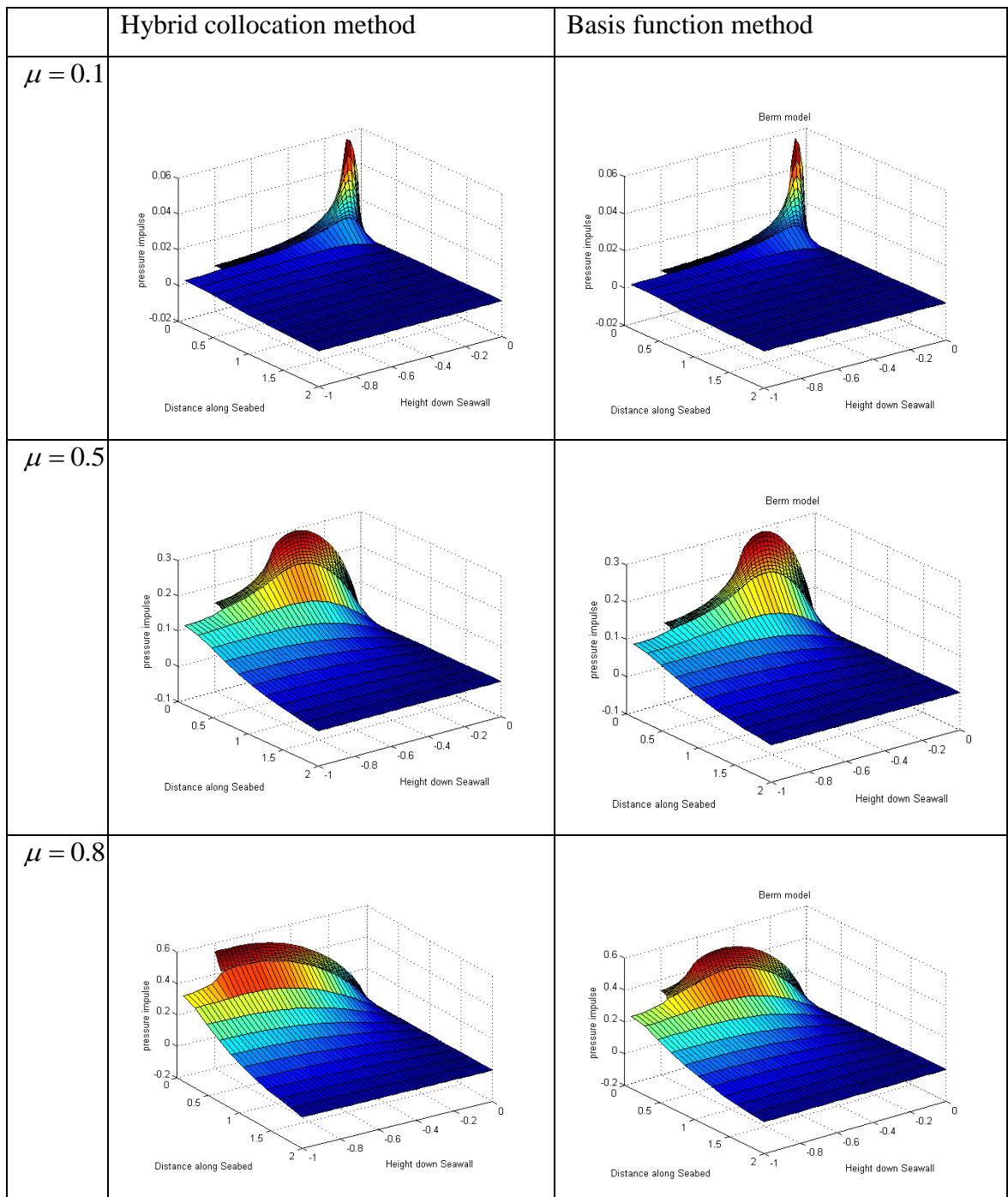
Figure 3.4.1: Comparison pressure impulse results for hybrid collocation method and basis function method for berm problem with $H_b = 0.8$, $B_1 = 0.1$, $B_2 = 2$, and $N = 30$.
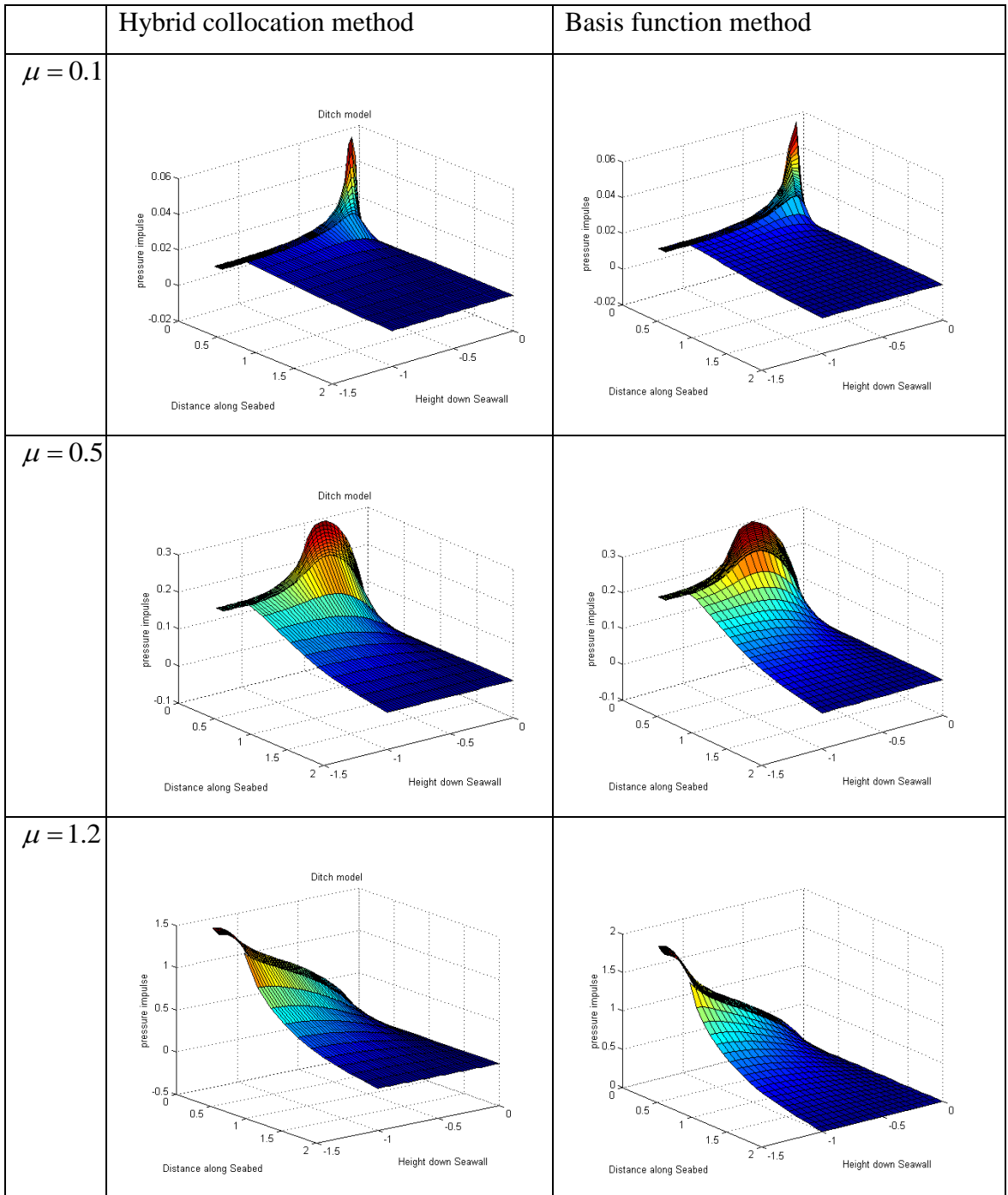
Figure 3.4.2: Comparison pressure impulse results for hybrid collocation method and basis function method for ditch problem with $H_b = 1.2$, $B_1 = 0.1$, $B_2 = 2$, $N = 50$.

Figure 3.4.1 and 3.4.2 show a comparison of the pressure impulse result by using hybrid collocation method and basis function method used in Greenhow (2006). They both give the same results except at the highest impact which is different. This is because the basis function method cannot include enough terms in the summations without encountering the problem of poorly-conditioned matrices discussed in §2.9.3. Hence the unexpected non-monotonicity of P with depth is not physical and the results for the basis function method are wrong.

3.4.2   Pressure impulse on the wall
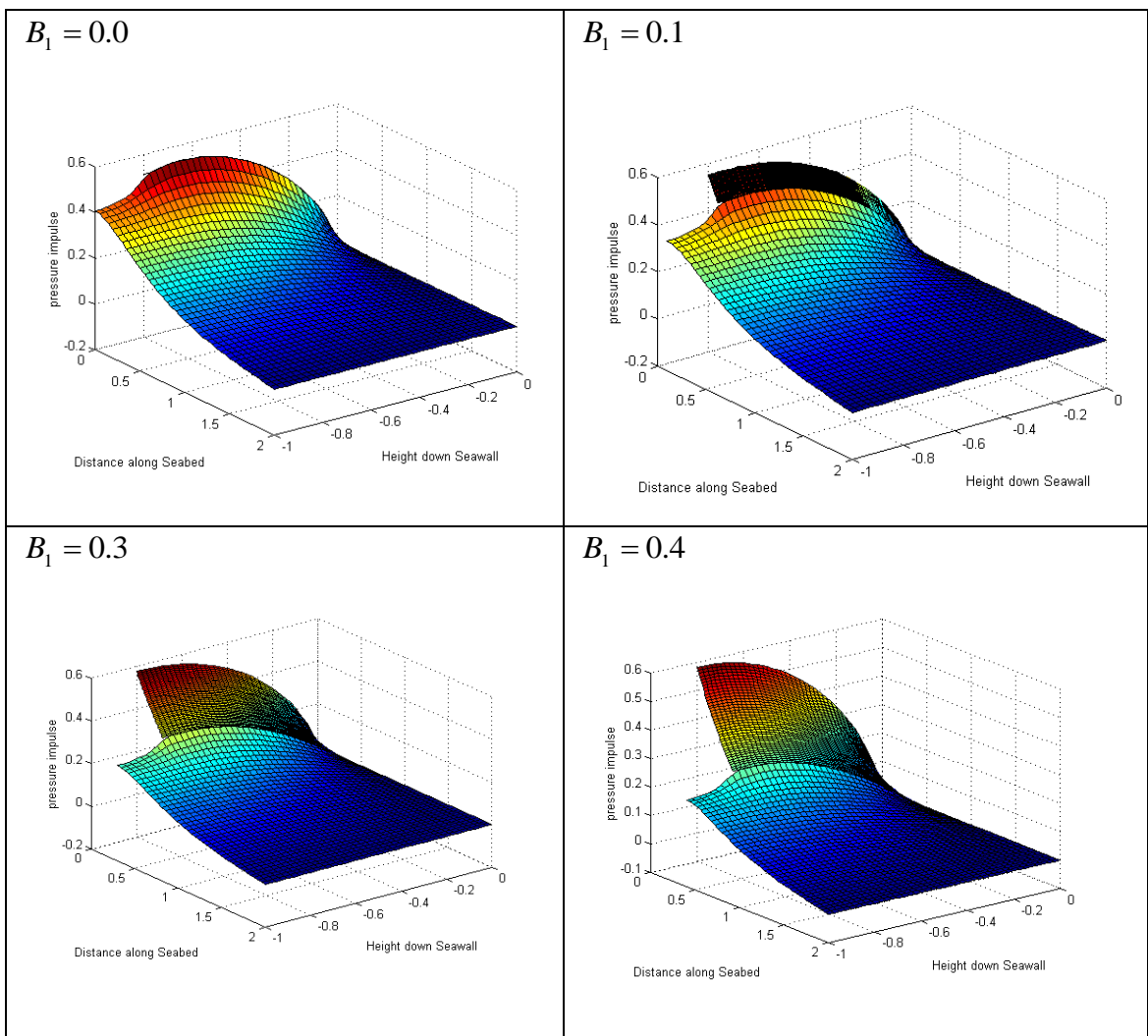
Figure 3.4.3: Pressure impulse for different width of berm with $H_b = 0.8$, $\mu = 0.8$ $B_2 = 2$, $N = 30$ using the collocation method.

Figure 3.4.3 shows that chosen the different width of the berm do not give much difference in maximum pressure impulse. Figure 3.4.4 shows that the greater impact region on the wall, the greater pressure impulse is obtained, as expected.
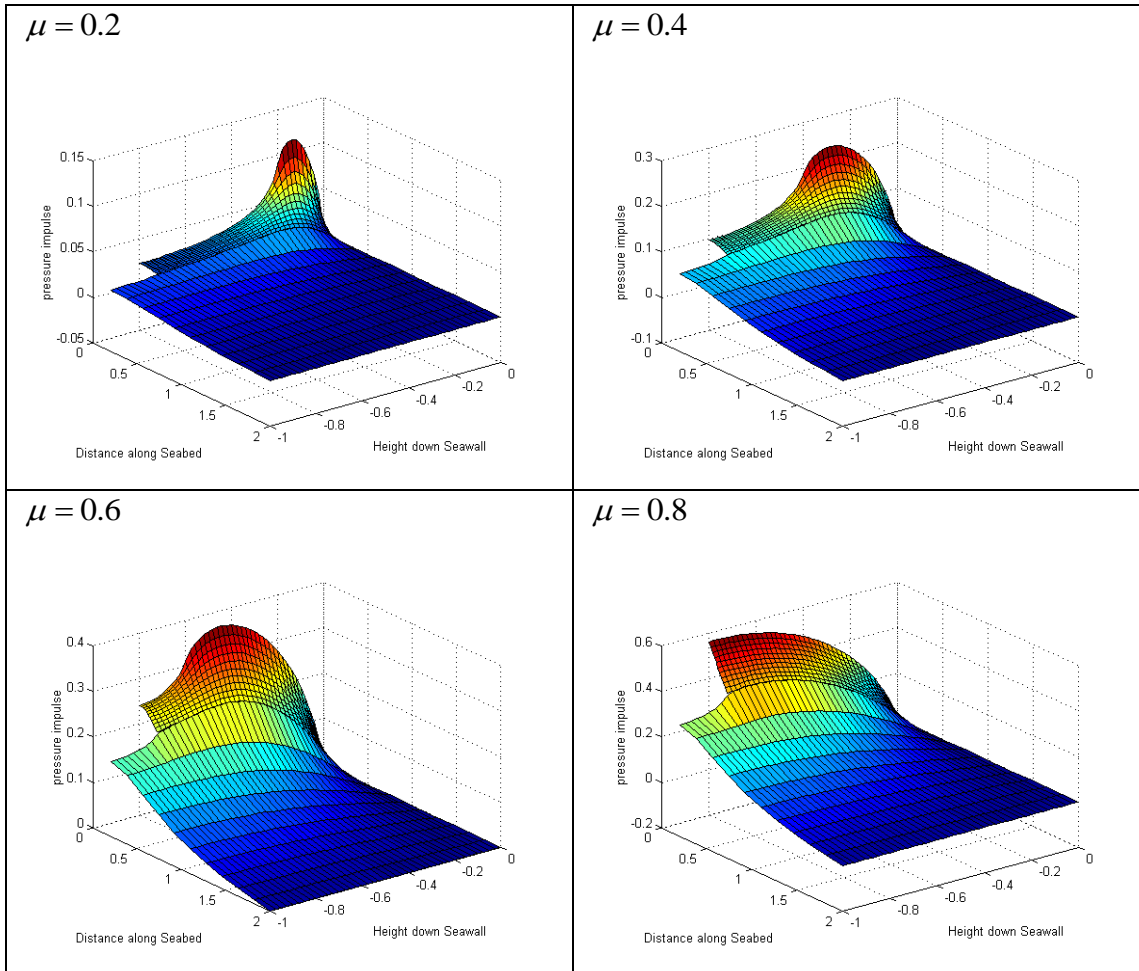
Figure 3.4.4: Pressure impulse for berm problem with different impact regions on the wall with $H_b = 0.8$, $B_2 = 0.2$, $B_2 = 2$, $N = 30$ using collocation method.
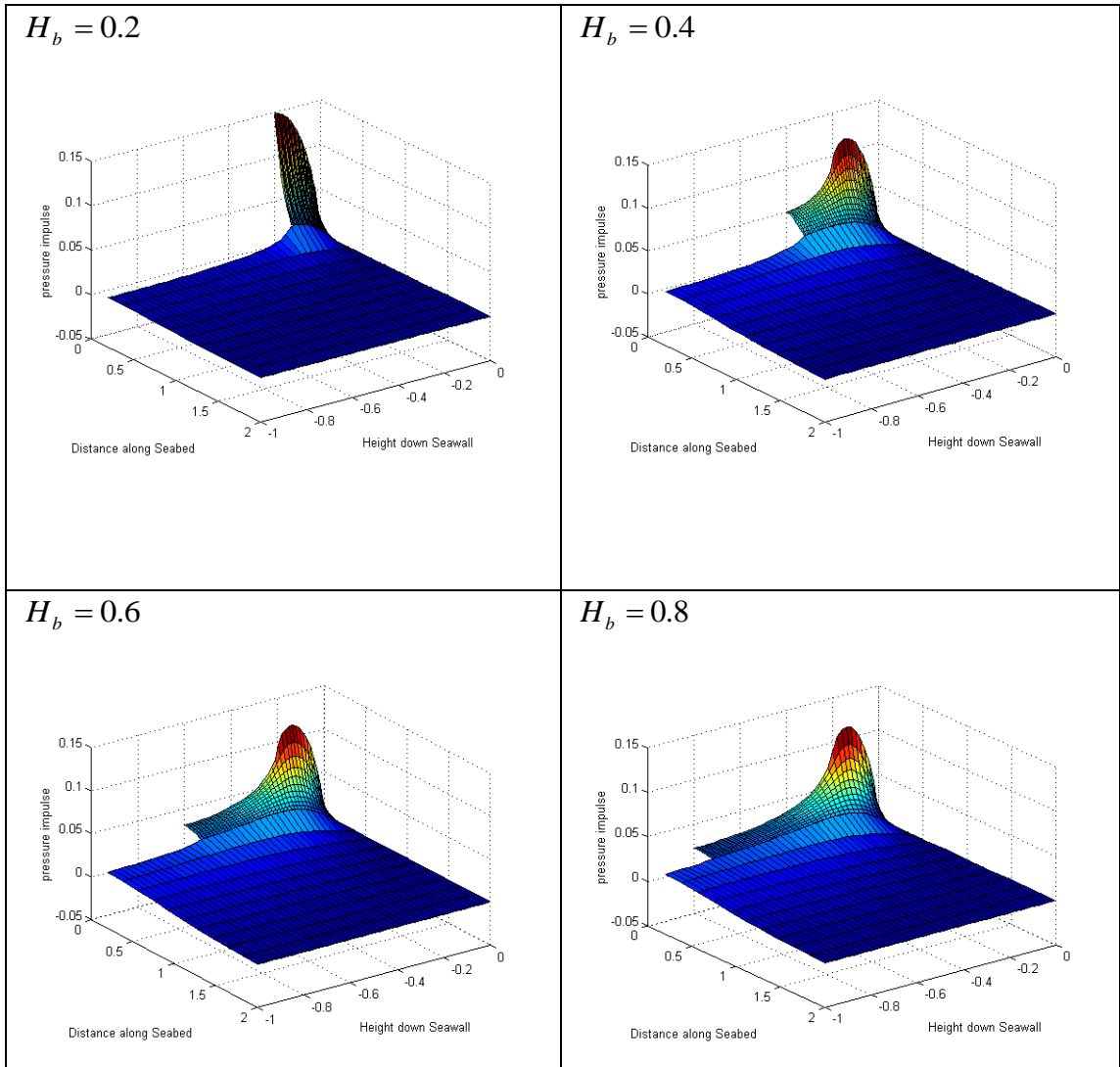
Figure 3.4.5: Pressure impulse with different depths of berm with $B_1 = 0.2$, $B_2 = 2$, $\mu = 0.2$, $N = 30$ using the collocation method.

Figure 3.4.5 shows that the pressure impulse for different depths of the berm gives almost the same results for the maximum pressure impulse, apart from the $H_b = 0.2$ case. Since the impact occurs near the free surface, the berm geometry for a deeply-submerged berm has only a small effect, as expected.
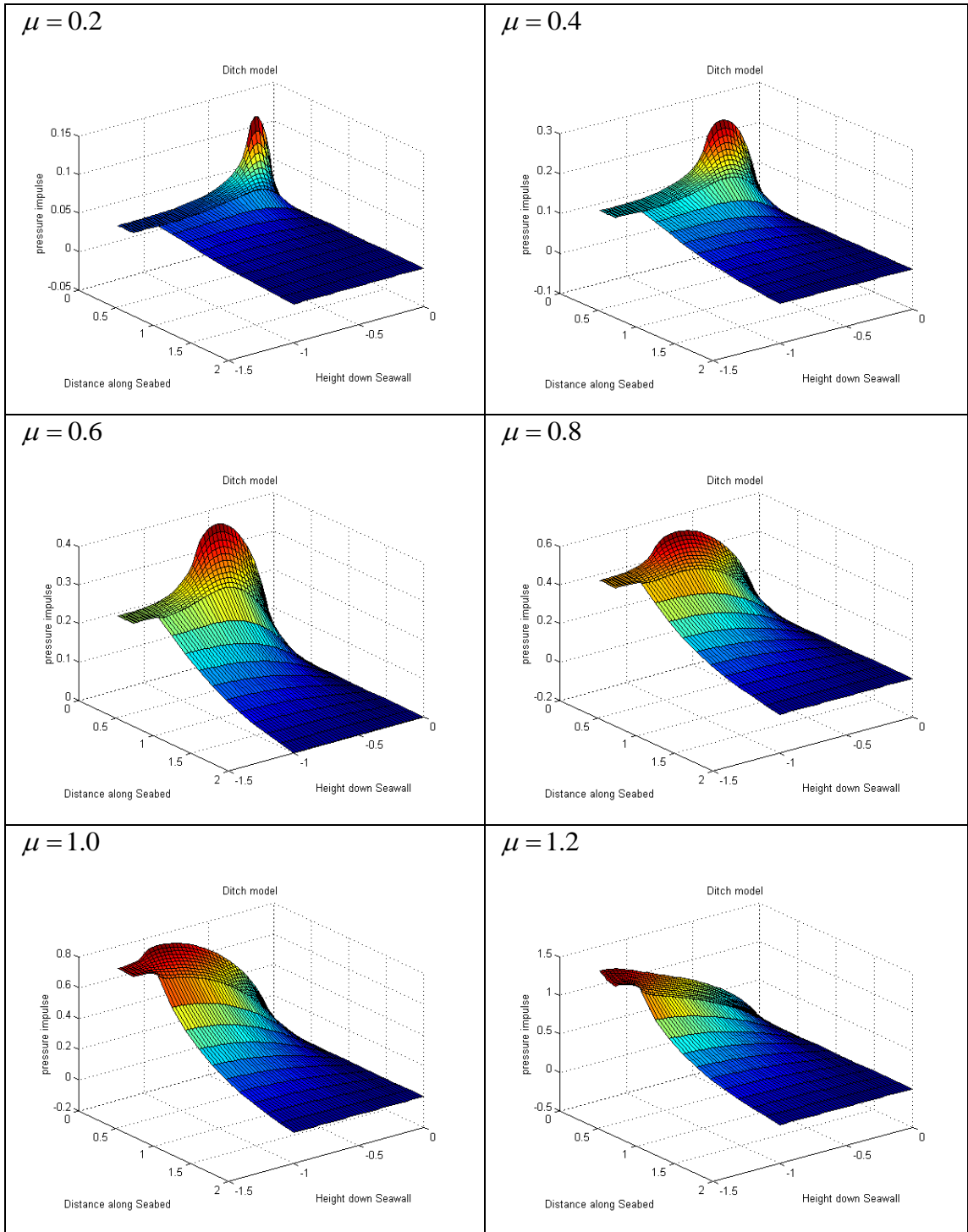
Figure 3.4.6: Pressure impulse for ditch problem with different impact regions on the wall with $H_b = 1.2$, $B_2 = 0.2$, $B_2 = 2$, $N = 50$ using the collocation method.

Figure 3.4.6 shows pressure impulse for different regions of impact for the ditch problem. As expected a greater region of impact will give higher pressure impulses.

Figure 3.4.7 shows that the depths of ditch not have much effect on the maximum pressure impact result. It is notable that within the ditch the pressure is virtually constant. This may have consequences for scour and the stability of the wall's foundation.
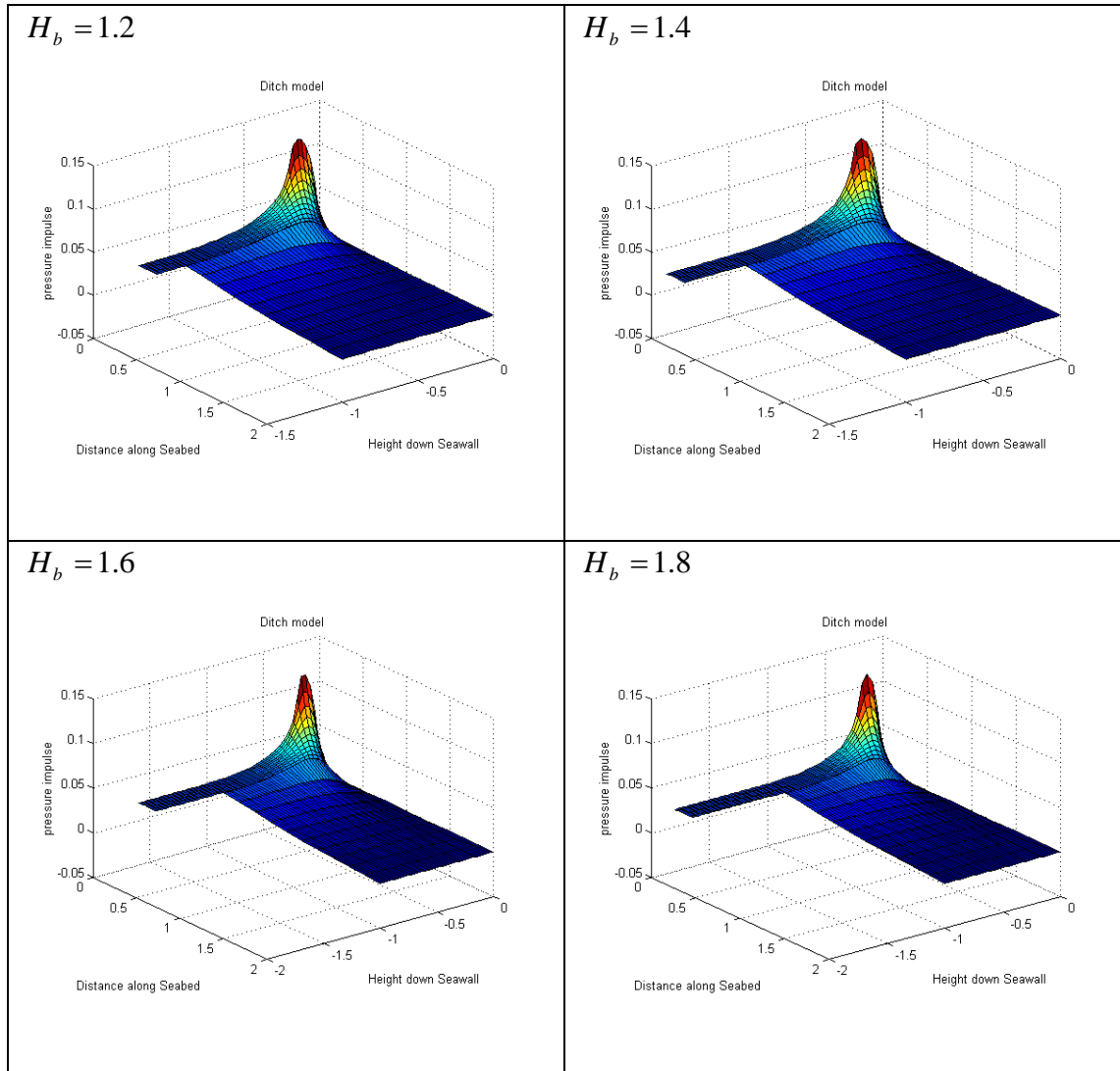
Figure 3.4.7: Pressure impulse with different depth of ditch with $B_1 = 0.2, B_2 = 2$, $\mu = 0.2, N = 50$ using the collocation method.

	Berm Problem with $H_b = 0.8$, $B_1 = 0.1$, $B_2 = 2$, $N = 30$	Ditch Problem with $H_b = 1.2$, $B_1 = 0.1$, $B_2 = 2$, $N = 50$	Cooker's Model
$\mu = 0.5$			
$\mu = 0.8$			
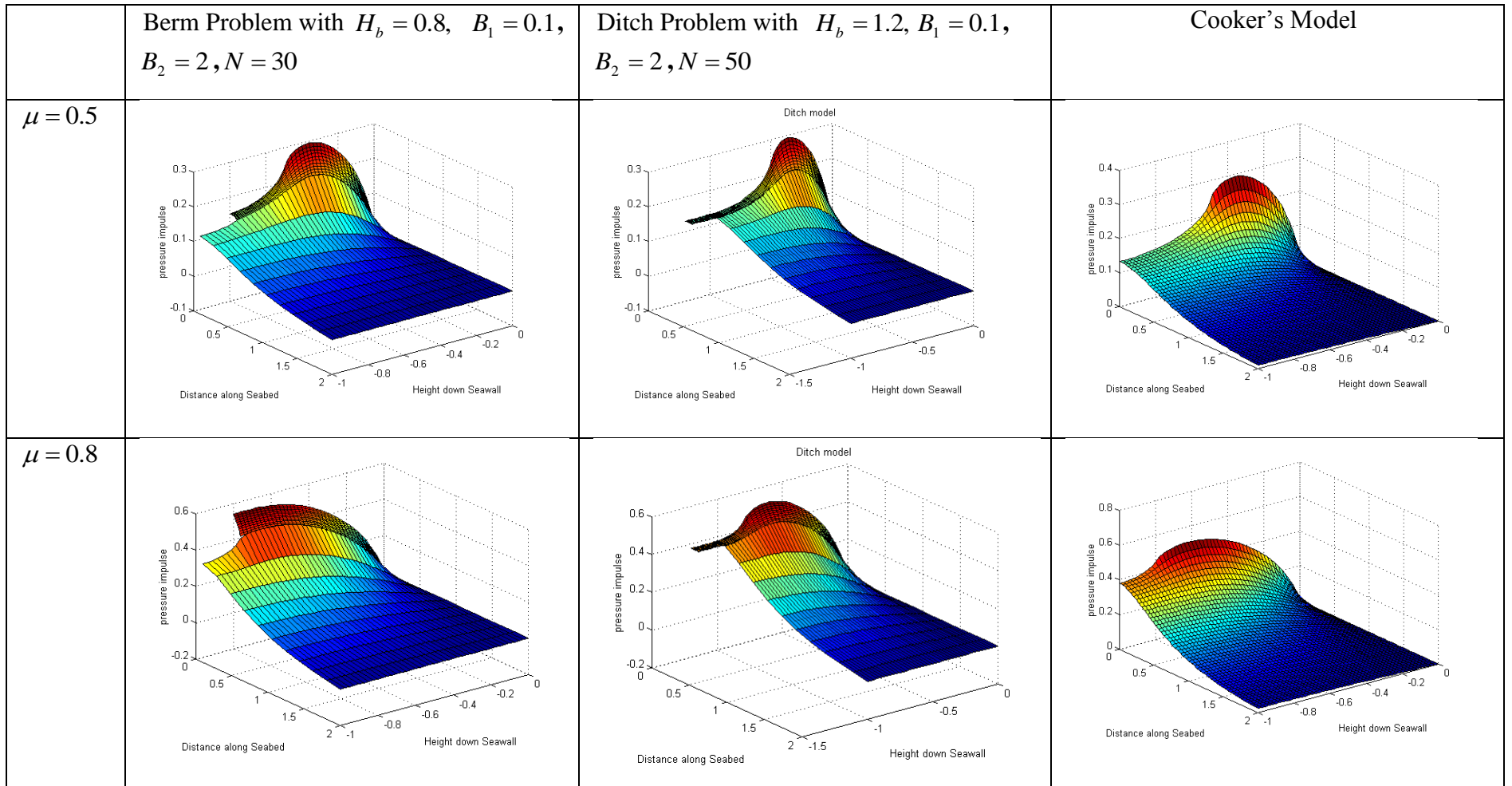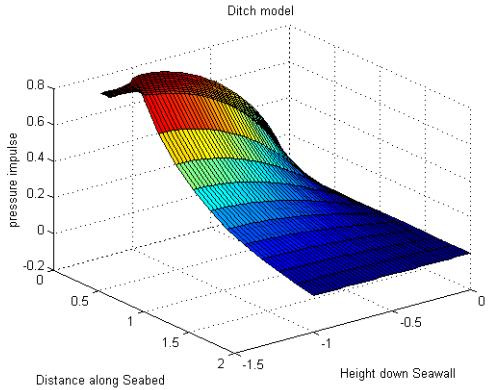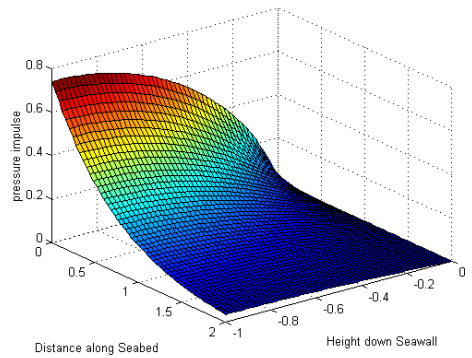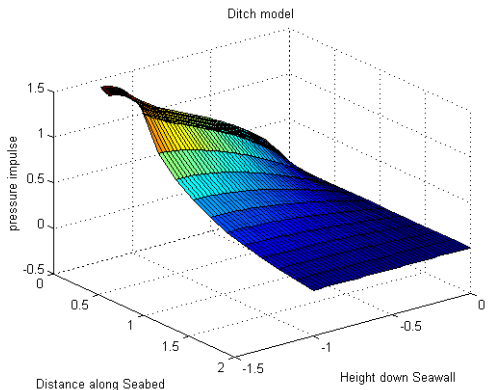
| $\mu = 1.0$ | Not possible. | | |
| $\mu = 1.2$ | Not possible. | | Not possible. |

Figure 3.4.8: Comparison result for berm and ditch problem with Cooker's Model for pressure impulse on the wall.

Figure 3.4.8 shows that for the full impact region on the wall $(\mu = 1.0)$, the pressure impulse for Cooker's model is about $0.742\,\rho U_0 H$. The pressure impulse for berm problem is about $0.570\,\rho U_0 H$ while pressure impulse for ditch problem is about 1.400 $\rho U_0 H$. We can concluded that having a berm can reduce the pressure impulse on the wall but having the ditch can make the pressure impulse on the wall double. These results show a good agreement with Greenhow (2006). We will extend this work by calculating the total impulse, moment impulse and overtopping for both problems in the next section.

Figure 3.4.9 shows that for the same moderate value of μ $(\mu = 0.5)$, the cases for berm, ditch and simple seawall give almost the same pressure impulse. However, for the largest possible impact for all values of μ, the ditch case gives the largest pressure impulse followed by the simple seawall and berm, as shown in figure 3.4.10.
Figure 3.4.11 and figure 3.4.12 show the pressure impulse on the wall with berm or ditch. Both cases show an increase of pressure impulse with μ increasing.
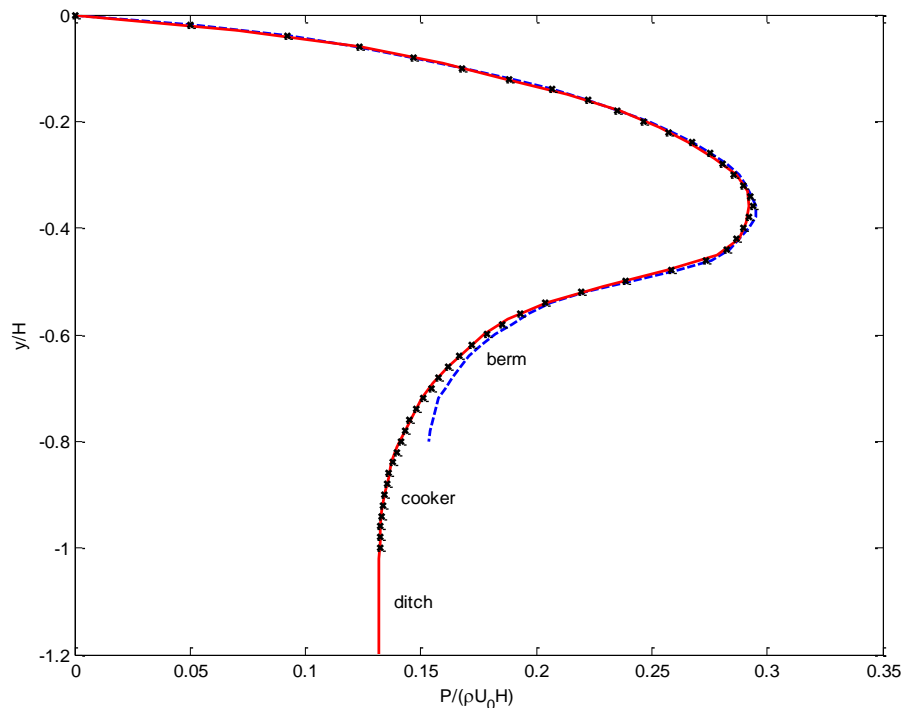
Figure 3.4.9: Pressure impulse on the wall $P(0, y)$, for the berm, ditch and Cooker model for $B_1 = 0.1, B_2 = 2, \mu = 0.5$.
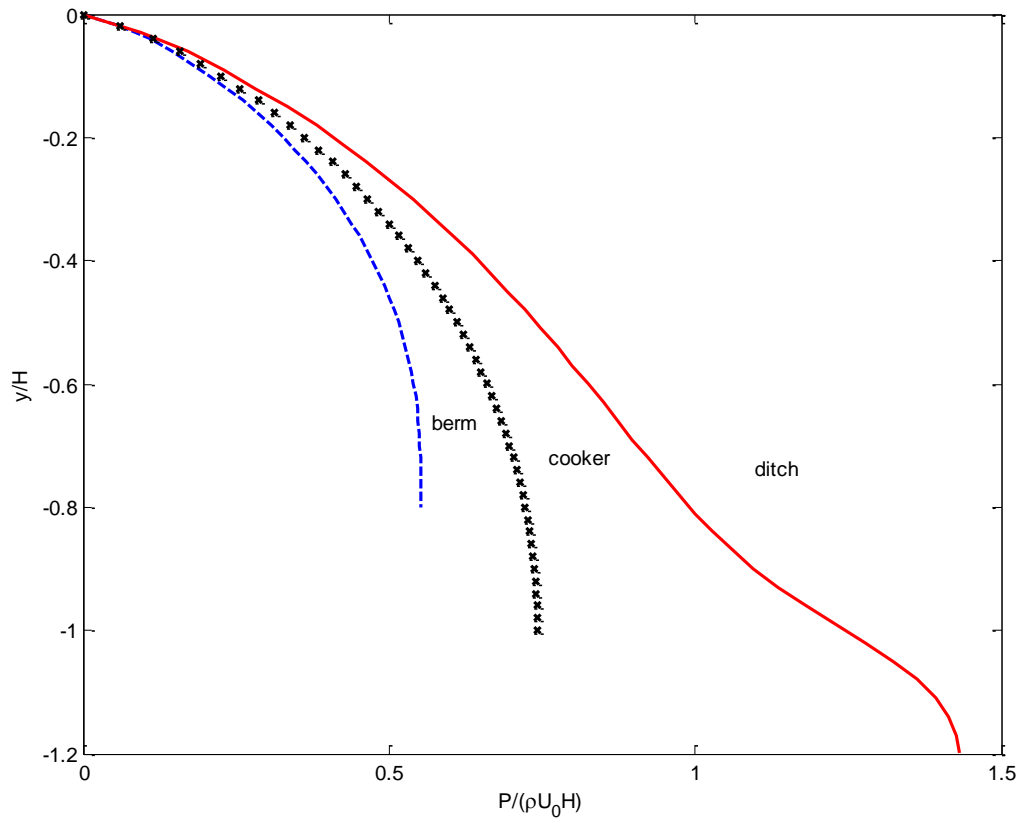
Figure 3.4.10: Maximum pressure impulse for any value of μ on the wall for the berm, ditch and Cooker model for $B_1 = 0.1, B_2 = 2$.
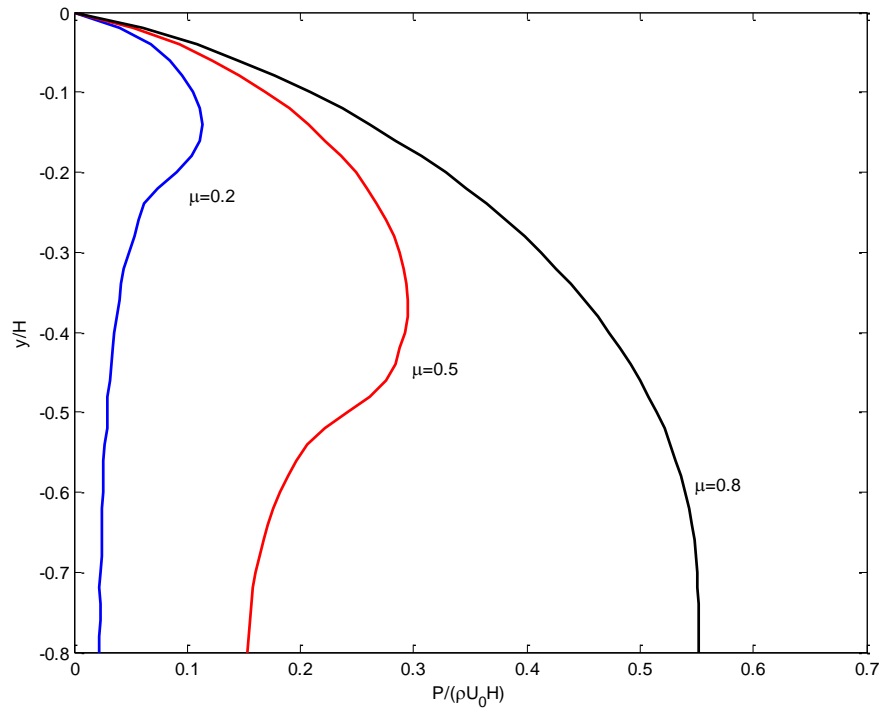
Figure 3.4.11: Pressure impulse on the wall for berm $H_b = 0.8$ for varying μ.
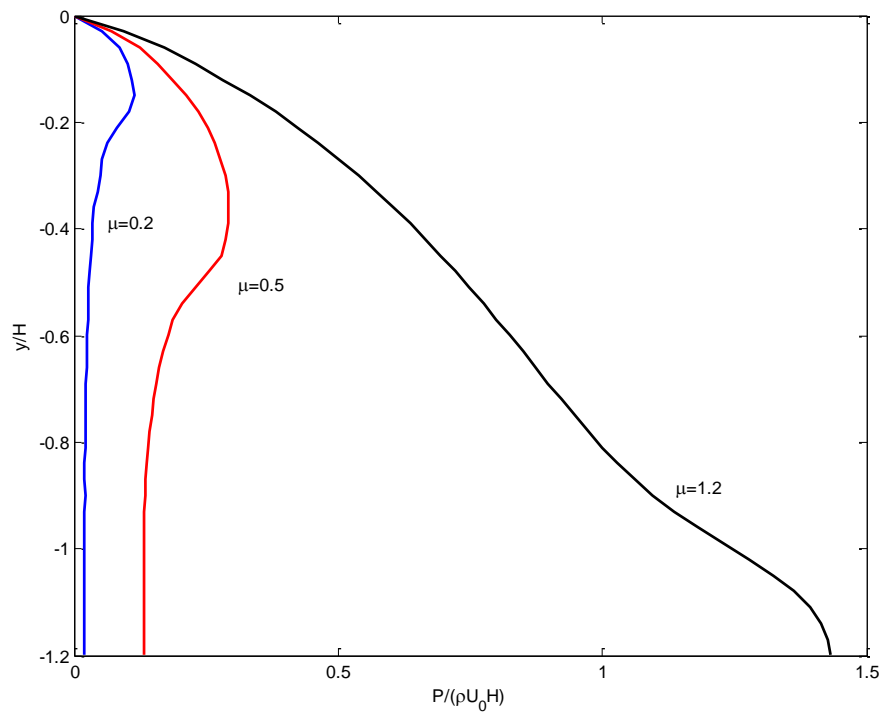
Figure 3.4.12: Pressure impulse on the wall for ditch $H_b = 1.2$ for varying μ

3.5 Total impulse on the wall and seabed

We now calculate the total impulse generated by the impact on the wall and seabed for berm and ditch problems. This is accomplished by integrating the pressure impulse over the domain being considered.
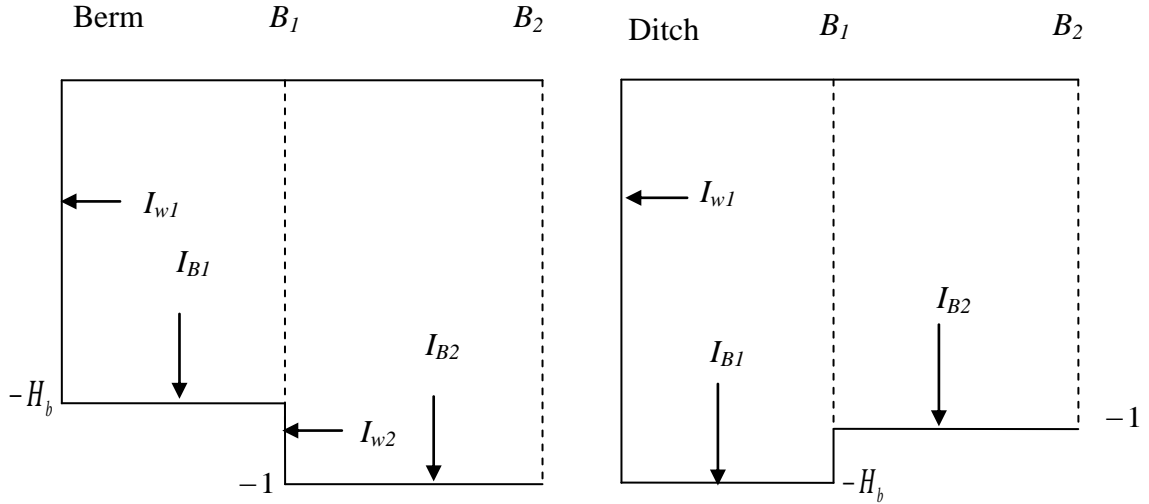
Figure 3.5.1: Total impulse diagrams for berm and ditch.

For the impulse on the wall I_w, we need:

$$I_{w1} = \int_{-H_b}^{0} P_1(0, y)\,dy \tag{3.5.1}$$

Solving this equation gives

$$I_{w1} = \sum_{n=1}^{\infty} \left\{ -\alpha_n \tanh\left(\frac{\lambda_n B_1}{H_b}\right) + \beta_n \right\} \int_{-H_b}^{0} \sin\left(\frac{\lambda_n y}{H_b}\right) dy$$

$$= \sum_{n=1}^{\infty} -\frac{H_b}{\lambda_n} \left\{ -\alpha_n \tanh\left(\frac{\lambda_n B_1}{H_b}\right) + \beta_n \right\} \tag{3.5.2}$$

This is the horizontal impulse for the ditch problem, I_{w1}. For the berm problem, the horizontal impulse is a combination of I_{w1} and I_{w2}. So calculating the I_{w2} for berm problem we need

$$I_{w2} = \int\limits_{-1}^{-H_b} P_2(B_1, y)\,dy \tag{3.5.3}$$

$$= \sum_{n=1}^{\infty} c_n \frac{\sinh(\lambda_n(B_1 - B2))}{\cosh(\lambda_n B_2)} \int\limits_{-1}^{-H_b} \sin(\lambda_n y)\,dy$$

$$I_{w2} = \sum_{n=1}^{\infty} c_n \frac{\sinh(\lambda_n(B_1 - B2))}{\cosh(\lambda_n B_2)} \left[-\frac{1}{\lambda_n} \cos(\lambda_n H_b) \right] \tag{3.5.4}$$

Therefore the total impulse on the wall/berm structure, I_w is

$$I_w = I_{w1} + I_{w2}$$

while the total impulse on the wall, I_w for the ditch problem is

$$I_w = I_{w1}.$$

The total vertical impulse on the seabed for both problems is given by:

$$I_B = I_{B1} + I_{B2}$$

where the total impulse is

$$I_B = \int\limits_{0}^{B_1} P_1(x, -H_b)\,dx + \int\limits_{B_1}^{B_2} P_2(x, -1)\,dx \tag{3.5.5}$$

$$= \sum_{n=1}^{\infty} \frac{\sin(-\lambda_n)}{\cosh\left(\dfrac{\lambda_n B_1}{H_b}\right)} \int\limits_{0}^{B_1} \left\{ \alpha_n \sinh\left(\frac{\lambda_n(x - B_1)}{H_b}\right) + \beta_n \cosh\left(\frac{\lambda_n(x - B_1)}{H_b}\right) \right\} dx$$

$$+ \sum_{n=1}^{\infty} c_n \frac{\sin(-\lambda_n)}{\cosh(\lambda_n B_2)} \int\limits_{B_1}^{B_2} \sinh(\lambda_n(x - B_2))\,dx$$

$$= \sum_{n=1}^{\infty} \frac{\sin(-\lambda_n)}{\cosh\left(\dfrac{\lambda_n B_1}{H_b}\right)} \left[\frac{H_b}{\lambda_n}\right] \left\{ \alpha_n \left[1 - \cosh\left(\frac{\lambda_n B_1}{H_b}\right)\right] + \beta_n \sinh\left(\frac{\lambda_n B_1}{H_b}\right) \right\}$$

$$+ \sum_{n=1}^{\infty} c_n \frac{\sin(-\lambda_n)}{\cosh(\lambda_n B_2)} \left[\frac{1}{\lambda_n} - \frac{1}{\lambda_n} \cosh(\lambda_n(B_1 - B_2)) \right] \tag{3.5.6}$$

Figure 3.5.2 to 3.5.4 show the total impulse on the wall and seabed for berm and ditch. The total impulse on the wall for the berm is greater than total impulse on the seabed and the same goes for the ditch case. The total impulse on the wall and seabed for the ditch is greater than total impulse on the wall and seabed for berm respectively. These cases can be compared with figure 2.5.2 for the Cooker model.

63
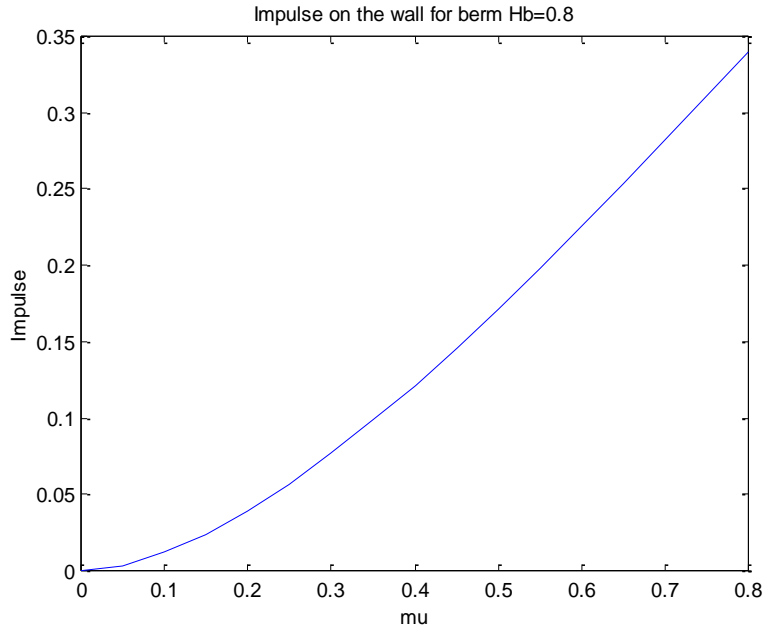
Figure 3.5.2: Total impulse on the wall with berm, with $H_b = 0.8, B_1 = 0.2, B_2 = 2$.
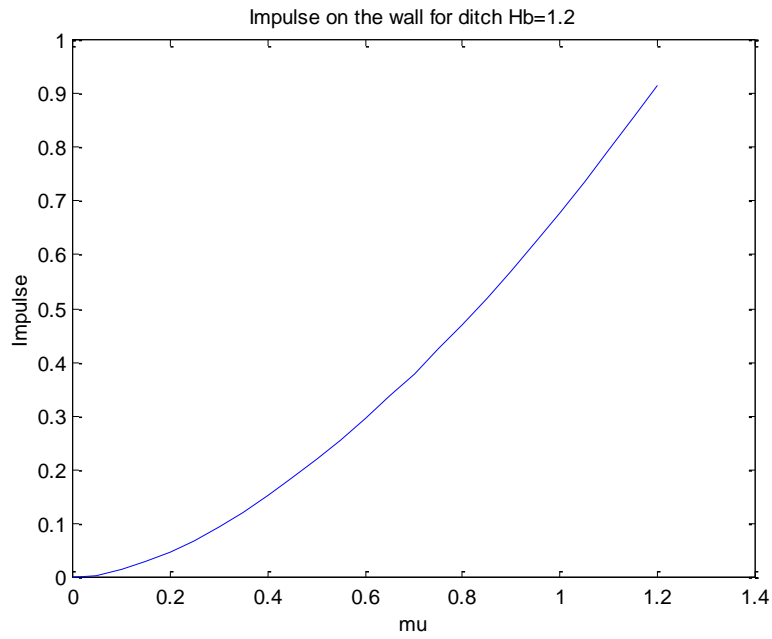
Figure 3.5.3: Total impulse on the wall with ditch, with $H_b = 1.2, B_1 = 0.2, B_2 = 2$.

Berm ($H_b = 0.8, B_1 = 0.2, B_2 = 2$)	**Ditch** ($H_b = 1.2, B_1 = 0.2, B_2 = 2$)
Total impulse = $I_{B1} + I_{B2}$	Total impulse = $I_{B1} + I_{B2}$
Total impulse, I_{B1}	Total impulse, I_{B1}
Total impulse, I_{B2}	Total impulse, I_{B2}
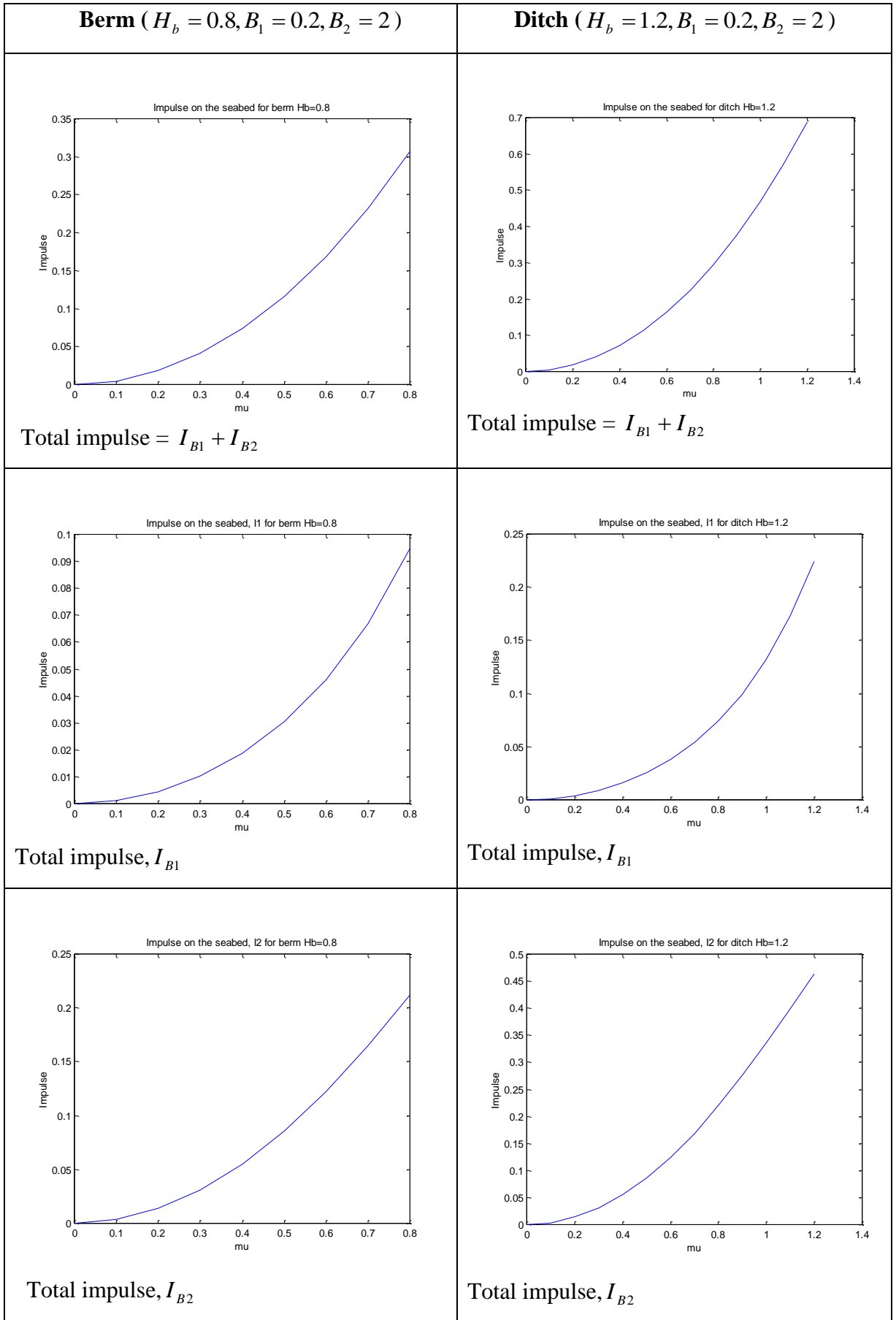
Figure 3.5.4 : Total impulse on the seabed for berm and ditch.

3.6   Moment impulse on the wall and seabed

The pressure impulse acting on a coastal structure generates moments that could move or even topple it. In this section we calculate the moment on the wall and seabed that may affect the seawall. For the following work clockwise moment will be considered to be positive and will be taken about the foot (●) of the wall, see figure (3.6.1).
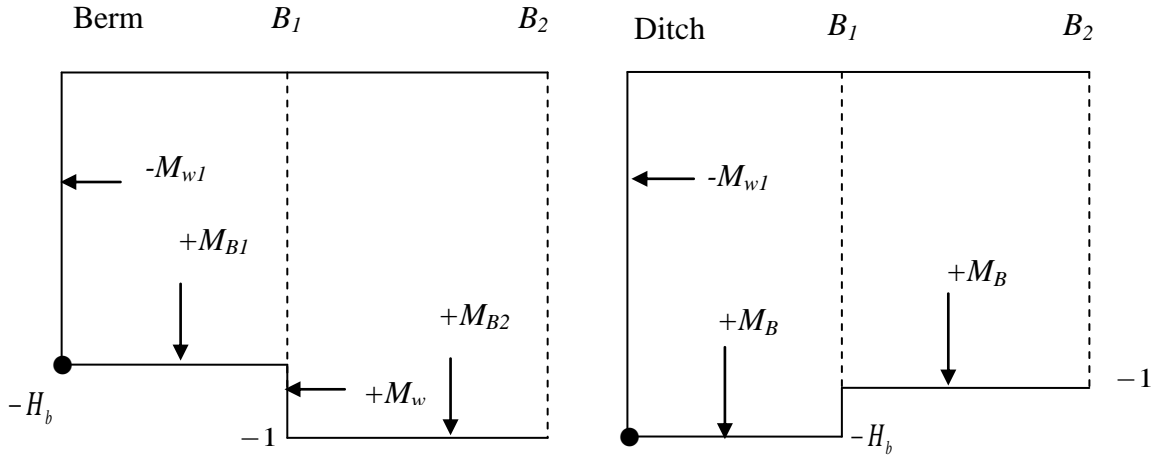
Figure 3.6.1: Moment impulse diagrams for berm and ditch.

The moment impulse on the wall given by:

$$M_{w1} = -\int_{-H_b}^{0}(1+y)P_1(0,y)dy \tag{3.6.1}$$

Solving this equation gives

$$M_{w1} = -\int_{-H_b}^{0}(1+y)\sum_{n=1}^{\infty}\sin\left(\frac{\lambda_n y}{H_b}\right)\left\{-\alpha_n\tanh\left(\frac{\lambda_n B_1}{H_b}\right)+\beta_n\right\}dy$$

$$= -\sum_{n=1}^{\infty}\left\{-\alpha_n\tanh\left(\frac{\lambda_n B_1}{H_b}\right)+\beta_n\right\}\int_{-H_b}^{0}(1+y)\sin\left(\frac{\lambda_n y}{H_b}\right)dy$$

$$= -\sum_{n=1}^{\infty}\left\{-\alpha_n\tanh\left(\frac{\lambda_n B_1}{H_b}\right)+\beta_n\right\}\left[\int_{-H_b}^{0}\sin\left(\frac{\lambda_n y}{H_b}\right)dy+\int_{-H_b}^{0}y\sin\left(\frac{\lambda_n y}{H_b}\right)dy\right]$$

$$= -\sum_{n=1}^{\infty}\left\{-\alpha_n\tanh\left(\frac{\lambda_n B_1}{H_b}\right)+\beta_n\right\}$$

$$\left[\left[-\frac{H_b}{\lambda_n}\cos\left(\frac{\lambda_n y}{H_b}\right)\right]_{-H_b}^{0}+\left[-\frac{H_b y}{\lambda_n}\cos\left(\frac{\lambda_n y}{H_b}\right)+\int_{-H_b}^{0}\frac{H_b}{\lambda_n}\cos\left(\frac{\lambda_n y}{H_b}\right)dy\right]\right]$$

$$=-\sum_{n=1}^{\infty}\left\{-\alpha_n\tanh\left(\frac{\lambda_n B_1}{H_b}\right)+\beta_n\right\}$$

$$\left[\left[-\frac{H_b}{\lambda_n}\cos\left(\frac{\lambda_n y}{H_b}\right)\right]_{-H_b}^{0}+\left[-\frac{H_b y}{\lambda_n}\cos\left(\frac{\lambda_n y}{H_b}\right)+\frac{H_b^2}{\lambda_n^2}\sin\left(\frac{\lambda_n y}{H_b}\right)\right]_{-H_b}^{0}\right]$$

$$=\sum_{n=1}^{\infty}\left[\frac{H_b}{\lambda_n}-\frac{H_b^2}{\lambda_n^2}\sin(\lambda_n)\right]\left\{\alpha_n\tanh\left(\frac{\lambda_n B_1}{H_b}\right)-\beta_n\right\}\qquad(3.6.2)$$

This gives the moment impulse on the wall for the ditch, $M_w=M_{w1}$. For the berm problem we need

$$M_{w2}=+\int_{-1}^{-H_b}(1+y)P_2(B_1,y)dy\qquad(3.6.3)$$

$$=\sum_{n=1}^{\infty}C_n\frac{\sinh(\lambda_n(B_1-B_2))}{\cosh(\lambda_n B_2)}\int_{-1}^{-H_b}(1+y)\sin(\lambda_n y)dy$$

$$=\sum_{n=1}^{\infty}C_n\frac{\sinh(\lambda_n(B_1-B_2))}{\cosh(\lambda_n B_2)}\left[-\frac{1}{\lambda_n}\cos(\lambda_n H_b)+\frac{H_b}{\lambda_n}\cos(\lambda_n H_b)-\frac{1}{\lambda_n^2}\sin(\lambda_n H_b)+\frac{1}{\lambda_n^2}\sin(\lambda_n)\right]$$

$$(3.6.4)$$

So that the moment impulse on the wall for the berm problem is $M_w=-M_{w1}+M_{w2}$

The moment impulse on the seabed is given by:

$$M_B=\int_{0}^{B_1}xP_1(x,-H_b)dx+\int_{B_1}^{B_2}xP_2(x,-1)dx\qquad(3.6.5)$$

$$=\sum_{n=1}^{\infty}\frac{\sin(-\lambda_n)}{\cosh\left(\frac{\lambda_n B_1}{H_b}\right)}\int_{0}^{B_1}\left\{\alpha_n x\sinh\left(\frac{\lambda_n(x-B_1)}{H_b}\right)+\beta_n x\cosh\left(\frac{\lambda_n(x-B_1)}{H_b}\right)\right\}dx$$

$$+\sum_{n=1}^{\infty}c_n\frac{\sin(-\lambda_n)}{\cosh(\lambda_n B_2)}\int_{B_1}^{B_2}x\sinh(\lambda_n(x-B_2))dx$$

$$= \sum_{n=1}^{\infty} \frac{\sin(-\lambda_n)}{\cosh\left(\dfrac{\lambda_n B_1}{H_b}\right)} \left\{ \alpha_n \left[\frac{H_b x}{\lambda_n} \cosh\left(\frac{\lambda_n (x - B_1)}{H_b} \right) - \frac{H_b^2}{\lambda_n^2} \sinh\left(\frac{\lambda_n (x - B_1)}{H_b} \right) \right]_0^{B_1} \right.$$

$$\left. + \beta_n \left[\frac{H_b x}{\lambda_n} \sinh\left(\frac{\lambda_n (x - B_1)}{H_b} \right) - \frac{H_b^2}{\lambda_n^2} \cosh\left(\frac{\lambda_n (x - B_1)}{H_b} \right) \right]_0^{B_1} \right\}$$

$$+ \sum_{n=1}^{\infty} c_n \frac{\sin(-\lambda_n)}{\cosh(\lambda_n B_2)} \left[\frac{x}{\lambda_n} \cosh(\lambda_n (x - B_2)) - \frac{1}{\lambda_n^2} \sinh(\lambda_n (x - B_2)) \right]_{B_1}^{B_2}$$

$$= \sum_{n=1}^{\infty} \frac{\sin(-\lambda_n)}{\cosh\left(\dfrac{\lambda_n B_1}{H_b}\right)} \left\{ \alpha_n \left[\frac{H_b B_1}{\lambda_n} - \frac{H_b^2}{\lambda_n^2} \sinh\left(\frac{\lambda_n B_1}{H_b} \right) \right] + \beta_n \left[- \frac{H_b^2}{\lambda_n^2} + \frac{H_b^2}{\lambda_n^2} \cosh\left(\frac{\lambda_n B_1}{H_b} \right) \right] \right\}$$

$$+ \sum_{n=1}^{\infty} c_n \frac{\sin(-\lambda_n)}{\cosh(\lambda_n B_2)} \left[\frac{B_2}{\lambda_n} - \frac{B_1}{\lambda_n} \cosh(\lambda_n (B_1 - B_2)) + \frac{1}{\lambda_n^2} \sinh(\lambda_n (B_1 - B_2)) \right]$$

(3.6.6)

The following graphs show the moment impulses that act on berm and ditch. From figure 3.6.2 and figure 3.6.3 we can see that moment impulse on the wall for ditch is greater than for the berm. Figure 3.6.4 shows the moment impulse on seabed for berm and ditch problems. We can see that the total moment impulse for the ditch problem is greater than for the berm but in the negative direction. Moment impulse in the inner region for both cases are in negative direction, and both in the positive direction in the outer region with the value for the ditch higher than that of the berm.
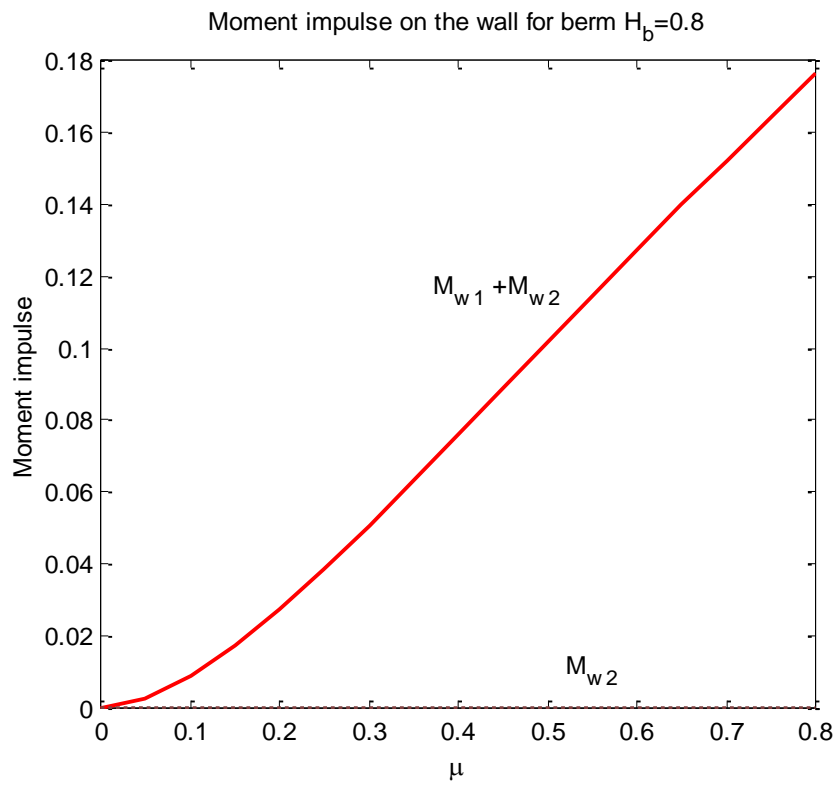
Figure 3.6.2: Moment impulse on the wall for a berm with $H_b = 0.8, B_1 = 0.2, B_2 = 2$.
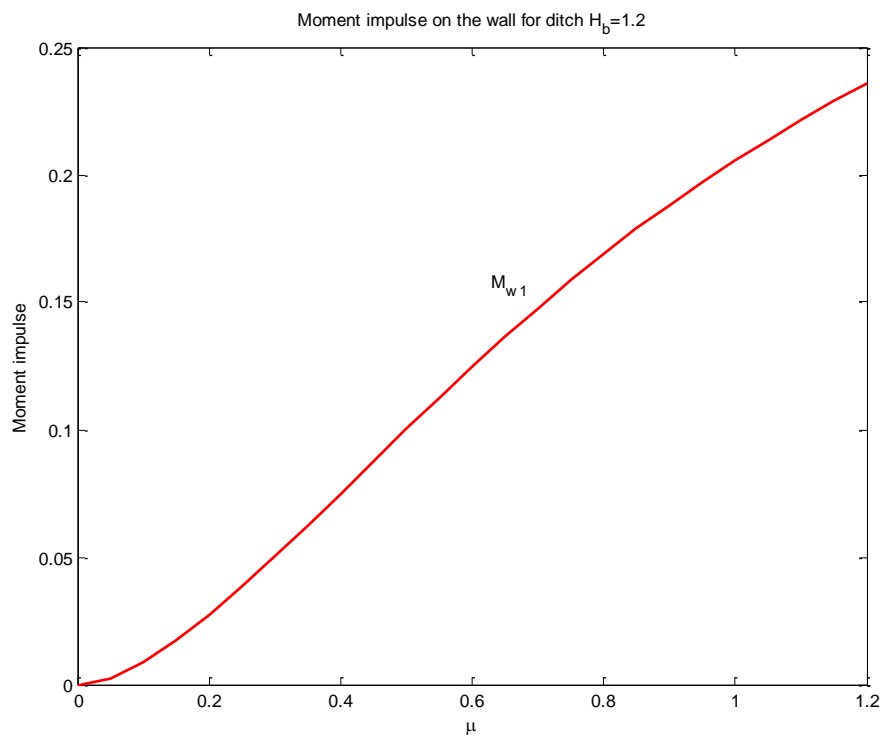
Figure 3.6.3: Moment impulse on the wall for a ditch, with $H_b = 1.2, B_1 = 0.2, B_2 = 2$.
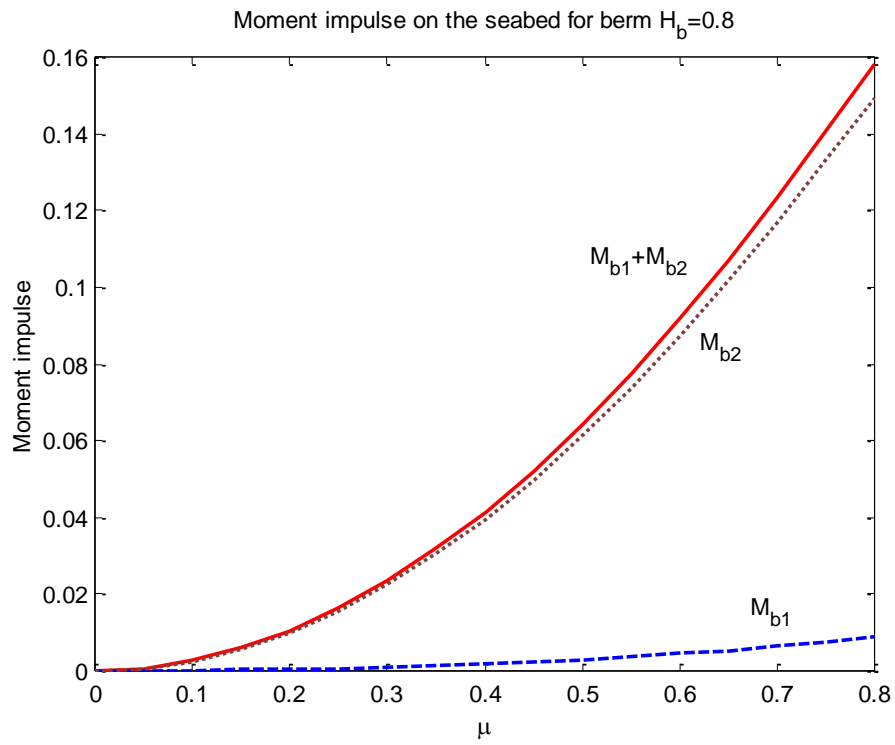
Figure 3.6.4: Moment impulse on the seabed for a berm.
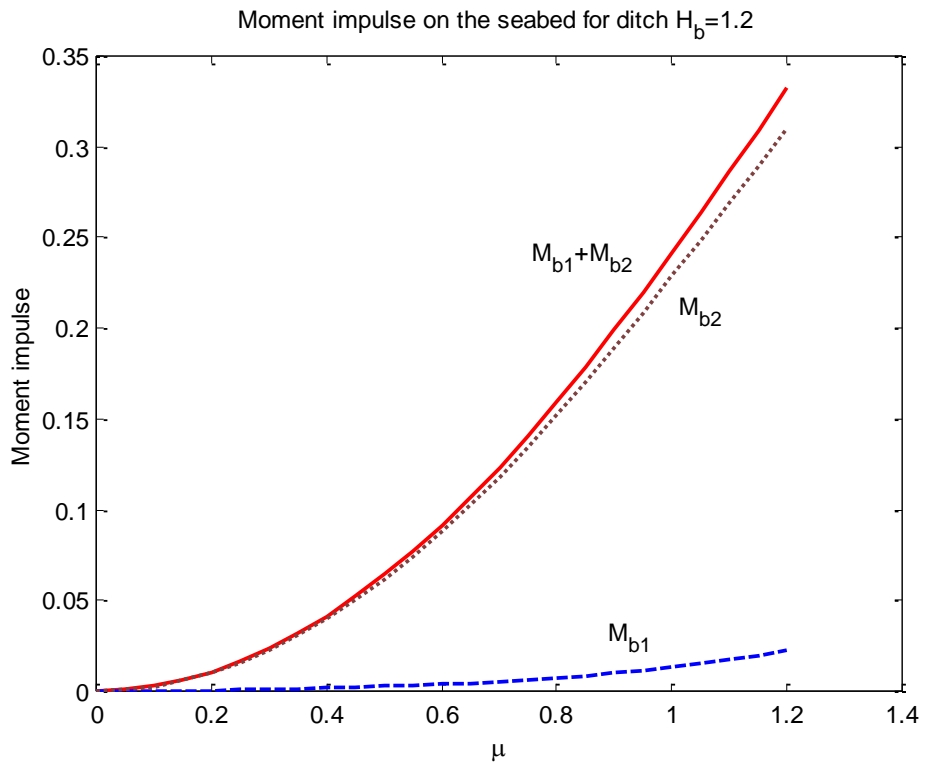
Figure 3.6.5: Moment impulse on the seabed for a ditch.

3.7   Overtopping

As in §2.6.1, we would like to present a simplified model of wave overtopping for berm and ditch problem. The calculation for both problems is the same since they have the same solution except for the value of coefficients.
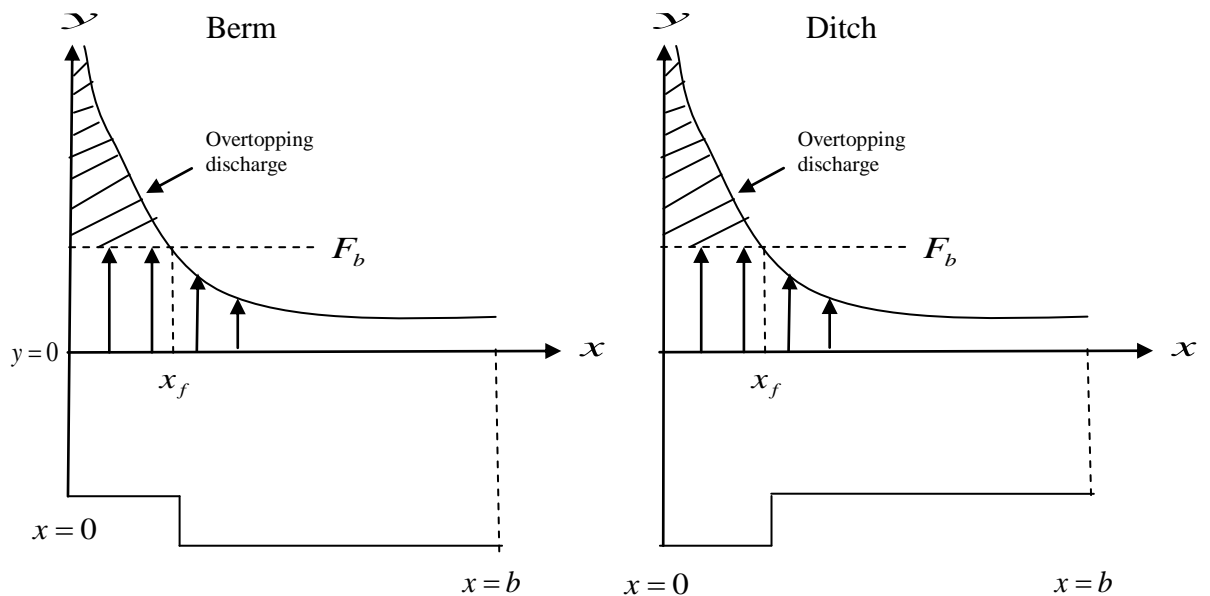
Figure 3.7.1: Overtopping definition sketch for berm and ditch.

The parameters of this situation remain the same as in §2.7.1:

F_b = the height of freeboard from the free surface

x_f = distance at which predicted free surface is at F_b

b = distant boundary

y_{max} = the highest vertical height of overtopping of free surface particles. This is a function of x.

We obtained equation (2.7.1) by assuming the jet of fluid is thin and the pressure gradients are low in the jet, so the jet particles move as free projectiles.

The upwards velocity (before impact) is zero the initial upward just after impact velocity is simply given by

$$v_y = \frac{\partial P}{\partial y} = \sum_{n=1}^{\infty} \frac{\lambda_n}{H_b} \frac{\cos\left(\frac{\lambda_n y}{H_b}\right)}{\cosh\left(\frac{\lambda_n B_1}{H_b}\right)} \left\{ \alpha_n \sinh\left(\frac{\lambda_n (x - B_1)}{H_b}\right) + \beta_n \cosh\left(\frac{\lambda_n (x - B_1)}{H_b}\right) \right\}$$

$$+ \sum_{n=1}^{\infty} c_n \lambda_n \frac{\cos(\lambda_n y)}{\cosh(\lambda_n B_2)} \sinh(\lambda_n (x - B_2)) \tag{3.7.1}$$

So that the initial velocity upward, when $y = 0$, gives

$$v_y = \frac{\partial P}{\partial y} = \sum_{n=1}^{\infty} \frac{\lambda_n}{H_b} \frac{1}{\cosh\left(\frac{\lambda_n B_1}{H_b}\right)} \left\{ \alpha_n \sinh\left(\frac{\lambda_n (x - B_1)}{H_b}\right) + \beta_n \cosh\left(\frac{\lambda_n (x - B_1)}{H_b}\right) \right\}$$

$$+ \sum_{n=1}^{\infty} \frac{c_n \lambda_n}{\cosh(\lambda_n B_2)} \sinh(\lambda_n (x - B_2)). \tag{3.7.2}$$

Hence the maximum vertical height of the jet is

$$y_{\max} = \frac{1}{2} F_r \left(\sum_{n=1}^{\infty} \frac{\lambda_n}{H_b} \frac{1}{\cosh\left(\frac{\lambda_n b_1}{H_b}\right)} \left\{ \alpha_n \sinh\left(\frac{\lambda_n (x - B_1)}{H_b}\right) + \beta_n \cosh\left(\frac{\lambda_n (x - B_1)}{H_b}\right) \right\} + \right.$$

$$\left. \sum_{n=1}^{\infty} \frac{c_n \lambda_n}{\cosh(\lambda_n b_2)} \sinh(\lambda_n (x - B_2)) \right)^2 \tag{3.7.3}$$

For freeboard, F_b we have as a condition on x_f:

$$F_b = \frac{1}{2} F_r \left(\sum_{n=1}^{\infty} \frac{\lambda_n}{H_b} \frac{1}{\cosh\left(\frac{\lambda_n B_1}{H_b}\right)} \left\{ \alpha_n \sinh\left(\frac{\lambda_n (x_f - B_1)}{H_b}\right) + \beta_n \cosh\left(\frac{\lambda_n (x_f - B_1)}{H_b}\right) \right\} + \right.$$

$$\left. \sum_{n=1}^{\infty} \frac{c_n \lambda_n}{\cosh(\lambda_n B_2)} \sinh(\lambda_n (x_f - B_2)) \right)^2 \tag{3.7.4}$$

So we can find F_b in terms of a parameter x_f, the distance at which F_b is achieved. Calculating the overtopping discharge, V

$$V = \int_0^{x_f} (y_{vert} - F_b)dx$$

gives,

$$V = \int_0^{x_f} y_{vert}dx - x_f F_b \qquad (3.7.5)$$

which is again evaluated numerically.

The result for the volume of overtopping subject to the height of freeboard is shown in figure 3.7.2. Given the assumption that particles in the jet move as free projectiles, the model will not be valid for very low freeboard since the pressure impulse gradients will be finite for region above F_b and away from the wall.

Figure 3.7.2 shows the overtopping discharge for a seawall with a berm and a ditch. We can see that the discharge of the overtopping for both cases is comparable for corresponding freeboard values. Having said that, the freeboard values for the berm are substantially higher than for the ditch, meaning that the berm's jet will reach far higher in the air.

Further results (not shown here) show that the ditch overtopping is largely insensitive to the ditch width (as expected because the ditch pressure is almost constant). More surprisingly, the berm overtopping is also quite insensitive to the berm size if the berm is submerged to at least half the water depth. On the other hand if the berm's top is near the bottom of the impact region then there is typically an increase of about 20% to 30% compared with a deeply submerged berm for any given freeboard.

Berm ($H_b = 0.8, B_1 = 0.2, B_2 = 2$)	**Ditch** ($H_b = 1.2, B_1 = 0.2, B_2 = 2$)
$\mu = 0.1$	$\mu = 0.1$
$\mu = 0.5$	$\mu = 0.5$
$\mu = 0.8$	$\mu = 1.2$
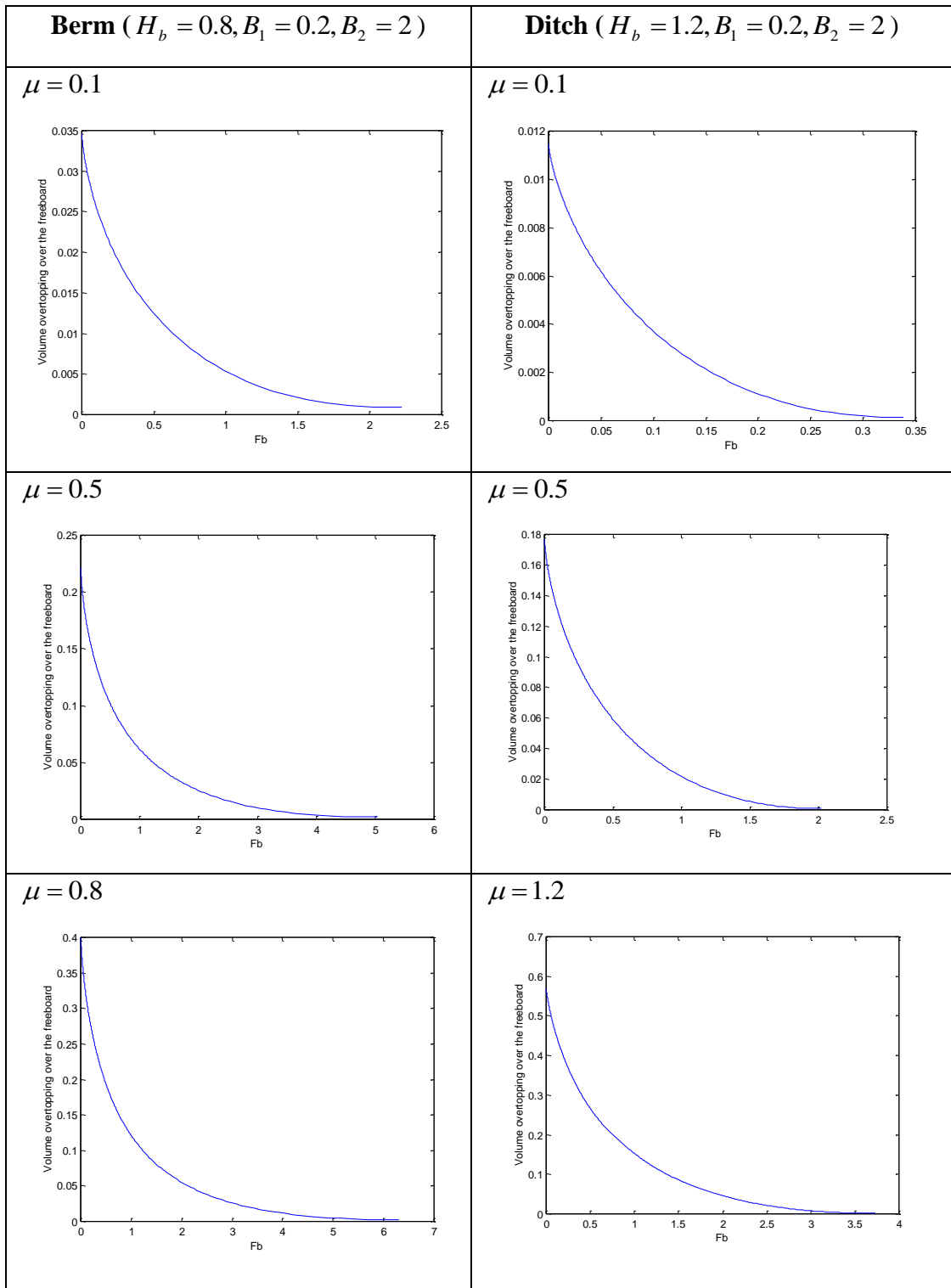
Figure 3.7.2: Overtopping discharge for seawall with a berm and a ditch as before F_b is the dimensionless freeboard reference to depth H and V is volume overtopping per unit length of seawall divided by H^2.

3.8 Conclusion

Here we compare the berm and ditch results with Cooker's model. We compare the worst cases i.e. those for the largest possible impact region;

- the seawall with a ditch has a largest maximum pressure impulse which is $1.400 \rho U_0 H$, with $\mu = 1.2$,

- the basic seawall (Cooker's model) has pressure impulse $0.742 \rho U_0 H$, with $\mu = 1.0$,

- the seawall with a berm has the smallest maximum pressure impulse which is $0.570 \rho U_0 H$, with $\mu = 0.8$.

Table 3.8.1: Total impulse on the wall and on the seabed for the seawall, berm and ditch for the maximum impact.

	Total impulse , $\rho U_0 H^2$		
	Seawall	Berm	Ditch
Wall	0.54	0.34	0.90
Seabed	0.45	0.31	0.70

From table 3.8.1, we can see that total impulse on the wall with a ditch is the greatest followed by the seawall and then the berm as expected. This is partly because a seawall with a ditch has the largest area of impact while the area of impact of seawall with a berm is much smaller than Cooker's model. The same trend occurs for the total impulse on the seabed as defined in figure 3.5.1

Table 3.8.2: Models impulse on the wall and on the seabed for the seawall, berm and ditch for the maximum impact.

	Moment impulse , $\rho U_0 H^3$		
	Seawall	Berm	Ditch
Wall	0.220	0.175	0.240
Seabed	0.340	0.150	0.345

Table 3.8.2, shows the moment impulse for the wall and seabed for the seawall, berm and ditch models. We can see that seawall with a ditch has a largest value of moment impulse on the wall and on the seabed. As expected, the moment impulse for a seawall with a berm has the smallest value compared to the other two problems.

We can conclude that a seawall with a berm has a beneficial effect on reducing pressure impulse while seawall with a ditch is very detrimental. This means that scour at the base of a seawall is likely to be extremely dangerous.

CHAPTER 4

MISSING BLOCK

4.1   Introduction

Now we extend the study by Greenhow (2006) who developed and applied a simple analytical model for pressure impulse for missing block problem based on Cooker's model. The motivation for this study is to examine the impact on a seawall when at is in a damaged condition, especially the pressure impulse in the missing block region which, if high, could cause further damage. This problem has been solved by Greenhow (2006) by using a basis function method which relies on matching the values and horizontal components of eigenfunction expansions in each of the rectangular regions that arise. We will use the basis function method in this problem as we will use this method in Chapter 7, but here working in dimensionless parameters. We will compare the results with Greenhow (2006) and calculate the impulse and moment for this problem.

4.2   Literature review

Greenhow (2006) continued his theoretical work by investigating the missing block problem, giving us an understanding into the spatial distribution of the pressure impulse in the fluid region, including the block region. The missing block region is assumed to

be filled with fluid and submerged below the impact region. He found that this situation will allow penetration of unreduced high pressures into the seawall core.

Cox and Cooker (2001) studied pressure impulse in a fluid saturated crack in a seawall. The crack might be the gap between two blocks in a blockwork breakwater, or the space opened up after a fracture in the brickwork or natural coastal structures. They also used pressure impulse, *P,* to model the problem in two-dimensions. They suggest that the impulse directed normal to the horizontal plane of the crack can lift of the large block above it.

Müller (1997) investigated experimentally the pressure propagation into cracks and fissures. He measured the impact pressures on a vertical seawall and then in a water-filled model of a crack inserted into the wall. He found that impact pressures on the wall can propagate into the crack, and the pressures in the experiment were higher at the back of the crack. This can lead to erosion of structures and seaward removal of blocks in the coastal zone.

Müller's (1997) results have been confirmed by Wolters and Müller (2004) by their series of model tests. They concluded that partially-filled cracks are more dangerous for the integrity of the structure than fully-filled cracks.

4.3 Missing Block Problem

We divide this problem into two regions. Region 1 is the missing block of height $H_2 - H_1$ which is filled by water and below the impact region, see figure 4.3.1. H_1 is the distance down the wall from the free surface to the roof of the missing block and H_2 is the distance down the wall from free surface to the base of the missing block. The width of the missing block is given by B_1. Notice that the region 2 is nearly identical to the Cooker model, and so the solution there is actually almost the same. In the region 1, we have two hyperbolic terms and introduce the new parameter, $\gamma = n\pi$. The distant boundary away from the seawall is given at $x = B_2$. We solved this using a basis function method with integral method on the impact wall and matching the horizontal components of eigenfunction expansions at $x = B_1$. We also work with

dimensionless pressure impulse and use P as dimensionless pressure impulse, which scales with $\rho U_0 H$. Under the assumptions stated above, the formulations involve equations from region 1 and region 2.

$$P_2 = 0 \qquad y = 0$$

$$\frac{\partial P_1}{\partial y} = 0 \qquad \frac{\partial P_2}{\partial x} = -1$$

$$y = -H_1 \qquad y = -\mu \qquad \text{Region 2}$$

$$\frac{\partial P_1}{\partial x} = 0 \qquad \text{Region 1} \qquad \nabla^2 P_2 = 0 \qquad P_2 = 0$$

$$y = -H_2 \qquad \nabla^2 P_1 = 0$$

$$x = 0 \quad \frac{\partial P_1}{\partial y} = 0 \qquad \frac{\partial P_2}{\partial x} = 0 \qquad y = -H_3$$

$$x = B_1 \qquad \frac{\partial P_2}{\partial y} = 0 \qquad x = B_2$$
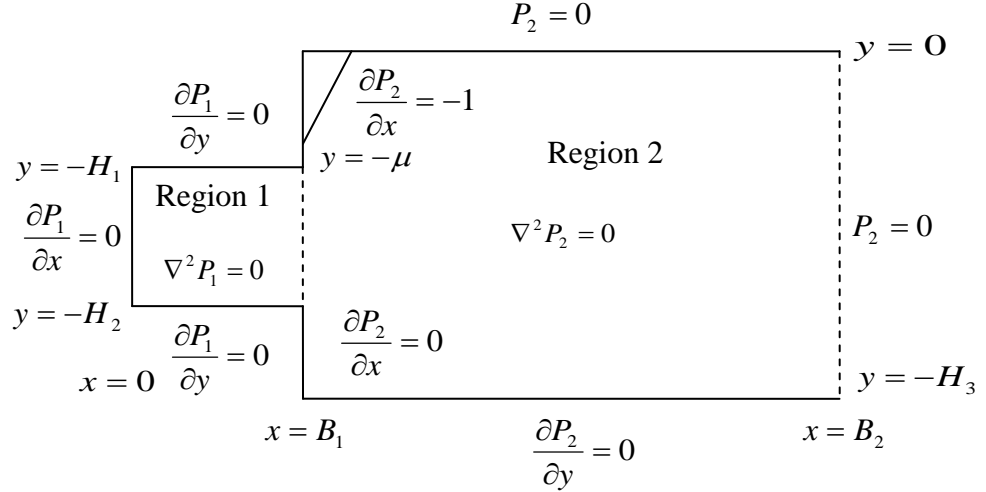
Figure 4.3.1: The boundary-value problem for the pressure impulse for impact over the upper part of a seawall.

We have the solution for the region 1 and region 2 given by the following eigenfunctions:

$$
\begin{aligned}
P_1(x, y) = &\sum_{n=1}^{\infty} a_n \frac{\cos\left(\dfrac{\gamma_n(2y + H_1 + H_2)}{H_2 - H_1}\right)}{\cosh\left(\dfrac{\gamma_n B_1}{H_2 - H_1}\right)} \cosh\left(\dfrac{2\gamma_n x}{H_2 - H_1}\right) \\
&+ \sum_{n=1}^{\infty} b_n \frac{\sin\left(\dfrac{\lambda_n(2y + H_1 + H_2)}{H_2 - H_1}\right)}{\cosh\left(\dfrac{\lambda_n B_1}{H_2 - H_1}\right)} \cosh\left(\dfrac{2\lambda_n x}{H_2 - H_1}\right) + A
\end{aligned}
\tag{4.3.1}
$$

Here we see a new constant term, A, not in the previous formulations since there $P = 0$ on $y = 0$. We call this a secular term.

$$P_2(x, y) = \sum_{n=1}^{\infty} c_n \frac{\sin\left(\frac{\lambda_n y}{H_3}\right)}{\cosh\left(\frac{\lambda_n B_2}{H_3}\right)} \sinh\left(\frac{\lambda_n(x - B_2)}{H_3}\right) \tag{4.3.2}$$

where $\lambda_n = (n - \frac{1}{2})\pi$ and $\gamma_n = n\pi$. Equation 4.3.1 above satisfies all the boundary

conditions for the problem shown in figure 4.3.1.

On $x = B_1$ we have $P_1 = P_2$ for $-H_2 \le y < -H_1$ and

$$\frac{\partial P_2}{\partial x} = \begin{cases} -\rho U(y) & \text{for} & -\mu H_3 \le y \le 0 \\ 0 & \text{for} & -H_1 \le y < -\mu H_3 \\ \dfrac{\partial P_1}{\partial x} & \text{for} & -H_2 \le y < -H_1 \\ 0 & \text{for} & -H_3 \le y < -H_2 \end{cases} \tag{4.3.3}$$

In the matching region, $x = B_1$ we have $P_1 = P_2$ for $-H_2 \le y < -H_1$ which gives us

$$\sum_{n=1}^{\infty} a_n \frac{\cos\left(\frac{\gamma_n(2y + H_1 + H_2)}{H_2 - H_1}\right)}{\cosh\left(\frac{\gamma_n B_1}{H_2 - H_1}\right)} \cosh\left(\frac{2\gamma_n B_1}{H_2 - H_1}\right) + \sum_{n=1}^{\infty} b_n \frac{\sin\left(\frac{\lambda_n(2y + H_1 + H_2)}{H_2 - H_1}\right)}{\cosh\left(\frac{\lambda_n B_1}{H_2 - H_1}\right)} \cosh\left(\frac{2\lambda_n B_1}{H_2 - H_1}\right)$$

$$+ A = \sum_{n=1}^{\infty} c_n \frac{\sin\left(\frac{\lambda_n y}{H_3}\right)}{\cosh\left(\frac{\lambda_n B_2}{H_3}\right)} \sinh\left(\frac{\lambda_n(B_1 - B_2)}{H_3}\right) \tag{4.3.4}$$

Simplify (4.3.4) gives us

$$\sum_{n=1}^{\infty} a_n \cos\left(\frac{\gamma_n(2y + H_1 + H_2)}{H_2 - H_1}\right) t_1(n) + \sum_{n=1}^{\infty} b_n \sin\left(\frac{\lambda_n(2y + H_1 + H_2)}{H_2 - H_1}\right) t_2(n) + A$$

$$- \sum_{n=1}^{\infty} c_n \frac{\sin\left(\frac{\lambda_n y}{H_3}\right)}{\cosh\left(\frac{\lambda_n B_2}{H_3}\right)} \sinh\left(\frac{\lambda_n(B_1 - B_2)}{H_3}\right) = 0 \tag{4.3.5}$$

with $t_1(n) = \dfrac{\cosh\left(\dfrac{2\gamma_n B_1}{H_2 - H_1}\right)}{\cosh\left(\dfrac{\gamma_n B_1}{H_2 - H_1}\right)}$ and $t_2(n) = \dfrac{\cosh\left(\dfrac{2\lambda_n B_1}{H_2 - H_1}\right)}{\cosh\left(\dfrac{\lambda_n B_1}{H_2 - H_1}\right)}$

To find the secular term, A, we apply $\displaystyle\int_{-H_2}^{-H_1}\ldots 1\,dy$ to (4.3.5) gives us:

$$\sum_{n=1}^{\infty} a_n t_1(n) \int_{-H_2}^{-H_1} \cos\left(\frac{\gamma_n(2y + H_1 + H_2)}{H_2 - H_1}\right)dy + \sum_{n=1}^{\infty} b_n t_2(n) \int_{-H_2}^{-H_1} \sin\left(\frac{\lambda_n(2y + H_1 + H_2)}{H_2 - H_1}\right)dy + A\int_{-H_2}^{-H_1} 1\,dy$$

$$-\sum_{n=1}^{\infty} c_n \frac{\sinh\left(\dfrac{\lambda_n(B_1 - B_2)}{H_3}\right)}{\cosh\left(\dfrac{\lambda_n B_2}{H_3}\right)} \int_{-H_2}^{-H_1} \sin\left(\frac{\lambda_n y}{H_3}\right)dy = 0$$

Hence

$$A = \sum_{n=1}^{\infty} \frac{c_n}{H_2 - H_1}\left[\frac{H_3}{\lambda_n}\left(\cos\left(\frac{-\lambda_n H_2}{H_3}\right) - \cos\left(\frac{-\lambda_n H_1}{H_3}\right)\right)\right] \frac{\sinh\left(\dfrac{\lambda_n(B_1 - B_2)}{H_3}\right)}{\cosh\left(\dfrac{\lambda_n B_2}{H_3}\right)} \qquad (4.3.6)$$

Now, we have $3N$ unknowns $\alpha_1, \alpha_2, \ldots \alpha_N, \beta_1, \beta_2, \ldots \beta_N$ and $c_1, c_2, \ldots c_N$. We match P_1 to P_2 in the block region $-H_2 \leq y < -H_1$ at $x = B_1$ as in equation (4.3.4). To solve this we apply:

$$\int_{-H_2}^{-H_1}\ldots \sin\left(\frac{\lambda_l(2y + H_1 + H_2)}{H_2 - H_1}\right)dy \quad \text{with } l = 1,2,\ldots N \text{ giving } N \text{ equations and}$$

$$\int_{-H_2}^{-H_1}\ldots \cos\left(\frac{\gamma_l(2y + H_1 + H_2)}{H_2 - H_1}\right)dy \quad \text{with } l = 1,2,\ldots N \text{ giving } N \text{ equations.}$$

The integrands here are respectively antisymmetric and symmetric about the centreline of the missing block i.e. $y = -\left(\dfrac{H_1 + H_2}{2}\right)$.

Applying $\displaystyle\int_{-H_2}^{-H_1} \ldots \sin\left(\dfrac{\lambda_l(2y + H_1 + H_2)}{H_2 - H_1}\right) dy$ to (4.3.5) gives

$$\sum_{n=1}^{\infty} a_n t_1(n) \int_{-H_2}^{-H_1} \sin\left(\frac{\lambda_l(2y + H_1 + H_2)}{H_2 - H_1}\right)\cos\left(\frac{\gamma_n(2y + H_1 + H_2)}{H_2 - H_1}\right) dy$$

$$+ \sum_{n=1}^{\infty} b_n t_2(n) \int_{-H_2}^{-H_1} \sin\left(\frac{\lambda_l(2y + H_1 + H_2)}{H_2 - H_1}\right)\sin\left(\frac{\lambda_n(2y + H_1 + H_2)}{H_2 - H_1}\right) dy$$

$$+ A \int_{-H_2}^{-H_1} \sin\left(\frac{\lambda_l(2y + H_1 + H_2)}{H_2 - H_1}\right) dy$$

$$- \sum_{n=1}^{\infty} c_n \frac{\sinh\left(\dfrac{\lambda_n(B_1 - B_2)}{H_3}\right)}{\cosh\left(\dfrac{\lambda_n B_2}{H_3}\right)} \int_{-H_2}^{-H_1} \sin\left(\frac{\lambda_l(2y + H_1 + H_2)}{H_2 - H_1}\right)\sin\left(\frac{\lambda_n y}{H_3}\right) dy = 0 \qquad (4.3.7)$$

Solving the integration in (4.3.7) gives us

$$\int_{-H_2}^{-H_1} \sin\left(\frac{\lambda_l(2y + H_1 + H_2)}{H_2 - H_1}\right)\cos\left(\frac{\gamma_n(2y + H_1 + H_2)}{H_2 - H_1}\right) dy = 0$$

$$\int_{-H_2}^{-H_1} \sin\left(\frac{\lambda_l(2y + H_1 + H_2)}{H_2 - H_1}\right)\sin\left(\frac{\lambda_n(2y + H_1 + H_2)}{H_2 - H_1}\right) dy = \begin{cases} \dfrac{H_2 - H_1}{2} & for \quad l = n \\[2ex] 0 & for \quad l \neq n \end{cases}$$

$$\int_{-H_2}^{-H_1} \sin\left(\frac{\lambda_l(2y + H_1 + H_2)}{H_2 - H_1}\right) dy = 0$$

$$\int_{-H_2}^{-H_1} \sin\left[\frac{\lambda_i\left(2y + H_1 + H_2\right)}{H_2 - H_1}\right]\sin\left(\frac{\lambda_k y}{H_3}\right)dy$$

$$= \frac{H_3\left(H_1 - H_2\right)}{2\left(H_1\lambda_k - H_2\lambda_k - 2H_3\lambda_l\right)}\left\{\sin\left(\frac{H_1\lambda_k - H_3\lambda_l}{H_3}\right) - \sin\left(\frac{H_2\lambda_k + H_3\lambda_l}{H_3}\right)\right\}$$

$$+ \frac{H_3\left(H_2 - H_1\right)}{2\left(H_1\lambda_k - H_2\lambda_k + 2H_3\lambda_l\right)}\left\{\sin\left(\frac{H_1\lambda_k + H_3\lambda_l}{H_3}\right) - \sin\left(\frac{H_2\lambda_k + H_3\lambda_l}{H_3}\right)\right\}$$

$$= f(l, k)$$

Applying $\int_{-H_2}^{-H_1} \dots \cos\left(\frac{\gamma_l\left(2y + H_1 + H_2\right)}{H_2 - H_1}\right)dy$ to (4.3.5) gives

$$\sum_{n=1}^{\infty} a_n t_1(n) \int_{-H_2}^{-H_1} \cos\left(\frac{\gamma_l\left(2y + H_1 + H_2\right)}{H_2 - H_1}\right)\cos\left(\frac{\gamma_n\left(2y + H_1 + H_2\right)}{H_2 - H_1}\right)dy$$

$$+ \sum_{n=1}^{\infty} b_n t_2(n) \int_{-H_2}^{-H_1} \cos\left(\frac{\gamma_l\left(2y + H_1 + H_2\right)}{H_2 - H_1}\right)\sin\left(\frac{\lambda_n\left(2y + H_1 + H_2\right)}{H_2 - H_1}\right)dy$$

$$+ A \int_{-H_2}^{-H_1} \cos\left(\frac{\gamma_l\left(2y + H_1 + H_2\right)}{H_2 - H_1}\right)dy$$

$$- \sum_{n=1}^{\infty} c_n \frac{\sinh\left(\frac{\lambda_n\left(B_1 - B_2\right)}{H_3}\right)}{\cosh\left(\frac{\lambda_n B_2}{H_3}\right)} \int_{-H_2}^{-H_1} \cos\left(\frac{\gamma_l\left(2y + H_1 + H_2\right)}{H_2 - H_1}\right)\sin\left(\frac{\lambda_n y}{H_3}\right)dy = 0 \qquad (4.3.8)$$

The integrations in (4.3.8) are

$$\int_{-H_2}^{-H_1} \cos\left(\frac{\gamma_l\left(2y + H_1 + H_2\right)}{H_2 - H_1}\right)\sin\left(\frac{\lambda_n\left(2y + H_1 + H_2\right)}{H_2 - H_1}\right)dy = 0$$

$$\int_{-H_2}^{-H_1} \cos\left(\frac{\gamma_l(2y+H_1+H_2)}{H_2-H_1}\right)\cos\left(\frac{\gamma_n(2y+H_1+H_2)}{H_2-H_1}\right)dy = \begin{cases} \dfrac{H_2-H_1}{2} & \text{for} \quad l=n \\[2mm] 0 & \text{for} \quad l \neq n \end{cases}$$

$$\int_{-H_2}^{-H_1} \cos\left(\frac{\gamma_l(2y+H_1+H_2)}{H_2-H_1}\right)dy = 0$$

$$\int_{-H_2}^{-H_1} \cos\left[\frac{\gamma_i(2y+H_1+H_2)}{H_2-H_1}\right]\sin\left(\frac{\lambda_k y}{H_3}\right)dy$$

$$= \frac{H_3(H_1-H_2)\cos\left(\dfrac{\gamma_l H_3 - H_1\lambda_k}{H_3}\right)}{2(2H_3\gamma_l - \lambda_k(H_1-H_2))} + \frac{H_3(H_2-H_1)\cos\left(\dfrac{\gamma_l H_3 - H_1\lambda_k}{H_3}\right)}{2(2H_3\gamma_l + \lambda_k(H_1-H_2))}$$

$$+ \frac{H_3(H_1-H_2)\cos\left(\dfrac{\gamma_l H_3 - H_2\lambda_k}{H_3}\right)}{2(2H_3\gamma_l + \lambda_k(H_1-H_2))} + \frac{H_3(H_2-H_1)\cos\left(\dfrac{\gamma_l H_3 + H_2\lambda_k}{H_3}\right)}{2(2H_3\gamma_l - \lambda_k(H_1-H_2))}$$

$$= g(l,k)$$

For the last equations we use (4.3.3) and apply the basis function $\sin\left(\dfrac{\lambda_l y}{H_3}\right)$ and integrating from $y = -H_3$ to 0 gives:

$$\sum_{n=1}^{\infty} \frac{c_n\lambda_n}{H_3}\frac{\cosh\left(\dfrac{\lambda_n(B_1-B_2)}{H_3}\right)}{\cosh\left(\dfrac{\lambda_n B_2}{H_3}\right)}\int_{-H_3}^{0}\sin\left(\frac{\lambda_l y}{H_3}\right)\sin\left(\frac{\lambda_n y}{H_3}\right)dy = -\int_{-\mu H_3}^{0}\sin\left(\frac{\lambda_l y}{H_3}\right)dy +$$

$$\sum_{n=1}^{\infty}\frac{4\alpha_n\gamma_n}{H_2-H_1}\sinh\left(\frac{\gamma_n y}{H_3}\right)\int_{-H_2}^{-H_1}\sin\left(\frac{\lambda_l y}{H_3}\right)\cos\left(\frac{\gamma_n(2y+H_1+H_2)}{H_2-H_1}\right)dy$$

$$+\sum_{n=1}^{\infty}\frac{4\beta_n\lambda_n}{H_2-H_1}\sinh\left(\frac{\lambda_n y}{H_3}\right)\int_{-H_2}^{-H_1}\sin\left(\frac{\lambda_l y}{H_3}\right)\sin\left(\frac{\lambda_n(2y+H_1+H_2)}{H_2-H_1}\right)dy$$

(4.3.9)

Solving the integration in (4.3.9) gives us

$$\int_{-H_3}^{0} \sin\left(\frac{\lambda_l y}{H_3}\right) \sin\left(\frac{\lambda_n y}{H_3}\right) dy = \begin{cases} \dfrac{H_3}{2} & for \quad l = n \\[2em] 0 & for \quad l \neq n \end{cases}$$

$$\int_{-\mu H_3}^{0} \sin\left(\frac{\lambda_l y}{H_3}\right) dy = \frac{H_3}{\lambda_l}\left(1 - \cos(\lambda_l \mu)\right)$$

$$\int_{-H_2}^{-H_1} \sin\left(\frac{\lambda_l y}{H_3}\right) \cos\left(\frac{\gamma_n\left(2y + H_1 + H_2\right)}{H_2 - H_1}\right) dy = g(l,n)$$

$$\int_{-H_2}^{-H_1} \sin\left(\frac{\lambda_l y}{H_3}\right) \sin\left(\frac{\lambda_n\left(2y + H_1 + H_2\right)}{H_2 - H_1}\right) dy = f(l,n)$$

Now we have $3N$ equations involving three unknown (a_i, b_i, c_i), $i = 1, 2, \ldots, N$ which gives us a square system of the equations. The impact region provides the right hand side of the matrix system. The system of equations is given in figure (4.3.2).

$$
\left(
\begin{array}{ccccc}
\begin{array}{c}(\textit{zero})\\[4pt] 0 \\[6pt] \vdots \\ \cdots \end{array}
&
\vdots
&
\begin{array}{c}(\textit{diagonal})\\[4pt] \dfrac{H_2-H_1}{2}\,t_2(i) \\[6pt] \vdots \\ \cdots \end{array}
&
\vdots
&
\begin{array}{c}(\textit{full})\\[4pt] \dfrac{-f(i,j)\sinh\!\left(\dfrac{\lambda_j(B_1-B_2)}{H_3}\right)}{\cosh\!\left(\dfrac{\lambda_j B_2}{H_3}\right)} \\[10pt] \vdots \\ \cdots \end{array}
\\[40pt]
\begin{array}{c}(\textit{diagonal})\\[4pt] \left(\dfrac{H_2-H_1}{2}\right)t_1(i) \\[6pt] \vdots \\ \cdots \end{array}
&
\vdots
&
\begin{array}{c}(\textit{zero})\\[4pt] 0 \\[6pt] \vdots \\ \cdots \end{array}
&
\vdots
&
\begin{array}{c}(\textit{full})\\[4pt] \dfrac{-g(i,j)\sinh\!\left(\dfrac{\lambda_j(B_1-B_2)}{H_3}\right)}{\cosh\!\left(\dfrac{\lambda_j B_2}{H_3}\right)} \\[10pt] \vdots \\ \cdots \end{array}
\\[40pt]
\begin{array}{c}(\textit{full})\\[4pt] \dfrac{4\gamma_j}{H_2-H_1}\sinh\!\left(\dfrac{\gamma_j B_1}{H_2-H_1}\right)h(i,j) \\[6pt] \vdots \end{array}
&
\vdots
&
\begin{array}{c}(\textit{full})\\[4pt] \dfrac{4\lambda_j}{H_2-H_1}\sinh\!\left(\dfrac{\lambda_j B_1}{H_2-H_1}\right)I(i,j) \\[6pt] \vdots \end{array}
&
\ddots
&
\begin{array}{c}(\textit{diagonal})\\[4pt] \dfrac{-\lambda_i}{2}\,\dfrac{\cosh\!\left(\dfrac{\lambda_j(B_1-B_2)}{H_3}\right)}{\cosh\!\left(\dfrac{\lambda_j B_2}{H_3}\right)} \\[10pt] \ddots \end{array}
\end{array}
\right)
\begin{pmatrix}
\alpha_1 \\ \vdots \\ \alpha_N \\ \cdots \\ \beta_1 \\ \vdots \\ \beta_N \\ \cdots \\ c_1 \\ \vdots \\ c_N
\end{pmatrix}
=
\begin{pmatrix}
0 \\[4pt] \cdots \\[4pt] 0 \\[4pt] \cdots \\[4pt] \left(\dfrac{\cos(\lambda_1\mu)-1}{\lambda_1}\right) \\[4pt] \vdots \\[4pt] \left(\dfrac{\cos(\lambda_N\mu)-1}{\lambda_N}\right)
\end{pmatrix}
$$

Figure 4.3.2: Matrix system of equations. The first M rows come from (4.3.7), the next from (4.3.8) and the last from (3.3.9).

4.4   Pressure Impulse

μ	**Missing block** $(h_1 = 0.4, h_2 = 0.5, B_1 = 0.2, B_2 = 2)$	**Cooker model**
0.2		
0.3		
0.4		

Figure 4.4.1: Comparison of pressure impulse results for the missing block with
Cooker's model

From the figure 4.4.1 above, we can see that there is not much difference between maximum pressure impulse on the wall for missing block problem and the Cooker model. The Cooker model gives slightly higher pressure compared to missing block problem.

μ	Missing block: width=0.1 $(H_1 = 0.4, H_2 = 0.5, B_1 = 0.1, B_2 = 2)$	Missing block: width=0.2 $(H_1 = 0.4, H_2 = 0.5, B_1 = 0.2, B_2 = 2)$	Missing block: width=0.3 $(H_1 = 0.4, H_2 = 0.5, B_1 = 0.3, B_2 = 2)$
0.2			
0.4			
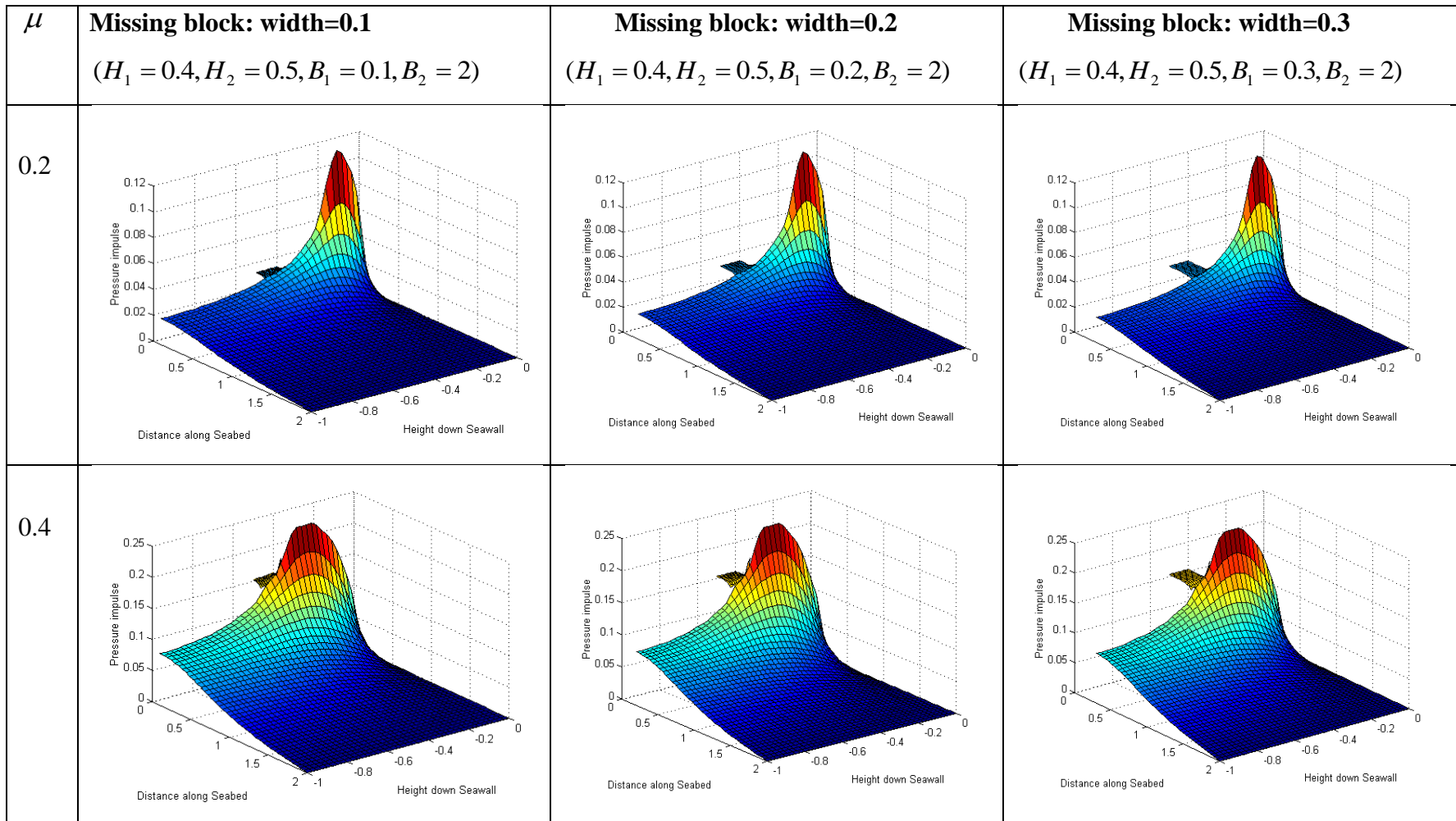
Figure 4.4.2: Missing block with different widths.

μ	**Missing block: depth=0.1** $(H_1 = 0.4, H_2 = 0.5, B_1 = 0.2, B_2 = 2)$	**Missing block: depth=0.2** $(H_1 = 0.4, H_2 = 0.6, B_1 = 0.2, B_2 = 2)$	**Missing block: depth=0.3** $(H_1 = 0.4, H_2 = 0.7, B_1 = 0.2, B_2 = 2)$
0.2			
0.4			
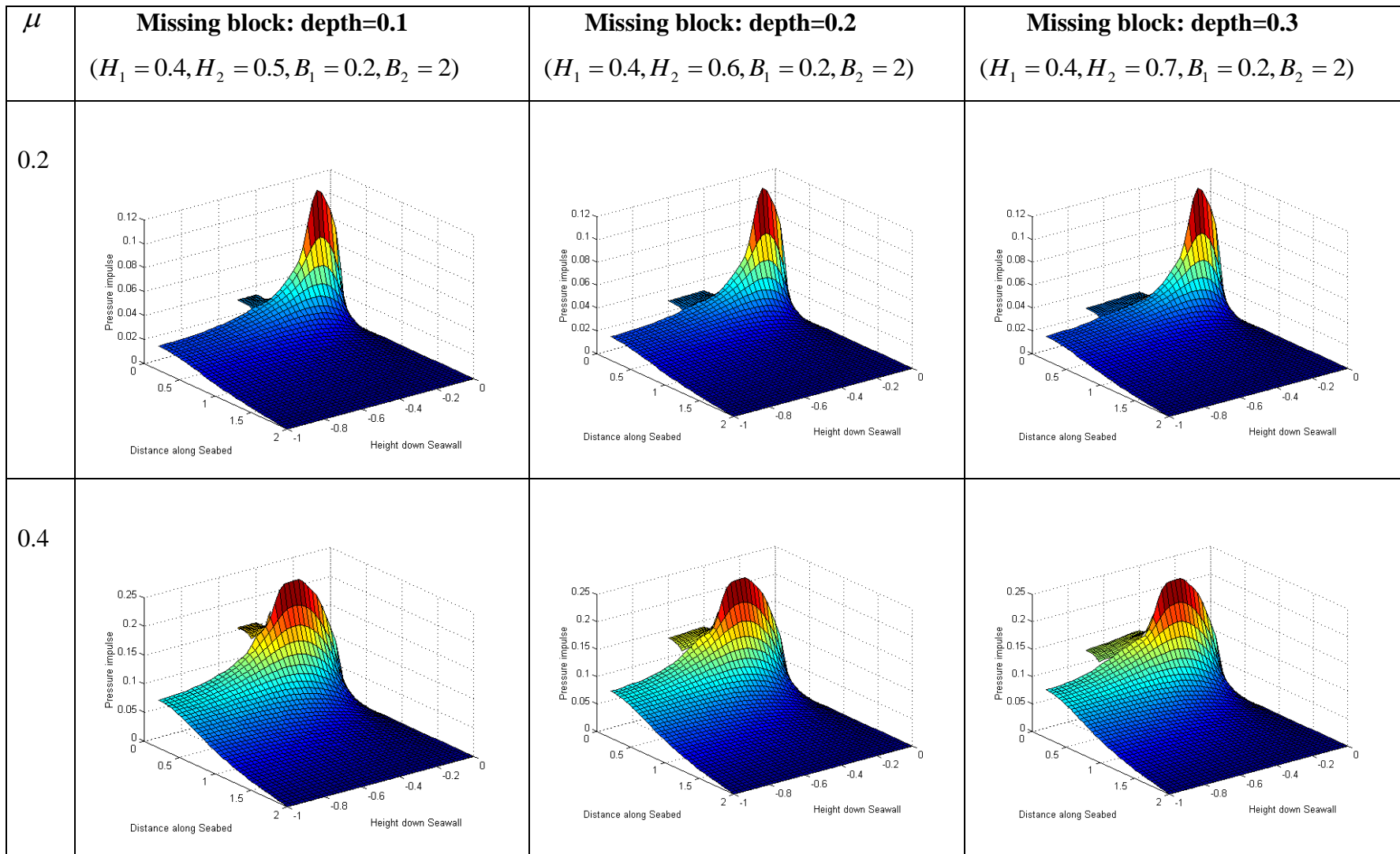
Figure 4.4.3: Missing block with different depths.

Figure 4.4.2 shows comparison results for different widths ($B_1 = 0.1, 0.2, 0.3$) of block with same depth ($H_2 - H_1 = 0.1$) of the missing block for varying μ. We can see that the pressure impulse decreases when the width of missing block increases. The pressure in the missing block region looks almost constant. As μ increases, the pressure impulse in this region also increases.

Figure 4.4.3 shows a comparison of results for different depths ($H_2 - H_1 = 0.1, 0.2, 0.3$) of block with the same width ($B_1 = 0.2$) for varying μ. We can see that the pressure impulse for different depths gives no significant difference, except for the pressure impulse in the missing block region, which shows slight decrease when the depth is increased. We can conclude that the thinner the missing block, the greater the pressure impulse on the walls of the missing block region. For the pressure impulse on the wall in the outer region, we get an increase when μ increases.

We can see that in both figures, the region 1 and 2 there is some matching discrepancies, but they are small enough to be ignored. In the next section, we investigate the total impulse and moment impulse in the inner and the outer regions.

4.5   Total Impulse on the wall and seabed

We continue the work by calculating the pressure impulse generated by the impact on the wall and the seabed for the missing block problem. This is accomplished by integrating the pressure impulse over the domain being considered.
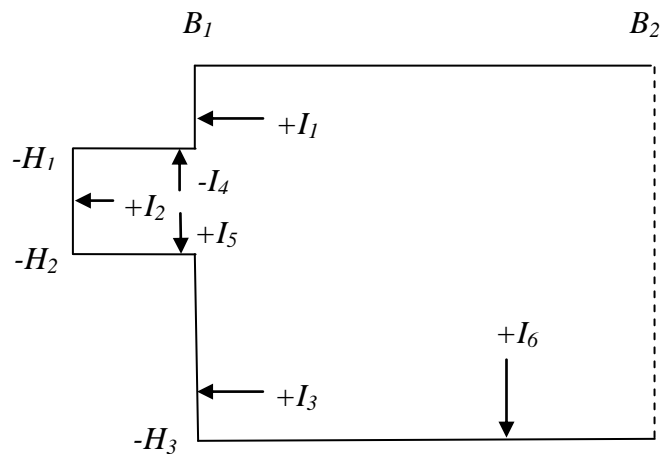
Figure 4.5.1: Total impulse definitions for the missing block problem.

For the total impulse on the impact region I_1, we need:

$$I_1 = \int_{-H_1}^{0} P_2(B_1, y) dy \tag{4.5.1}$$

Evaluating this equation gives

$$I_1 = \sum_{n=1}^{\infty} c_n \frac{\sinh\left(\dfrac{\lambda_n(B_1 - B_2)}{H_3}\right)}{\cosh\left(\dfrac{\lambda_n B_2}{H_3}\right)} \int_{-H_1}^{0} \sin\left(\frac{\lambda_n y}{H_3}\right) dy$$

$$= \sum_{n=1}^{\infty} -\frac{c_n H_3}{\lambda_n} \frac{\sinh\left(\dfrac{\lambda_n(B_1 - B_2)}{H_3}\right)}{\cosh\left(\dfrac{\lambda_n B_2}{H_3}\right)} \left(\cos\left(-\frac{\lambda_n H_1}{H_3}\right) - 1\right) \tag{4.5.2}$$

The total impulse on the wall at the inner region is given by

$$I_2 = \int_{-H_2}^{-H_1} P_1(0, y) dy \tag{4.5.3}$$

$$= \sum_{n=1}^{\infty} \frac{a_n}{\cosh\left(\dfrac{\gamma_n B_1}{H_2 - H_1}\right)} \int_{-H_2}^{-H_1} \cos\left(\frac{\gamma_n(2y + H_1 + H_2)}{H_2 - H_1}\right) dy$$

$$+ \sum_{n=1}^{\infty} \frac{b_n}{\cosh\left(\dfrac{\gamma_n B_1}{H_2 - H_1}\right)} \int_{-H_2}^{-H_1} \sin\left(\frac{\lambda_n(2y + H_1 + H_2)}{H_2 - H_1}\right) dy + \int_{-H_2}^{-H_1} A \, dy$$

$$= A(H_2 - H_1) \tag{4.5.4}$$

We also need to calculate the total impulse on the bottom of the wall of the outer region

$$I_3 = \int_{-H_3}^{-H_2} P_2(B_1, y) dy \tag{4.5.5}$$

$$= \sum_{n=1}^{\infty} -\frac{c_n H_3}{\lambda_n} \frac{\sinh\left(\dfrac{\lambda_n(B_1 - B_2)}{H_3}\right)}{\cosh\left(\dfrac{\lambda_n B_2}{H_3}\right)} \cos\left(-\frac{\lambda_n H_2}{H_3}\right) \tag{4.5.6}$$

For the total impulse on the top of the block region we have,

$$I_4 = -\int_0^{B_1} P_1(x,-H_1)dx \tag{4.5.7}$$

$$= -\sum_{n=1}^{\infty} \frac{a_n \cos(\gamma_n)}{\cosh\left(\dfrac{\gamma_n B_1}{H_2 - H_1}\right)} \int_0^{B_1} \cosh\left(\frac{2\gamma_n x}{H_2 - H_1}\right) dx$$

$$-\sum_{n=1}^{\infty} \frac{b_n \sin(\lambda_n)}{\cosh\left(\dfrac{\lambda_n B_1}{H_2 - H_1}\right)} \int_0^{B_1} \cosh\left(\frac{2\lambda_n x}{H_2 - H_1}\right) dx - \int_0^{B_1} A dx$$

$$= -\sum_{n=1}^{\infty} a_n \frac{H_2 - H_1}{2\gamma_n} \frac{\cos(\gamma_n)}{\cosh\left(\dfrac{\gamma_n B_1}{H_2 - H_1}\right)} \sinh\left(\frac{2\gamma_n B_1}{H_2 - H_1}\right)$$

$$-\sum_{n=1}^{\infty} b_n \frac{H_2 - H_1}{2\lambda_n} \frac{\sin(\lambda_n)}{\cosh\left(\dfrac{\lambda_n B_1}{H_2 - H_1}\right)} \sinh\left(\frac{2\lambda_n B_1}{H_2 - H_1}\right) - AB_1 \tag{4.5.8}$$

and the total impulse on the bottom of the block region given by

$$I_5 = \int_0^{B_1} P_1(x,-H_2)dx \tag{4.5.9}$$

$$= \sum_{n=1}^{\infty} \frac{a_n \cos(-\gamma_n)}{\cosh\left(\dfrac{\gamma_n B_1}{H_2 - H_1}\right)} \int_0^{B_1} \cosh\left(\frac{2\gamma_n x}{H_2 - H_1}\right) dx$$

$$+\sum_{n=1}^{\infty} \frac{b_n \sin(-\lambda_n)}{\cosh\left(\dfrac{\lambda_n B_1}{H_2 - H_1}\right)} \int_0^{B} \cosh\left(\frac{2\lambda_n x}{H_2 - H_1}\right) dx + \int_0^{B_1} A dx$$

$$= \sum_{n=1}^{\infty} a_n \frac{H_2 - H_1}{2\gamma_n} \frac{\cos(\gamma_n)}{\cosh\left(\dfrac{\gamma_n B_1}{H_2 - H_1}\right)} \sinh\left(\frac{2\gamma_n B_1}{H_2 - H_1}\right)$$

$$-\sum_{n=1}^{\infty} b_n \frac{H_2 - H_1}{2\lambda_n} \frac{\sin(\lambda_n)}{\cosh\left(\dfrac{\lambda_n B_1}{H_2 - H_1}\right)} \sinh\left(\frac{2\lambda_n B_1}{H_2 - H_1}\right) + AB_1 \tag{4.5.10}$$

The total impulse on the seabed for missing block given by

$$I_6 = \int_{B_1}^{B_2} P_2(x, -H_3) dx \tag{4.5.11}$$

$$= \sum_{n=1}^{\infty} c_n \frac{\sin(-\lambda_n)}{\cosh\left(\dfrac{\lambda_n B_2}{H_3}\right)} \int_{B_1}^{B_2} \sinh\left(\frac{\lambda_n(x - B_2)}{H_3}\right) dx$$

$$= \sum_{n=1}^{\infty} c_n \frac{H_3}{\lambda_n} \frac{\sin(-\lambda_n)}{\cosh\left(\dfrac{\lambda_n B_2}{H_3}\right)} \left[1 - \cosh\left(\frac{\lambda_n(B_1 - B_2)}{H_3}\right)\right] \tag{4.5.12}$$

The results for the total impulse on seawall, the total impulse on the inner region (top and bottom of the block) and on the seabed can be seen in figure 4.5.2 to 4.5.5. Figure 4.5.2, figure 4.5.3 and figure 4.5.4 show the total impulse on the wall and on the top and bottom of the missing block, with different location of the missing block but the same width and depth. We can see that when the location of the missing block is closer to the seabed, the total impulse for each face increases. For instances, for total impulse on the wall, the first location which near to the free surface $(H_1 = 0.2, H_2 = 0.3)$ has a total impulse of $0.0425 \, \rho U H^2$, the second location $(H_1 = 0.5, H_2 = 0.6)$ has a total impulse of $0.190 \, \rho U H^2$ and for the location near to the seabed $(H_1 = 0.8, H_2 = 0.9)$ has a total impulse of $0.380 \, \rho U H^2$.

We also can see there is a total impulse on the vertical wall at the inner region but it is small compared to vertical wall at the outer region. However, it can be larger than total impulse at the bottom of the vertical wall of the outer region when the location of the missing block is near to the seabed. The total impulse on the top and bottom of the inner region largely cancel each other. Given the almost constancy of the pressure in the missing block region, this is expected. These impulses do not move the wall vertically but may tend to open cracks in the missing block region.

Figure 4.5.5 shows the impulse on the seabed for each location stated above. We can see that the total impulse increases when the location of the missing block moves down to the seabed. The total impulse on the wall is larger than the impulse on the seabed in all cases.
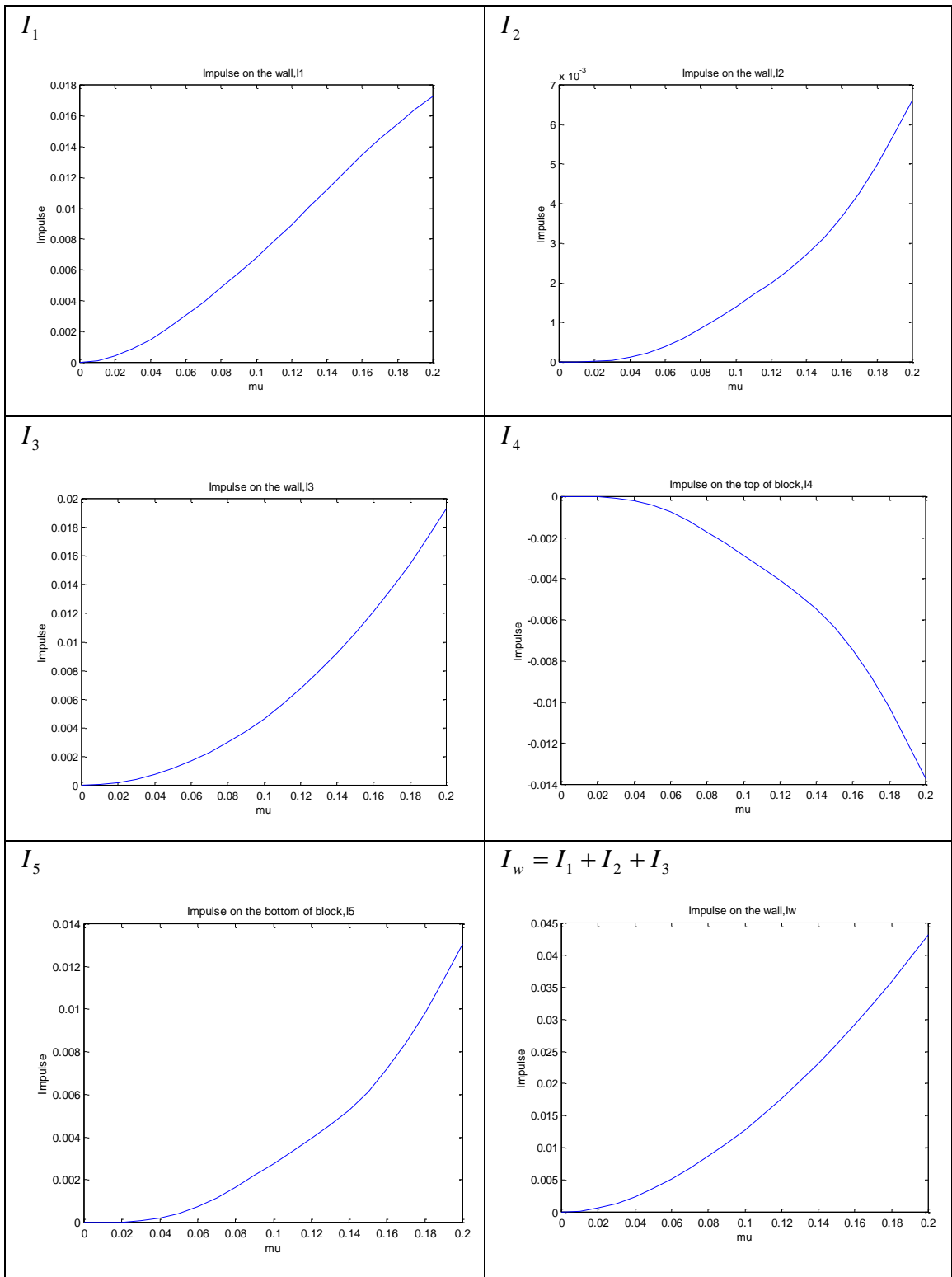
Figure 4.5.2: Total impulse for missing block with

$$H_1 = 0.2, H_2 = 0.3, H_3 = 1, B_1 = 0.2, B_2 = 2.$$
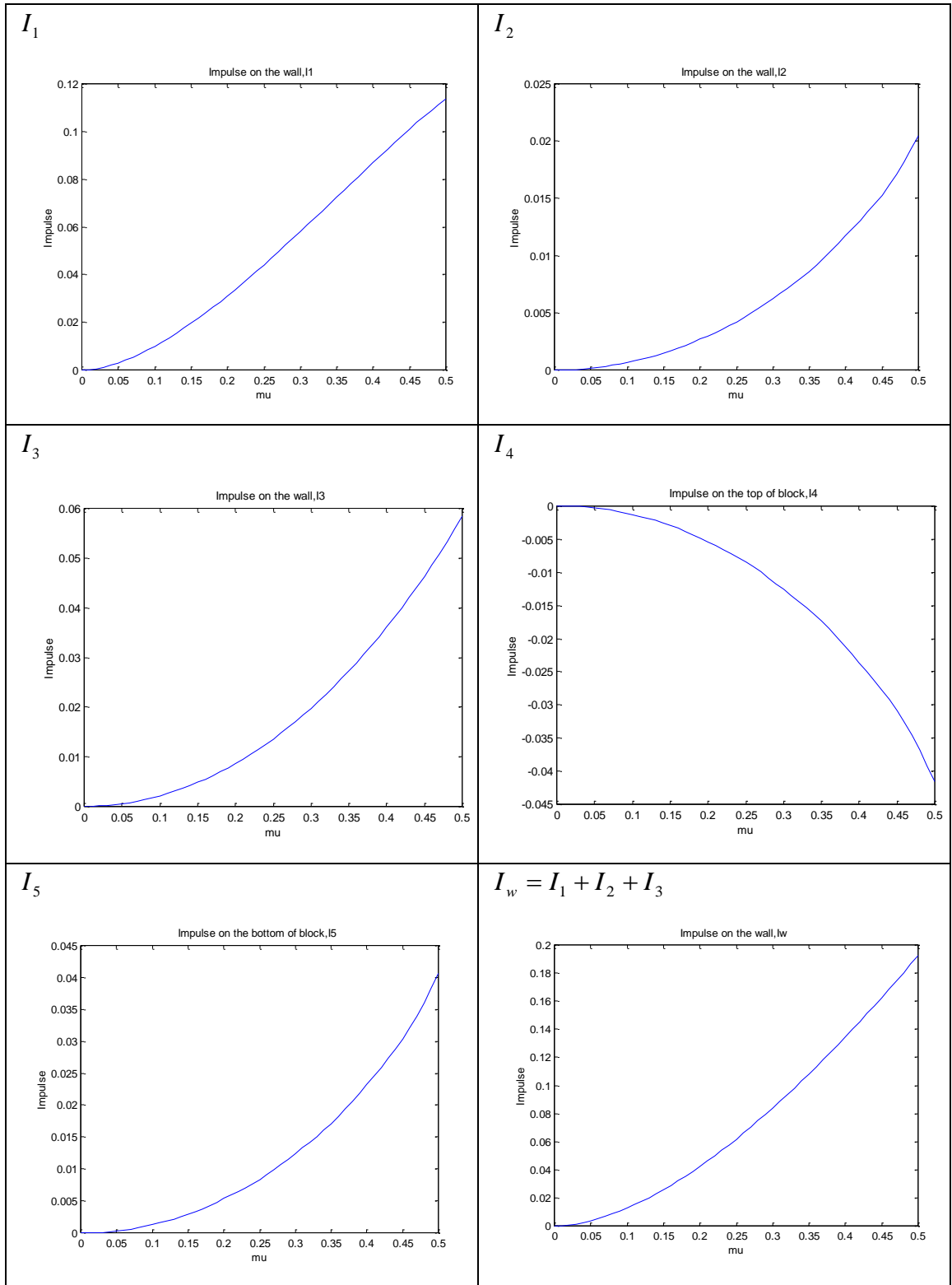
Figure 4.5.3: Total impulse for missing block with

$$H_1 = 0.5, H_2 = 0.6, H_3 = 1, B_1 = 0.2, B_2 = 2.$$
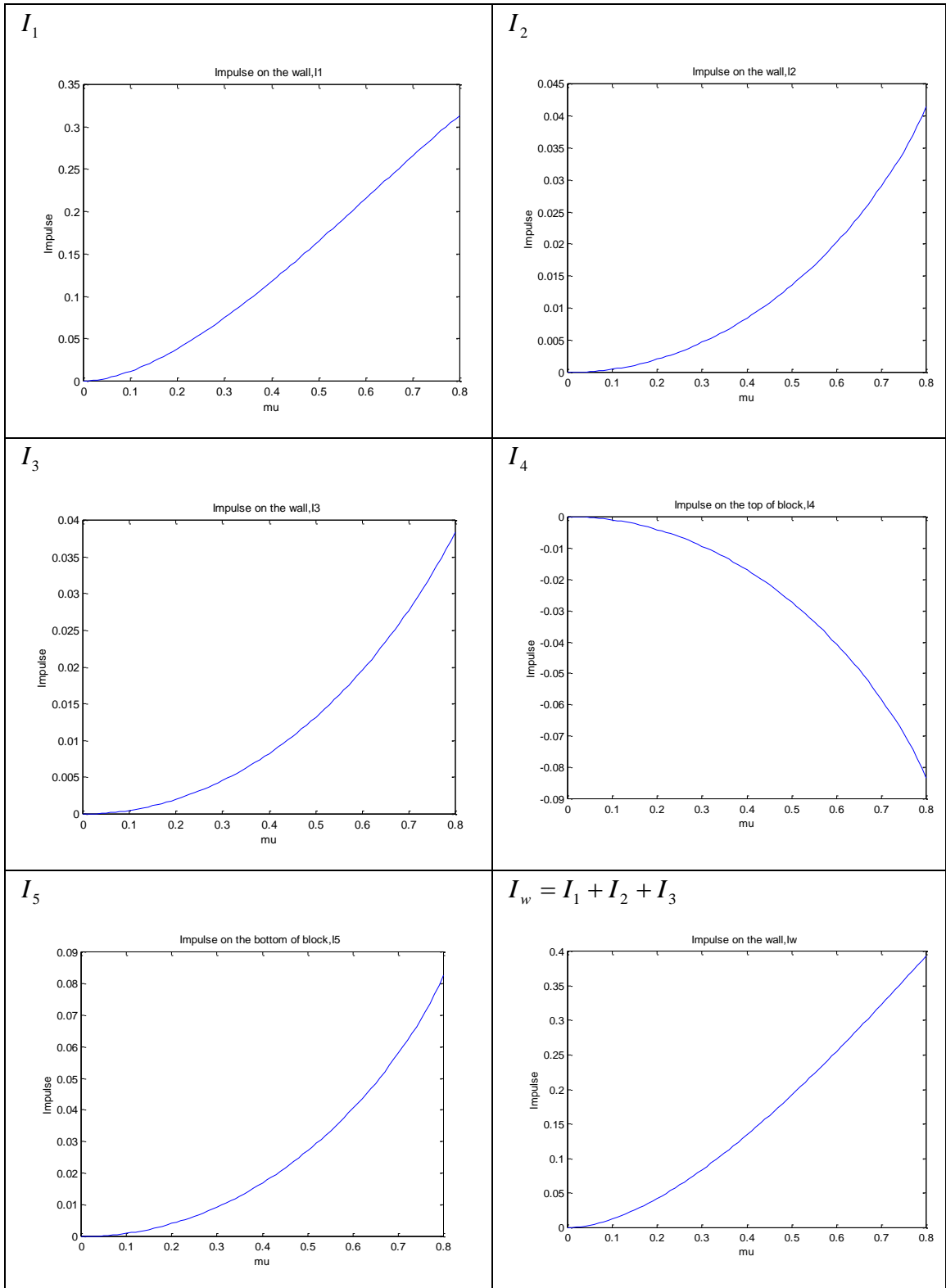
Figure 4.5.4: Total impulse for missing block with

$$H_1 = 0.8, H_2 = 0.9, H_3 = 1, B_1 = 0.2, B_2 = 2.$$

$H_1 = 0.2, H_2 = 0.3, H_3 = 1, B_1 = 0.2, B_2 = 2$	$H_1 = 0.5, H_2 = 0.6, H_3 = 1, B_1 = 0.2, B_2 = 2$	$H_1 = 0.8, H_2 = 0.9, H_3 = 1, B_1 = 0.2, B_2 = 2$
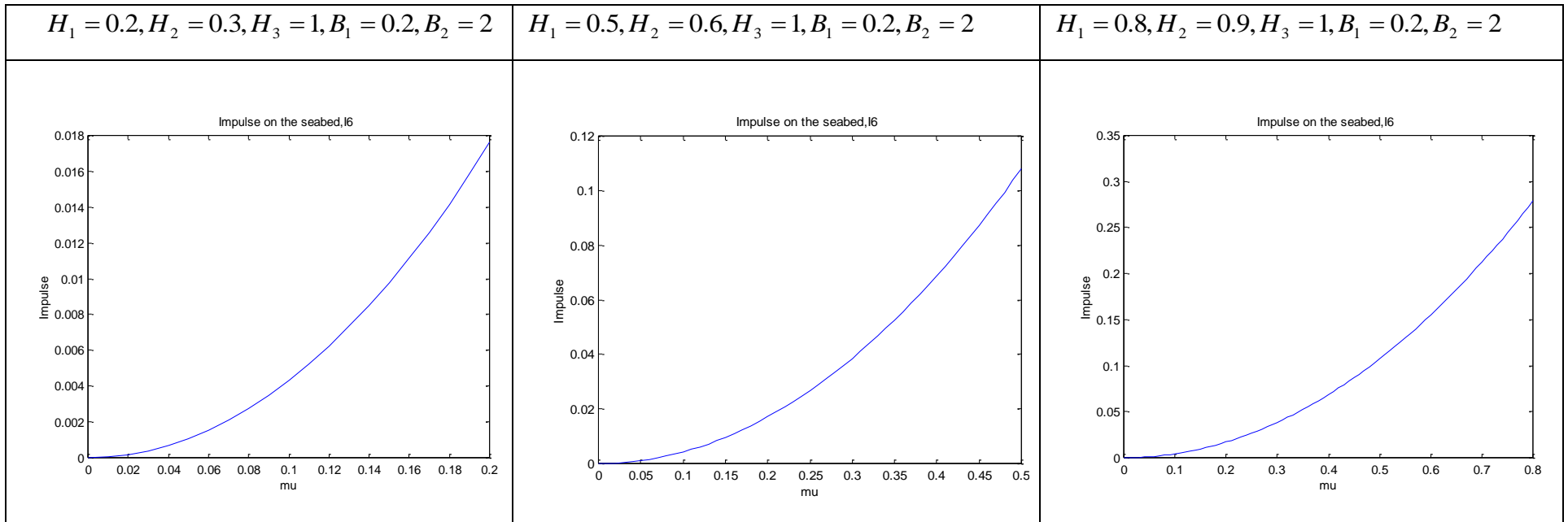
Figure 4.5.5: Total impulse on seabed for missing block .

4.6 Moment impulse on the wall and seabed

In this section we need to calculate the moment on the wall and seabed that will affect the seawall. For the following work clockwise moment will be considered to be positive and will be taken about the foot (●) of the wall.
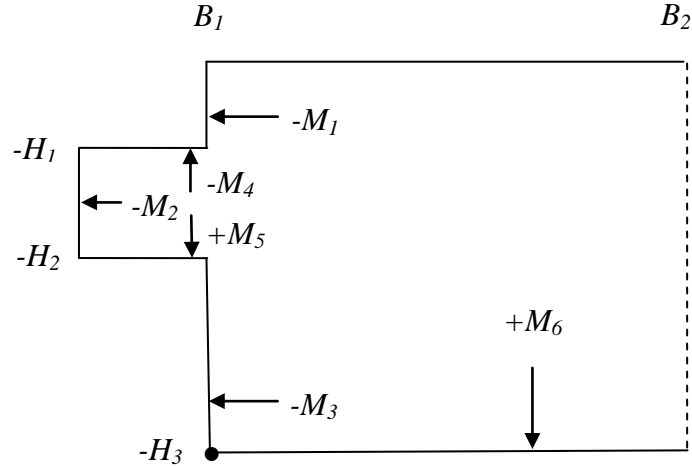
Figure 4.6.1: Moment impulse definitions for the missing block problem.

The moment impulse on the wall given by:

$$M_1 = -\int_{-H_1}^{0}(1+y)P_2(B_1,y)dy \qquad (4.6.1)$$

Solving this equation, the moment impulse on the impact region is given by

$$M_1 = -\int_{-H_1}^{0}(1+y)\sum_{n=1}^{\infty}c_n \sin\left(\frac{\lambda_n y}{H_3}\right)\frac{\sinh\left(\frac{\lambda_n(B_1-B_2)}{H_3}\right)}{\cosh\left(\frac{\lambda_n B_2}{H_3}\right)}dy$$

$$= -\sum_{n=1}^{\infty}c_n \frac{\sinh\left(\frac{\lambda_n(B_1-B_2)}{H_3}\right)}{\cosh\left(\frac{\lambda_n B_2}{H_3}\right)}\left[\int_{-H_1}^{0}\sin\left(\frac{\lambda_n y}{H_3}\right)dy - \int_{-H_1}^{0} y\sin\left(\frac{\lambda_n y}{H_3}\right)dy\right]$$

98

$$= \sum_{n=1}^{\infty} \frac{c_n H_3}{\lambda_n} \frac{\sinh\left(\frac{\lambda_n (B_1 - B_2)}{H_3}\right)}{\cosh\left(\frac{\lambda_n B_2}{H_3}\right)} \left[-\cos\left(\frac{-\lambda_n H_1}{H_3}\right) + 1 + H_1 \cos\left(\frac{-\lambda_n H_1}{H_3}\right) \right.$$

$$\left. + \frac{H_3}{\lambda_n} \sin\left(\frac{-\lambda_n H_1}{H_3}\right) \right] \tag{4.6.2}$$

We need to calculate moment impulse on the wall at the inner region which is given by

$$M_2 = -\int_{-H_2}^{-H_1} (1 + y) P_1(0, y) dy \tag{4.6.3}$$

Solving this gives

$$= -\sum_{n=1}^{\infty} a_n \frac{1}{\cosh\left(\frac{\gamma_n B_1}{H_2 - H_1}\right)} \int_{-H_2}^{-H_1} (1 + y) \cos\left(\frac{\gamma_n (2y + H_1 + H_2)}{H_2 - H_1}\right) dy$$

$$- \sum_{n=1}^{\infty} b_n \frac{1}{\cosh\left(\frac{\lambda_n B_1}{H_2 - H_1}\right)} \int_{-H_2}^{-H_1} (1 + y) \sin\left(\frac{\lambda_n (2y + H_1 + H_2)}{H_2 - H_1}\right) dy - A \int_{-H_2}^{-H_1} (1 + y) dy$$

$$= \sum_{n=1}^{\infty} a_n \frac{1}{\cosh\left(\frac{\gamma_n B_1}{H_2 - H_1}\right)} \left[-\frac{(H_2 - H_1)^2}{4\gamma_n^2} \cos(\gamma_n) + \frac{(H_2 - H_1)^2}{4\gamma_n^2} \cos(-\gamma_n) \right]$$

$$+ \sum_{n=1}^{\infty} b_n \frac{1}{\cosh\left(\frac{\lambda_n B_1}{H_2 - H_1}\right)} \left[-\frac{(H_2 - H_1)^2}{4\lambda_n^2} \sin(\lambda_n) + + \frac{(H_2 - H_1)^2}{4\lambda_n^2} \sin(-\lambda_n) \right]$$

$$+ A \left[+ H_1 - \frac{H_1^2}{2} - H_2 + \frac{H_2^2}{2} \right]$$

$$\tag{4.6.4}$$

For the moment impulse on the bottom of wall at outer region, we have

$$M_3 = -\int_{-H_3}^{-H_2} (1 + y) \sum_{n=1}^{\infty} c_n \sin\left(\frac{\lambda_n y}{H_3}\right) \frac{\sinh\left(\frac{\lambda_n (B_1 - B_2)}{H_3}\right)}{\cosh\left(\frac{\lambda_n B_2}{H_3}\right)} dy \tag{4.6.5}$$

$$= \sum_{n=1}^{\infty} \frac{c_n H_3}{\lambda_n} \frac{\sinh\left(\dfrac{\lambda_n(B_1 - B_2)}{H_3}\right)}{\cosh\left(\dfrac{\lambda_n B_2}{H_3}\right)} \left[\cos\left(\frac{-\lambda_n H_2}{H_3}\right) - H_2 \cos\left(\frac{-\lambda_n H_2}{H_3}\right) \right.$$

$$\left. - \frac{H_3}{\lambda_n} \sin\left(\frac{-\lambda_n H_2}{H_3}\right) + \frac{H_3}{\lambda_n} \sin(-\lambda_n) \right] \tag{4.6.6}$$

The moment impulse on the seabed given by:

$$M_6 = \int_{b_1}^{b_2} x P_2(x, -H_3) dx \tag{4.6.7}$$

$$= \sum_{n=1}^{\infty} c_n \frac{\sin(-\lambda_n)}{\cosh\left(\dfrac{\lambda_n B_2}{H_3}\right)} \left[\frac{H_3 B_2}{\lambda_n} - \frac{H_3 B_1}{\lambda_n} \cosh\left(\frac{\lambda_n(B_1 - B_2)}{H_3}\right) \right.$$

$$\left. + \frac{H_3^2}{\lambda_n^2} \sinh\left(\frac{\lambda_n(B_1 - B_2)}{H_3}\right) \right] \tag{4.6.8}$$

We need to calculate the moment impulse on the top and bottom of the missing block regions, i.e. M_4 and M_5 respectively.

$$M_4 = -\int_0^{B_1} x P_1(x, -H_1) dx \tag{4.6.9}$$

Solving this gives

$$= -\sum_{n=1}^{\infty} a_n \frac{\cos(\gamma_n)}{\cosh\left(\dfrac{\gamma_n B_1}{H_2 - H_1}\right)} \int_0^{B_1} x \cosh\left(\frac{2\gamma_n x}{H_2 - H_1}\right) dx$$

$$- \sum_{n=1}^{\infty} b_n \frac{\sin(\lambda_n)}{\cosh\left(\dfrac{\lambda_n B_1}{H_2 - H_1}\right)} \int_0^{B_1} x \cosh\left(\frac{2\lambda_n x}{H_2 - H_1}\right) dx - A \int_0^{B_1} x dx$$

$$= -\sum_{n=1}^{\infty} a_n \frac{\cos(\gamma_n)}{\cosh\left(\dfrac{\gamma_n B_1}{H_2 - H_1}\right)} \left[\frac{B_1(H_2 - H_1)}{2\gamma_n} \sinh\left(\frac{2\gamma_n B_1}{H_2 - H_1}\right) \right.$$

$$- \frac{(H_2 - H_1)^2}{4\gamma_n^2}\left(\cosh\left(\frac{2\gamma_n B_1}{H_2 - H_1}\right) - 1\right)\right] - \sum_{n=1}^{\infty} b_n \frac{\sin(\lambda_n)}{\cosh\left(\dfrac{\lambda_n B_1}{H_2 - H_1}\right)}$$

$$\left[\frac{B_1(H_2 - H_1)}{2\lambda_n}\sinh\left(\frac{2\lambda_n B_1}{H_2 - H_1}\right) - \frac{(H_2 - H_1)^2}{4\lambda_n^2}\left(\cosh\left(\frac{2\lambda_n B_1}{H_2 - H_1}\right) - 1\right)\right]$$

$$- \frac{AB_1^2}{2} \tag{4.6.10}$$

and

$$M_5 = \int_0^{B_1} x P_1(x, -H_2)\,dx \tag{4.6.11}$$

$$= \sum_{n=1}^{\infty} a_n \frac{\cos(-\gamma_n)}{\cosh\left(\dfrac{\gamma_n B_1}{H_2 - H_1}\right)}\left[\frac{B_1(H_2 - H_1)}{2\gamma_n}\sinh\left(\frac{2\gamma_n B_1}{H_2 - H_1}\right)\right.$$

$$\left. - \frac{(H_2 - H_1)^2}{4\gamma_n^2}\left(\cosh\left(\frac{2\gamma_n B_1}{H_2 - H_1}\right) - 1\right)\right] + \sum_{n=1}^{\infty} b_n \frac{\sin(-\lambda_n)}{\cosh\left(\dfrac{\lambda_n B_1}{H_2 - H_1}\right)}$$

$$\left[\frac{B_1(H_2 - H_1)}{2\lambda_n}\sinh\left(\frac{2\lambda_n B_1}{H_2 - H_1}\right) - \frac{(H_2 - H_1)^2}{4\lambda_n^2}\left(\cosh\left(\frac{2\lambda_n B_1}{H_2 - H_1}\right) - 1\right)\right]$$

$$+ \frac{AB_1^2}{2} \tag{4.6.12}$$

Figures 4.6.2 to 4.6.4 show the moment impulses for different locations of the missing block. We do not plot the graph for moment on the top and bottom of the missing block, M_4 and M_5 because they almost cancel each other. We can see that the deeper the location of the missing block, the bigger the overturning moment impulse. We also can see that the moment impulse on the seabed for each case is lower than the total moment impulse on the wall.
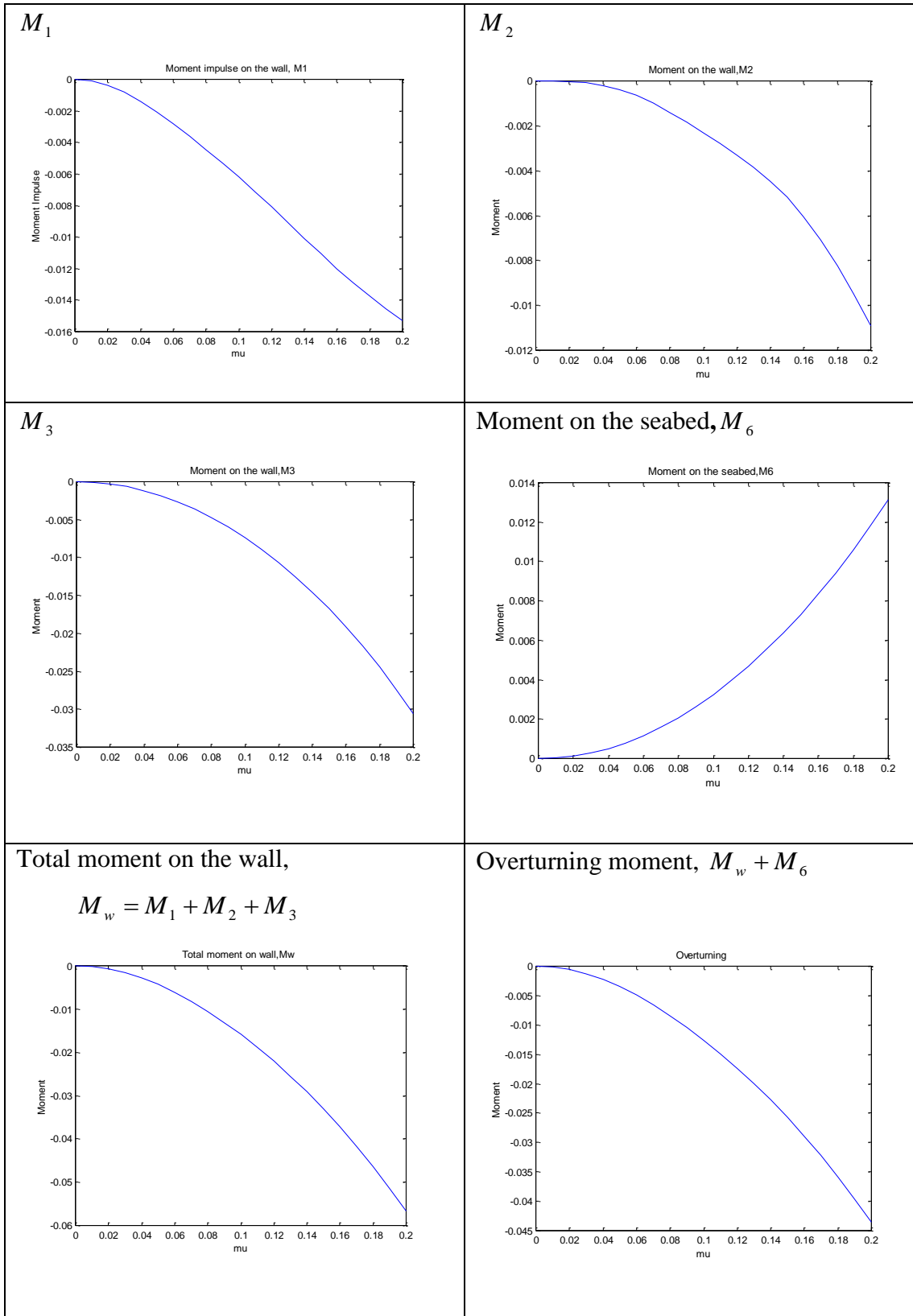
Figure 4.6.2: Moment impulse for missing block with

$$H_1 = 0.2, H_2 = 0.3, H_3 = 1, B_1 = 0.2, B_2 = 2$$
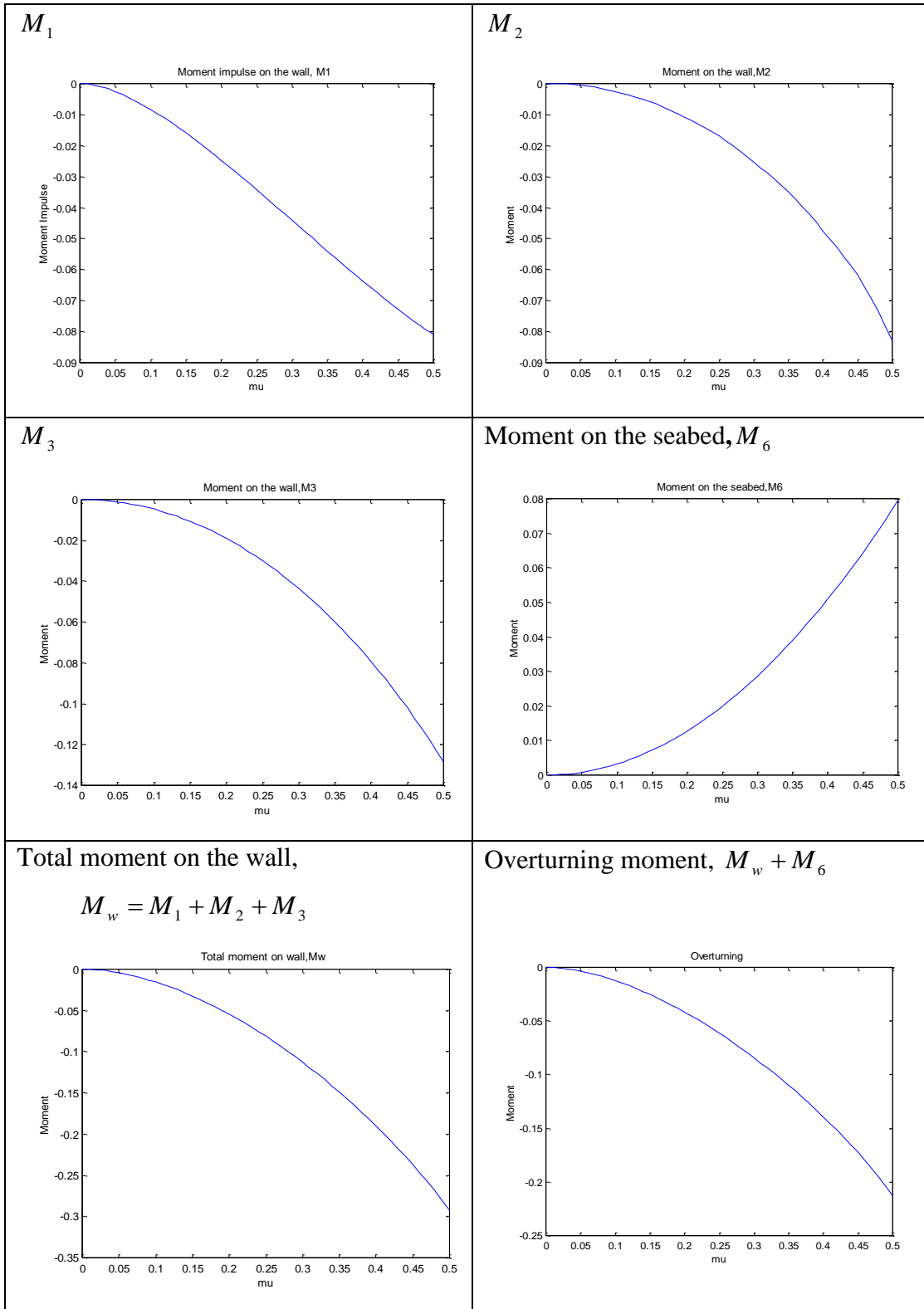
Figure 4.6.3: Moment impulse for missing block with

$$H_1 = 0.5, H_2 = 0.6, H_3 = 1, B_1 = 0.2, B_2 = 2$$

M_1

M_2

M_3

Moment on the seabed, M_6

Total moment on the wall,

$$M_w = M_1 + M_2 + M_3$$

Overturning moment, $M_w + M_6$
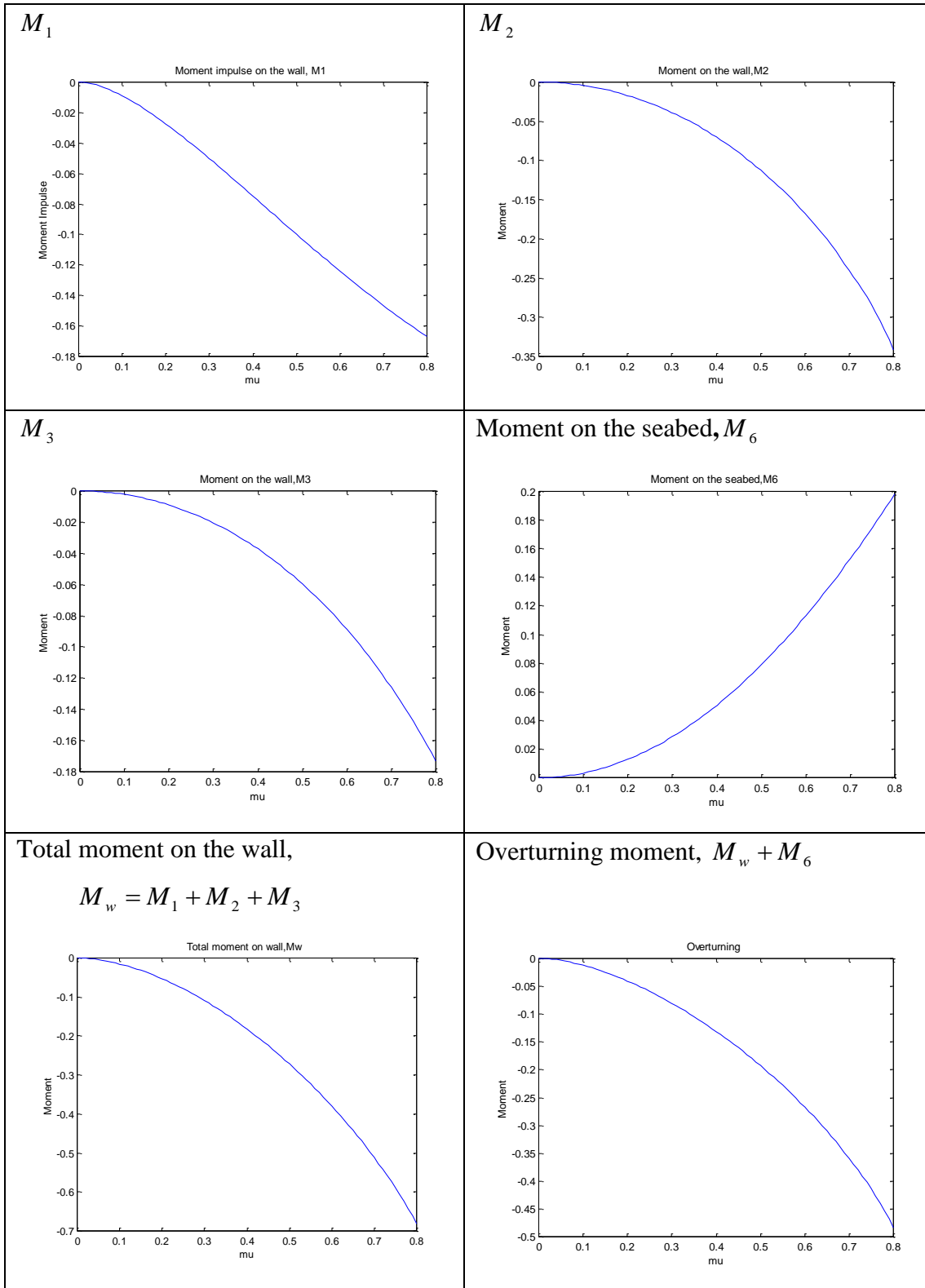
Figure 4.6.4: Moment impulse for missing block with

$$H_1 = 0.8, H_2 = 0.9, H_3 = 1, B_1 = 0.2, B_2 = 2$$

Since region 2 is largely unaffected by the missing block, the overtopping calculations will be almost the same as for the simple seawall.

4.7 Conclusion

The results of figure 4.4.1 show no noticeable decrease in pressure impulse due to the missing block. The total impulse on the wall for the missing block problem is greater when the location of the missing block is close to the seabed. However it is still smaller than the total impulse on the vertical wall. The same trend happens to the total impulse on the seabed.

The moment impulse on the wall and the seabed for the missing block problem is greater when the location of the missing block is close to the seabed. The moment impulse on the wall for the missing block is greater than the moment impulse on the vertical wall. However for the moment impulse on the seabed is smaller when a block is missing than when the wall is vertical.

CHAPTER 5

IMPACT ON A WALL WITH A DECK

5.1 Introduction

In this chapter we model a wave travelling from the right impacting against a vertical seawall with a small deck on the top located at the wave crest level. This model extends the work of Cooker and Peregrine (1990, 1995) who idealized the geometry of the wave as a rectangular region which is filled by fluid. We calculate the field of the pressure impulse, P, when a rectangular wave hits a vertical wall, and the total impulse and moment impulse beneath the deck and on the seawall. The purpose of this chapter is to derive P throughout the fluid, theoretically investigate the impulsive fluid force on the structures and also present a simplified model of overtopping. The results obtained will be compared with Cooker and Peregrine (1990, 1995).

5.2 Literature Review

Equation (2.2.1) which satisfies Laplace equation, gave Cooker and Peregrine (1990, 1995) a Fourier series solution of the pressure impulse after the mixed boundary conditions had been applied. Then they calculated the impulse (force impulse) and moment on the wall and on the seabed. Cooker (1990) showed that his theoretical work was in good agreement with the experimental works such as Bagnold (1939) and Nagai (1960). He concluded for small μ, his model gives the same trend as the empirical rules for the maximum value of the pressure on the wall p_{peak} occurring near the SWL (still water level), with the pressure decreasing towards the bed. In the following, since no freeboard is involved, no air cushion can form beneath the deck and so this situation can be regarded as worst-case, or design, scenario.

5.3　Mathematical Model

Figure 5.1 shows the fluid-structure system and the Cartesian coordinates. The horizontal flat deck lies at $y = 0$ from $x = 0$ to $x = b_1$. The free surface beyond the deck is also taken to be flat, from $x = b_1$ to $x = b_2$. We make the problem dimensionless by choosing units for which the water depth, $H = 1$. The seabed is also assumed to be horizontal. The wave strikes a fraction μ of the wall. The fluid is assumed to be incompressible and inviscid and the domain is defined by $0 \le x < \infty$, $-1 \le y \le 0$. The wavefront moves in the negative x direction.
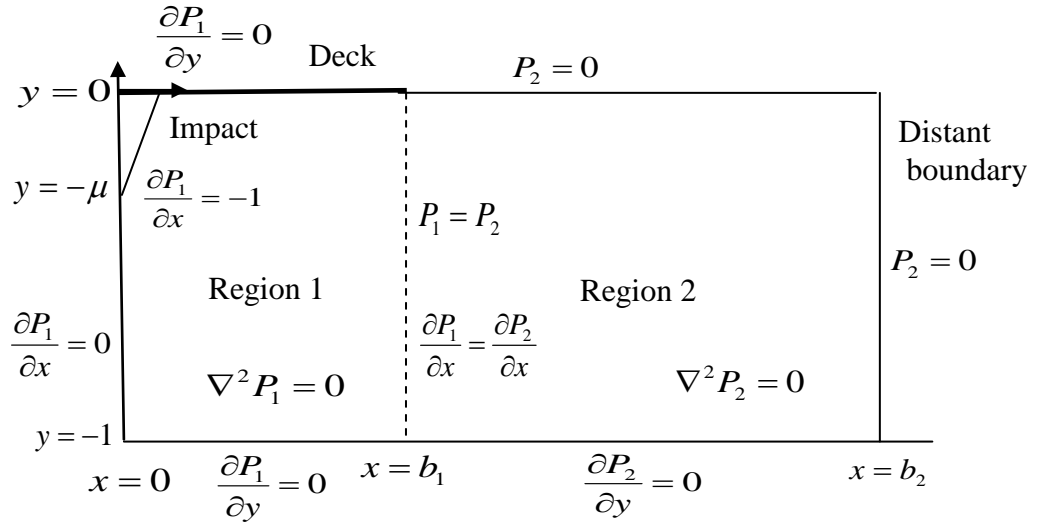
Figure 5.3.1: The dimensionless boundary-value problem for the pressure impulse for wave impact on a vertical seawall with a deck.

We take U_0 to be a uniform horizontal velocity in the impact region and work in dimensionless parameters. We continue to use P as dimensionless pressure impulse, which scales with $\rho U_0 H$. Under the assumptions stated above, the formulations involve two expressions for regions 1 and 2 and they need to be matched at $x = b_1$. The boundary conditions for this problem are then:

$$\frac{\partial P_1}{\partial y}(x,0) = 0, \qquad \text{for } x \in [0, b_1] \tag{5.3.1}$$

$$\frac{\partial P_1}{\partial y}(x,-1) = 0, \qquad \text{for } x \in [0, b_1] \tag{5.3.2}$$

$$\frac{\partial P_1}{\partial x}(0, y) = \begin{cases} -1 & \text{for } y \in [-\mu, 0) \\ 0 & \text{otherwise} \end{cases} \tag{5.3.3}$$

where $0 \le \mu \le 1$

In the above equations, we specify two dimensionless regions on the wall; the impact zone $-\mu \le y \le 0$, and the lower region on the wall, $-1 \le y < -\mu$. The boundary conditions on the impact zone gives the normal derivative of the pressure-impulse. This is chosen to be constant with the height up the wall, and models the impacting wave face. For the lower region, this is zero corresponding to the zero normal water velocity at the wall before and after the impacting wave arrives.

$$P_2(x,0) = 0, \qquad \text{for } x \in (b_1, b_2) \tag{5.3.4}$$

$$P_2(b_2, y) = 0, \qquad \text{for } y \in [-1, 0] \tag{5.3.5}$$

$$\frac{\partial P_2}{\partial y}(x, -1) = 0, \qquad \text{for } x \in (b_1, b_2] \tag{5.3.6}$$

The pressure impulse equation in both regions satisfies Laplace's equation:

$$\nabla^2 P(x) = 0 \tag{5.3.7}$$

We now solve using the separation of variables method. For the inner region (region 1 in figure 5.3.1), the upper and bed boundary conditions are satisfied by the eigenfunction expression:

$$P_1(x,y) = \sum_{n=1}^{\infty} \cos(\gamma_n y) \left\{ \alpha_n \frac{\cosh(\gamma_n(x-b_1))}{\cosh(\gamma_n b_1)} + \beta_n \frac{\sinh(\gamma_n(x-b_1))}{\sinh(\gamma_n b_1)} \right\} + Ax + C \tag{5.3.8}$$

where $\gamma_n = n\pi$, $n \in (1,2,3\ldots,N)$

for $-1 \le y \le 0$, and $0 \le x \le b_1$

The Fourier coefficients α_n, β_n and the so-called secular terms, A and C are to be found. For the outer region (region 2 in figure 5.3.1), the free surface, far field and bed boundary conditions are satisfied by the eigenfunction expression.

$$P_2(x, y, \mu) = \sum_{n=1}^{\infty} c_n \sin(\lambda_n y) \frac{\sinh(\lambda_n(x - b_2))}{\cosh(\lambda_n b_2)} \tag{5.3.9}$$

where $\qquad \lambda_n = \left(n - \frac{1}{2}\right)\pi$, $n = 1,2,3\dots, N$.

for $\qquad -1 \le y \le 0$, and $b_1 \le x \le b_2$

and c_n are Fourier coefficients to be found. Equation (5.3.9) is identical to the solution in Cooker and Peregrine (1995) except that different coefficients need to be found by solving the dimensionless boundary conditions. The choices of the denominator term in equation (5.3.9) is somewhat arbitrary, other choices simply altering the coefficients c_n values.

Applying the wall condition (5.3.3), we multiply by the basis functions $\cos(\gamma_l y)$ and integrate from $y = -1$ to 0 give:

$$-\alpha_n \tanh(\gamma_n b_1) - \beta_n \coth(\gamma_n b_1) = \frac{-2\sin(\mu\gamma_n)}{\gamma_n^2} \tag{5.3.10}$$

Further, by multiplying by the basis function 1 and integrating from $y = -1$ to 0 we obtain:

$$A = -\mu \tag{5.3.11}$$

We now impose the boundary conditions at the boundary between region 1 and region 2 which is at $x = b_1$ for $-1 \le y \le 0$. Pressure is continuous across this boundary, so

$$P_1 = P_2 \tag{5.3.12}$$

and this gives us

$$\sum_{n=1}^{\infty} \cos(\gamma_n y) \left\{ \frac{\alpha_n}{\cosh(\gamma_n b_1)} \right\} + \mu b_1 + C = \sum_{n=1}^{\infty} c_n \sin(\lambda_n y) \frac{\sinh(\lambda_n(b_1 - b_2))}{\cosh(\lambda_n b_2)} \tag{5.3.13}$$

Multiplying (5.3.13) by the same basis functions as used for (5.3.11) and integrating gives

$$C = -\mu b_1 - \sum_{n=1}^{\infty} c_n \frac{1}{\lambda_n} \frac{\sinh(\lambda_n(b_1 - b_2))}{\cosh(\lambda_n b_2)} \tag{5.3.14}$$

Substituting (5.3.14) into (5.3.13) gives

$$\sum_{n=1}^{\infty} \alpha_n \frac{\cos(\gamma_n y)}{\cosh(\gamma_n b_1)} - \sum_{n=1}^{\infty} c_n \frac{\sinh(\lambda_n (b_1 - b_2))}{\cosh(\lambda_n b_2)} \left[\frac{1}{\lambda_n} + \sin(\lambda_n y) \right] = 0 \qquad (5.3.15)$$

Matching the horizontal velocities on each side of the interface before and after impact gives:

$$\frac{\partial P_1}{\partial x} = \frac{\partial P_2}{\partial x} \qquad (5.3.16)$$

and this gives us

$$\sum_{n=1}^{\infty} \beta_n \gamma_n \frac{\cos(\gamma_n y)}{\sinh(\gamma_n b_1)} - \sum_{n=1}^{\infty} c_n \lambda_n \sin(\lambda_n y) \frac{\cosh(\lambda_n (b_1 - b_2))}{\cosh(\lambda_n b_2)} = -\mu \qquad (5.3.17)$$

Thus, the pressure impulse can be calculated by finding the three sets of unknown Fourier coefficients (α_i, β_i, c_i) $i = 1, 2, \ldots, N$ and evaluating the Fourier series which are all truncated at $n = M$. This can be done by using MATLAB with $3M$ conditions for the collocation points, and $3N$ equations (5.3.10), (5.3.15) and (5.3.17) which gives us $3M = 3N$ so that $M = N$. The systems of the equations are shown schematically in figure 5.3.2.

We now have an expression for the pressure impulse distribution throughout the fluid domain. Using this we can understand what occurs to the pressures and the change in the velocity field during impact by calculating the pressure impulse, total impulse and moment impulse. The areas of most interest are on the wall, along the seabed and beneath the deck. All the results converged at $N = 20$ using the criteria established in section §2.8. Hence we can expect the results to be accurate to within in 0.1% general.

$$
\begin{pmatrix}
\begin{array}{c} (diagonal) \\ -\tanh(\gamma_n b_1) \\ \vdots \\ \cdots \quad \cdots \quad \cdots \\ (diagonal) \\ \dfrac{\cos(\gamma_n y)}{\cosh(\gamma_n b1)} \\ \vdots \\ \cdots \quad \cdots \quad \cdots \\ (zero) \\ 0 \\ \vdots \end{array}
&
\begin{array}{c} \vdots \\ \vdots \\ \vdots \\ \cdots \\ \vdots \\ \vdots \\ \vdots \\ \cdots \\ \vdots \\ \vdots \\ \vdots \end{array}
&
\begin{array}{c} (diagonal) \\ -\tanh(\gamma_n b_1) \\ \vdots \\ \cdots \\ (zero) \\ 0 \\ \vdots \\ \cdots \\ (full) \\ \gamma_n \dfrac{\cos(\gamma_n y)}{\sinh(\gamma_n b1)} \\ \vdots \end{array}
&
\begin{array}{c} \vdots \\ \vdots \\ \vdots \\ \cdots \\ \vdots \\ \vdots \\ \vdots \\ \cdots \\ \ddots \\ \vdots \\ \vdots \end{array}
&
\begin{array}{c} (zero) \\ 0 \\ \\ \cdots \\ (diagonal) \\ \dfrac{\cos(\gamma_n y)}{\cosh(\gamma_n b1)}\left[\dfrac{1}{\lambda_n}+\sin(\lambda_n y)\right] \\ \\ \cdots \\ (full) \\ \lambda_n \sin(\lambda_n y)\dfrac{\cosh(\lambda_n(b_1-b_2))}{\cosh(\lambda_n b_2)} \\ \end{array}
&
\begin{array}{c} \cdots \\ \\ \\ \cdots \\ \\ \\ \\ \cdots \\ \\ \\ \ddots \end{array}
\end{pmatrix}
\begin{pmatrix} \alpha_1 \\ \vdots \\ \alpha_N \\ \cdots \\ \beta_1 \\ \vdots \\ \beta_N \\ \cdots \\ c_1 \\ \vdots \\ c_N \end{pmatrix}
=
\begin{pmatrix} \dfrac{-2\sin(\mu\gamma_1)}{\gamma_1^2} \\ \vdots \\ \dfrac{-2\sin(\mu\gamma_N)}{\gamma_N^2} \\ \cdots \\ 0 \\ \\ \cdots \\ -\mu \\ \vdots \\ -\mu \end{pmatrix}
$$

Figure 5.3.2: Matrix system of equations. The first M rows come from (5.3.10), the next from (5.3.15) and the last from (5.3.17).

5.4   Pressure Impulse

Before we analyse the data, we compare the pressure impulse results for deck problem with Cooker's model, taking $b_1 = 0.01$ for length of the deck and $b_2 = 2$ for the free surface. In this case we expect that the smaller the size of the deck we chose, the closer we get to the Cooker's model. The results obtained are given as three dimensional surface plots.

The plots show us how the pressure impulse is distributed over the surface of the seawall. The result are made dimensionless by choosing units for which $H = 1$ and the pressure impulse is in the form of $P\!\!\Big/\!\rho U_0 H$.

5.4.1 Comparison results between deck problem and Cooker's model for Pressure Impulse on the wall

	Deck Problem with $b_1 = 0.01$	Cooker's Model
$\mu = 0.2$		
$\mu = 0.5$		
$\mu = 1$		
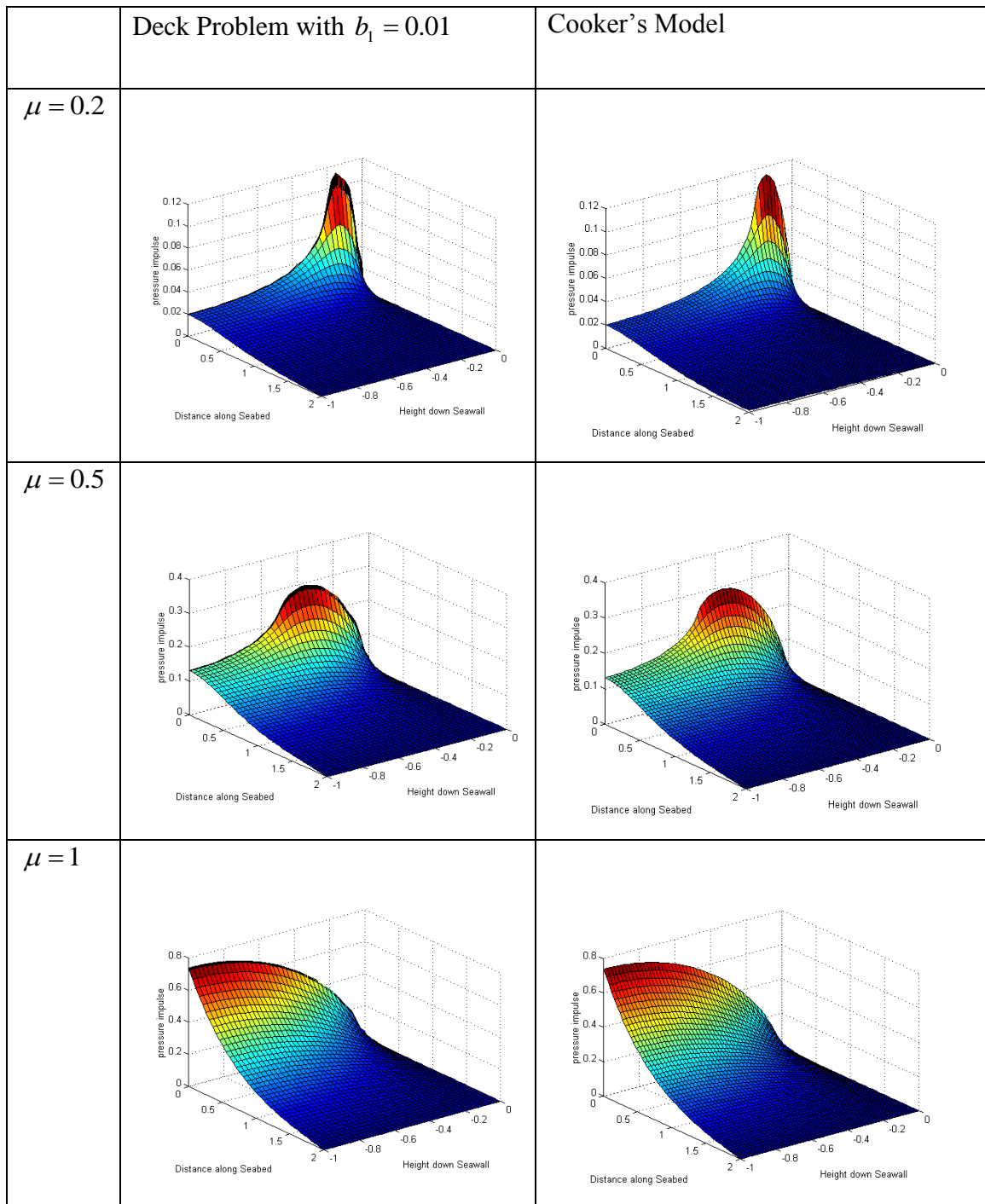
Figure 5.4.1: Comparison result for deck problem with Cooker's Model for pressure impulse on the wall.

From the figure above, we can see the pressure impulse profile for both cases is virtually the same for any given μ, as expected.

113

5.4.2 Pressure Impulse on the Wall

Now we look back at our original problem, the effect of a deck on the top of the seawall. In this case, the length of the deck, b_1 cannot be greater than 0.5 as this will give an ill-conditioned matrix. For example, taking $b_1 = 0.5$ and $b_1 = 0.6$, MATLAB will gives us a sensible graph but with a warning for $b_1 = 0.6$. For $b_1 = 0.7$, we will get a non-sensical graph and a warning from MATLAB. The matrices for $b_1 = 0.6$ and $b_1 = 0.7$ are badly conditioned. Hence for the accurate results we will take $b_1 \leq 0.5$, which corresponds to more realistic engineering situations in any case. The reasons for poorly conditioned matrices will be discussed in §8.1.

The following contour plots show the pressure impulse for deck problem. We will take varying values of μ and b_1 so that we can see the changes in pressure impulse in each case. The distribution of the pressure impulse on the wall will give useful information as waves strike coastal structures.
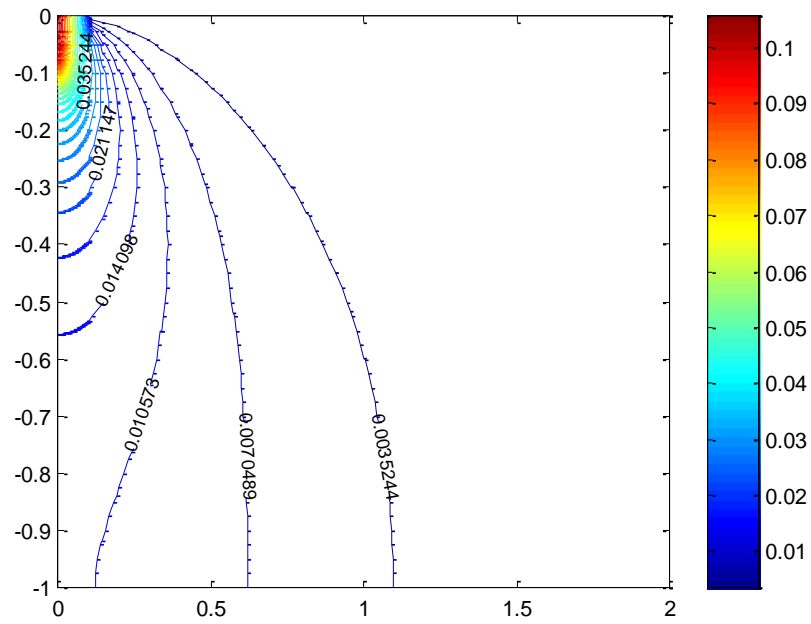
Figure 5.4.2 : Plot showing the pressure impulse on the wall generated by deck problem formulation with $b_1 = 0.1$, $b_2 = 2$, and $\mu = 0.1$. The maximum pressure impulse is $0.1059\,\rho U_0 H$ and occurs at $y = -0.0250$.
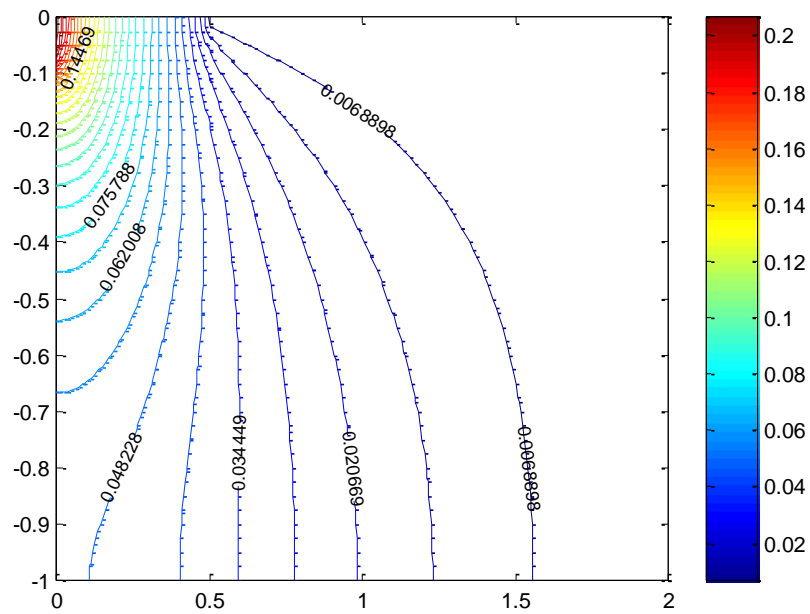
Figure 5.4.3 : Plot showing the pressure impulse on the wall generated by deck problem formulation with $b_1 = 0.5$, $b_2 = 2$, and $\mu = 0.1$. The maximum pressure impulse is $0.2136\,\rho U_0 H$ and occurs at $y = 0$.
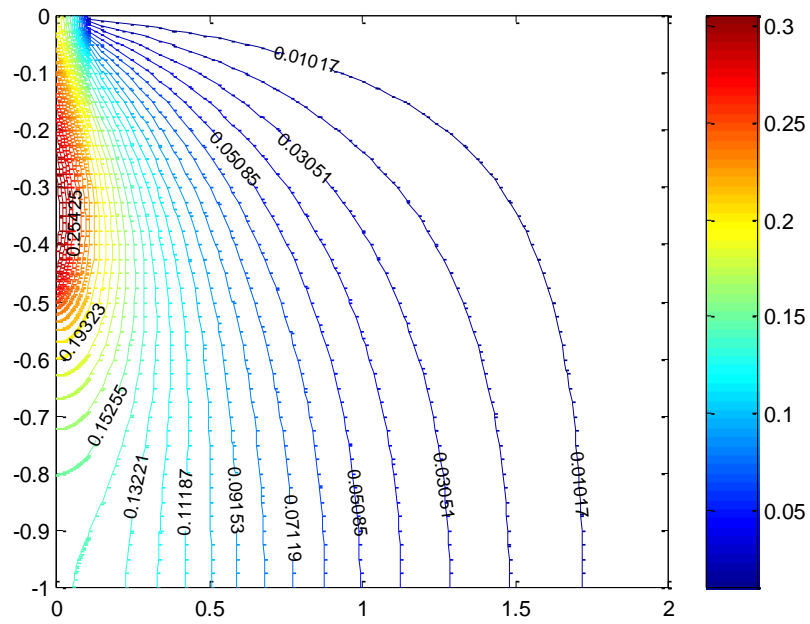
Figure 5.4.4: Plot showing the pressure impulse on the wall generated by deck problem formulation with $b_1 = 0.1$, $b_2 = 2$, and $\mu = 0.5$. The maximum pressure impulse is $0.3153\, \rho U_0 H$ occurs at $y = -0.35$.
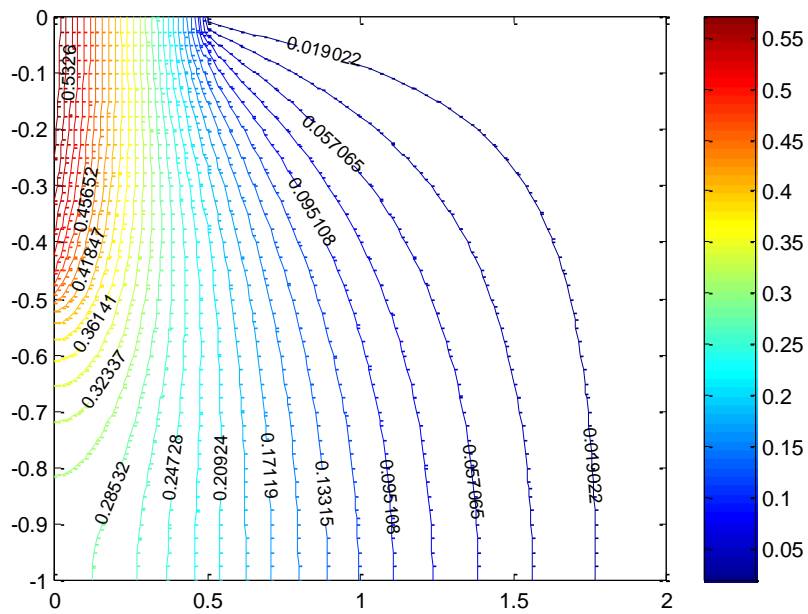
Figure 5.4.5 : Plot showing the pressure impulse on the wall generated by deck problem formulation with $b_1 = 0.5$, $b_2 = 2$, and $\mu = 0.5$. The maximum pressure impulse is $0.5897\, \rho U_0 H$ occurs at $y = -0.025$.
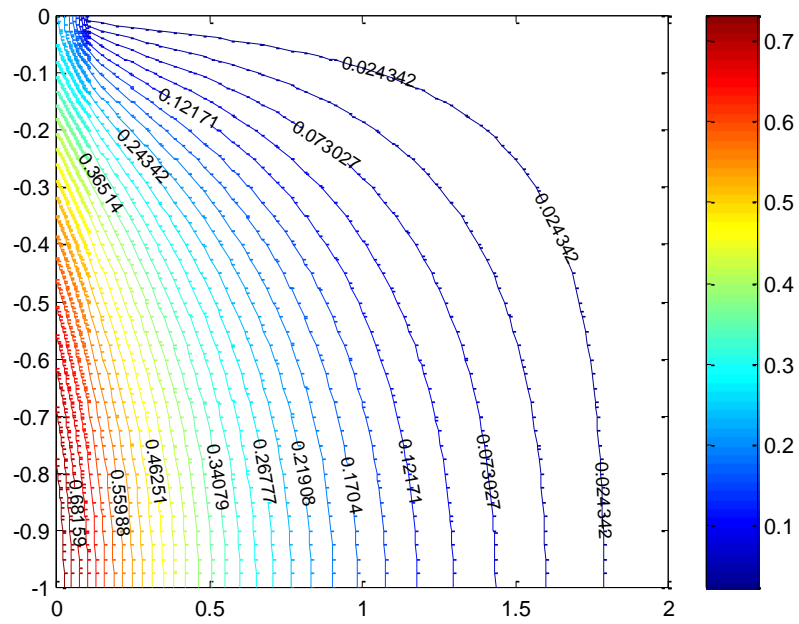
Figure 5.4.6 : Plot showing the pressure impulse on the wall generated by deck problem formulation with $b_1 = 0.1$, $b_2 = 2$, and $\mu = 1.0$. The maximum pressure impulse is $0.7546\,\rho U_0 H$ occurs at $y = -1$.
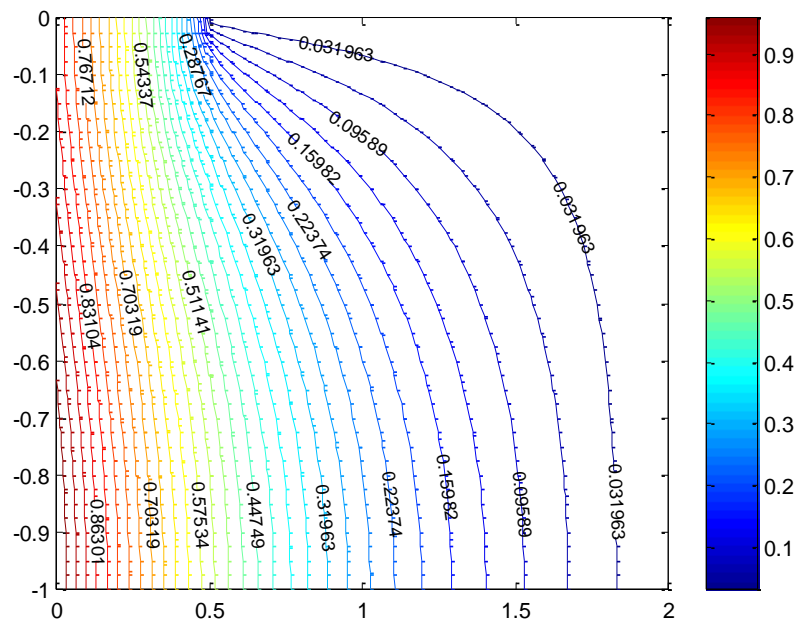
Figure 5.4.7 :Plot showing the pressure impulse on the wall generated by deck problem formulation with $b_1 = 0.5$, $b_2 = 2$, and $\mu = 1.0$. The maximum pressure impulse is $0.9909\,\rho U_0 H$ occurs at $y = -1$.

From the figure above, we notice that the value of pressure impulse increases when the value of μ increases for each length of the deck. If we compare the result between the different values of length of deck, we can see the pressure impulse also increases when the length of the deck increases. The largest value of pressure impulse is when $\mu = 1.0$ which is $0.7546 \, \rho U_0 H$ and $0.9909 \, \rho U_0 H$ for $b_1 = 0.1$ and $b_1 = 0.5$ respectively for depth 1 below the free surface. The first shows the good agreement with Cooker and Peregrine (1995) as they discovered the maximum value of pressure impulse is 0.742 $\rho U_0 H$ when $\mu = 1.0$ for depth 1 below the free surface. Figure 5.4.8 shows 3-D plot for pressure impulse on the wall for varying μ and b_1. Plots of the pressure impulse on the wall for different values of μ for $b_1 = 0.1$ are given in figure 5.4.7.

	$b_1 = 0.1$	$b_1 = 0.5$
$\mu = 0.1$		
$\mu = 0.5$		
$\mu = 1$		
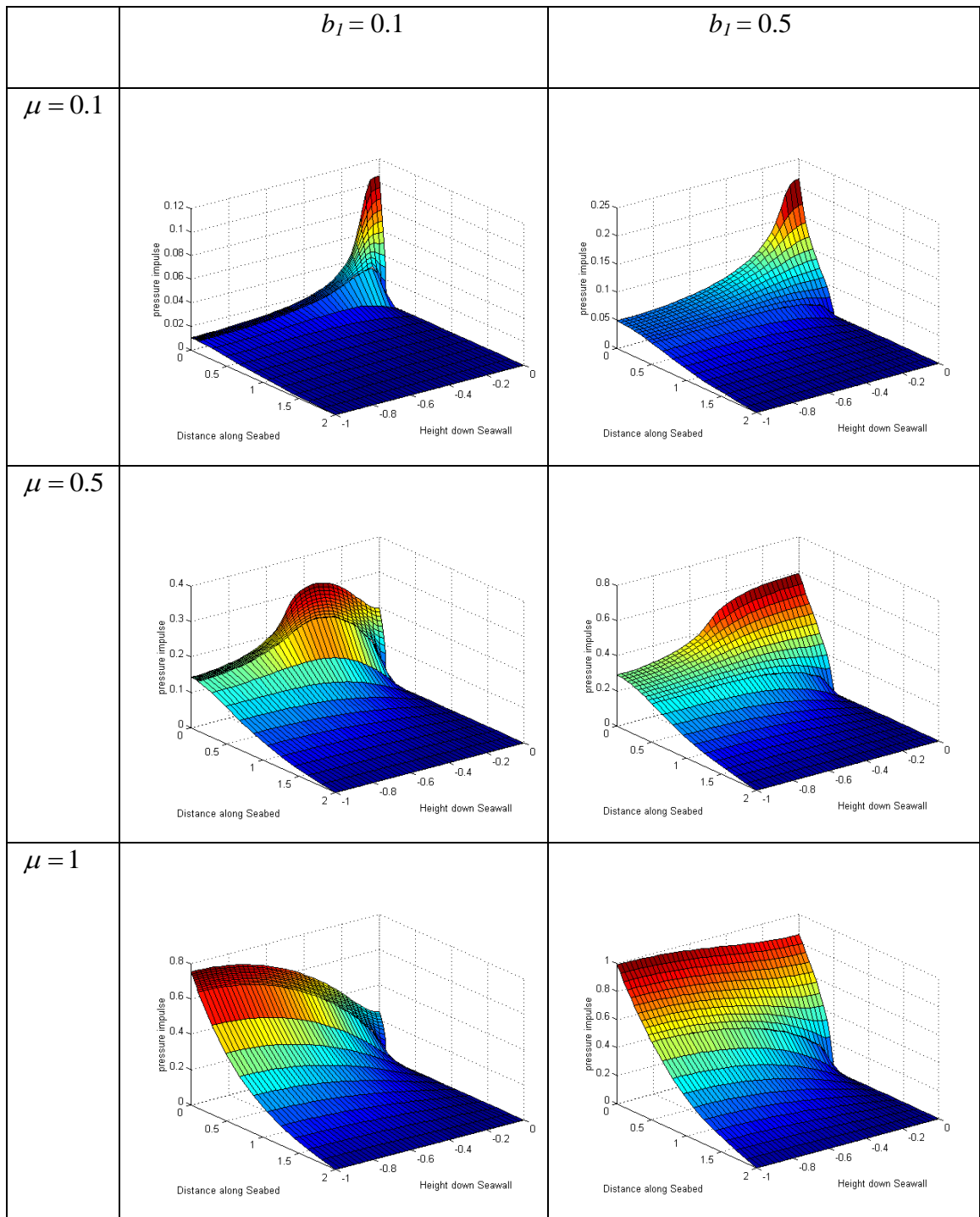
Figure 5.4.8: Pressure impulse on the wall for deck problem in 3-D.

From the observation of the 3-D plot, we can see the peak pressure point of the graphs become more rounded for $\mu = 1$ and almost constant with depth when the value of μ is increased. The area on the seawall affected by the peak pressure also increases. In table 5.4.1 we will compare our result with Cooker and Peregrine (1990, 1995).

Table 5.4.1: Maximum pressure impulse on the wall for $H = \rho = U_0 = 1$, and $\mu = 0.5$ and $\mu = 1.0$.

Author	Length of deck (from wall)	Free surface lengths (from deck/wall)	Pressure Impulse for $\mu = 0.5$ $(\rho U_0 H)$	Pressure Impulse for $\mu = 1.0$ $(\rho U_0 H)$
Cooker and Peregrine	No deck	$b = 1$	0.2826	0.6753
		$b = 2$	0.2927	0.7394
		$b = 5$	0.2932	0.7424
Present result	$b_1 = 0.1$	$b_2 = 1$	0.3041	0.6875
		$b_2 = 2$	0.3153	0.7546
		$b_2 = 5$	0.3158	0.7578
	$b_1 = 0.5$	$b_2 = 1$	0.5512	0.8552
		$b_2 = 2$	0.5897	0.9909
		$b_2 = 5$	0.5915	0.9976

From table 5.4.1, we can see the two examples of wall with a deck with different lengths of deck and lengths of free surface (from the structure to the distant boundary at $x = b_2$). We can see that for each case, with different distance of free surface, the maximum pressure impulse is more consistent when $b_2 = 2$ or higher. The difference between $b_2 = 2$ and $b_2 = 5$ in pressure impulse is from 0.001 to 0.007 $\rho U_0 H$. We do not choose $b_2 = 1$, because the difference between $b_2 = 2$ is quite big (0.01 to 0.06 $\rho U_0 H$). In this study, the free surface $b_2/H = 2$ is probably a fair model with a length of deck $b_1/H \leq 0.5$. A good agreement is also shown in Cooker and Peregrine (1995), in which the different impact lengths give very similar pressure impulse distributions near the impact wall.

We can also see that having a deck on the top of the wall can dramatically increase the pressure impulse on the wall. The position of the maximum P can move to the corner between the vertical wall and the deck, see figures 5.4.9 and 5.4.10. (The small irregularity in the lines for $\mu = 0.1$ are due to truncation of the series expansion.) Hence we can conclude that having a deck on the top of the seawall increases the value of the maximum pressure impulse and the extent down the seawall of a high pressure impulse region. These results show a good agreement with those of Oumeraci (1994), which gave a high pressure impulse on the breakwater resulting from wave impact on the deck.
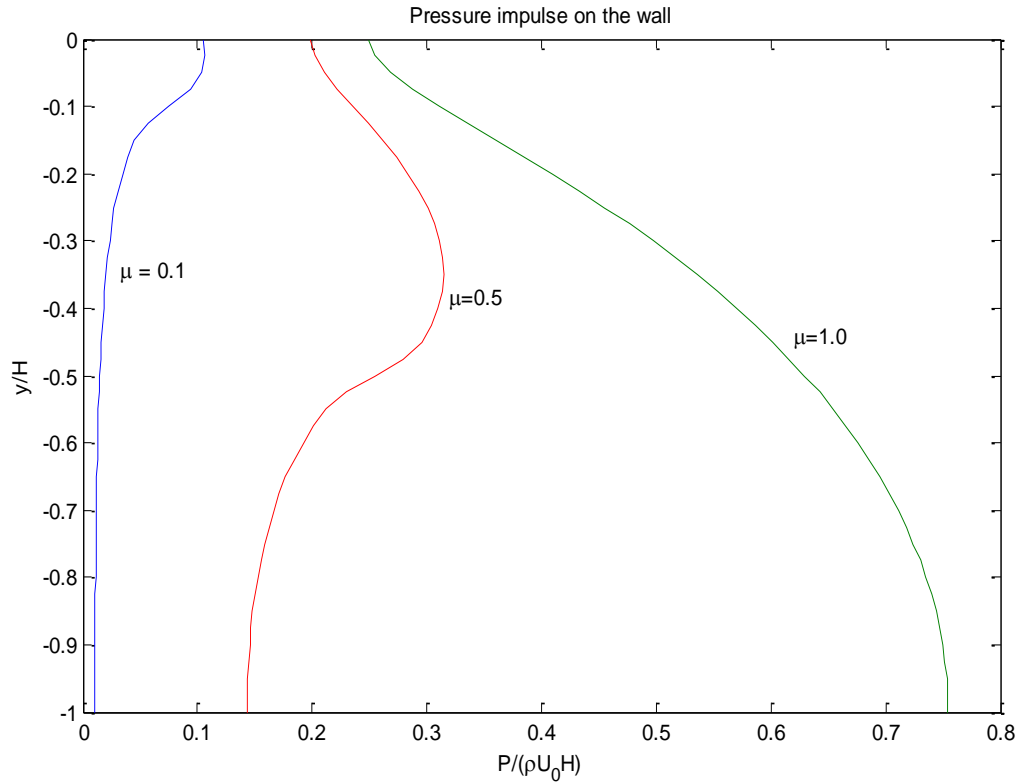
Figure 5.4.9: Plot showing the pressure impulse along the wall for $b_1 = 0.1$
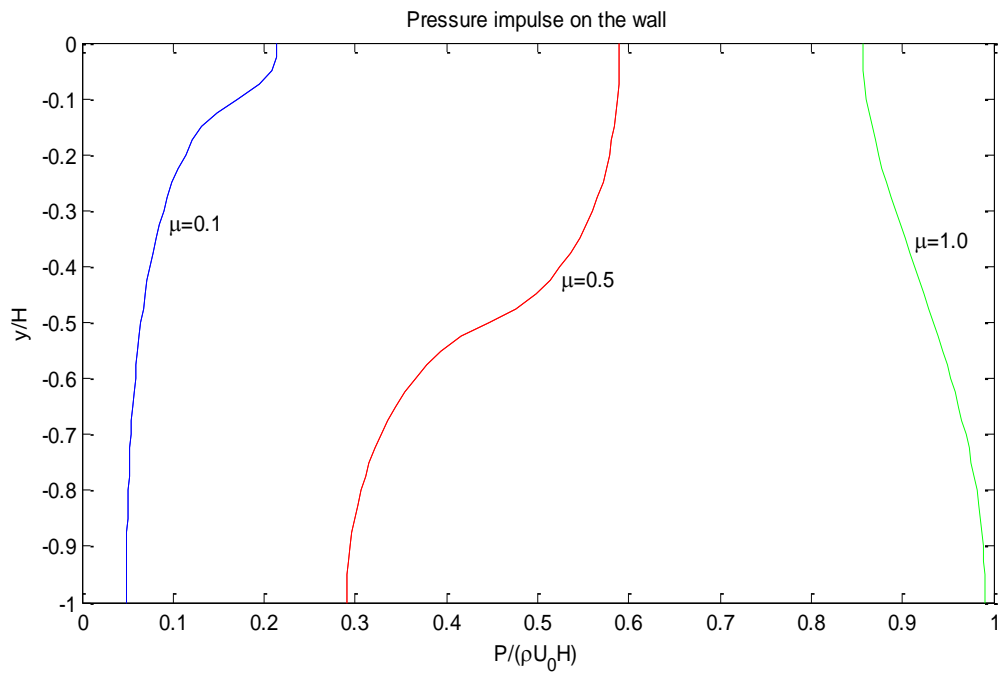
Figure 5.4.10: Plot showing the pressure impulse along the wall for $b_1 = 0.5$.

5.4.3   Pressure Impulse on the Seabed and the Deck

It is interesting to examine the pressure impulse, P along the seabed. This may provide information about erosion effects occurring at the base of a structure, allowing engineers to consider what extra protection is needed there. Poor designs may require constant maintenance as waves erode the base of the seawall. Figures 5.4.11 and 5.4.12 show plots of the pressure impulse along the seabed for different values of μ and b_1. The highest values for pressure impulse occur at the wall and the region beneath the deck. As μ increases towards 1 the maximum value increases, as expected, and as we can see the pressure impulse also increases as the length of the deck increases.

Figures 5.4.13 and 5.4.14 show the distribution of pressure impulse in the water beneath the deck for different values of μ and b_1. The highest values of pressure impulse occur at the landward end and it increases as μ increases toward 1. The values of pressure impulse for $b_1 = 0.5$ are more than 50% greater than those for $b_1 = 0.1$ for each value of μ. Overall we can see that pressure impulse beneath the deck is greater than pressure impulse along the seabed.
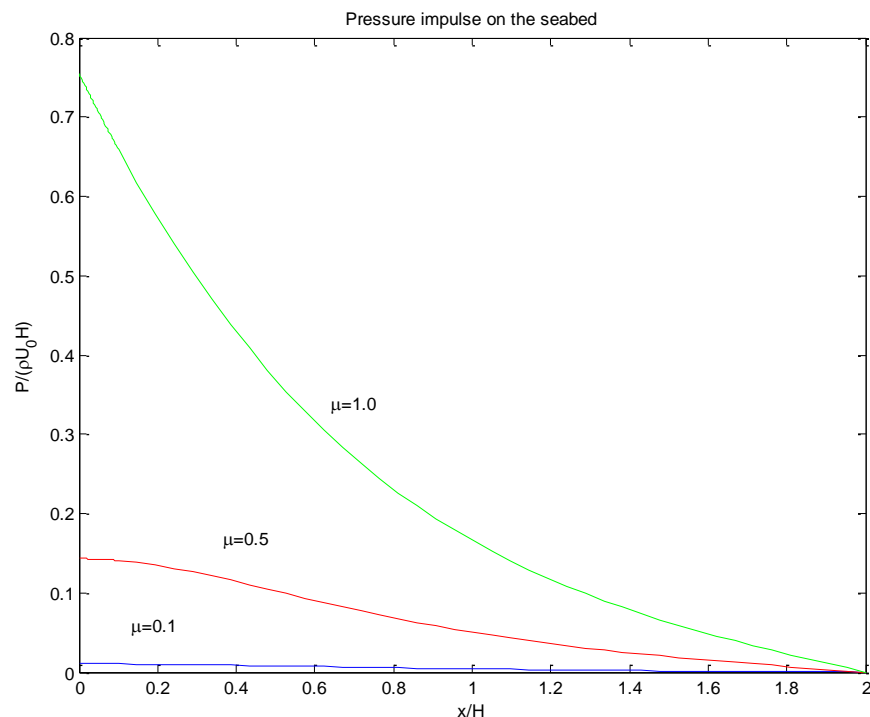
Figure 5.4.11: Plot showing the pressure impulse along the seabed for $b_1 = 0.1$.
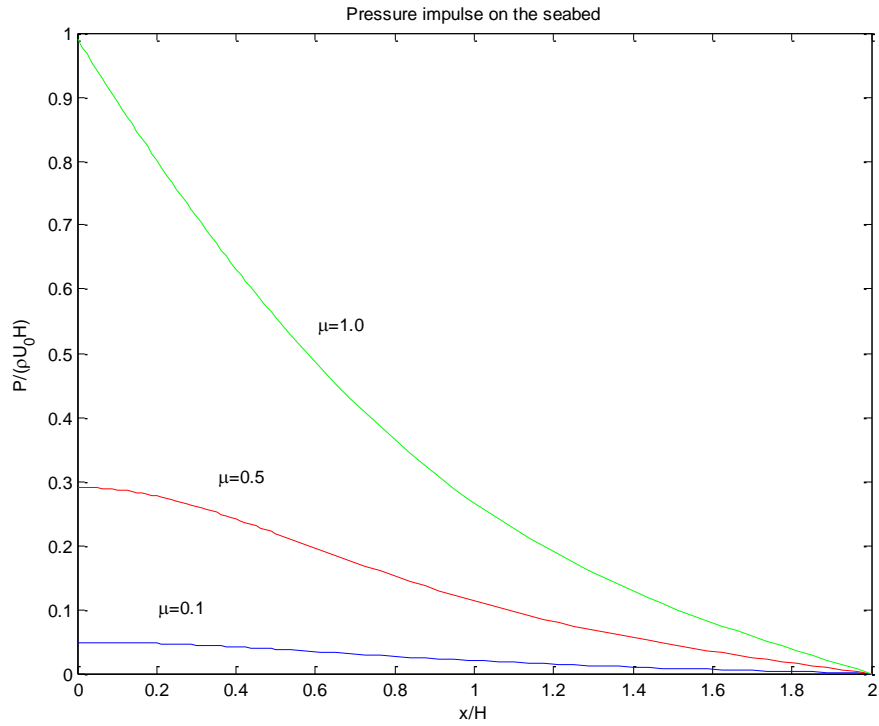
Figure 5.4.12: Plot showing the pressure impulse along the seabed for $b_1 = 0.5$.
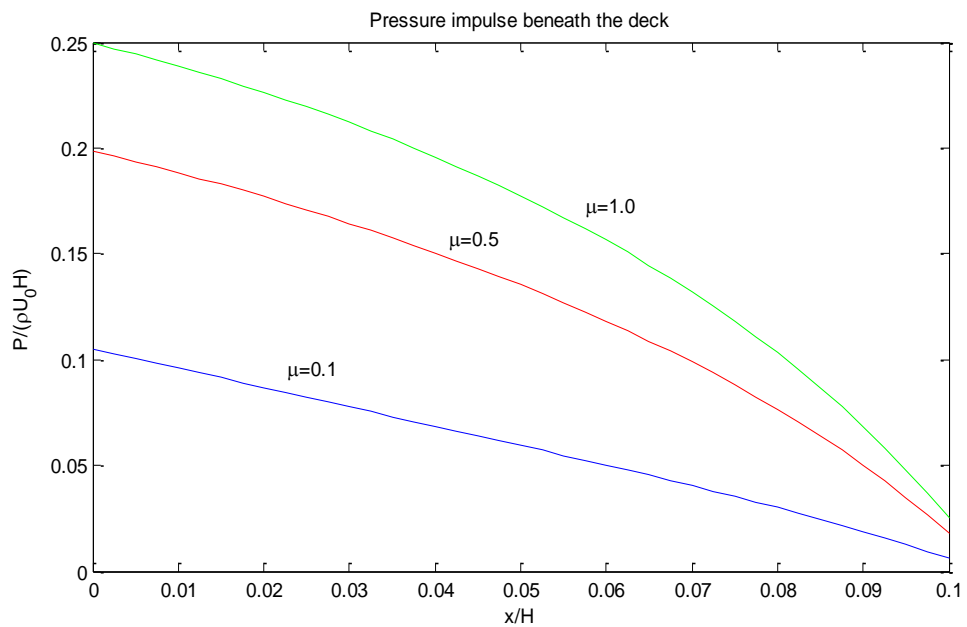
Figure 5.4.13: Plot showing the pressure impulse beneath the deck for $b_1 = 0.1$.

124
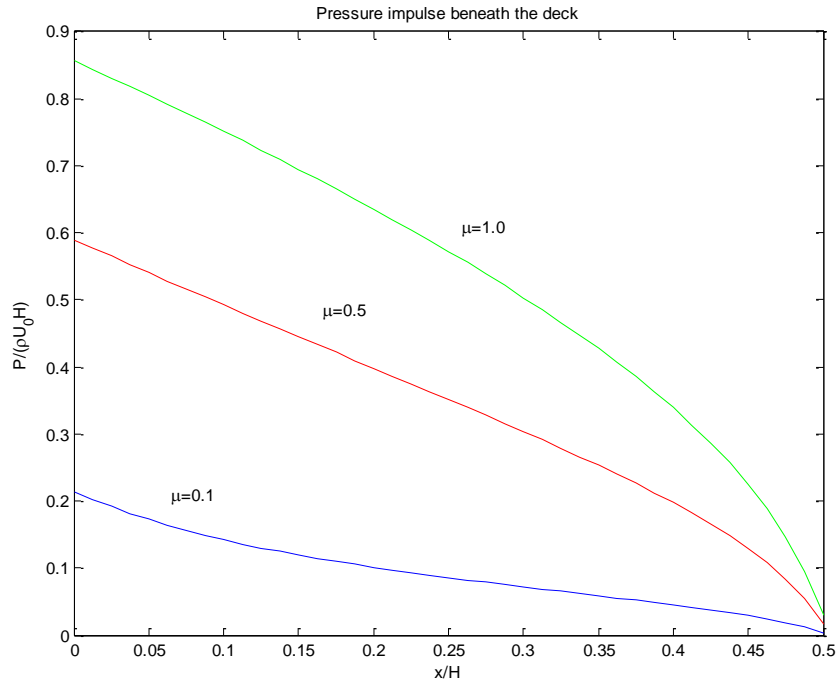
Figure 5.4.14: Plot showing the pressure impulse beneath the deck for $b_1 = 0.5$.

5.5   Total Impulse

As in the previous chapter, we calculate the total impulse for the wall, seabed and beneath the deck for this problem. The direction of the total impulse is given as figure 5.5.1.
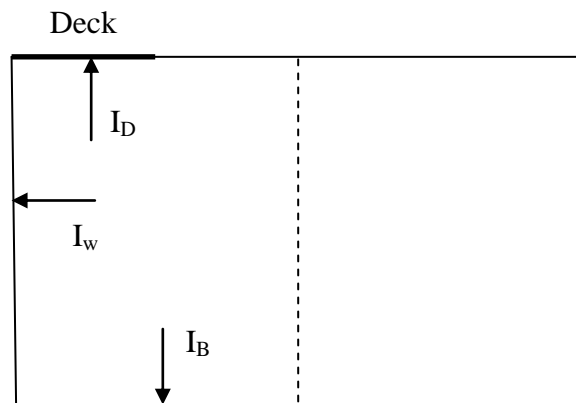
Figure 5.5.1: Total impulse definitions for deck.

5.5.1 Total impulse on the wall

To calculate the total impulse exerted by the fluid on the wall, I_w we need the expression for the pressure impulse at $x = 0$ given in equation (5.3.8). Integrating over the wall gives:

$$I_w = \int_{-1}^{0} P_1(0, y)dy \tag{5.5.1}$$

Solving this equation gives

$$
\begin{aligned}
I_w &= \int_{-1}^{0} P(0, y)dy \\
&= \int_{-1}^{0} \sum_{n=1}^{\infty} \{\alpha_n - \beta_n\}\cos(\gamma_n y) + C\, dy \\
&= \sum_{n=1}^{\infty} \{\alpha_n - \beta_n\} \int_{-1}^{0} \cos(\gamma_n y)dy + \int_{-1}^{0} C\, dy \\
&= C
\end{aligned}
$$

$$\tag{5.5.2}$$

Substituting (5.3.14) into (5.5.2):

$$I_w = -\mu b_1 - \sum_{n=1}^{\infty} c_n \frac{1}{\lambda_n} \frac{\sinh(\lambda_n(b_1 - b_2))}{\cosh(\lambda_n b_2)} \tag{5.5.3}$$

Equation (5.5.3) is dimensionless and is plotted in figure 5.5.2 as a function in μ. The result for the total impulse in the form $\dfrac{I_w}{\rho U_0 H^2}$. From the figure we can see that as μ increases from 0 to 1, $\dfrac{I_w}{\rho U_0 H^2}$ increases from 0 to the maximum impulse value which occurs at $\mu = 1.0$. The relationship between μ and $\dfrac{I_w}{\rho U_0 H^2}$ is almost linear from $0.6 \le \mu \le 1$ for length of deck $b_1 = 0.1$ and even more so for $b_1 = 0.5$. The maximum impulse value for different lengths of deck, $b_1 = 0.1$, and $b_1 = 0.5$ are approximately $0.580\, \rho U_0 H^2$, and $0.920\, \rho U_0 H^2$ respectively. We can conclude that the total impulse on the wall increases as the length of the deck increases.

5.5.2 Total impulse on the seabed

The total impulse on the seabed, I_B is given from the pressure impulse expression at $y = -1$. Integrating over the seabed gives us:

$$I_B = \int_0^{b_1} P_1(x,-1)dx + \int_{b_1}^{b_2} P_2(x,-1)dx \tag{5.5.4}$$

Solving this equation gives

$$I_B = \sum_{n=1}^{\infty} \cos(-\gamma_n) \int_0^{b_1} \left\{ \alpha_n \frac{\cosh(\gamma_n(x-b_1))}{\cosh(\gamma_n b_1)} + \beta_n \frac{\sinh(\gamma_n(x-b_1))}{\sinh(\gamma_n b_1)} \right\} dx + \int_0^{b_1} Ax + Cdx$$

$$+ \sum_{n=1}^{\infty} c_n \sin(-\lambda_n) \int_{b_1}^{b_2} \frac{\sinh(\lambda_n(x-b_2))}{\cosh(\lambda_n b_2)} dx$$

giving

$$I_B = \sum_{n=1}^{\infty} \cos(-\gamma_n) \left\{ \frac{\alpha_n}{\cosh(\gamma_n b_1)} \left[\frac{1}{\gamma_n} \sinh(\gamma_n(x-b_1)) \right]_0^{b_1} + \frac{\beta_n}{\sinh(\gamma_n b_1)} \left[\frac{1}{\gamma_n} \cosh(\gamma_n(x-b_1)) \right]_0^{b_1} \right\}$$

$$\left[\frac{Ax^2}{2} + Cx \right]_0^{B_1} + \sum_{n=1}^{\infty} c_n \frac{\sin(-\lambda_n)}{\cosh(\lambda_n b_2)} \left[\frac{1}{\lambda_n} \cosh(\lambda_n(x-b_2)) \right]_{b_1}^{b_2}$$

$$= \sum_{n=1}^{\infty} \cos(-\gamma_n) \left\{ \frac{\alpha_n}{\gamma_n} \tanh(\gamma_n b_1) + \beta_n \left(\frac{1}{\gamma_n \sinh(\gamma_n B_1)} - \frac{1}{\gamma_n} \coth(\gamma_n b_1) \right) \right\} + \frac{Ab_1^2}{2} + Cb_1$$

$$+ \sum_{n=1}^{\infty} c_n \frac{\sin(-\lambda_n)}{\cosh(\lambda_n b_2)} \left[\frac{1}{\lambda_n} - \frac{1}{\lambda_n} \cosh(\lambda_n(b_1-b_2)) \right]$$

$$\tag{5.5.5}$$

Equation (5.5.5) is plotted in figure 5.5.2 as a function in μ. The result for the total impulse on the seabed is of the form $\dfrac{I_B}{\rho U_0 H^2}$. From the figure we can see that as μ increases from 0 to 1, $\dfrac{I_B}{\rho U_0 H^2}$ increases from 0 to the maximum impulse value which occurs at $\mu = 1.0$. The maximum total impulse value for different lengths of deck, $b_1 = 0.1$, and $b_1 = 0.5$ are approximately $0.470 \rho U_0 H^2$, and $0.680 \rho U_0 H^2$ respectively. We can conclude that the total impulse on the seabed increases as the length of the deck increases. The maximum total impulse on the seabed for each length of the deck is smaller than the maximum total impulse on the wall.

5.5.3   Total impulse beneath the deck

The total upward impulse on the deck, I_D is given by the integral of the pressure impulse expression at $y = 0$ over the deck. This is

$$I_D = \int_0^{b_1} P_1(x,0)dx \tag{5.5.7}$$

Thus:

$$I_D = \sum_{n=1}^{\infty} \int_0^{b_1} \left\{ \alpha_n \frac{\cosh(\gamma_n(x-b_1))}{\cosh(\gamma_n b_1)} + \beta_n \frac{\sinh(\gamma_n(x-b_1))}{\sinh(\gamma_n b_1)} \right\} + Ax + Cdx$$

$$= \sum_{n=1}^{\infty} \alpha_n \frac{1}{\gamma_n} \tanh(\gamma_n b_1) + \sum_{n=1}^{\infty} \beta_n \frac{1}{\gamma_n} \left[\frac{1}{\sinh(\gamma_n b_1)} - \coth(\gamma_n b_1) \right]$$

$$+ \frac{Ab_1^2}{2} + Cb_1 \tag{5.5.8}$$

Substituting (5.3.11) and (5.3.14) into (5.5.8) and simplifying gives:

$$I_D = \sum_{n=1}^{\infty} \alpha_n \frac{1}{\gamma_n} \tanh(\gamma_n b_1) + \sum_{n=1}^{\infty} \beta_n \frac{1}{\gamma_n} \left[\frac{1}{\sinh(\gamma_n b_1)} - \coth(\gamma_n b_1) \right]$$

$$- \sum_{n=1}^{\infty} c_n \frac{b_1}{\lambda_n} \frac{\sinh(\lambda_n(b_1 - b_2))}{\cosh(\lambda_n b_2)} - \frac{\mu b_1^2}{2} \tag{5.5.9}$$

We plot the equation (5.5.9) in figure 5.5.2 as a function of μ. The result for the total impulse beneath the deck is the form $\dfrac{I_D}{\rho U_0 H^2}$. From the figure we can see that as μ increases from 0 to 1, $\dfrac{I_D}{\rho U_0 H^2}$ increases from 0 to its maximum impulse value which occurs at $\mu = 0.1$. The maximum total impulse value for different lengths of deck, $b_1 = 0.1$, and $b_1 = 0.5$ are approximately $0.017 \rho U_0 H^2$, and $0.270 \rho U_0 H^2$ respectively. As expected, the maximum value increases as the length of the deck increases. The total impulse beneath the deck is much smaller compared to that on the wall and along the seabed, partly because P is much smaller.

b₁=0.1	b₁=0.5
Total impulse on the wall	**Total impulse on the wall**
Total impulse on the seabed	**Total impulse on the seabed**
Total impulse beneath the deck	**Total impulse beneath deck**
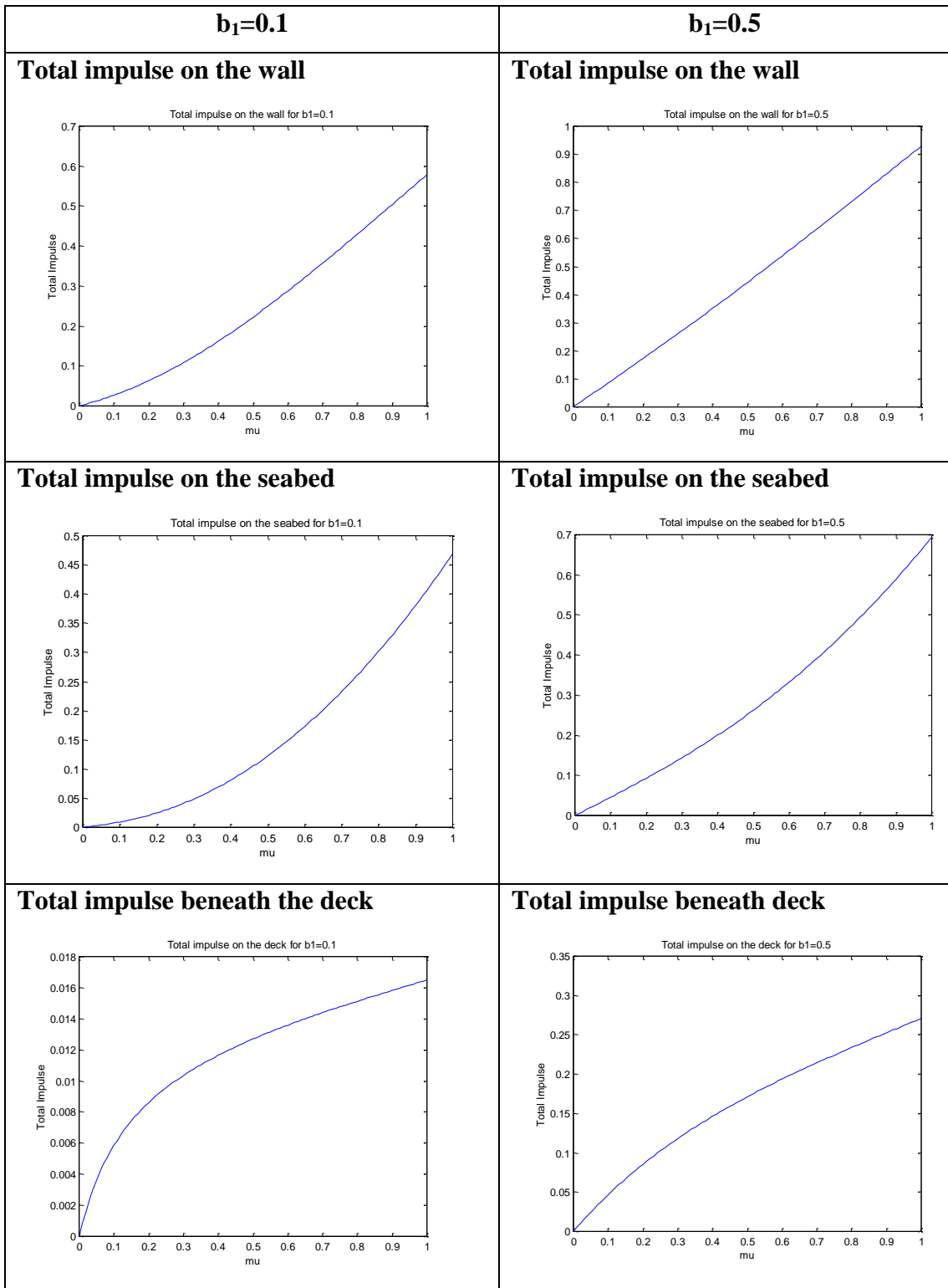
Figure 5.5.2: Total impulse on the wall, seabed and beneath the deck for $b_1 = 0.1$ and $b_1 = 0.5$.

5.6 Moment Impulse

We calculate the moment impulse on the wall, on the seabed and on the deck. We take the direction of the moment impulse as in figure 5.6.1.
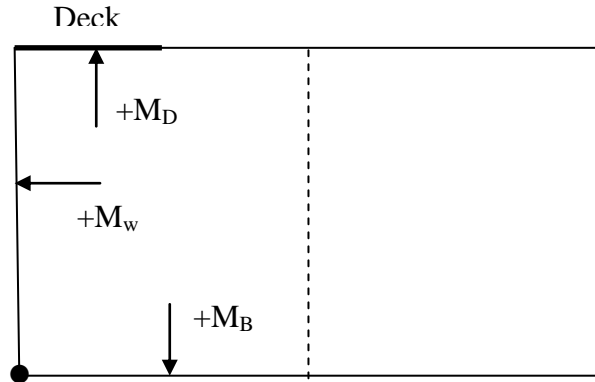
Figure 5.6.1: Moment impulse diagram for the deck.

5.6.1 Moment Impulse on the Wall

Cooker (1990) introduced the expression for moment impulse on the wall, M_w about an axis at its bottom, due to the pressure impulse on the wall.

For the deck problem, the expression is again

$$M_w = \int_{-1}^{0} (1 + y) P_1(0, y) dy \tag{5.6.1}$$

The moment impulse, M_w is positive in the anti-clockwise sense about the base of the wall. Evaluating (5.6.1) gives

$$
\begin{aligned}
M_w &= \sum_{n=1}^{\infty} \{\alpha_n - \beta_n\} \int_{-1}^{0} (1 + y) \cos(\gamma_n y) dy + \int_{-1}^{0} (1 + y) C dy \\
&= \sum_{n=1}^{\infty} \{\alpha_n - \beta_n\} \left[\int_{-1}^{0} \cos(\gamma_n y) dy + \int_{-1}^{0} y \cos(\gamma_n y) dy \right] + \int_{-1}^{0} C dy + \int_{-1}^{0} C y dy \\
&= \sum_{n=1}^{\infty} \{\alpha_n - \beta_n\} \left[\frac{1}{\gamma_n^2} - \frac{1}{\gamma_n^2} \cos(-\gamma_n) \right] + \frac{C}{2}
\end{aligned}
$$

$$\tag{5.6.2}$$

Substituting (5.3.14) into (5.6.2) and simplifying gives:

$$M_w = \sum_{n=1}^{\infty} \{\alpha_n - \beta_n\} \left[\frac{1}{\gamma_n^2} - \frac{1}{\gamma_n^2} \cos(-\gamma_n) \right] - \sum_{n=1}^{\infty} c_n \frac{1}{2\lambda_n} \frac{\sinh(\lambda_n(b_1 - b_2))}{\cosh(\lambda_n b_2)} - \frac{\mu b_1}{2}$$

(5.6.3)

We plot equation (5.6.3) in figure 5.6.2 as a function in μ. The result for the moment impulse on the wall is in the form $\dfrac{M_w}{\rho U_0 H^3}$. From the figure we can see that as μ increases from 0 to 1, $\dfrac{M_w}{\rho U_0 H^3}$ increases from 0 to the maximum moment impulse value which occurs at $\mu = 1.0$. The maximum moment impulse value for different lengths of deck, $b_1 = 0.1$, $b_1 = 0.3$ and $b_1 = 0.5$ are approximately $0.245 \, \rho U_0 H^3$, $0.345 \, \rho U_0 H^3$ and $0.451 \, \rho U_0 H^3$ respectively. As expected, the maximum values increase as the length of the deck increases. The maximum value for deck problem is large compared to Cooker (1990), which is about $0.218 \, \rho U_0 H^3$.

5.6.2 Moment impulse on the seabed and deck

As in Cooker (1990), the moment impulse on the seabed, M_B about the base of seawall is

$$M_B = \int_0^{B_2} x P(x, -1) dx$$

(5.6.4)

We assume the moment impulse, M_B is positive in the clockwise sense about the base of the wall. Evaluating (5.6.4)

$$M_B = \int_0^{b_1} x P_1(x, -1) dx + \int_{b_1}^{b_2} x P_2(x, -1) dx$$

$$= \sum_{n=1}^{\infty} \alpha_n \frac{\cos(-\gamma_n)}{\cosh(\gamma_n b_1)} \int_0^{b_1} x \cosh(\gamma_n(x - b_1)) dx + \sum_{n=1}^{\infty} \beta_n \frac{\cos(-\gamma_n)}{\sinh(\gamma_n b_1)} \int_0^{b_1} x \sinh(\gamma_n(x - b_1)) dx$$

$$+ \int_0^{b_1} A x^2 \, dx + \int_0^{b_1} C x dx + \sum_{n=1}^{\infty} c_n \frac{\sin(-\lambda_n)}{\cosh(\lambda_n b_2)} \int_{b_1}^{b_2} x \sinh(\lambda_n(x - b_2)) dx$$

$$= \sum_{n=1}^{\infty} \alpha_n \frac{\cos(-\gamma_n)}{\cosh(\gamma_n b_1)} \left[\frac{1}{\gamma_n^2} \cosh(\gamma_n b_1) - \frac{1}{\gamma_n^2} \right] + \sum_{n=1}^{\infty} \beta_n \frac{\cos(-\gamma_n)}{\sinh(\gamma_n b_1)} \left[\frac{b_1}{\gamma_n} - \frac{1}{\gamma_n^2} \sinh(\gamma_n b_1) \right]$$

$$+ \sum_{n=1}^{\infty} c_n \frac{\sin(-\lambda_n)}{\cosh(\lambda_n b_2)} \left[\frac{b_2}{\lambda_n} - \frac{b_1}{\lambda_n} \cosh(\lambda_n (b_1 - b_2)) + \frac{1}{\lambda_n^2} \sinh(\lambda_n (b_1 - b_2)) \right]$$

$$+ \frac{Ab_1^3}{3} + \frac{Cb_1^2}{2} \tag{5.6.5}$$

The moment impulse beneath the deck, M_D is given by:

$$M_D = \int_0^{b_1} x P_1(x,0) dx \tag{5.6.6}$$

We assume the moment impulse, M_D is positive in the clockwise sense about the base of the wall. Evaluating (5.6.6)

$$M_D = \sum_{n=1}^{\infty} \frac{\alpha_n}{\cosh(\gamma_n b_1)} \int_0^{b_1} x \cosh(\gamma_n (x - b_1)) dx + \sum_{n=1}^{\infty} \frac{\beta_n}{\sinh(\gamma_n b_1)} \int_0^{b_1} x \sinh(\gamma_n (x - b_1)) dx$$

$$+ \int_0^{b_1} Ax^2 \, dx + \int_0^{b_1} Cx dx$$

$$M_D = \sum_{n=1}^{\infty} \frac{\alpha_n}{\cosh(\gamma_n b_1)} \left[\frac{1}{\gamma_n^2} \cosh(\gamma_n b_1) - \frac{1}{\gamma_n^2} \right] + \sum_{n=1}^{\infty} \frac{\beta_n}{\sinh(\gamma_n b_1)} \left[\frac{b_1}{\gamma_n} - \frac{1}{\gamma_n^2} \sinh(\gamma_n b_1) \right]$$

$$+ \frac{Ab_1^3}{3} + \frac{Cb_1^2}{2} \tag{5.6.7}$$

The moment impulse is positive (clockwise) sense about the base of the wall. Equation (5.6.5) is plotted figure 5.6.2. From the figure we can see that as μ increases from 0 to 1, $\frac{M_B}{\rho U_0 H^3}$ increases from 0 to the maximum moment impulse value which occurs at $\mu = 1.0$. The maximum total moment impulse value for different lengths of deck, $b_1 = 0.1$, $b_1 = 0.3$ and $b_1 = 0.5$ are approximately $0.243 \rho U_0 H^3$, $0.296 \rho U_0 H^3$ and $0.378 \rho U_0 H^3$ respectively.

From figure 5.6.2, we can see that the largest values of M_w and M_B (as well as M_D) occurs at $\mu = 1.0$. The maximum moment impulse on the wall is larger than the maximum moment impulses on the seabed or beneath the deck (b_1 increases 0.1 to 0.5 M_D increases by factor 20). This is total contrast with Cooker's model. Results for moment impulse on the wall, on the seabed and beneath the deck are given in figure 5.6.2. This is reasonable given that Cooker's model has $P = 0$ at $y = 0$ whilst we have a large value of P here and this gives a substantial moment.

b₁=0.1	b₁=0.5
Moment impulse on the wall	**Moment impulse on the wall**
Moment impulse on the seabed	**Moment impulse on the seabed**
Moment impulse beneath the deck	**Moment impulse beneath the deck**
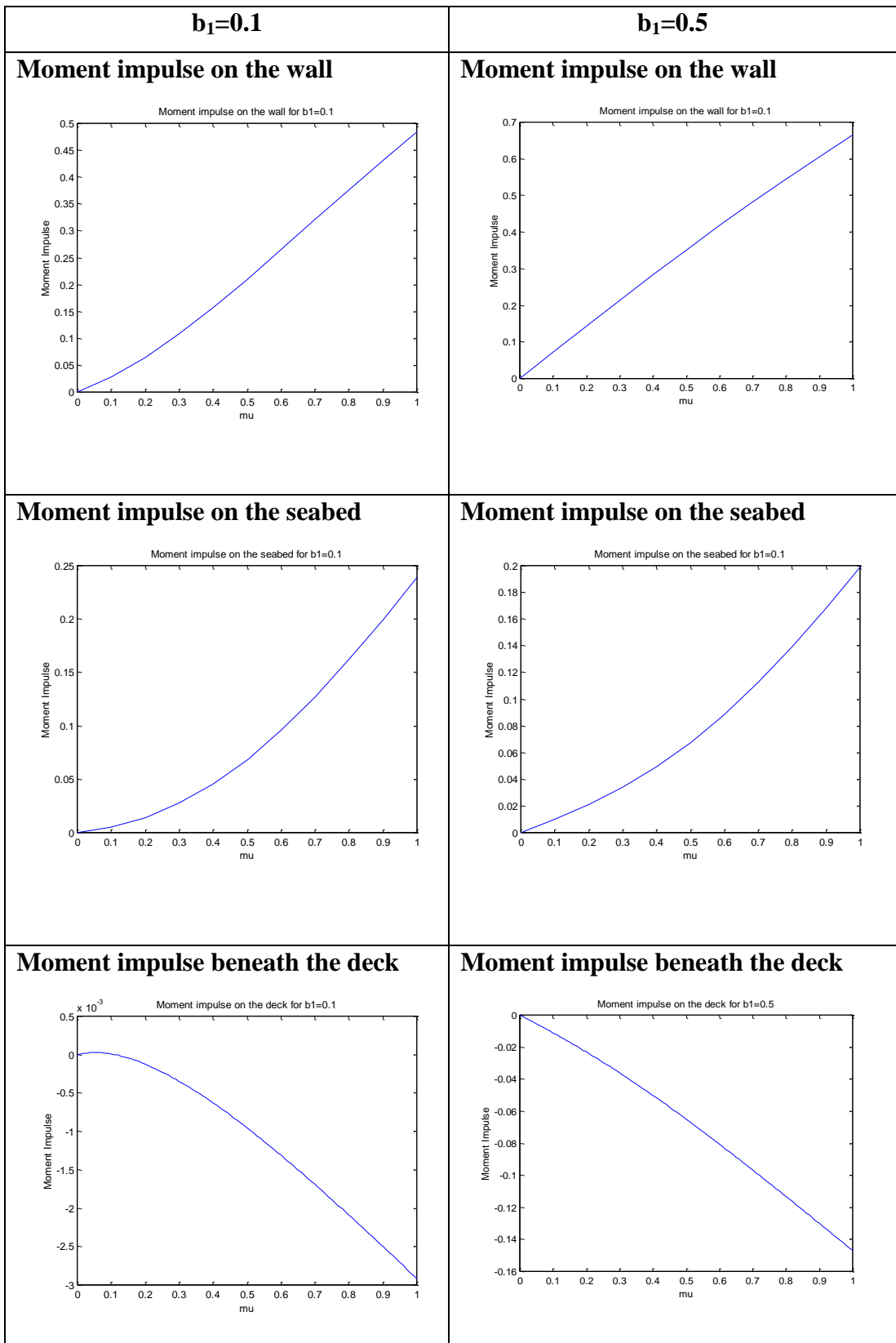
Figure 5.6.2: Moment impulse on the wall, seabed and beneath the deck for $b_1 = 0.1$ and $b_1 = 0.5$.

5.7 A Mathematical model for wave overtopping
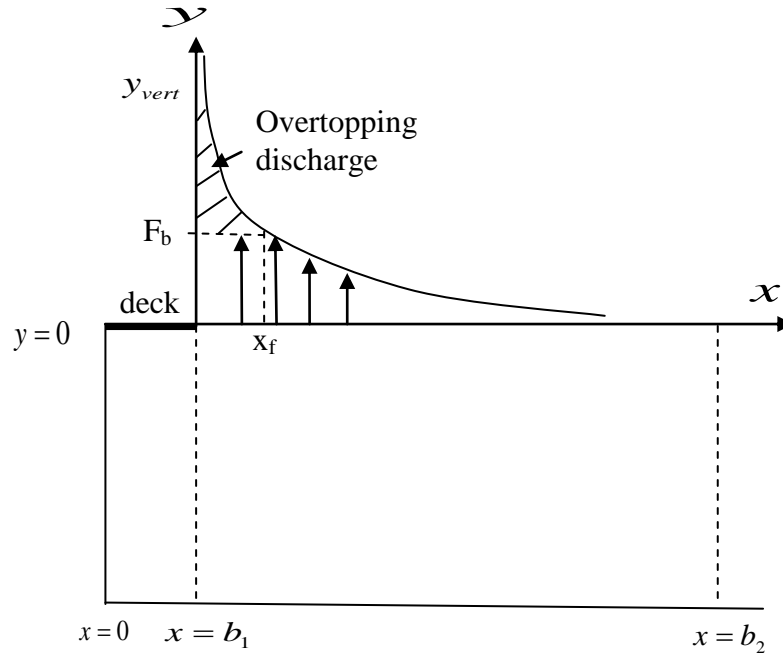
Figure 5.7.1: Overtopping definition sketch for deck.

As before in §2.7, we assume a free projectile model for overtopping. Since the initial upward velocities (before impact) are zero, the velocity afterwards is simply given by

$$v_y = \frac{\partial P_2}{\partial y} = \sum_{n=1}^{\infty} c_n \lambda_n \cos(\lambda_n y) \frac{\sinh(\lambda_n(x - b_2))}{\cosh(\lambda_n b_2)} \qquad (5.7.1)$$

So that the initial velocity upward at $y = 0$ gives

$$v_y = \sum_{n=1}^{\infty} c_n \lambda_n \frac{\sinh(\lambda_n(x - b_2))}{\cosh(\lambda_n b_2)} \qquad (5.7.2)$$

Hence the maximum height of jet is

$$y_{max} = \frac{1}{2} F_r \left(\sum_{n=1}^{\infty} c_n \lambda_n \frac{\sinh(\lambda_n(x - b_2))}{\cosh(\lambda_n b_2)} \right)^2 \qquad (5.7.3)$$

For freeboard, F_B we have

$$F_B = \frac{1}{2} F_r \left(\sum_{n=1}^{\infty} c_n \lambda_n \frac{\sinh(\lambda_n(x_f - b_2))}{\cosh(\lambda_n b_2)} \right)^2 \qquad (5.7.4)$$

135

So we can find F_B in terms of a parameter x_f, the distance at which F_B is achieved. Calculating the overtopping discharge, V

$$V = \int_0^{x_f} \left(y_{\max t} - F_b \right) dx$$

gives,

$$V = \int_0^{x_f} y_{\max} dx - x_f F_b \qquad (5.7.5)$$

Assuming shallow water theory and taking the impact velocity U_0 to be the wave speed $\sqrt{gH}$ gives $F_r = 1$. Plotting equation (5.7.5) by using MATLAB and comparing with Cooker's model, we get results as in figure 5.7.2. Given the assumption that particles in the jet move as free projectiles, the model will not be valid for very low freeboard since the pressure impulse gradients will be finite for the region above F_b and away from the edge of the deck. On the other hand, the pressure impulse gradient increases as we approaches the edge of the deck so the very large vertical velocities will give the assumed free projectile motion. At the deck edge itself, the velocity is singular, being locally similar to the flow around the end of a plate in unbounded fluid. This singularity is of square root form and is hence integrable. Of course, the truncated series expansions used here model this singular behaviour only rather crudely.

$b_1 = 0$	Deck ($b_1 = 0.1$)
$\mu = 0.1$	$\mu = 0.1$
$\mu = 0.5$	$\mu = 0.5$
$\mu = 1.0$	$\mu = 1.0$
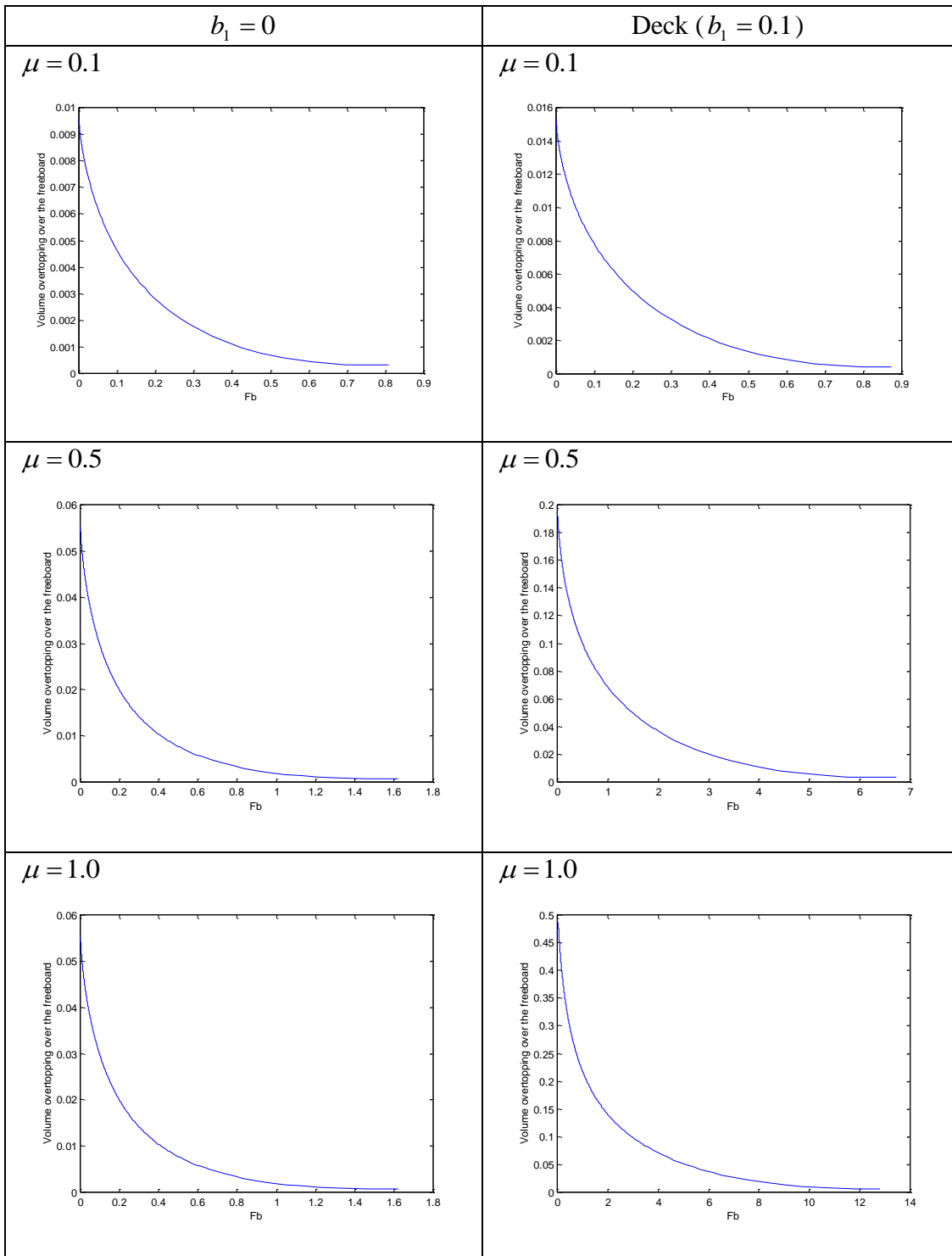
Figure 5.7.2: Overtopping discharge.

We can see that the larger the region of impact, the more volume of overtopping we have for any freeboard. We note that the seawall with a deck has a much greater volume of overtopping compared to a seawall without a deck. For instance, consider the case with, $H = 2m$, $\mu = 0.1$ and $F_b = 0.5$. The volume of overtopping, $V = 0.002H^2$ per impact, gives us

$0.002(2)^2 = 0.008m^2$ each wave impacts.

1 impact in 10 waves of 10 sec ~ 100 sec. This gives:

$V = 8 \times 10^{-5} m^3 s^{-1}$ per metre frontage.

$V \approx 0.08 ls^{-1}$ per metre frontage.

which is almost double compared to volume of overtopping when there is no deck i.e. $b_1 = 0$.

5.8   Conclusions

It is found that the maximum pressure impulse on the wall is greater as the length of the deck is increased. For the same length of deck, the pressure impulse is greater when the impact region is larger.

The total impulse for a seawall with a deck is greater than the total impulse for a vertical wall. When the length of deck increases, the total impulse increases. The total impulse on the seabed for a seawall with a deck is greater than that for the vertical wall. When the length of deck increases, the total impulse increases. The total impulse beneath the deck is greater when the length of the deck is bigger.

The moment impulse on the wall for a seawall with a deck is almost double that for a vertical wall. It increases when the length of the deck increases.

The moment impulse beneath the deck becomes larger when the length of the deck is bigger. The pressure of a deck increases the overtopping.

CHAPTER 6

IMPACT ON A DECK PROJECTING FROM A SEAWALL

6.1   Introduction

In this chapter we consider the same geometry as in the previous chapter, but the wave comes from below and impacts against the whole of the underside of a horizontal deck projecting from the wall. For this case, the boundary condition and the equations are slightly different. This problem of impact on a deck can be traced back to the study of wave impact on the underside of projecting surface i.e. the flat deck which is close to the mean water level, studied by Wood and Peregrine (1998). We calculate the pressure impulse when a rectangular wave hits a horizontal deck and total impulse beneath the deck for finite depth. The pressure impulse, $P,$ is used to model the effect of the wave impact. The purpose of this chapter is to derive the two-dimensional field for P throughout the fluid, solved by the previous mathematical modelling but with a different approach, and theoretically investigate the impulsive fluid force on the structures.

6.2   Literature review

Wood and Peregrine (1998) presented a theoretical model for the pressure impulse on the underside of a projecting surface. They calculated the impact pressures on a vertical wall and beneath the horizontal deck by using a pressure impulse approach.
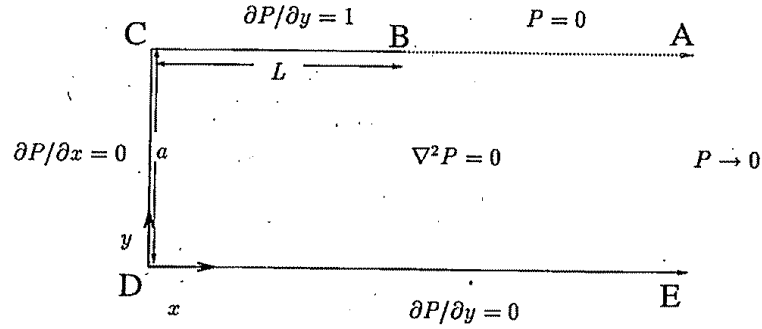
Figure 6.2.1: The boundary-value problem for pressure impulse. Image taken from Wood and Peregrine (1996) figure 1.

The wave is assumed to hit upward under a flat deck, which is at the mean water level and jutting out from a wall. The impact region is beneath the whole deck of length L with upward velocity V so that the boundary condition beneath the deck is $\partial P/\partial y = V$. Wood and Peregrine make the problem dimensionless by choosing units which gives $V = 1$. The vertical wall of height a for finite depth has boundary condition $\partial P/\partial x = 0$. Boundary conditions $P = 0$ are prescribed on the free surface at BA, $P \to 0$ as $x \to \infty$ and $\partial P/\partial y = 0$ on the sea floor. They considered two cases of water depth, finite and infinite depth and two cases of deck length, a finite and infinitely long deck. They solved this problem by considering the direct analogy of velocity potential of irrotational flow, see Faltinsen and Timokha (2009). Another solution using conformal mapping is also discussed in Wood and Peregrine (1996).

We are interested in finite depth and a finite deck length. By using conformal mapping, Wood and Peregrine map the original problem in the z plane in figure 6.2.1 to a complex plane $\varsigma = \xi + i\eta$. They solve Laplace's equations in the region by separation variables. The expression for the pressure impulse is given by:

$$P = \sum_n A_n e^{-\alpha_n \xi} \cos(\alpha_n \eta)$$ (6.2.1)

and

$$A_m = \frac{2}{\alpha_m a} \int_0^a \frac{1}{M} \frac{\sin(\pi\eta/a)\cos(\alpha_m\eta)}{\sqrt{b^2-1}} d\eta.$$ (6.2.2)

where α_n and M are defined as in Wood and Peregrine (1998). They evaluated (6.2.2) by using a NAG numerical routine and the results as shown in figures 6.2.2 and 6.2.3.
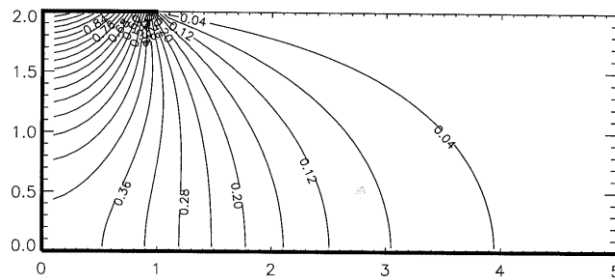
Figure 6.2.2: Pressure-impulse contour with $a = 2.0$. Total pressure impulse on the deck and wall respectively are 0.81 and 1.02. Image taken from Wood and Peregrine (1998) figure 6.
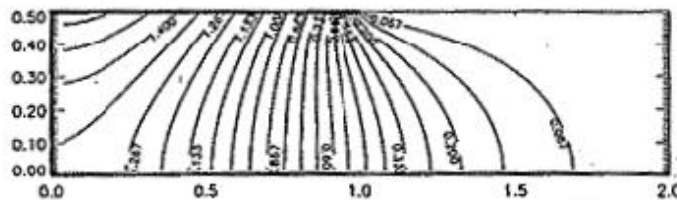
Figure 6.2.3: Pressure-impulse contour with $a = 0.5$. Total pressure impulse on the deck and wall respectively are 1.193 and 0.440. Image taken from Wood and Peregrine (1998) figure 8.

From the numerical solution they found that the impulse on the deck increased as the water depth decreased. Wood and Peregrine (1996) reported that the strong pressure gradient beneath the deck is near the seaward edge of the impact region and that causes a shearing stress on structures. The maximum pressure-impulse is at the landward end of the impact zone in the corner between the wall and deck.

6.3 Mathematical model

Figure 6.3.1 shows the fluid-structure system and the boundary conditions. The horizontal flat deck lies from $x = 0$ to $x = b_1$. The free surface beyond the deck is also taken to be flat, from $x = b_1$, and $x = b_2$. We make the problem dimensionless by choosing units for which water depth, $H = 1$. The seabed is horizontal. The fluid is assumed to be incompressible, inviscid and irrotational and the domain is defined by $0 \le x < \infty$, $-1 \le y \le 0$. The wave hits the whole deck in the upward direction. We will make comparison of the results with Wood and Peregrine (1996).
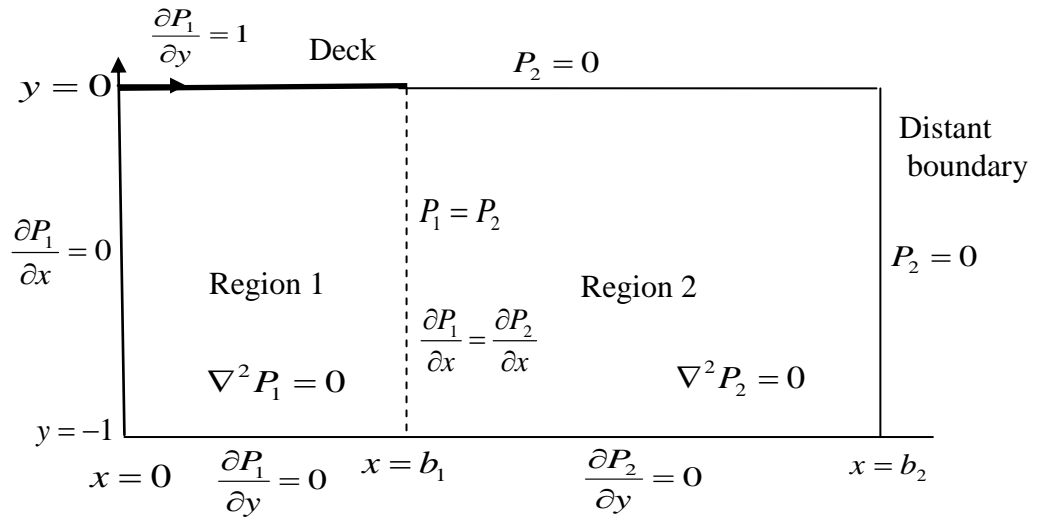
Figure 6.3.1: The dimensionless boundary-value problem for the pressure impulse for wave impact beneath a deck on the top of a seawall.

As in the previous chapter, we also work with dimensionless pressure impulse and we continue to use P as dimensionless pressure impulse, that scales with $\rho U_0 H$. Under the assumptions stated above, the formulations involve two equations from region 1 and region 2 and need to be matched at $x = b_1$.

The boundary conditions we have in this problem:

$$\frac{\partial P_1}{\partial y}(x,0) = 1 \qquad \text{for } x \in [0, b_1] \qquad (6.3.1)$$

$$\frac{\partial P_1}{\partial x}(0, y) = 0 \qquad \text{for } y \in [-1, 0] \qquad (6.3.2)$$

$$P_2(x,0) = 0, \qquad \text{for } x \in (b_1, b_2) \qquad (6.3.3)$$

$$P_2(b_2, y) = 0, \qquad \text{for } y \in [-1, 0] \qquad (6.3.4)$$

$$\frac{\partial P_1}{\partial y}(x,-1) = 0, \qquad \text{for } x \in [0, b_1] \qquad (6.3.5)$$

$$\frac{\partial P_2}{\partial y}(x,-1) = 0, \qquad \text{for } x \in (b_1, b_2] \qquad (6.3.6)$$

The pressure impulse equation in both regions satisfies Laplace's equation:

$$\nabla^2 P(x) = 0 \qquad (6.3.7)$$

We now solve using separation of variables method. For the inner region (region 1 in figure 6.3.1), the upper and bed boundary conditions are satisfied by the eigenfunction expansions:

$$P_1(x, y) = \sum_{n=1}^{\infty} \alpha_n \cos(\gamma_n y) \frac{\cosh(\gamma_n x)}{\cosh(\gamma_n b_1)} + \sum_{n=1}^{\infty} \beta_n \sin(\lambda_n y) \frac{\cosh(\lambda_n x)}{\cosh(\lambda_n b_1)} + A \qquad (6.3.8)$$

where $\qquad \gamma_n = n\pi$, $n \in (1,2,3\ldots, N)$

and $\qquad \lambda_n = \left(n - \frac{1}{2}\right)\pi$, $n = 1,2,3\ldots, N$.

for $\qquad -1 \le y \le 0,$ and $0 \le x \le b_1$

The Fourier coefficients α_n, β_n and secular term, A are to be found. For the outer region, the free surface, far field and seabed boundary conditions are satisfied by the eigenfunction expansions:

$$P_2(x, y, \mu) = \sum_{n=1}^{\infty} c_n \sin(\lambda_n y) \frac{\sinh(\lambda_n(x - b_2))}{\cosh(\lambda_n b_2)} \qquad (6.3.9)$$

143

where $\lambda_n = \left(n - \frac{1}{2}\right)\pi$, $n = 1,2,3\ldots, N$.

for $-1 \le y \le 0$, and $b_1 \le x \le b_2$

and c_n are Fourier coefficients to be found.

From equation (6.3.1) we have $\dfrac{\partial P_1}{\partial y} = 1$ at $y = 0$ and this gives us

$$\sum_{n=1}^{\infty} \beta_n \lambda_n \frac{\cosh(\lambda_n x)}{\cosh(\lambda_n b_1)} = 1 \tag{6.3.10}$$

At the matching region $x = b_1$ for $-1 \le y \le 0$, the pressure impulse is continuous across this boundary so that

$$P_1 = P_2 \tag{6.3.11}$$

and this gives us

$$\sum_{n=1}^{\infty} \alpha_n \cos(\gamma_n y) + \sum_{n=1}^{\infty} \beta_n \sin(\lambda_n y) + A = \sum_{n=1}^{\infty} c_n \sin(\lambda_n y) \frac{\sinh(\lambda_n (b_1 - b_2))}{\cosh(\lambda_n b_2)} \tag{6.3.12}$$

Multiplying (6.3.12) by the basis functions 1 and integrating from $y = -1$ to 0 gives the secular term

$$A = \sum_{n=1}^{\infty} \frac{\beta_n}{\lambda_n} - \sum_{n=1}^{\infty} \frac{c_n}{\lambda_n} \frac{\sinh(\lambda_n (b_1 - b_2))}{\cosh(\lambda_n b_2)} \tag{6.3.13}$$

Substituting (6.3.13) into (6.3.12) and simplifying gives

$$\sum_{n=1}^{\infty} \alpha_n \cos(\gamma_n y) + \sum_{n=1}^{\infty} \beta_n \left[\sin(\lambda_n y) + \frac{1}{\lambda_n}\right] - \sum_{n=1}^{\infty} c_n \frac{\sinh(\lambda_n (b_1 - b_2))}{\cosh(\lambda_n b_2)}\left[\sin(\lambda_n y) + \frac{1}{\lambda_n}\right] = 0 \tag{6.3.14}$$

Matching the horizontal derivatives on each side of the interface at $x = b_1$ for $-1 \le y \le 0$ gives

$$\frac{\partial P_1}{\partial x} = \frac{\partial P_2}{\partial x} \tag{6.3.15}$$

Differentiating equation (6.3.8) and (6.3.9) gives

$$\sum_{n=1}^{\infty} \alpha_n \gamma_n \cos(\gamma_n y) \tanh(\gamma_n b_1) + \sum_{n=1}^{\infty} \beta_n \lambda_n \sin(\lambda_n y) \tanh(\lambda_n b_1)$$

$$-\sum_{n=1}^{\infty} c_n \lambda_n \sin(\lambda_n y) \frac{\cosh(\lambda_n (b_1 - b_2))}{\cosh(\lambda_n b_2)} = 0 \tag{6.3.16}$$

We solve the truncated forms of equations (6.3.10), (6.3.14) and (6.3.16) by finding the three sets of unknown Fourier coefficients (α_i, β_i, c_i) $i = 1,2,3,\cdots,N$ and evaluate the truncated series to calculate the pressure impulse. The system of equations can be simplified as figure 6.3.2. We now have an expression for the pressure impulse distribution throughout the fluid domain. This can be used to understand what occurs to the pressures and the change in the velocity field during impact by calculating the pressure impulse, impulses and moments. The areas of most interest are on the wall, along the seabed and beneath the deck. All these results converge by $N = 40$ using the criteria established in §2.8. Hence we can expect the results to be accurate to within 0.1% in general.

$$\left(\begin{array}{ccccccc}
\begin{array}{c}(zero)\\ 0\end{array} & \vdots & \begin{array}{c}(diagonal)\\ \dfrac{\lambda_n\cosh(\lambda_n y)}{\cosh(\lambda_n b_1)}\end{array} & \vdots & \begin{array}{c}(zero)\\ 0\end{array} & & \\[2em]
\cdots \quad \cdots \quad \cdots & \vdots & \cdots & \vdots & \cdots & \cdots & \\[1em]
\begin{array}{c}(diagonal)\\ \cos(\gamma_n y)\end{array} & \vdots & \begin{array}{c}(full)\\ \sin(\lambda_n y)+\dfrac{1}{\lambda_n}\end{array} & \vdots & \begin{array}{c}(diagonal)\\ -\dfrac{\sinh(\lambda_n(b_1-b_2))}{\cosh(\lambda_n b1)}\left[\dfrac{1}{\lambda_n}+\sin(\lambda_n y)\right]\end{array} & & \\[2em]
\cdots \quad \cdots \quad \cdots & \vdots & \cdots & \vdots & \cdots & \cdots & \\[1em]
\begin{array}{c}(full)\\ \gamma_n\cos(\gamma_n y)\tanh(\gamma_n b_1)\end{array} & \vdots & \begin{array}{c}(full)\\ \lambda_n\cos(\lambda_n y)\tanh(\lambda_n b_1)\end{array} & \vdots\;\ddots & \begin{array}{c}(full)\\ -\lambda_n\sin(\lambda_n y)\dfrac{\cosh(\lambda_n(b_1-b_2))}{\cosh(\lambda_n b_2)}\end{array} & & \ddots
\end{array}\right)
\left(\begin{array}{c}\alpha_1\\ \vdots\\ \alpha_N\\ \cdots\\ \beta_1\\ \vdots\\ \beta_N\\ \cdots\\ c_1\\ \vdots\\ c_N\end{array}\right)
=
\left(\begin{array}{c}1\\ \vdots\\ 1\\ \cdots\\ 0\\ \cdots\\ 0\end{array}\right)$$

Figure 6.3.2: Matrix system of equations. The first M rows come from (6.3.10), the next from (6.3.14) and the last from (6.3.16).

6.4   Pressure Impulse

Figures 6.4.1, 6.4.2, and 6.4.3 show in perspective plots the results for pressure impulse beneath the deck for different length of deck, $b_1 = 0.1$, $b_1 = 0.3$ and $b_1 = 0.5$ respectively. From the figures we can see that at the point of peak for pressure, the graphs become more rounded as the length of the deck increases. In figure 6.4.4, figure 6.4.5, and figure 6.4.6 show the contour plot for each profile. We note the differing contours intervals, and the increasing pressure impulse on the deck as the length of the deck b_1 is increased.
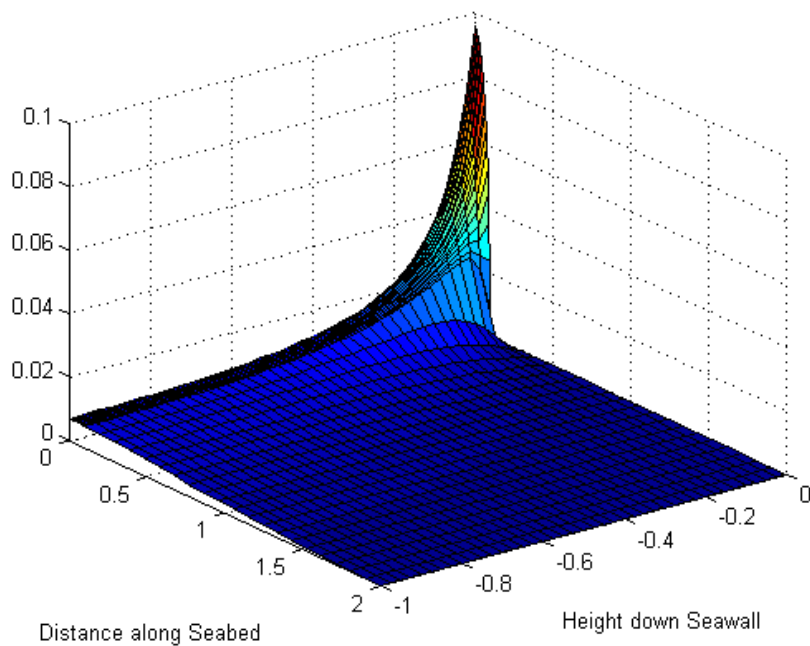
Figure 6.4.1: Pressure impulse profile for $b_1 = 0.1$.
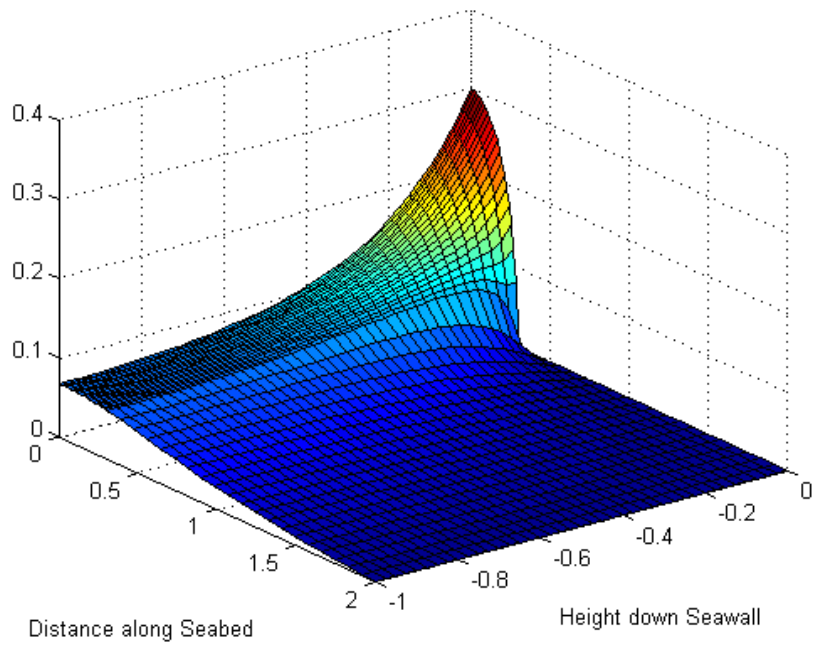
Figure 6.4.2: Pressure impulse profile for $b_1 = 0.3$.
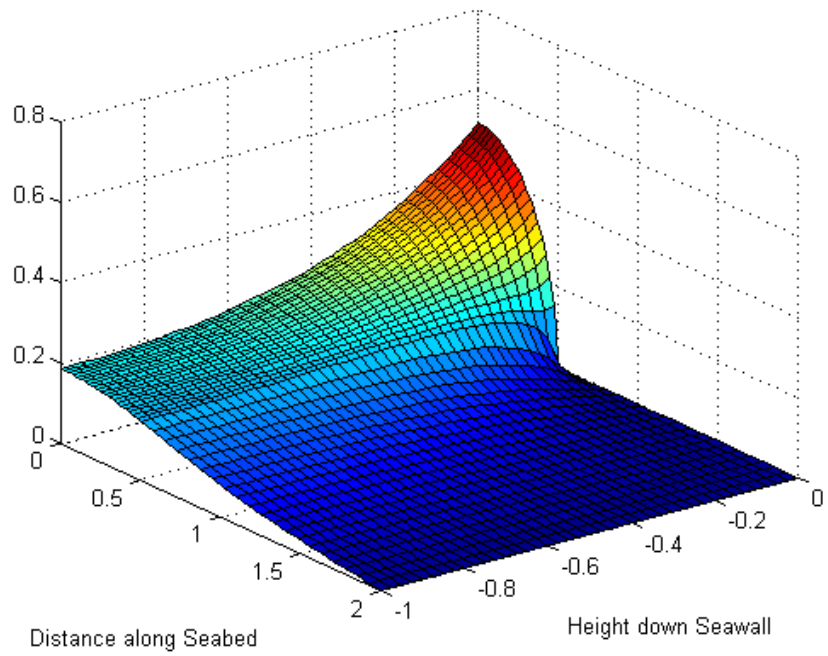
Figure 6.4.3: Pressure impulse profile for $b_1 = 0.5$.
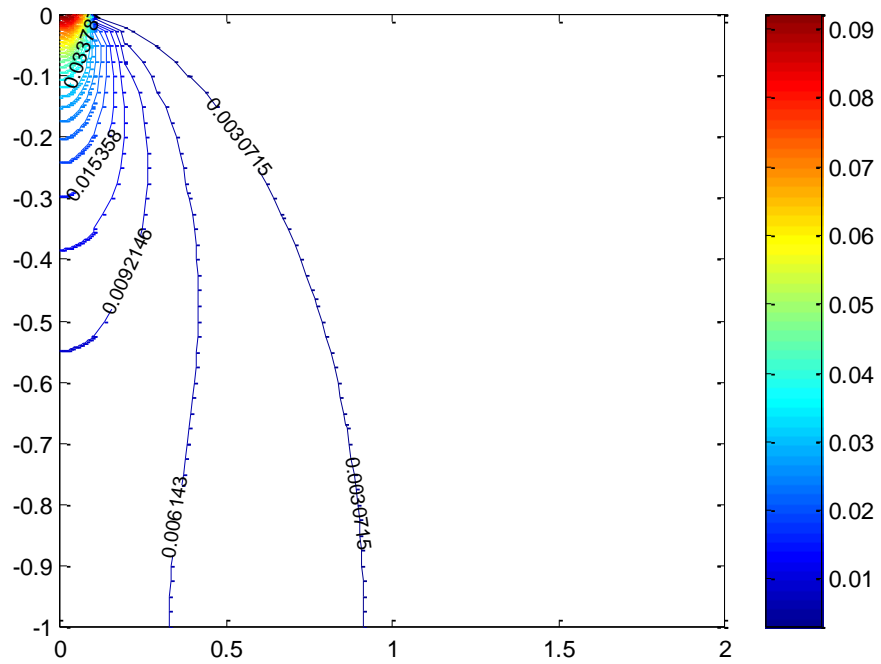
Figure 6.4.4 : Plot showing the pressure impulse on the deck generated by deck problem formulation with $b_1 = 0.1$. The maximum pressure impulse is 0.0952 $\rho U_0 H$ and occurs $y = 0$ and $x = 0$.
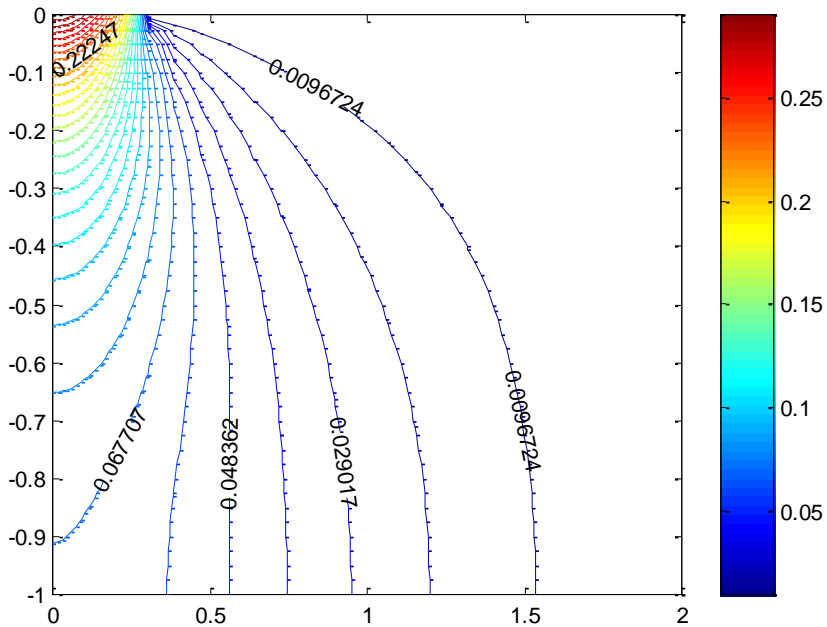
Figure 6.4.5 : Plot showing the pressure impulse on the deck generated by deck problem formulation with $b_1 = 0.3$. The maximum pressure impulse is 0.2997 $\rho U_0 H$ and occurs $y = 0$ and $x = 0.0075$.
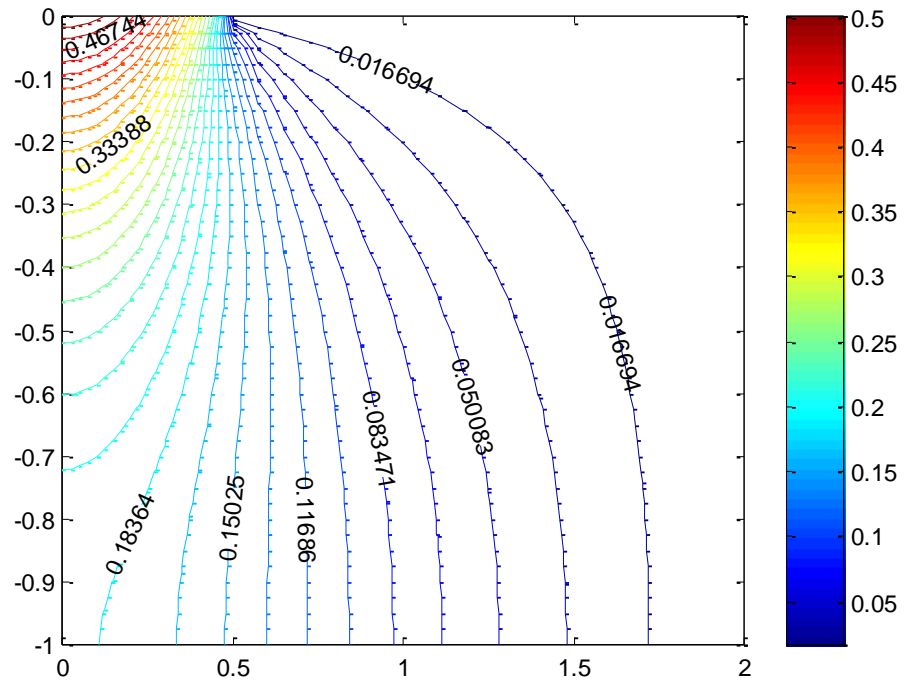
Figure 6.4.6 : Plot showing the pressure impulse on the deck generated by deck problem formulation with $b_1 = 0.5$. The maximum pressure impulse is 0.5175 $\rho U_0 H$ and occurs $y = 0$ and $x = 0$.

We can conclude that when the deck's length to depth ratio is increased, the pressure impulse will increase. The same trend was described by Wood and Peregrine (1996).

Pressure impulse on the wall, seabed and deck
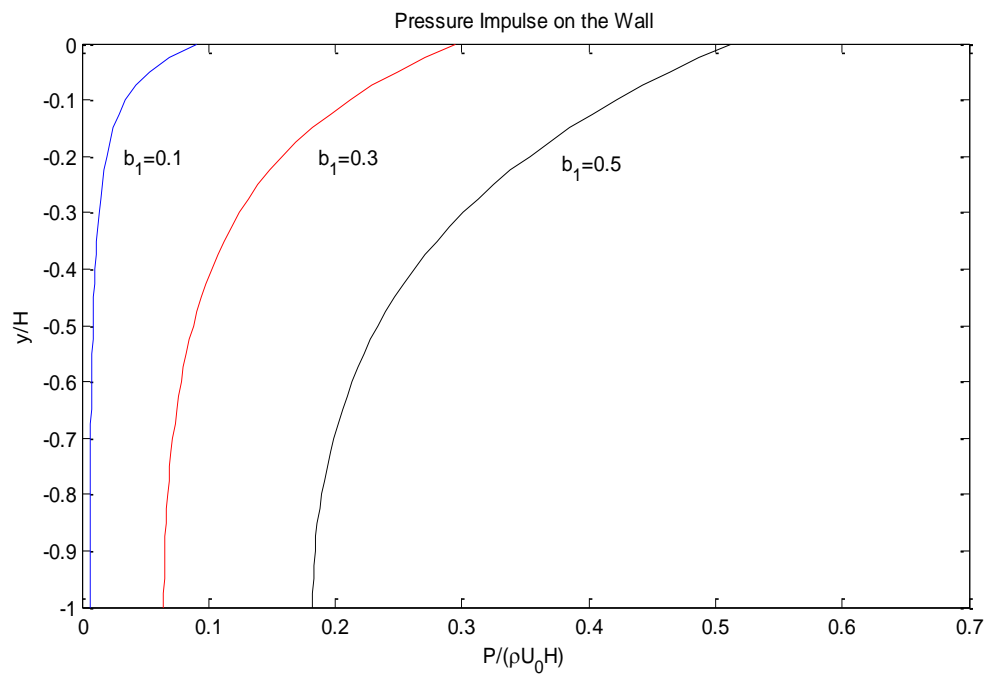
Figure 6.4.7: Plot showing the pressure impulse on the wall generated by the deck problem formulation for varying b_1. The maximum pressure impulse is $0.5175 \, \rho U_0 H$.
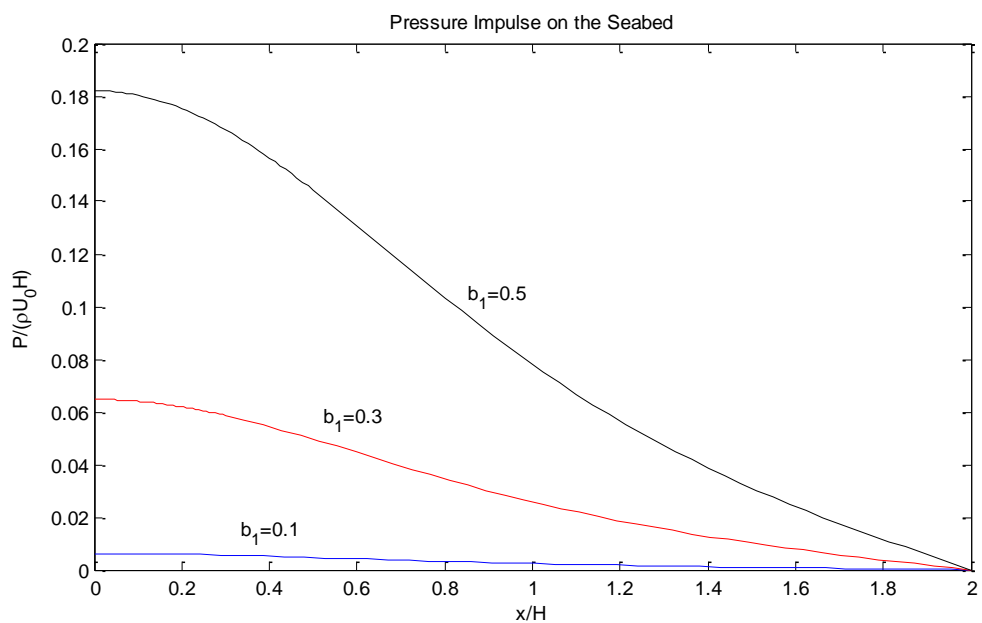
Figure 6.4.8: Plot showing the pressure impulse on the wall generated by the deck problem formulation for varying b_1. The maximum pressure impulse is $0.182 \, \rho U_0 H$.
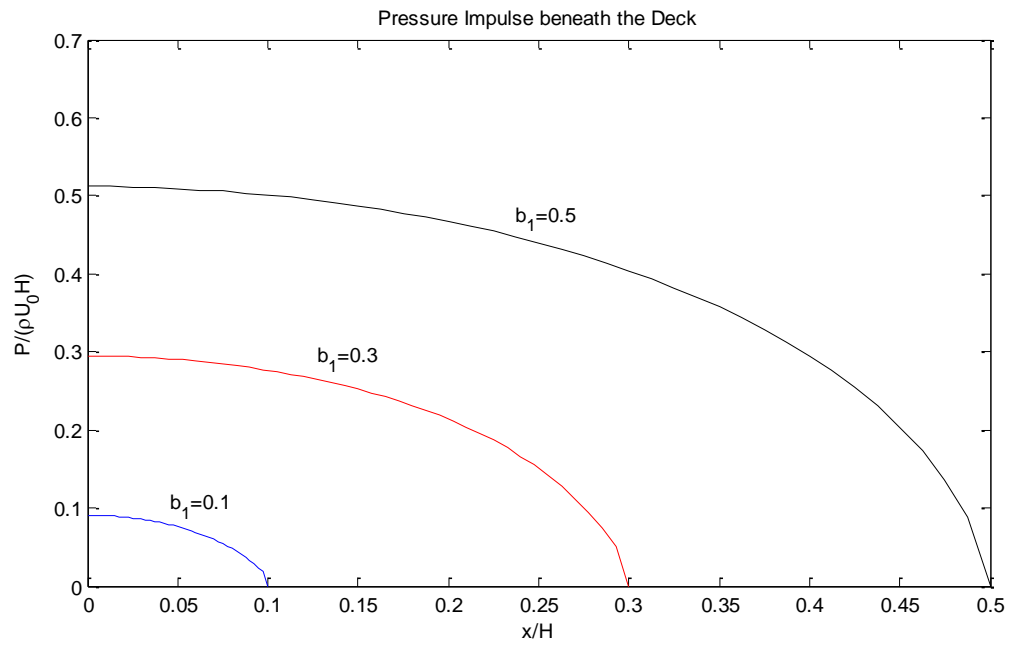
Figure 6.4.9: Plot showing the pressure impulse on the wall generated by impact under the deck for varying b_1. The maximum pressure impulse is $0.520\,\rho U_0 H$.

6.5 Total impulse on the wall, seabed and on the deck

We take the direction of total impulse as the same as in Chapter 5 as follows
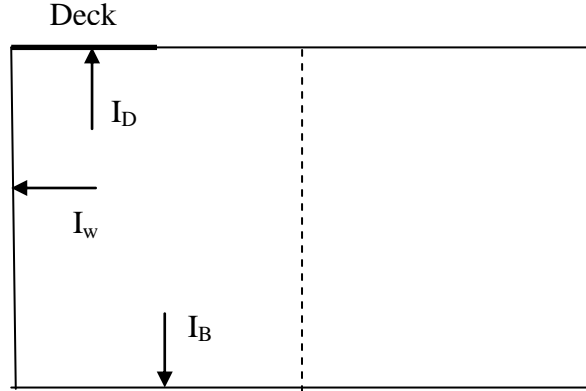
Figure 6.5.1: Total impulse definitions for deck.

The total impulse on the wall, I_w given by

$$I_w = \int_{-1}^{0} P_1(0, y) \ dy \tag{6.5.1}$$

Integrating gives:

$$I_w = -\sum_{n=1}^{\infty} \frac{\beta_n}{\lambda_n \cosh(\lambda_n b_1)} + A \tag{6.5.2}$$

The total impulse on the seabed, I_B given by

$$I_B = \int_{0}^{b_1} P_1(x, -1) \ dx + \int_{b_1}^{b_2} P_2(x, -1) \ dx \tag{6.5.3}$$

Integrating gives:

$$I_B = \sum_{n=1}^{\infty} \frac{\alpha_n}{\gamma_n} \cos(-\gamma_n) \tanh(\gamma_n b_1) + \sum_{n=1}^{\infty} \frac{\beta_n}{\lambda_n} \sin(-\lambda_n) \tanh(\lambda_n b_1) +$$

$$\sum_{n=1}^{\infty} \frac{c_n}{\lambda_n} \frac{\sin(-\lambda_n)}{\cosh(\lambda_n b_2)} [1 - \cosh(\lambda_n (b_1 - b_2))] + A b_1$$

$$\tag{6.5.4}$$

The total impulse on the deck, I_D given by

$$I_D = \int_0^{b_1} P_1(x,0) \ dx \tag{6.5.5}$$

Integrating gives:

$$I_D = \sum_{n=1}^{\infty} \frac{\alpha_n}{\gamma_n} \tanh(\gamma_n b_1) + A b_1 \tag{6.5.6}$$

Table 6.5.1: Total impulse for varying length of deck

Length of the deck	Total impulse on the wall	Total impulse on the seabed	Total impulse beneath the deck
$b_1 = 0.1$	0.0171	0.0063	0.0073
$b_1 = 0.3$	0.1172	0.0616	0.0698
$b_1 = 0.5$	0.2742	0.1772	0.2014

We can see that the total impulse on the seawall is greater than total impulse on the deck. The total impulse increases when length of the deck increases.

6.6 Moment impulse on the wall, seabed, and on the deck

We calculate the moment impulse on the wall, on the seabed and on the deck. We take the direction of the moment impulse as in figure 5.6.1

Deck

$+M_D$

$+M_w$

$+M_B$
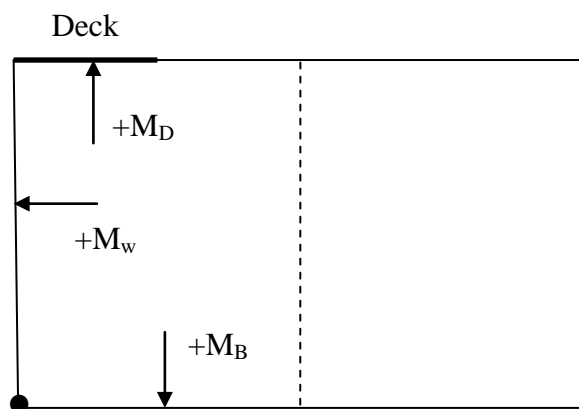
Figure 6.6.1: Moment impulse diagram for the deck.

154

The moment on the wall given by

$$M_w = \int_{-1}^{0} (1+y)P_1(0,y) \ dy \tag{6.6.1}$$

Integrating gives:

$$M_w = \sum_{n=1}^{\infty} \frac{\alpha_n}{\lambda_n \cosh(\gamma_n b_1)} \left[\frac{1}{\gamma_n^2} - \frac{1}{\gamma_n^2} \cos(-\gamma_n) \right]$$

$$+ \sum_{n=1}^{\infty} \frac{\beta_n}{\lambda_n \cosh(\gamma_n b_1)} \left[-\frac{1}{\lambda_n} - \frac{1}{\lambda_n^2} \sin(-\lambda_n) \right] + \frac{A}{2} \tag{6.6.2}$$

The moment on the seabed given by

$$M_b = \int_{0}^{b_1} xP_1(x,-1) \ dx + \int_{b_1}^{b_2} xP_2(x,-1) \ dx \tag{6.6.3}$$

Integrating gives:

$$M_b = \sum_{n=1}^{\infty} \alpha_n \frac{\cos(-\gamma_n)}{\cosh(\gamma_n b_1)} \left[\frac{b_1}{\gamma_n} \sinh(\gamma_n b_1) - \frac{1}{\gamma_n^2} \cosh(\gamma_n b_1) + \frac{1}{\gamma_n^2} \right]$$

$$+ \sum_{n=1}^{\infty} \beta_n \frac{\sin(-\lambda_n)}{\cosh(\lambda_n b_1)} \left[\frac{b_1}{\lambda_n} \sinh(\lambda_n b_1) - \frac{1}{\lambda_n^2} \cosh(\lambda_n b_1) + \frac{1}{\lambda_n^2} \right]$$

$$+ \sum_{n=1}^{\infty} c_n \frac{\sin(-\lambda_n)}{\cosh(\lambda_n b_2)} \left[\frac{b_2}{\lambda_n} - \frac{b_1}{\lambda_n} \cosh(\lambda_n(b_1 - b_2)) + \frac{1}{\lambda_n^2} \sinh(\lambda_n(b_1 - b_2)) \right]$$

$$+ \frac{Ab_1^2}{2} \tag{6.6.4}$$

The moment on the deck given by

$$M_d = \int_{0}^{b_1} xP_1(x,0) \ dx \tag{6.6.5}$$

Integrating gives:

$$M_d = \sum_{n=1}^{\infty} \frac{\alpha_n}{\cosh(\gamma_n b_1)} \left[\frac{b_1}{\gamma_n} \sinh(\gamma_n b_1) - \frac{1}{\gamma_n^2} \cosh(\gamma_n b_1) + \frac{1}{\gamma_n^2} \right] + \frac{Ab_1^2}{2} \tag{6.6.6}$$

Table 6.6.1: Moment impulse for varying length of deck

Length of the deck	Moment impulse on the wall	Moment impulse on the seabed	Moment impulse beneath the deck
$b_1=0.1$	0.2611	0.0037	0.0003
$b_1=0.3$	0.4232	0.0364	0.0089
$b_1=0.5$	0.4938	0.1070	0.0424

From table 6.6.1 we can see that the moment impulse on the seawall is much larger than moment impulse on the seabed and beneath the deck.

Comparison of results

We now can compare our result with Wood and Peregrine (1997). We consider for deck length of deck is 0.5 and water depth is 1.0.

Table 6.6.2: Results comparison.

	Wood and Peregrine	Present results
Deck length	$L = 0.5$	$b_1 = 0.5$
Water depth	$a = 1.0$	$H = 1.0$
Total Impulse on the deck	0.3000 (approximately)	0.2014
Total Impulse on the wall	0.2750 (approximately)	0.2742
Maximum pressure impulse	0.5200 (approximately)	0.5175
Dimensionless unit	$\rho V H$	$\rho U_0 H$

We can see that, the results have a good agreement with Wood and Peregrine (1996).

6.7   Conclusions

From the numerical solution we found that the pressure impulse on the deck increases when the length of deck increases. There is a strong pressure gradient beneath the deck is near the seaward edge. Similar results were found in Wood and Peregrine (1996) which studied the pressure impulse beneath the deck for different depth of water for the same length of deck. We also agree that the maximum pressure impulse is at the landward end of the impact zone.

CHAPTER 7

WAVE IMPACTS ON STRUCTURES WITH BAFFLES

7.1   Introduction

In this chapter we consider another model of violent fluid motion applied to wave impact against a vertical structure. Again, we model a rectangular wave but with a baffle between the two regions. The purpose of this chapter is to quantify the effect of having a baffle between two regions when a wave breaks against the baffle and on the wall when we have a vertical baffle on the seabed. The theory of pressure impulse on the baffle, to the author knowledge, has not yet been investigated.

We consider four classes of problem:

    (i)   A vertical baffle at free surface; (Problem 1)

    (ii)   A vertical baffle in front of a wall; (Problem 2)

    (iii)   A vertical baffle at a deck in front of a seawall; (Problem 3)

    (iv)   A vertical baffle on the seabed in front of a wall. (Problem 4)

For this chapter, we solved the problems by using a basis function method. As a practical application, (ii) and (iii) could model an oscillating water column wave energy device with the turbine valve open/closed respectively, whilst (iii) and (iv) are also pertinent to sloshing impacts in liquefied natural gas (LNG) carriers and other liquid-transport tanks. We will compare our results with basic model by Cooker (1990). The total impulse and moment impulses are also calculated for each problem and examples for using the results are given at the end of this chapter.

7.2   Literature Review

A fluid-structure interaction phenomenon is an important consideration in several engineering fields. When a tank truck is braking, turning or in collision, the liquid in the partially-filled tank will slosh or even splash due to the oscillating of the unrestrained free surface of the liquid. This kind of phenomenon is also important in marine transport. For example, during the marine transportation of the liquefied natural gas (LNG), sloshing inside the LNG tank is one of the most important concerns of design. In such circumstances, an accident may result from wandering, capsize or from prolonging the stopping distance. The study of the pressure impulse on the baffles and walls can provide data on the impacts acting on the tank and baffles which can be used for simulating handling stability, especially for planes, rockets and spacecraft.

Many general and basic problems of liquid sloshing have been studied. Most studies involved simple tank structures, but the inner structures of liquefied natural gas tank carriers are more complex. Eswaran et al. (2009) analyzed sloshing waves for baffled and un-baffled tanks and the study shows that the wave pressures on the walls decrease with baffles compare with the one without baffles. Armenio and Rocca (1996) presented an analysis of sloshing of water in rectangular open tanks by using two mathematical models: the Reynolds Averaged Navier-Stokes Equations (RANSE) and the Shallow Water Equations (SWE). They found that the presence of a vertical baffle at the middle of the tank dramatically reduced the sloshing-induced wave loads on the vertical wall compared to the unbaffled configuration. Liu and Lin (2009) investigated the effect of the baffle in three-dimensional (3D) liquid tank by using spatially-averaged Navier-Stokes equations and solving a numerical model. They found that a vertical baffle is a

159

more effective tool in reducing the impulse pressure compared to a horizontal baffle. They first investigated the two-dimensional (2D) liquid sloshing with baffles and without baffles. The numerical results were compared with others results in the literature and showed favourable agreement. Akyildiz and Ünal (2005) conducted a series of experiments to obtain pressure variations on baffled and unbaffled liquid sloshing tanks.

All of these studies are concerned with wave generation. This is important because conditions can then arise for impacts and extremely high pressures of short duration. The difference of our studies from other researchers is that we have distant boundary conditions on the right-hand region. In this chapter, mathematical modelling of wave impact on a baffle in different conditions is introduced using the pressure impulse theory. The influence of the depth of baffle penetration, and the size of the impact region is studied.

To investigate these effects, vertical baffles are added to tanks reaching down from the ceiling or up from the floor of the tank. Horizontal baffles may also be added to the side walls. The idea is also to detune the natural frequencies from the range of forcing frequencies, for example the frequencies of ocean waves in a rolling or pitching ship (Faltinsen and Timokha, 2009). However, adding baffles does not prevent sloshing or the possibility of wave impact on the baffle. This is the subject of this chapter.

7.3   Mathematical Modelling of problems 1, 2, 3 and 4

We now consider a rectangular model with wave impact on a fraction μ of the baffle. Note that we have a baffle of height H_b, the depth of penetration. On the right hand side of the baffle for all four problems we have the free surface at $y = 0$. The pressure impulse P satisfies Laplace's equation throughout the fluid and is zero on the free surface. Since the wave comes from the right, the normal derivative of P at the back of the baffle is zero.

7.3.1 A vertical baffle at free surface (problem 1)

Figure 7.3.1: The dimensionless boundary-value problem for the pressure impulse for wave impact on a baffle.

The parameters of this situation are:

H_b = Height of baffle from the free surface

b_1 = size of the first region from the baffle

b_2 =size of the second region from the baffle

μ = parameter of impact region $0 \le y \le \mu H_b$

The fluid domain defined by $b_1 \le x < b_2$, with $b_1 < 0$ and $-1 \le y \le 0$. The boundary-value problem for $P(x, y)$ is then

$$\nabla^2 P = 0 \text{ everywhere in the fluid} \tag{7.3.1}$$

$$P_1(x,0) = 0, \qquad \text{for } x \in (b_1,0) \tag{7.3.2}$$

$$P_1(b_1, y) = 0, \qquad \text{for } y \in (-1,0) \tag{7.3.3}$$

$$P_2(x,0) = 0, \qquad \text{for } x \in (0,b_2) \tag{7.3.4}$$

$$P_2(b_2, y) = 0, \qquad \text{for } y \in [-1,0] \tag{7.3.5}$$

$$\frac{\partial P_1}{\partial y}(x,-1) = 0, \qquad \text{for } x \in [b_1,0] \tag{7.3.6}$$

$$\frac{\partial P_2}{\partial y}(x,-1)=0, \quad \text{for } x \in (0,b_2] \tag{7.3.7}$$

At $x=0$ we have to apply matching/ baffle conditions.

- $\dfrac{\partial P_1}{\partial x}(0,y)=0$ \hspace{2cm} for $y \in (-H_b,0]$ \hfill (7.3.8)

- $\dfrac{\partial P_2}{\partial x}(0,y)=\begin{cases} -1 & \text{for } y \in (-\mu,0) \\ 0 & \text{for } y \in (-H_b,-\mu) \\ \partial P_1/\partial x & \text{for } y \in (-1,-H_b) \end{cases}$ \hfill (7.3.9)

- $P_1 = P_2$ \hspace{3cm} for $y \in (-1,H_b)$ \hfill (7.3.10)

as shown in figure 7.3.1. The left, upper and bed boundary conditions are satisfied by the eigenfunction expansion:

$$P_1(x,y)=\sum_{n=1}^{\infty}\alpha_n \sin(\lambda_n y)\frac{\sinh(\lambda_n(x-b_1))}{\cosh(\lambda_n b_1)} \tag{7.3.11}$$

where $\qquad \lambda_n = \left(n-\tfrac{1}{2}\right)\pi$, $n \in (1,2,3\ldots,N)$

for $\qquad -1 \le y \le 0$, and $b_1 \le x \le 0$

and the solution which satisfies the boundary conditions in region 2 is given by:

$$P_2(x,y)=\sum_{n=1}^{\infty}\beta_n \sin(\lambda_n y)\frac{\sinh(\lambda_n(x-b_2))}{\cosh(\lambda_n b_2)} \tag{7.3.12}$$

where $\qquad \lambda_n = \left(n-\tfrac{1}{2}\right)\pi$, $n \in (1,2,3\ldots,N)$

for $\qquad -1 \le y \le 0$, and $0 \le x \le b_2$

Applying $\displaystyle\int_{-H_b}^{0}\ldots\sin(\lambda_m y)dy$, $m=1,2,\ldots,M$ to equation (7.3.8) and integrating gives:

$$\sum_{n=1}^{\infty}\alpha_n\lambda_n\int_{-H_b}^{0}\sin(\lambda_n y)\sin(\lambda_m y)dy = 0 \qquad (7.3.13)$$

Applying $\displaystyle\int_{-1}^{0}\ldots\sin(\lambda_m y)dy$, $m=1,2,\ldots,M$ to equation (7.3.9) and integrating gives:

$$-\sum_{n=1}^{\infty}\alpha_n\lambda_n\int_{-1}^{-H_b}\sin(\lambda_n y)\sin(\lambda_m y)dy + \sum_{n=1}^{\infty}\beta_n\lambda_n\int_{-1}^{0}\sin(\lambda_n y)\sin(\lambda_m y)dy = \frac{1}{\lambda_m}\left[1-\cos(-\mu\lambda_m)\right]$$

$$(7.3.14)$$

The second integral is simply $\dfrac{\delta_{m,n}}{2}$ by orthogonality.

Applying $\displaystyle\int_{-1}^{-H_b}\ldots\sin(\lambda_m y)dy$, $m=1,2,\ldots,M$ to equation (7.3.10) and integrating gives:

$$-\sum_{n=1}^{\infty}\alpha_n\tanh(\lambda_n b_1)\int_{-1}^{-H_b}\sin(\lambda_n y)\sin(\lambda_m y)dy + \sum_{n=1}^{\infty}\beta_n\tanh(\lambda_n b_2)\int_{-1}^{-H_b}\sin(\lambda_n y)\sin(\lambda_m y)dy = 0$$

$$(7.3.15)$$

These three equations, are truncated at $n=N$ giving a system of equations $3M\times 2N$ as in figure 7.3.2. We then choose $N=\dfrac{3M}{2}$ to make the system square. We have two sets of unknown Fourier coefficients (α_i,β_i) $i=1,2,3,\ldots,N$ to be found so that we can calculate the pressure impulse for this problem. This was done by using MATLAB.

$$
\begin{pmatrix}
 & & \vdots & \dfrac{\lambda_j}{2}\psi_2 & & \\
-\lambda_j\psi_1 & & \vdots & & \ddots & \\
(\text{full matrix}) & & \vdots & (\text{diagonal matrix}) & \dfrac{\lambda_j}{2}\psi_2 & \\
\cdots & \cdots & \cdots \;\vdots\; \cdots & \cdots & \cdots & \cdots \\
 & & \vdots & & & \\
\lambda_j\psi_3 & & \vdots & 0 & & \\
(\text{full matrix}) & & \vdots & (\text{zero matrix}) & & \\
\cdots & \cdots & \cdots \;\vdots\; \cdots & \cdots & \cdots & \cdots \\
 & & \vdots & & & \\
-\tanh(\lambda_j b_1)\psi_1 & & \vdots & \tanh(\lambda_j b_2)\psi_1 & & \\
(\text{full matrix}) & & \vdots & (\text{full matrix}) & &
\end{pmatrix}
\begin{pmatrix}
\alpha_1 \\ \vdots \\ \alpha_N \\ \cdots \\ \beta_1 \\ \vdots \\ \beta_N
\end{pmatrix}
=
\begin{pmatrix}
\dfrac{1}{\lambda_i}(1-\cos(\lambda_i\mu)) \\
\dfrac{1}{\lambda_N}(1-\cos(\lambda_i\mu)) \\
\cdots \\
0 \\
\cdots \\
0
\end{pmatrix}
$$

Figure 7.3.2 : Matrix system of equations for problem 1. The first *M* rows come from (7.3.14), the next from (7.3.13) and the last from (7.3.15). The functions $\psi_1 \ldots \psi_3$ are the integrals in equations (7.3.13) to (7.3.15).
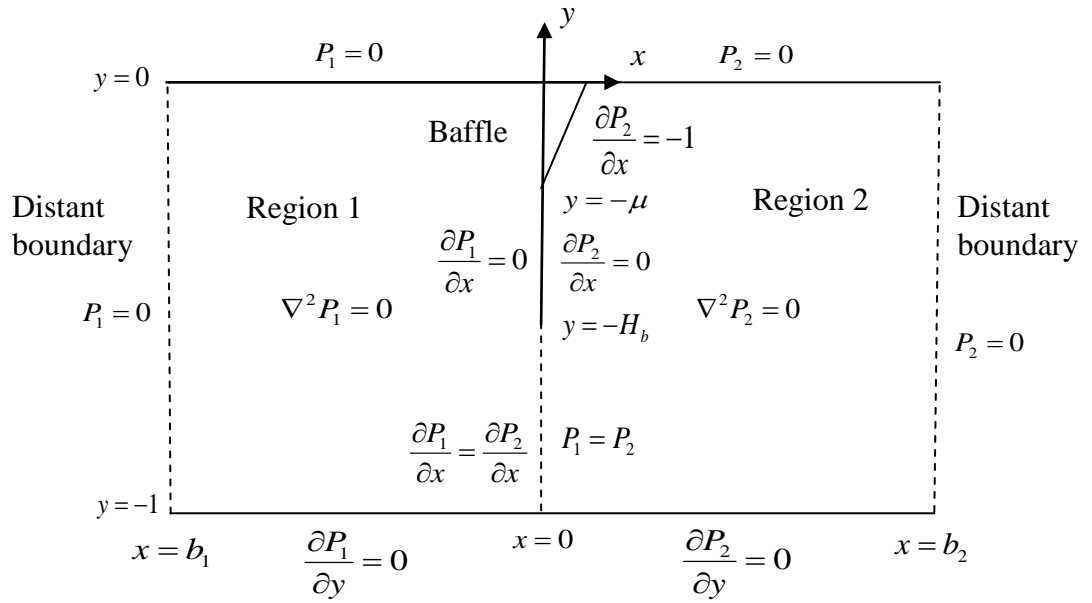
7.3.2 A vertical baffle in front of a wall (problem 2)
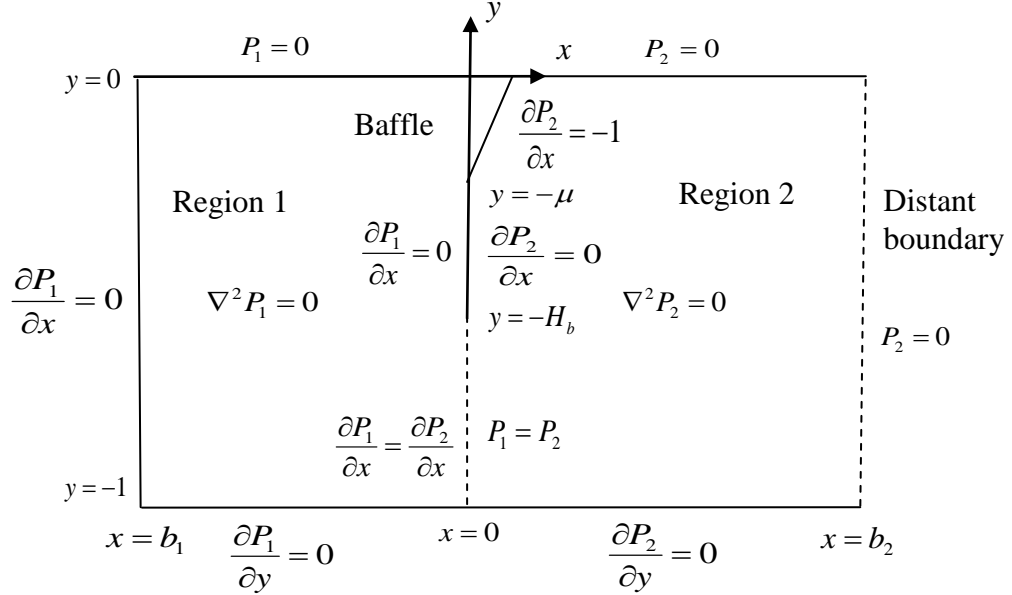
Figure 7.3.3: The dimensionless boundary-value problem for the pressure impulse for wave impact on a baffle.

For the second problem we have a baffle in front of seawall. The parameters of this situation are same with problem 1. The boundary-value problem for $P(x, y)$ is as in (7.3.1) to (7.3.10) but equation (7.3.3) is replaced by

$$\frac{\partial P_1}{\partial x}(b_1, y) = 0, \qquad \text{for } y \in (-1,0) \tag{7.3.16}$$

as shown in figure 7.3.3. The solution that satisfies the boundary condition in region 1 given by:

$$P_1(x, y) = \sum_{n=1}^{\infty} \alpha_n \sin(\lambda_n y) \frac{\cosh(\lambda_n (x - b_1))}{\cosh(\lambda_n b_1)} \tag{7.3.17}$$

where $\qquad \lambda_n = \left(n - \frac{1}{2}\right)\pi$, $n \in (1,2,3\ldots, N)$

for $\qquad -1 \le y \le 0,$ and $b_1 \le x \le 0$

and the solution which satisfies the boundary condition in the region 2 as in (7.3.11). The conditions at $x = 0$ are as before, equations (7.3.8) to (7.3.10). Applying the same procedure as for §7.3.1 for each equation respectively we get:

$$-\sum_{n=1}^{\infty} \alpha_n \lambda_n \tanh(\lambda_n b_1) \int_{-H_b}^{0} \sin(\lambda_n y)\sin(\lambda_m y)dy = 0 \tag{7.3.18}$$

$$\sum_{n=1}^{\infty} \alpha_n \lambda_n \tanh(\lambda_n b_1) \int_{-1}^{-H_b} \sin(\lambda_n y)\sin(\lambda_m y)dy + \sum_{n=1}^{\infty} \beta_n \lambda_n \int_{-1}^{0} \sin(\lambda_n y)\sin(\lambda_m y)dy$$

$$= \frac{1}{\lambda_m}[1 - \cos(-\mu\lambda_m)] \tag{7.3.19}$$

The second integral is simply $\dfrac{\delta_{m,n}}{2}$ by orthogonality.

$$\sum_{n=1}^{\infty} \alpha_n \int_{-1}^{-H_b} \sin(\lambda_n y)\sin(\lambda_m y)dy + \sum_{n=1}^{\infty} \beta_n \tanh(\lambda_n b_2) \int_{-1}^{-H_b} \sin(\lambda_n y)\sin(\lambda_m y)dy = 0 \tag{7.3.20}$$

These three equations also give us a system of $3M \times 2N$ equations as shown in figure 7.3.4 below with $N = \dfrac{3M}{2}$ again. We have two set of unknown Fourier coefficients $(\alpha_i, \beta_i), i = 1,2,3,\ldots,N$ to find to calculate the pressure impulse for this problem.

$$
\left(
\begin{array}{ccccccc}
 & & \vdots & \dfrac{\lambda_j}{2}\psi_2 & & & \\
-\lambda_j\tanh(\lambda_i b_1)\psi_1 & & \vdots & & \ddots & & \\
(\text{full matrix}) & & \vdots & (\text{diagonal matrix}) & \dfrac{\lambda_j}{2}\psi_2 & \\
\cdots & \cdots & \cdots \vdots & \cdots & \cdots & \cdots \\
 & & \vdots & & & \\
-\lambda_j\tanh(\lambda_i b_1)\psi_3 & & \vdots & 0 & & \\
(\text{full matrix}) & & \vdots & (\text{zero matrix}) & & \\
\cdots & \cdots & \cdots \vdots & \cdots & \cdots & \cdots \\
 & & \vdots & & & \\
1 & & \vdots & \tanh(\lambda_j b_2)\psi_1 & & \\
(\text{full matrix}) & & \vdots & (\text{full matrix}) & &
\end{array}
\right)
\left(
\begin{array}{c}
\alpha_1 \\ \vdots \\ \alpha_N \\ \cdots \\ \beta_1 \\ \vdots \\ \beta_N
\end{array}
\right)
=
\left(
\begin{array}{c}
\dfrac{1}{\lambda_i}(1-\cos(\lambda_i\mu)) \\[2mm]
\dfrac{1}{\lambda_N}(1-\cos(\lambda_i\mu)) \\[2mm]
\cdots \\[2mm]
0 \\[2mm]
\cdots \\[2mm]
0
\end{array}
\right)
$$

Figure 7.3.4 : Matrix system of equations for problem 2. The first M rows come from (7.3.19), the next from (7.3.18) and the last from (7.3.20). The functions $\psi_1\ldots\psi_3$ are the integrals in equations (7.3.18) to (7.3.20).

7.3.3 A vertical baffle and a deck in front of a seawall (problem 3)
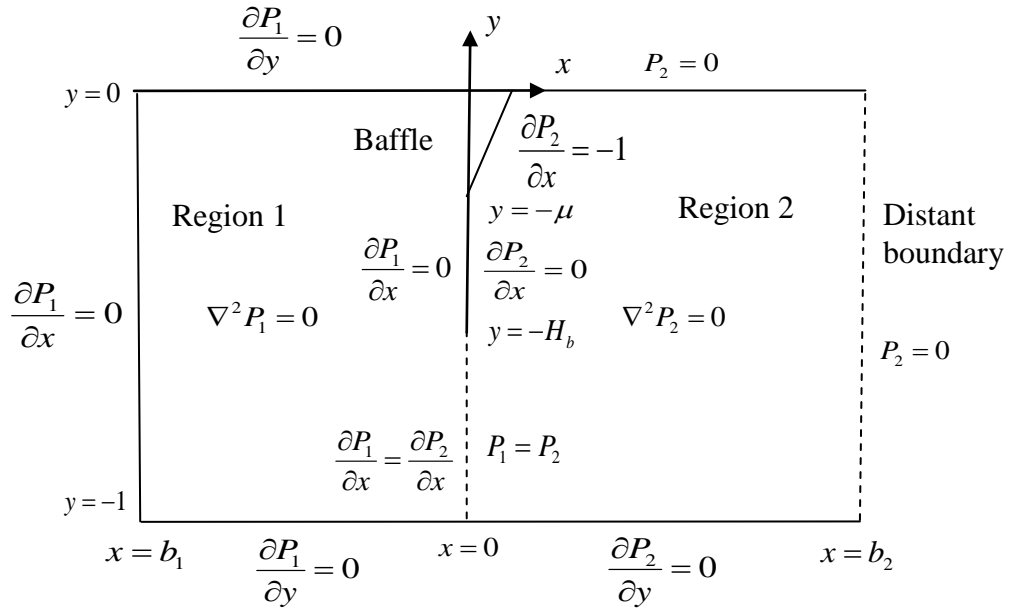
Figure 7.3.5: The dimensionless boundary-value problem for the pressure impulse for wave impact on a baffle.

The boundary conditions for region 1 are now:

$$\frac{\partial P_1}{\partial y}(x,0) = 0, \qquad \text{for } x \in (b_1, 0) \tag{7.3.21}$$

$$\frac{\partial P_1}{\partial x}(b_1, y) = 0, \qquad \text{for } y \in (-1, 0) \tag{7.3.22}$$

together with equations (7.3.1) and (7.3.4) to (7.3.10) as shown in figure 7.3.5. When we have a horizontal deck projecting from the seawall and a vertical baffle at the end of the deck, the eigenfuction expansion becomes

$$P_1(x,y) = \sum_{n=1}^{\infty} \alpha_n \cos(\gamma_n y) \frac{\cosh(\gamma_n(x-b_1))}{\cosh(\gamma_n b_1)} + C \tag{7.3.23}$$

where $\qquad \gamma_n = n\pi \ , \ n \in (1,2,3\ldots,N)$

for $\qquad -1 \le y \le 0, \text{and } b_1 \le x \le 0$

The solution in region 2 and the conditions at $x = 0$ are as before, i.e., equations (7.3.12) and (7.3.8) to (7.3.10) respectively.

Applying $\int_{-H_b}^{0} \ldots \cos(\gamma_m y)dy$, $m = 1,2,\ldots,M$ to equation (7.3.8) and integrating gives:

$$-\sum_{n=1}^{\infty} \alpha_n \gamma_n \tanh(\gamma_n b_1) \int_{-H_b}^{0} \cos(\gamma_n y)\cos(\gamma_m y)dy = 0 \qquad (7.3.24)$$

Applying $\int_{-1}^{0} \ldots \sin(\lambda_m y)dy$, $m = 1,2,\ldots,M$ to equation (7.3.9) and integrating gives:

$$\sum_{n=1}^{\infty} \alpha_n \gamma_n \tanh(\gamma_n b_1) \int_{-1}^{-H_b} \cos(\gamma_n y)\sin(\lambda_m y)dy + \sum_{n=1}^{\infty} \beta_n \lambda_n \int_{-1}^{0} \sin(\lambda_n y)\sin(\lambda_m y)dy$$

$$= \frac{1}{\lambda_m}\left[1 - \cos(-\mu\lambda_m)\right] \qquad (7.3.25)$$

The second integral is simply $\dfrac{\delta_{m,n}}{2}$ by orthogonality.

Applying $\int_{-1}^{-H_b} \ldots \sin(\lambda_m y)dy$, $m = 1,2,\ldots,M$ to equation (7.3.10) and integrating gives:

$$\sum_{n=1}^{\infty} \alpha_n \int_{-1}^{-H_b} \cos(\gamma_n y)\sin(\lambda_m y)dy + A \int_{-1}^{-H_b} \sin(\lambda_m y)dy + \sum_{n=1}^{\infty} \beta_n \tanh(\lambda_n b_2) \int_{-1}^{-H_b} \sin(\lambda_n y)\sin(\lambda_m y)dy = 0$$

$$(7.3.26)$$

where

$$A = -\frac{1}{1-H_b}\sum_{n=1}^{\infty} \frac{\alpha_n}{\gamma_n}\sin(-\gamma_n H_b) + \frac{1}{1-H_b}\sum_{n=1}^{\infty} \frac{b_n}{\lambda_n}\tanh(\lambda_n b_2)\cos(-\lambda_n H_b)$$

From these three equations, it also gives us a system of $3M \times 2N$ equations such in figure 7.3.6 with $N = \dfrac{3M}{2}$. We have two sets of unknown Fourier coefficients $(\alpha_i, \beta_i), i = 1,2,3,\ldots,N$ to find to calculate the pressure impulse for this problem.

$$\begin{pmatrix} \gamma_j \tanh(\gamma_i b_1)\zeta_1 & \vdots & \dfrac{\lambda_j}{2}\psi_1 & & \\ \text{(full matrix)} & \vdots & & \ddots & \\ & \vdots & \text{(diagonal matrix)} & & \dfrac{\lambda_j}{2}\psi_1 \\ \cdots \quad \cdots \quad \cdots & \vdots & \cdots & \cdots & \cdots \\ & \vdots & & & \\ -\gamma_j \tanh(\gamma_i b_1)\psi_2 & \vdots & & 0 & \\ \text{(full matrix)} & \vdots & & \text{(zero matrix)} & \\ \cdots \quad \cdots \quad \cdots & \vdots & \cdots & & \cdots \\ & \vdots & & & \\ \zeta_2 + \left(\dfrac{\cos(-\lambda_i H_b)}{\lambda_i}\right)\left(\dfrac{sin(-\gamma_i H_b)}{\gamma_j(1-H_b)}\right) & \vdots & \tanh(\lambda_j b_2)\varepsilon_1 - \left(\dfrac{\cos(-\lambda_i H_b)}{\lambda_i}\right)\left(\dfrac{\tanh(\lambda_j b_2)}{\lambda_j(1-H_b)}\cos(-\lambda_j H_b)\right) & & \\ \text{(full matrix)} & \vdots & \text{(full matrix)} & & \end{pmatrix} \begin{pmatrix} \alpha_1 \\ \vdots \\ \alpha_N \\ \cdots \\ \beta_1 \\ \vdots \\ \beta_N \end{pmatrix} = \begin{pmatrix} \dfrac{1}{\lambda_M}(1-\cos(\lambda_i \mu)) \\ \dfrac{1}{\lambda_M}(1-\cos(\lambda_i \mu)) \\ \cdots \\ 0 \\ \cdots \\ 0 \end{pmatrix}$$

Figure 7.3.6 : Matrix system of equations for problem 3. The first M rows come from (7.3.25), the next from (7.3.24) and the last from (7.3.26). The functions $\psi_1, \psi_2, \zeta_1, \zeta_2$ and ε_1 are the integrals in equations (7.3.24) to (7.3.26).

7.3.4 A vertical baffle on the seabed in front of a seawall (problem 4)
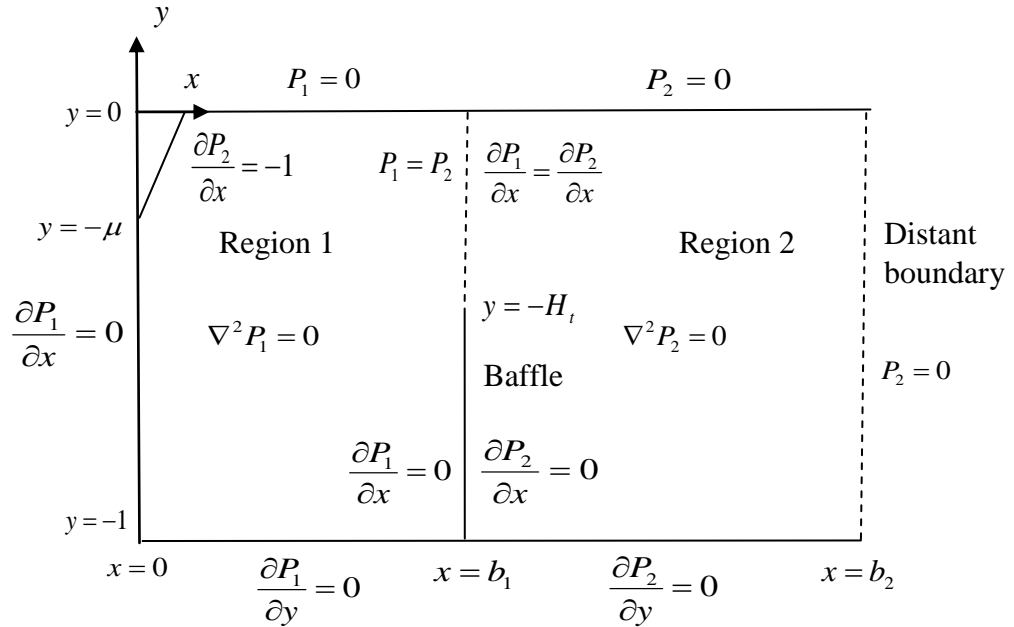
Figure 7.3.7: The dimensionless boundary-value problem for the pressure impulse for wave impact on a wall with vertical baffle on seabed. Relative to problems 1,2 and 3 here b_1 changes sign.

For this problem, we put our origin at the wall and we have a vertical baffle on the seabed. The parameters of this situation become:

H_t = depth of water from free surface to the top of the baffle

b_1 = distance of the baffle from the wall

b_2 = distance of the far boundary from the wall

μ = parameter of impact region $0 \leq y \leq \mu$

The fluid domain defined by $0 \leq x < b_2$, and $-1 \leq y \leq 0$. On the wall we have boundary-condition as below:

$$\frac{\partial P_1}{\partial x} = \begin{cases} -1 & \text{for} \quad -\mu \leq y \leq 0 \\ 0 & \text{for} \quad -1 \leq y < -\mu \end{cases} \tag{7.3.27}$$

together with equations (7.3.1) to (7.3.10) except (7.3.3) as shown in figure 7.3.4. The expression which satisfies the boundary-condition in region 1 is

$$P_1(x, y) = \sum_{n=1}^{\infty} \sin(\lambda_n y) \left\{ \alpha_n \frac{\sinh(\lambda_n (x - b_1))}{\cosh(\lambda_n b_1)} + \beta_n \frac{\cosh(\lambda_n (x - b_1))}{\cosh(\lambda_n b_1)} \right\} \qquad (7.3.28)$$

where $\qquad \lambda_n = \left(n - \frac{1}{2}\right)\pi$, $n \in (1, 2, 3 \ldots, N)$

for $\qquad -1 \le y \le 0$, and $0 \le x \le b_2$

The solution in region 2 is as equation (7.3.12) and we have matching/baffle conditions at $x = b_1$ as follows:

- $\qquad P_1 = P_2$ $\qquad\qquad$ for $y \in [0, -H_t)$ $\qquad\qquad$ (7.3.29)

- $\qquad \dfrac{\partial P_1}{\partial x} = \dfrac{\partial P_2}{\partial x}$ $\qquad\qquad$ for $y \in [0, -H_t)$ $\qquad\qquad$ (7.3.30)

- $\qquad \dfrac{\partial P_1}{\partial x} = 0$ $\qquad\qquad$ for $y \in (-H_t, -1]$ $\qquad\qquad$ (7.3.31)

- $\qquad \dfrac{\partial P_2}{\partial x} = 0$ $\qquad\qquad$ for $y \in (-H_b, -1]$ $\qquad\qquad$ (7.3.32)

Applying $\int_{-1}^{0} \ldots \sin(\lambda_m y) dy$, $m = 1, 2, \ldots, M$ on the wall and integrating, we get

$$\alpha_n - \beta_n \tanh(\lambda_n b_1) = \frac{2}{\lambda_m^2} (1 - \cos(\lambda_m \mu)) \qquad (7.3.33)$$

At $x = b_1$, apply $\int_{-1}^{0} \ldots \sin(\lambda_m y) dy$, $\quad m = 1, 2, \ldots, M$ to equations (7.3.29) to (7.3.32) and integrating for each equation gives 4 equations:

172

$$\sum_{n=1}^{\infty} \frac{\beta_n}{\cosh(\lambda_n b_1)} \int_{-H_t}^{0} \sin(\lambda_n y)\sin(\lambda_m y)dy$$

$$-\sum_{n=1}^{\infty} \frac{c_n \sinh(\lambda_n(b_1 - b_2))}{\cosh(\lambda_n b_2)} \int_{-H_t}^{0} \sin(\lambda_n y)\sin(\lambda_m y)dy = 0 \tag{7.3.34}$$

$$\sum_{n=1}^{\infty} \frac{\alpha_n \lambda_n}{\cosh(\lambda_n b_1)} \int_{-H_t}^{0} \sin(\lambda_n y)\sin(\lambda_m y)dy$$

$$-\sum_{n=1}^{\infty} c_n \lambda_n \frac{\sinh(\lambda_n(b_1 - b_2))}{\cosh(\lambda_n b_2)} \int_{-H_t}^{0} \sin(\lambda_n y)\sin(\lambda_m y)dy = 0 \tag{7.3.35}$$

$$\sum_{n=1}^{\infty} \frac{\alpha_n \lambda_n}{\cosh(\lambda_n b_1)} \int_{-1}^{-H_t} \sin(\lambda_n y)\sin(\lambda_m y)dy = 0 \tag{7.3.36}$$

$$\sum_{n=1}^{\infty} c_n \lambda_n \frac{\cosh(\lambda_n(b_1 - b_2))}{\cosh(\lambda_n b_2)} \int_{-1}^{-H_t} \sin(\lambda_n y)\sin(\lambda_m y)dy = 0 \tag{7.3.37}$$

From equations (7.3.33) to (7.3.37) gives us system of $5M = 3N$ equations such as in figure 7.3.8 with $N = \dfrac{5M}{3}$. We have three sets of unknown Fourier coefficients (α_i, β_i, c_i), $i = 1,2,3,\ldots,N$ to find to calculate the pressure impulse in this problem.

$$
\left(
\begin{array}{ccccccccc}
1 & & & : & -\tanh(\lambda_j b_1) & & : & & \\
& \ddots & & : & & \ddots & : & 0 & \\
& \text{(diagonal matrix)} & 1 & : & \text{(diagonal matrix)} & -\tanh(\lambda_j b_1) & : & \text{(zero matrix)} & \\
\dots & \dots & \dots & : & \dots & \dots & : \dots & \dots & \dots \\
& & & : & & & : & & \\
& 0 & & : & \dfrac{1}{\cosh(\lambda_j b_1)}\varepsilon_1 & & : & \dfrac{1}{\cosh(\lambda_j b_1)}\varepsilon_2 & \\
& \text{(zero matrix)} & & : & \text{(full matrix)} & & : & \text{(full matrix)} & \\
\dots & \dots & \dots & : & \dots & \dots & : \dots & \dots & \dots \\
& & & : & & & : & & \\
& \dfrac{\lambda_j}{\cosh(\lambda_j b_1)}\varepsilon_3 & & : & 0 & & : & \dfrac{\lambda_j\cosh(\lambda_j(b_1-b_2))}{\cosh(\lambda_j b_2)}\varepsilon_4 & \\
& \text{(full matrix)} & & : & \text{(zero matrix)} & & : & \text{(full matrix)} & \\
\dots & \dots & \dots & : & \dots & \dots & : \dots & \dots & \dots \\
& & & : & & & : & & \\
& \dfrac{\lambda_j}{\cosh(\lambda_j b_1)}\varepsilon_5 & & : & 0 & & : & 0 & \\
& \text{(full matrix)} & & : & \text{(zero matrix)} & & : & \text{(zero matrix)} & \\
\dots & \dots & \dots & : & \dots & \dots & : \dots & \dots & \dots \\
& & & : & & & : & & \\
& 0 & & : & 0 & & : & \dfrac{\lambda_j\cosh(\lambda_j(b_1-b_2))}{\cosh(\lambda_j b_2)}\varepsilon_6 & \\
& \text{(zero matrix)} & & : & \text{(zero matrix)} & & : & \text{(full matrix)} &
\end{array}
\right)
\left(
\begin{array}{c}
\alpha_1 \\ \vdots \\ \alpha_N \\ \dots \\ \beta_1 \\ \vdots \\ \beta_N \\ \dots \\ c_1 \\ \vdots \\ c_N
\end{array}
\right)
=
\left(
\begin{array}{c}
\dfrac{2}{\lambda_1^2}(1-\cos(\lambda_1\mu)) \\ \vdots \\ \dfrac{2}{\lambda_M^2}(1-\cos(\lambda_M\mu)) \\ \dots \\ 0 \\ \vdots \\ 0 \\ \dots \\ 0 \\ \vdots \\ 0 \\ \dots \\ 0 \\ \vdots \\ 0 \\ \dots \\ 0 \\ \vdots \\ 0
\end{array}
\right)
$$

Figure 7.3.8 : Matrix system of equations for problem 4. The first M rows come from (7.3.33), and followed by (7.3.34) to (7.3.37).
The functions $\varepsilon_1 \dots \varepsilon_6$ are the integrals in equations (7.3.33) to (7.3.37).

7.4 Pressure Impulse

The pressure impulse for each problem is given below. We can see that for problem 1 in figures 7.4.1 and 7.4.2 the pressure impulse on the baffle increases when μ increases. For small μ, the pressure impulse is almost same for different length of baffle but when μ is greater, the pressure impulse is higher the greater the length of the baffle.

For problem 2 in figures 7.4.3 and 7.4.4, the behaviour is almost the same as in problem 1 but we have a wall behind the baffle. The pressure behind the baffle increases when μ increases but it decreases when the length of baffle increases.

For problem 3 in figures 7.4.5 and 7.4.6 we can see there is a high pressure behind the baffle when we have a closed surface between the wall and baffle. For the same size of impact, let say $\mu = 0.5$, the pressure impulse behind the baffle is greater when the length of baffle increases.

We have different case for problem 4 in figures 7.4.7, 7.4.8 and 7.4.9. The baffle is located on the seabed in front of the wall. We can see that pressure impulse on the wall is greater when μ increases and the pressure behind the baffle increases for higher lengths of baffle for the same impact.

Figures 7.4.10 to 7.4.12 show the comparison between four problems for the same baffle length and μ. We can see that the pressure on the baffle for problem 1 to 3 is almost the same and they have a small increase when the length of baffle increases. For problem 2, the pressure impulse behind the baffle at the bottom is high and it decreases when length of baffle increases. For problem 3, the pressure behind the baffle under the closed region is higher when the length of baffle is smaller. It contrast with problem 4, which we can see the pressure impulse on the wall is greater than on the baffle for problem 1, 2 and 3 and the pressure impulse behind the baffle is greater when the baffle is higher.

$\mu = 0.1$	$\mu = 0.3$	$\mu = 0.5$
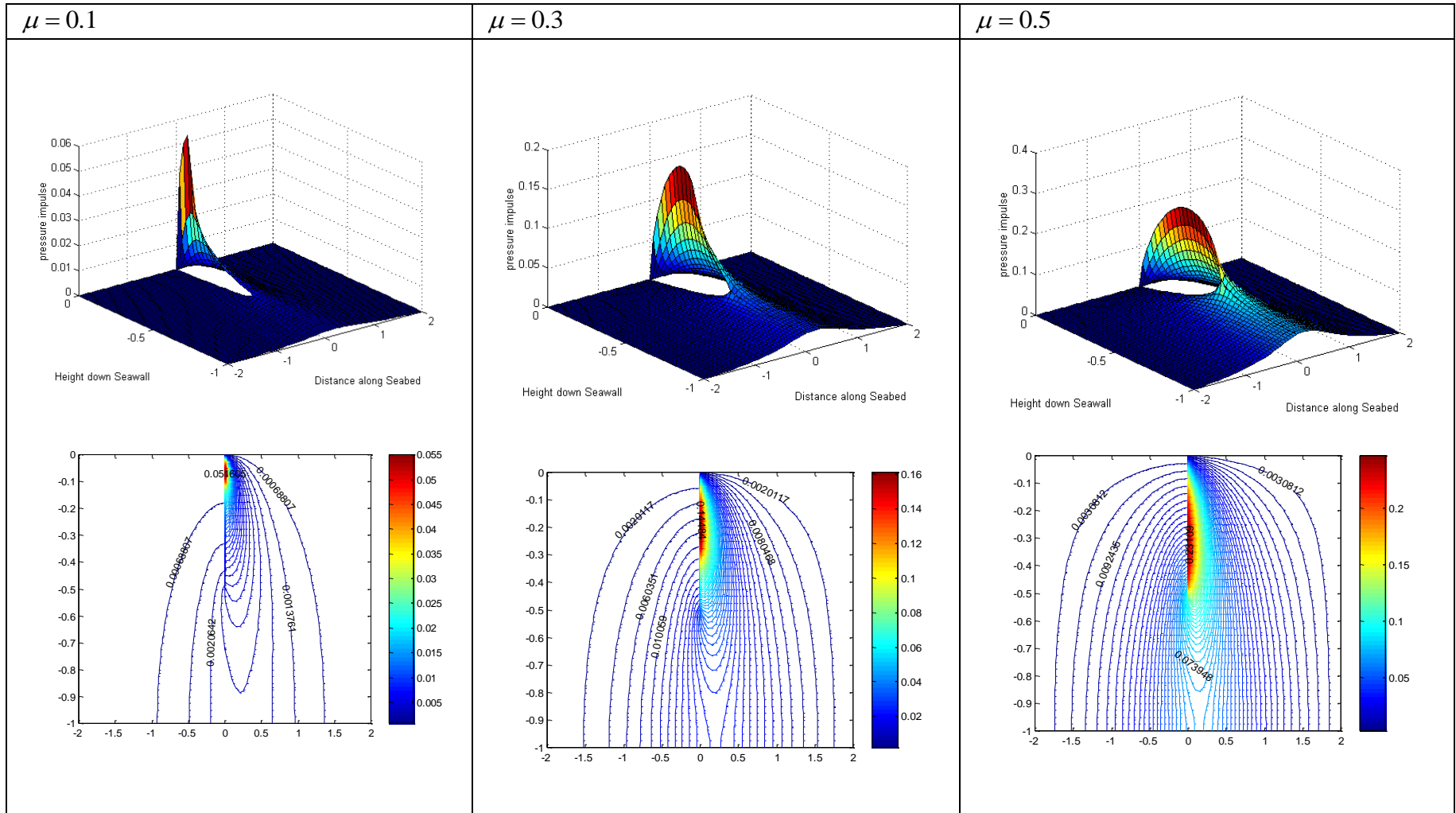
Figure 7.4.1: Problem 1 for $H_b = 0.5$ ($b_1 = -2$, $b_2 = 2$)

| $\mu = 0.1$ | $\mu = 0.5$ | $\mu = 0.8$ |
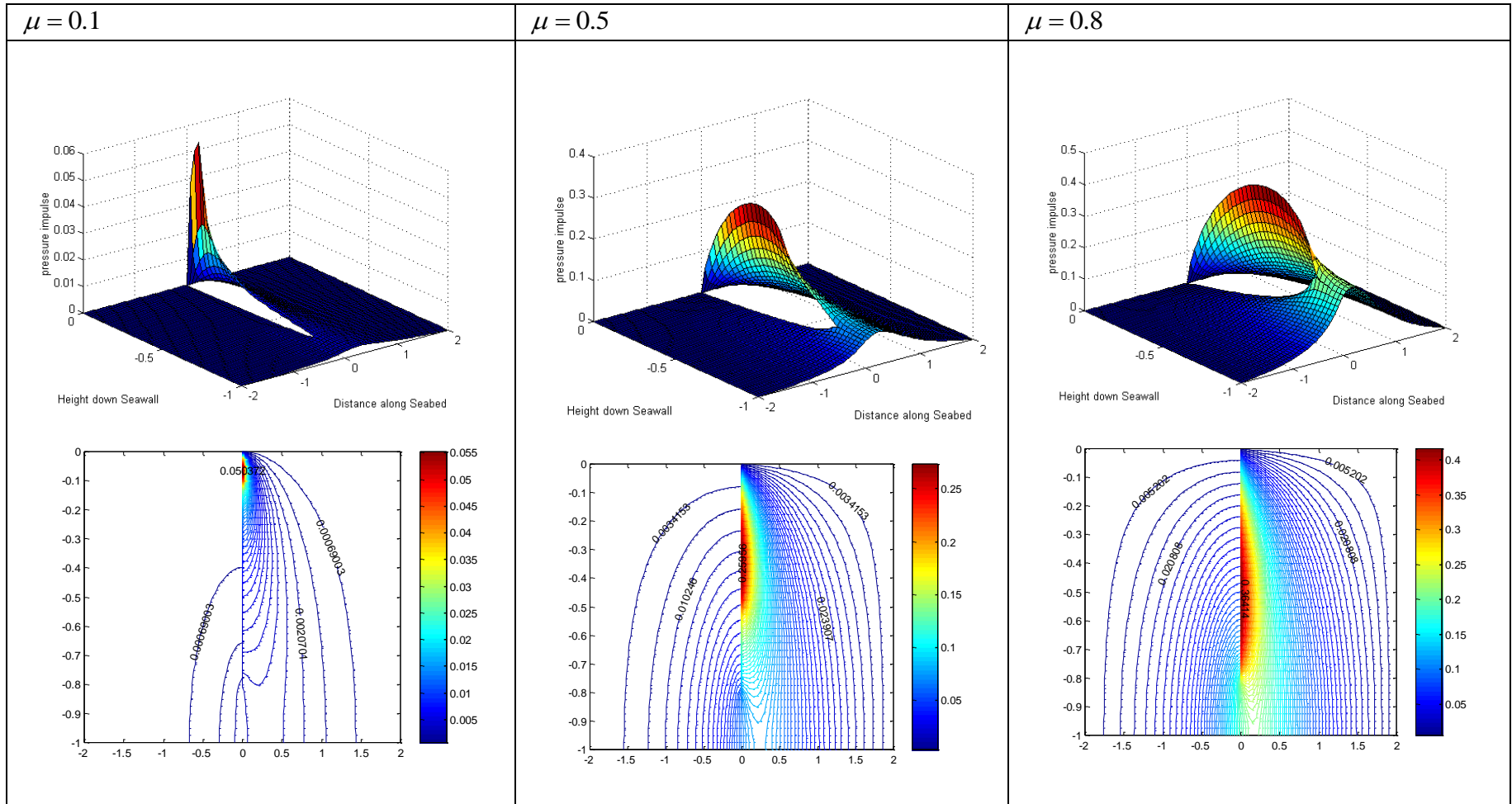
Figure 7.4.2: Problem 1 for $H_b = 0.8$ ($b_1 = -2$, $b_2 = 2$)
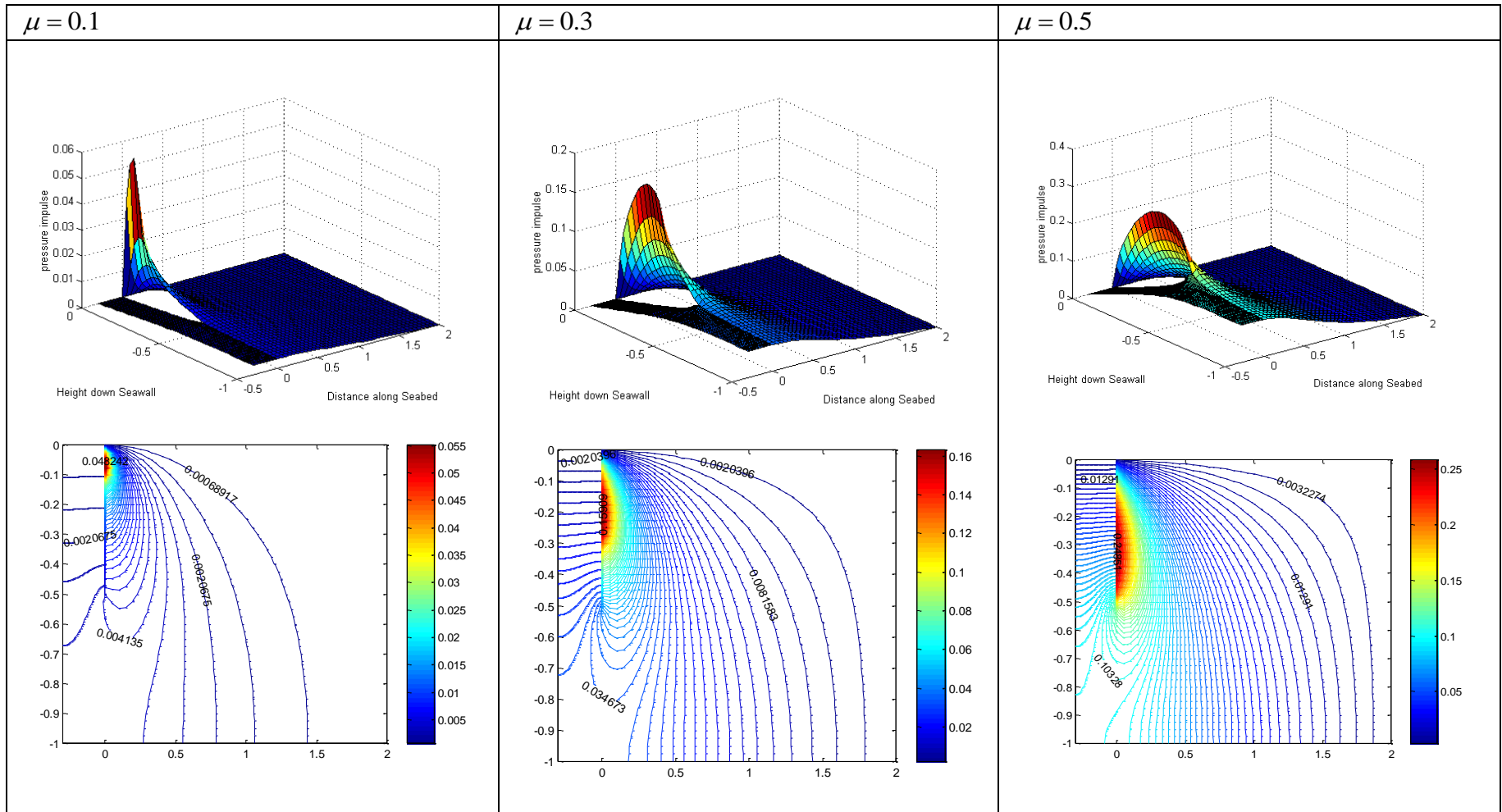
Figure 7.4.3: Problem 2 for $H_b = 0.5$ ($b_1 = -0.3, b_2 = 2$)
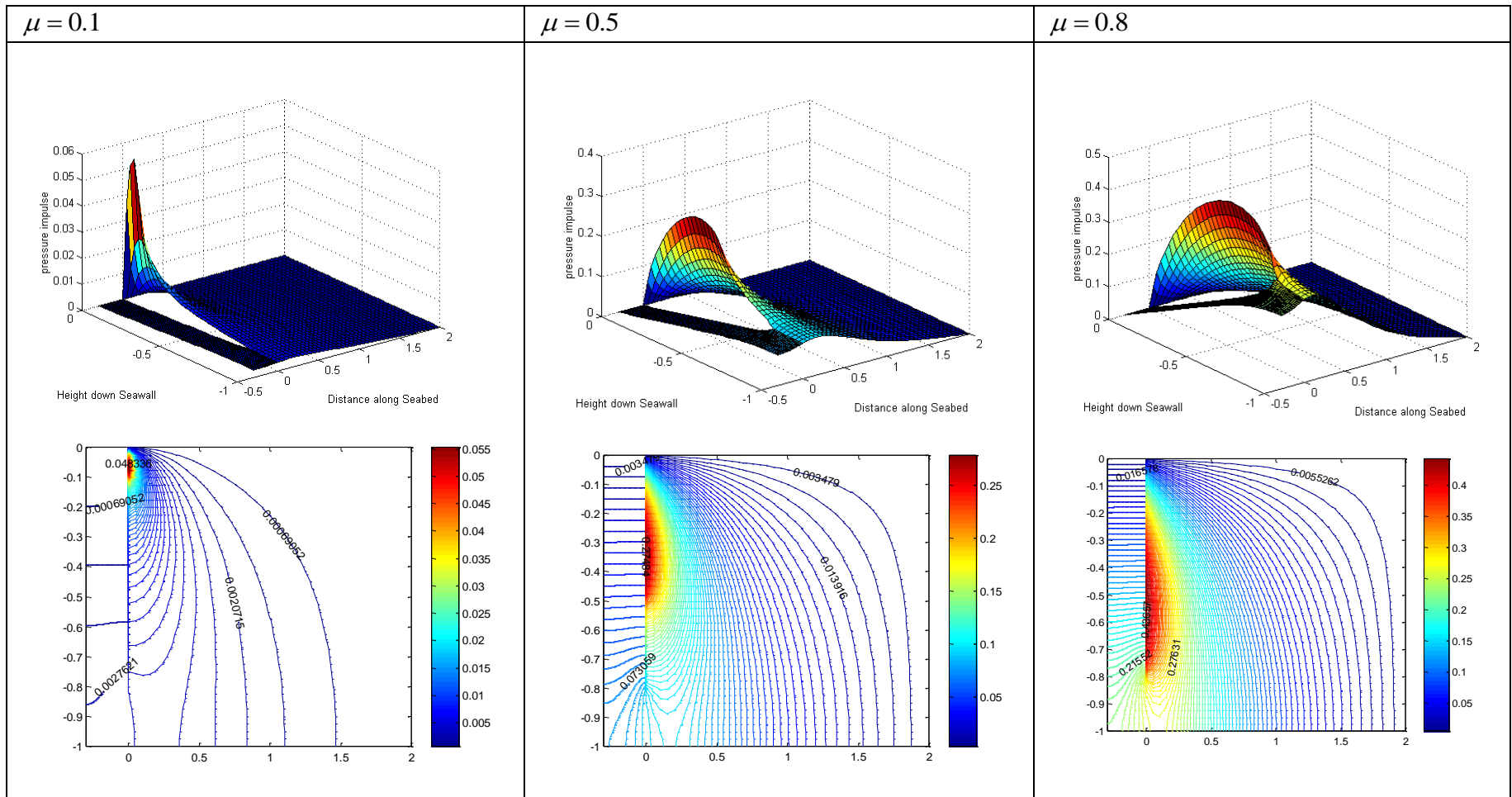
Figure 7.4.4: Problem 2 for $H_b = 0.8$ ($b_1 = -0.3, b_2 = 2$)

| $\mu = 0.1$ | $\mu = 0.3$ | $\mu = 0.5$ |
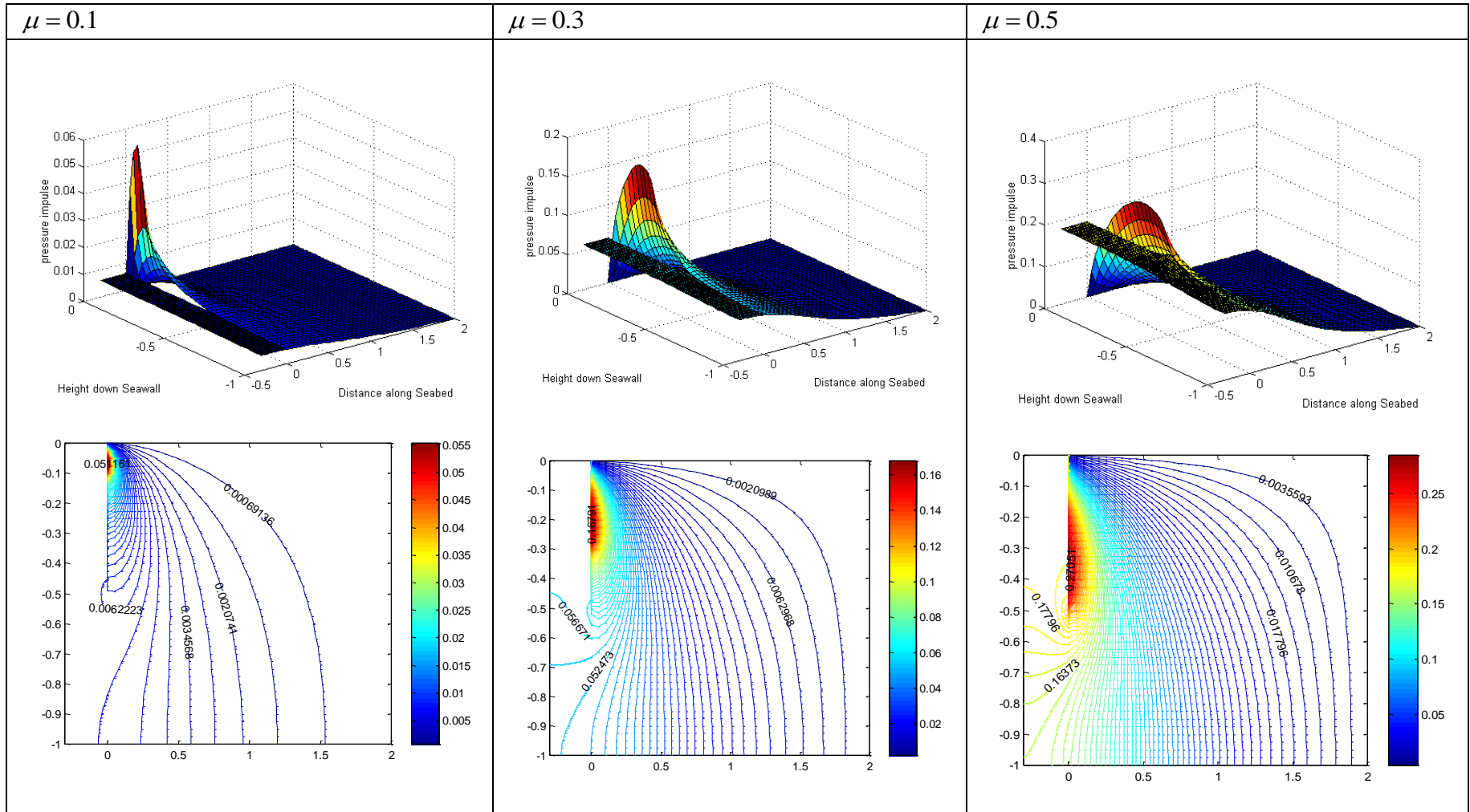
Figure 7.4.5: Problem 3 for $H_b = 0.5$ ($b_1 = -0.3, b_2 = 2$)

| $\mu = 0.1$ | $\mu = 0.5$ | $\mu = 0.8$ |
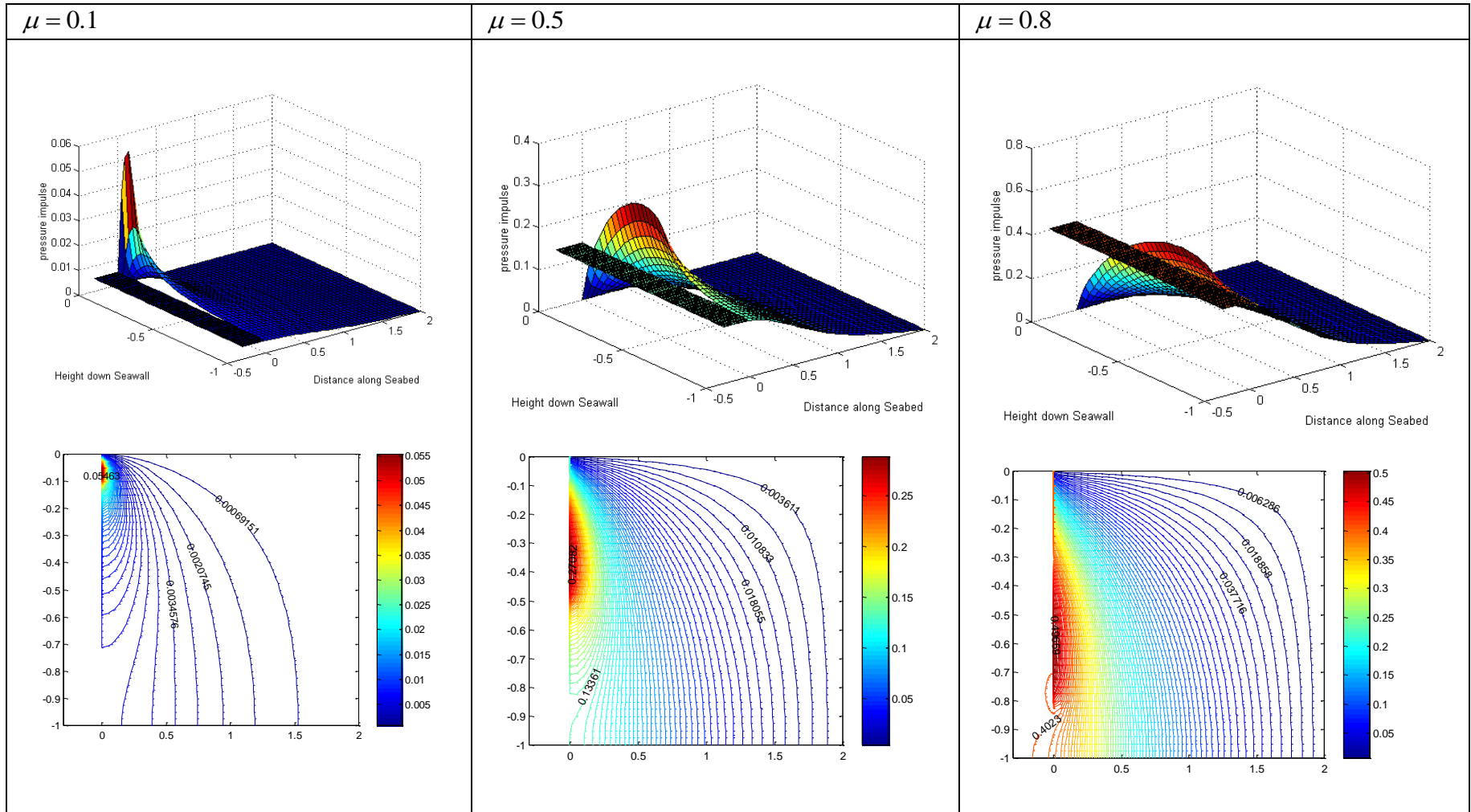
Figure 7.4.6: Problem 3 for $H_b = 0.8$ $(b_1 = -0.3, b_2 = 2)$

| $\mu = 0.1$ | $\mu = 0.5$ | $\mu = 0.8$ |
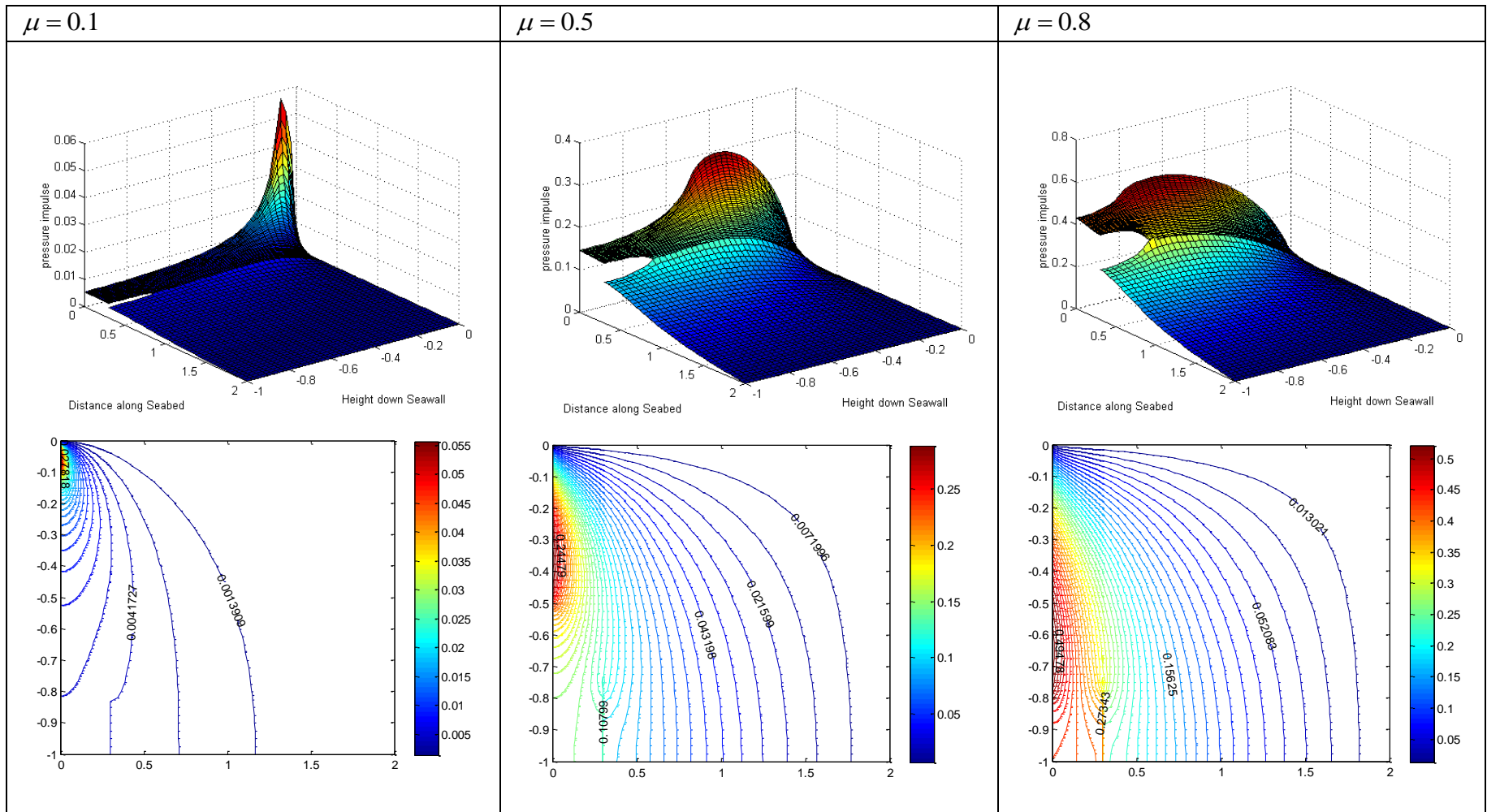
Figure 7.4.7: Problem 4 for $H_b = 0.2$ ($b_1 = 0.3, b_2 = 2$)
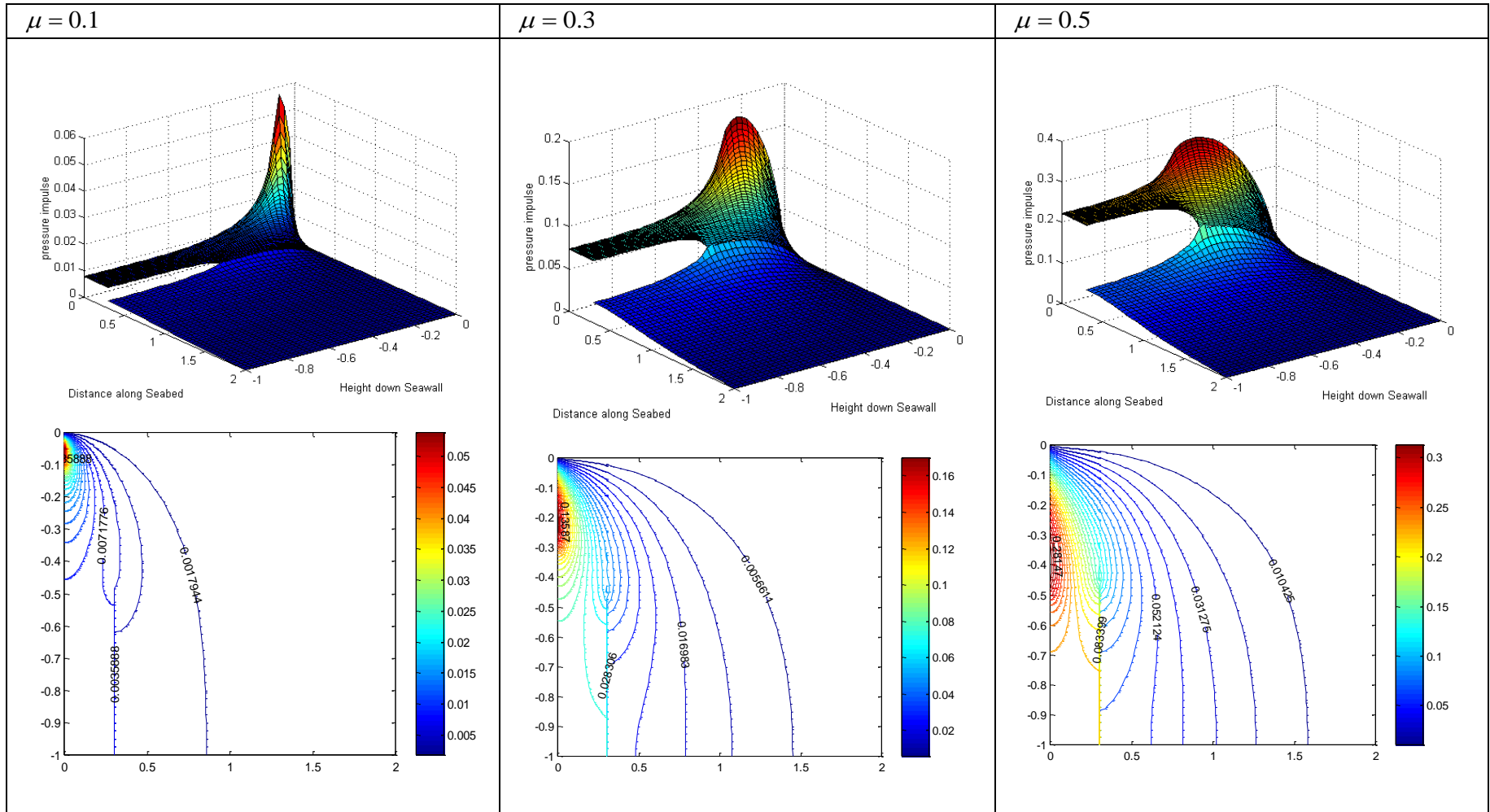
Figure 7.4.8: Problem 4 for $H_b = 0.5$ ($b_1 = 0.3, b_2 = 2$)

| $\mu = 0.1$ | $\mu = 0.3$ | $\mu = 0.5$ |

Figure 7.4.9: Problem 4 for $H_b = 0.8$ ($b_1 = 0.3, b_2 = 2$)
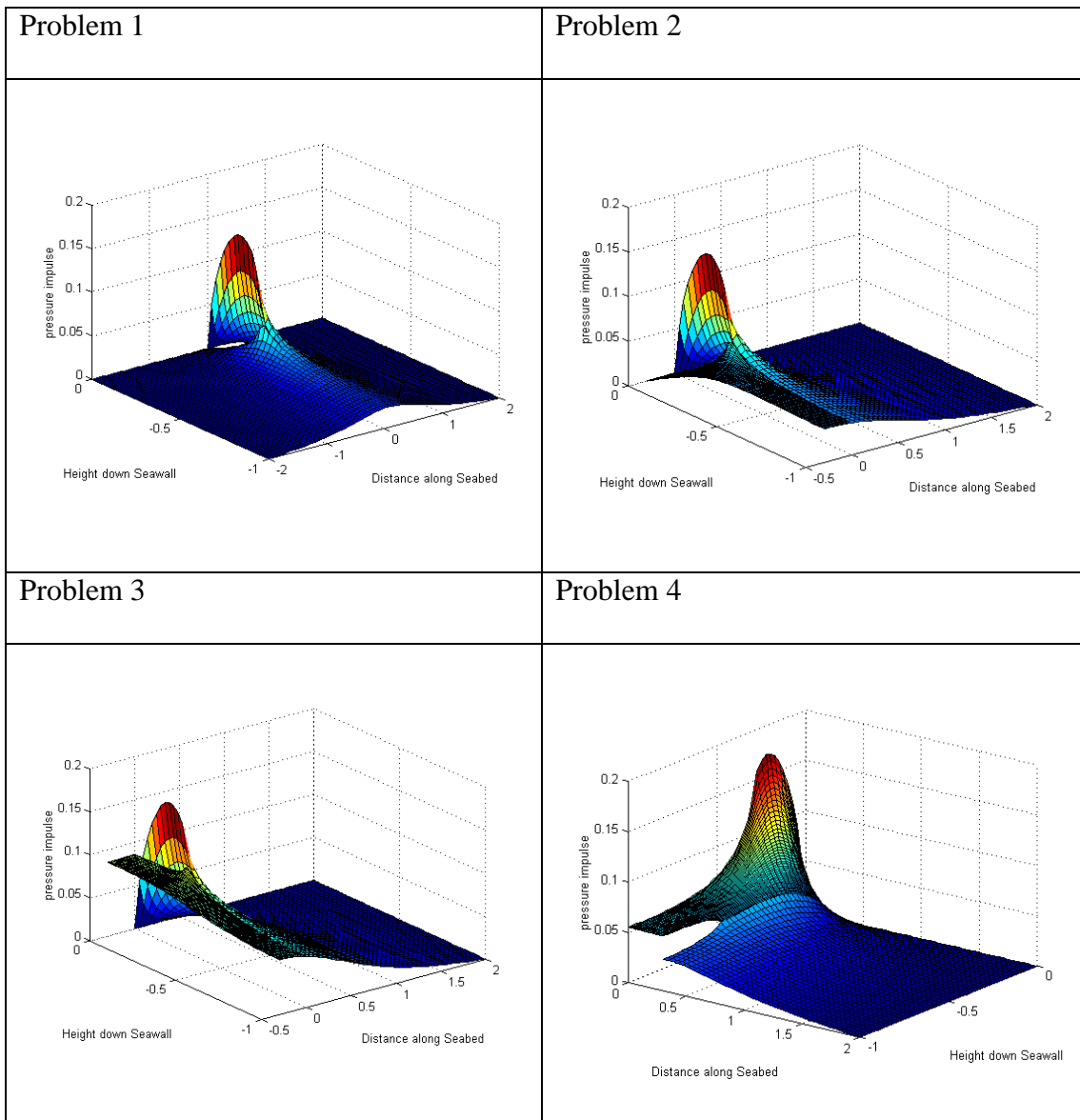
Figure 7.4.10: Comparison between four problems for $H_b = 0.3$ and $\mu = 0.3$. Problem 4 is rotated for clarity.
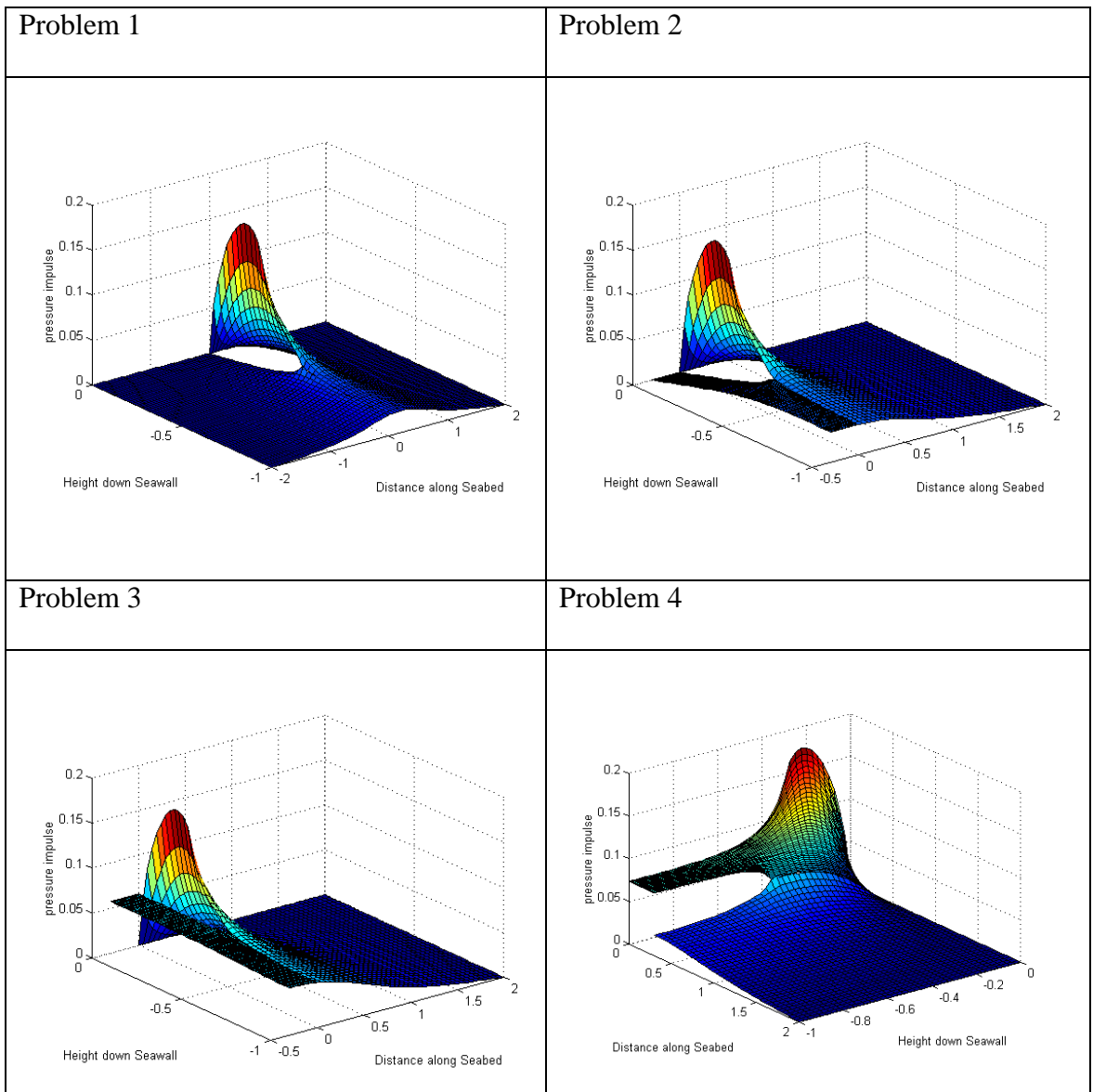
Figure 7.4.11: Comparison between four problems for $H_b = 0.5$ and $\mu = 0.3$.
Problem 4 is rotated for clarity.
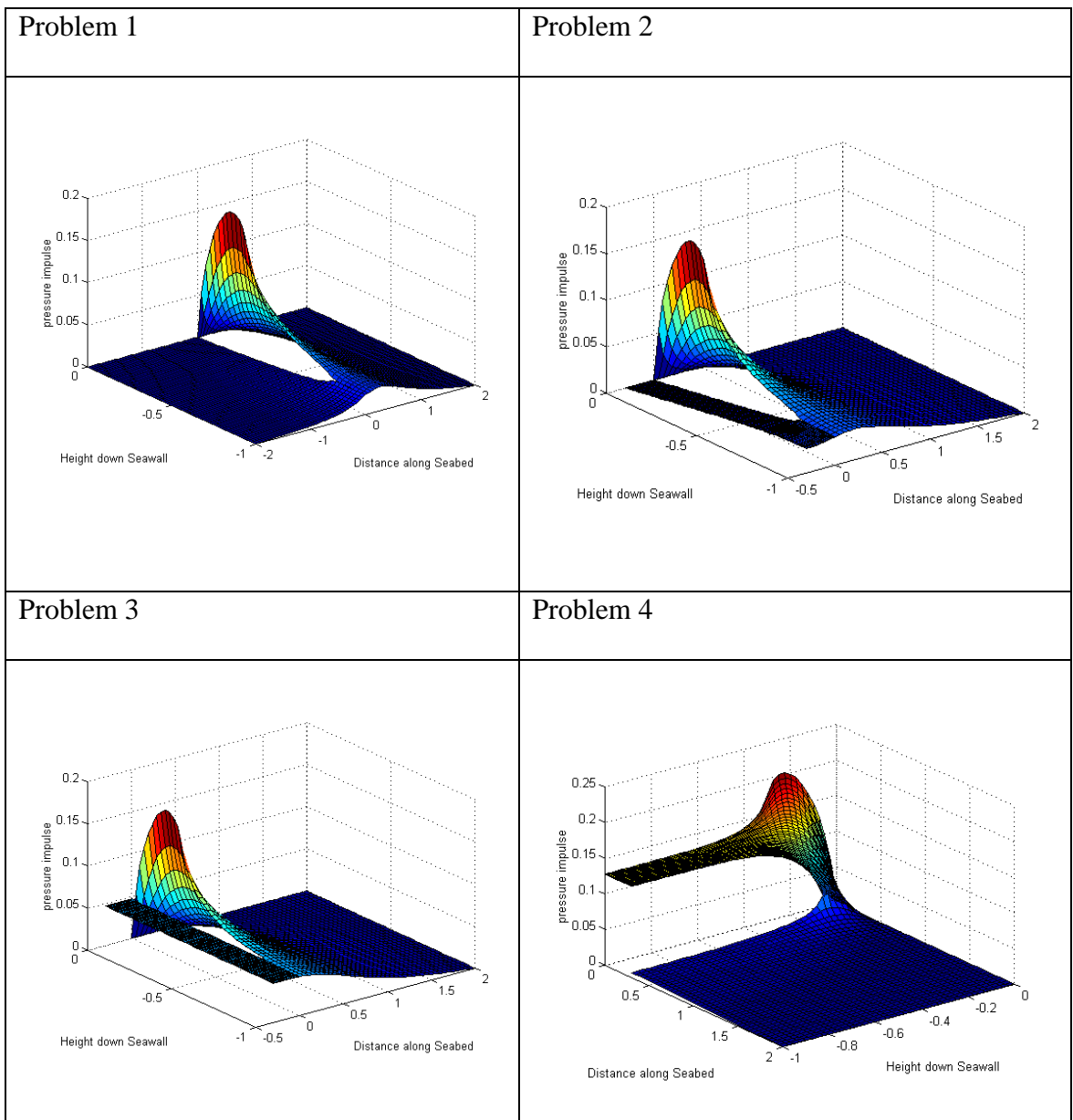
Figure 7.4.12: Comparison between four problems for $H_b = 0.8$ and $\mu = 0.3$
Problem 4 is rotated for clarity.

7.5 Total Impulse

In this section we will calculate the total impulse on the baffle, I_b on the wall, I_w on the seabed, I_s and on the deck, I_d for each problem. We take the left/down direction as positive impulse as follows:
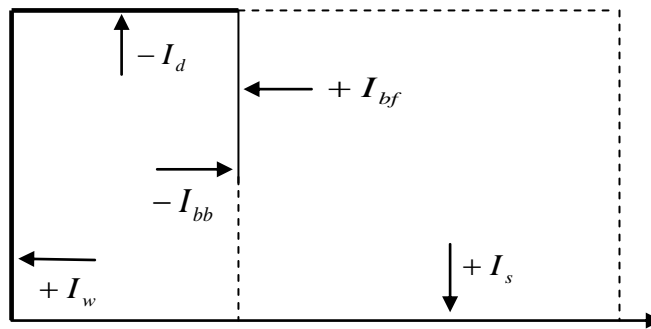
Figure 7.5.1: The direction of the force impulse.

7.5.1 Total impulse on the baffle

The total impulse on the baffle, I_b is given by adding the impulse on back of the baffle, I_{bb} and impulse on the front of baffle, I_{bf} as following equation.

$$I_b = - \int_{-H_b}^{0} P_1(x, y)dy + \int_{-H_b}^{0} P_2(x, y)dy$$

The impulse on the baffle for each problem we can see as below:
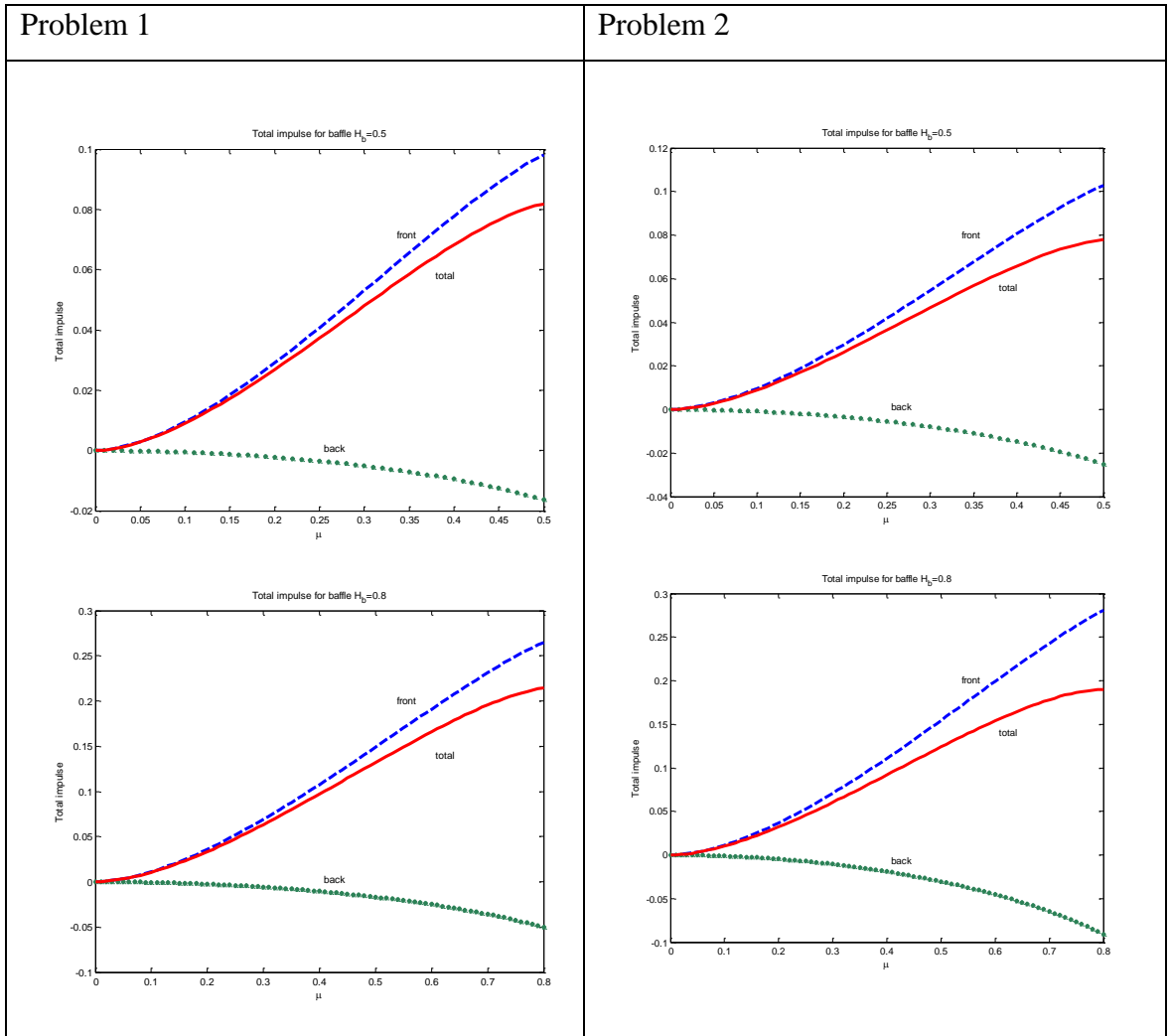
Problem 1	Problem 2

Figure 7.5.2: Impulse on baffle for $H_b = 0.5$ and $H_b = 0.8$

In figure 7.5.2 we can see that the total impulse in front of the baffle for problem 1 and 2 is higher than the total impulse behind the baffle. The total impulse on the front of the baffle and behind the baffle for problem 2 is higher than problem 1 respectively. However the total impulse after adding the total impulse on the front and on the back of the baffle, shows problem 1 is only slightly higher. The total impulse for both problems increases when the length of the baffle increases.
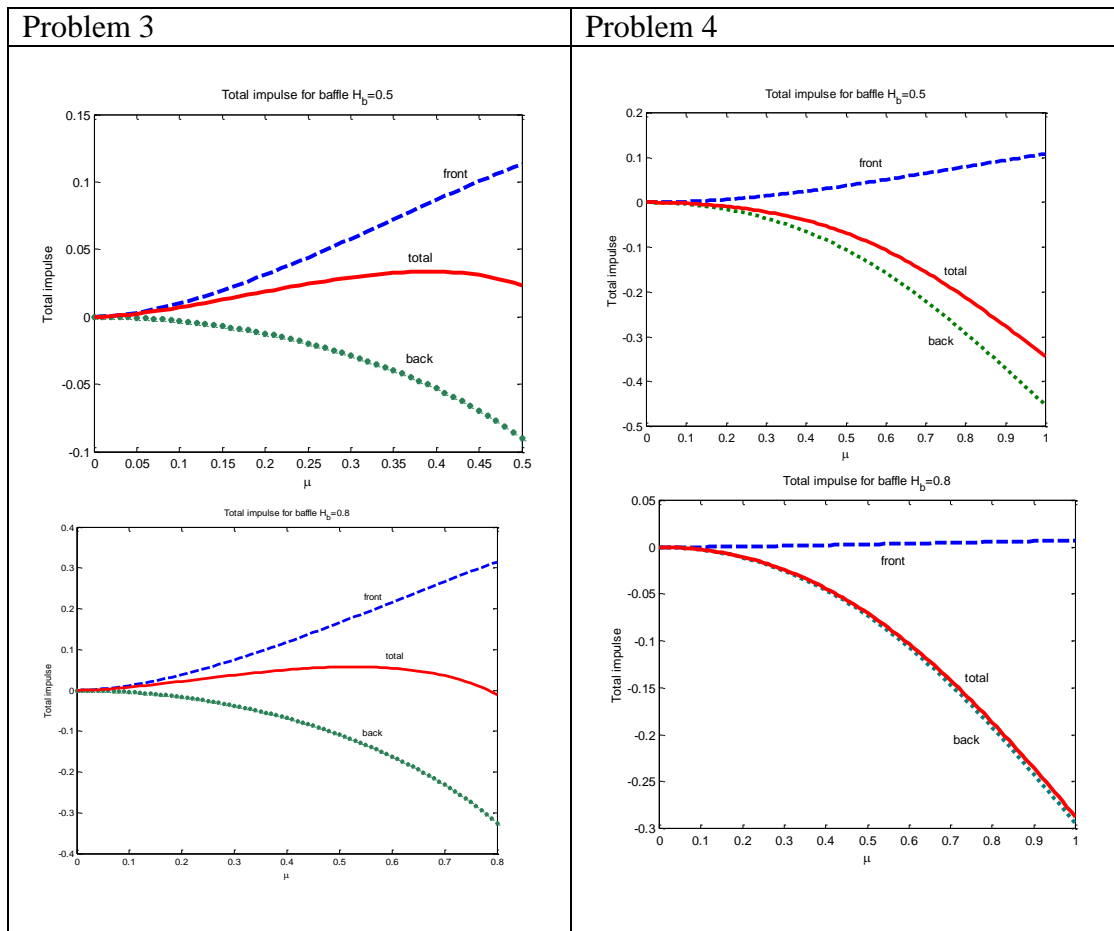
Problem 3	Problem 4

Figure 7.5.3: Impulse on baffle for $H_b = 0.5$ and $H_b = 0.8$

In figure 7.5.3 we can see that the total impulse on the front of the baffle for problem 3 is higher than the total impulse behind the baffle. However we can see that when the length of baffle increases, the total impulse at the back is slightly higher than at the front. The total impulse after adding the total impulse at the back and in front of baffle is smaller than problems 1 and 2. For problem 4 we can see that the total impulse at the back is greater than at the front of the baffle.

In figure 7.5.4, we can see that when the baffle length is 1, it is same as the Cooker's model and the total impulse on the baffle is the same as the total impulse on the vertical wall.

In figure 7.5.3, the total impulse at the back for problem 3 is higher than total impulse on the front of baffle, so it will push the baffle to the seaward. This is a somewhat unexpected result and may have engineering significance, see Cooker and Peregrine (1992).

The total impulse on the baffle when $H_b = 1.0$ is the same as Cooker's model for problem 1 and 2:
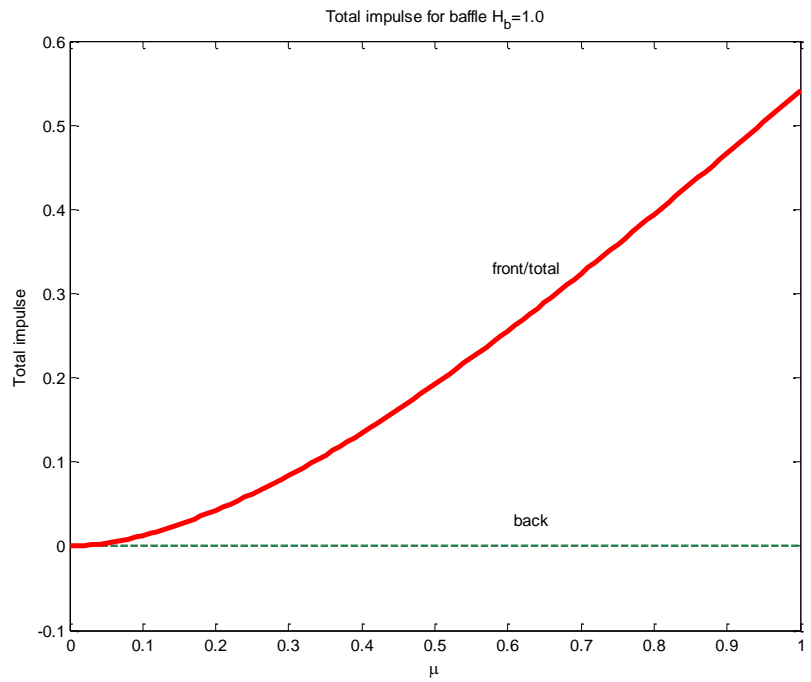
Figure 7.5.4: Total impulse on baffle for $H_b = 1.0$

The total impulse on the baffle when $H_b \approx 1.0$ for problem 3:
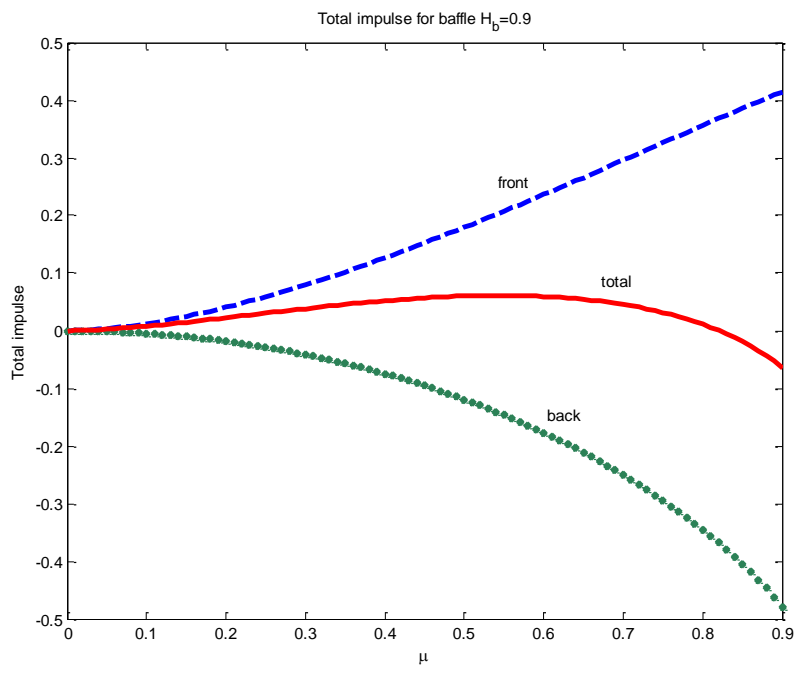
Figure 7.5.5: Total impulse on baffle for $H_b = 0.9$

7.5.2 Total impulse on the seabed

Total impulse on the seabed, I_s is given by the integral of $P(x, y)$ from $x = b_1$ to $x = b_2$:

$$I_s = \int_{b_1}^{0} P_1(x, y)dy + \int_{0}^{b_2} P_2(x, y)dy$$

The total impulse on the seabed for each problem we can see as figure 7.5.6.

The total impulse on the baffle when $H_b = 1.0$ is the same as Cooker's model for problem 1 and 2, as in figure 7.5.6:
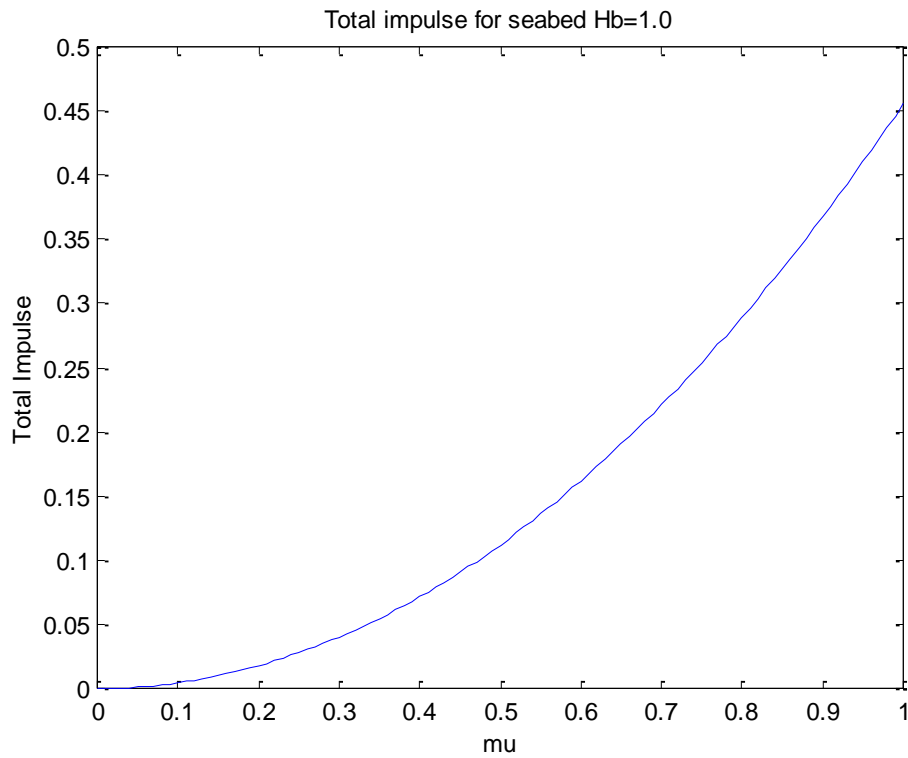
Figure 7.5.6: Total impulse on the seabed for $H_b = 1.0$

The total impulse on the baffle when $H_b \approx 1.0$ for problem 3, is greater than problem 1 and 2 as in figure 7.5.7 below.
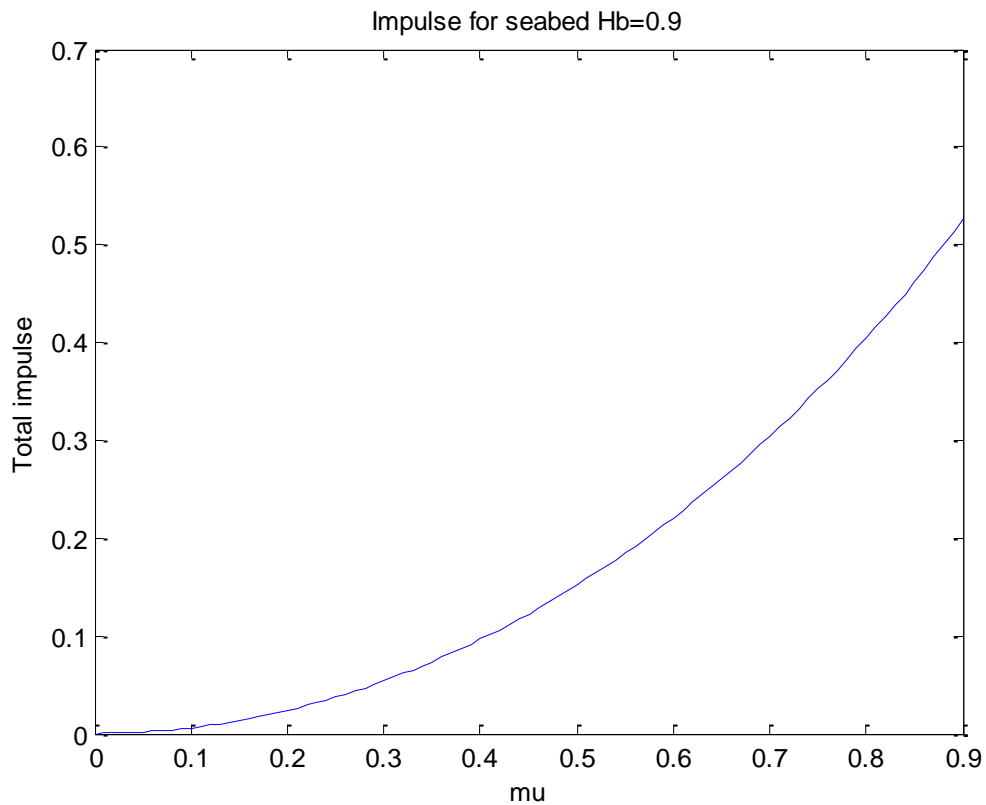
Figure 7.5.7: Total impulse on the seabed for $H_b = 0.9$

Figure 7.5.8 and 7.5.9 show the comparison of the total impulse on seabed for the four problems. We can see that the highest total impulse on the seabed for problem 3 (for both lengths of baffles), and for problem 1,2 and 4, they have almost same figures for $H_b = 0.5$. All problems have higher total impulse on seabed when the length of baffle increases. When $H_b = 0.8$, total impulse on seabed for problem 4 is slightly higher than problem 1 and 2.
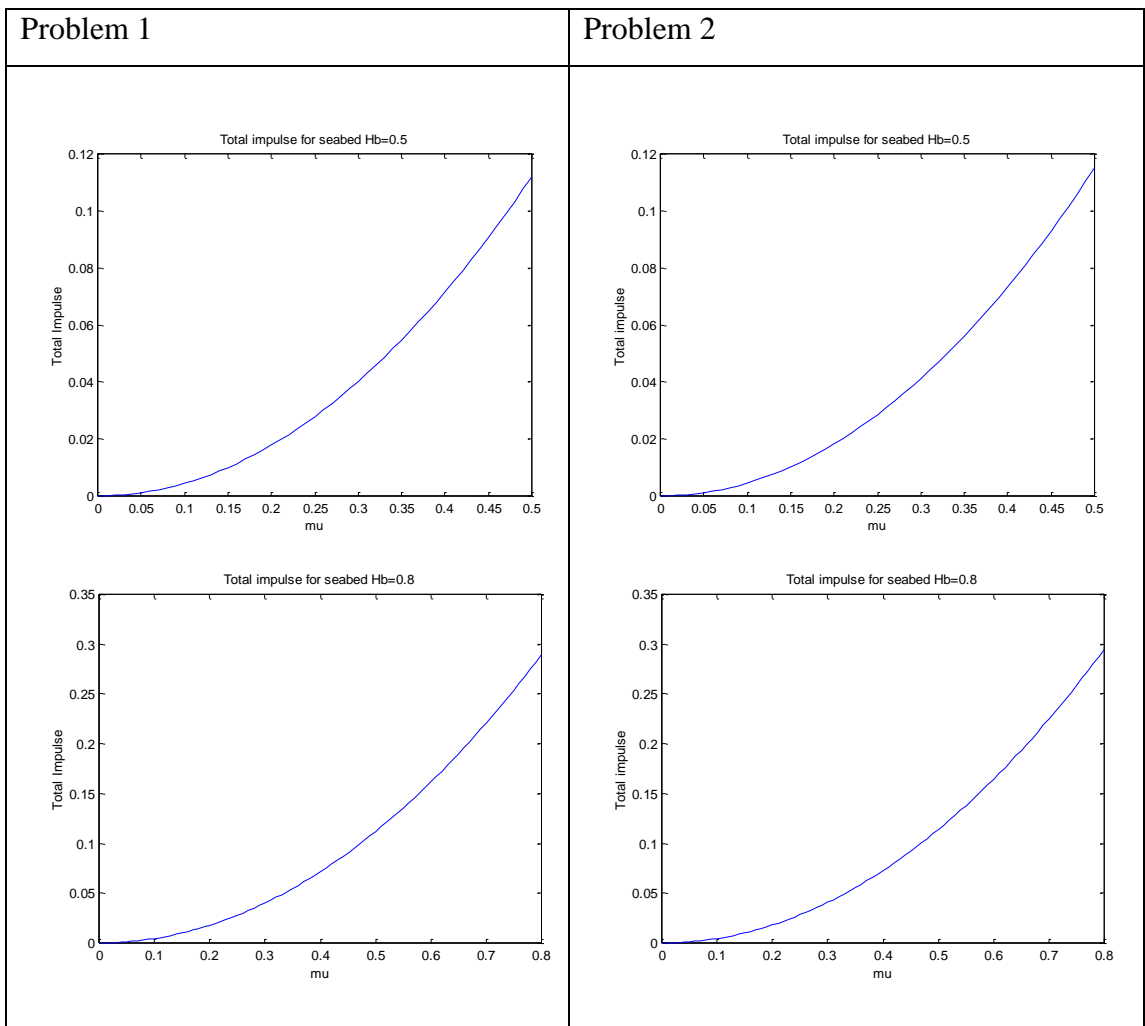
Problem 1	Problem 2

Figure 7.5.8: Total impulse on the seabed for $H_b = 0.5$ and $H_b = 0.8$
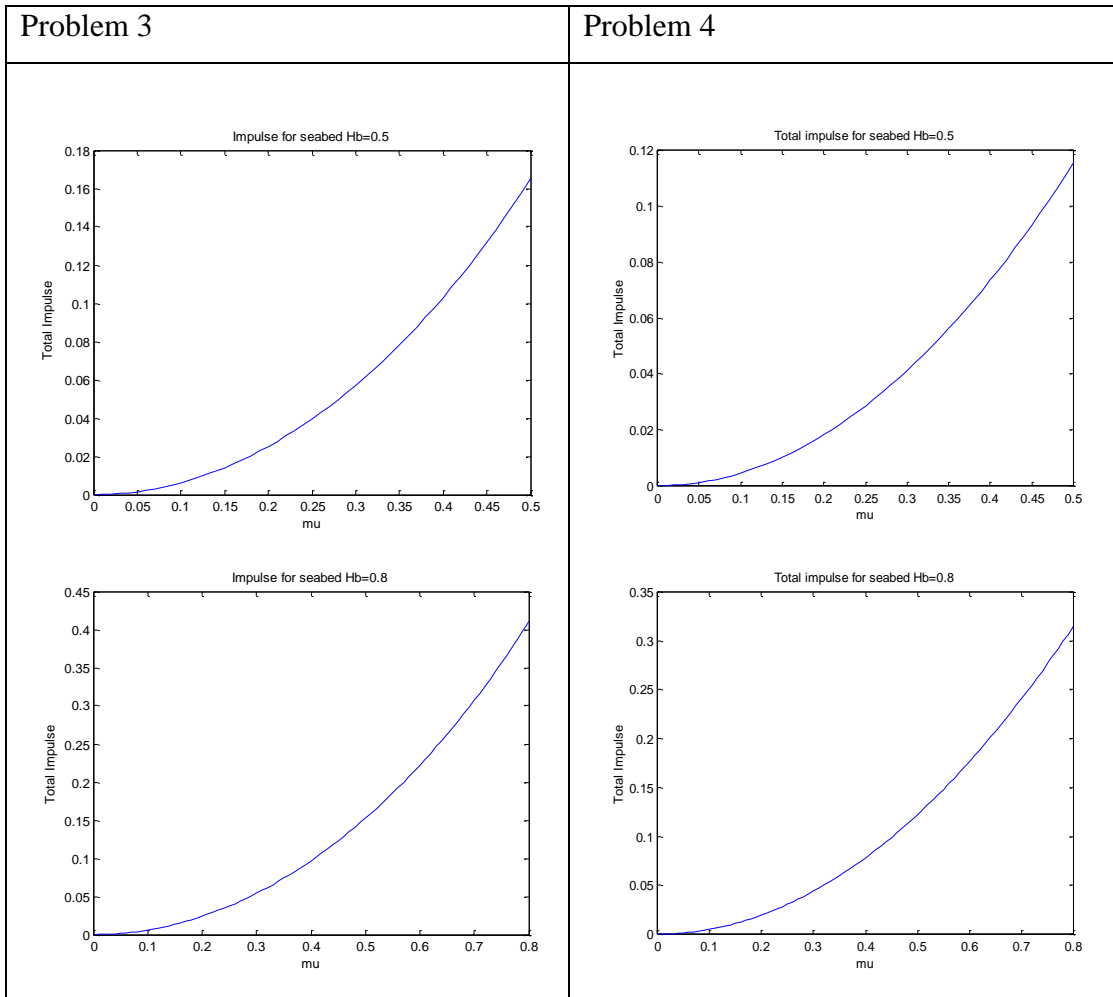
Problem 3	Problem 4

Figure 7.5.9: Total impulse on the seabed for $H_b = 0.5$ and $H_b = 0.8$

7.5.3 Total impulse on the wall

The total impulse on the wall, I_w is given by the integral of $P_1(x, y)$, (which $x = b_1$ for problems 2 and 3 and $x = 0$ for problem 4) from $y = -1$ to $y = 0$:

$$I_w = \int_{-1}^{0} P_1(x, y)\,dy$$

as is shown in figure 7.5.7. We can see that the lowest total impulse on the wall is in problem 2. The highest is in problem 4 as expected because the baffle is located on the seabed. The total impulse on the wall for problem 3 is higher than problem 2, and in the seaward direction.

Problem 2	Problem 3	Problem 4
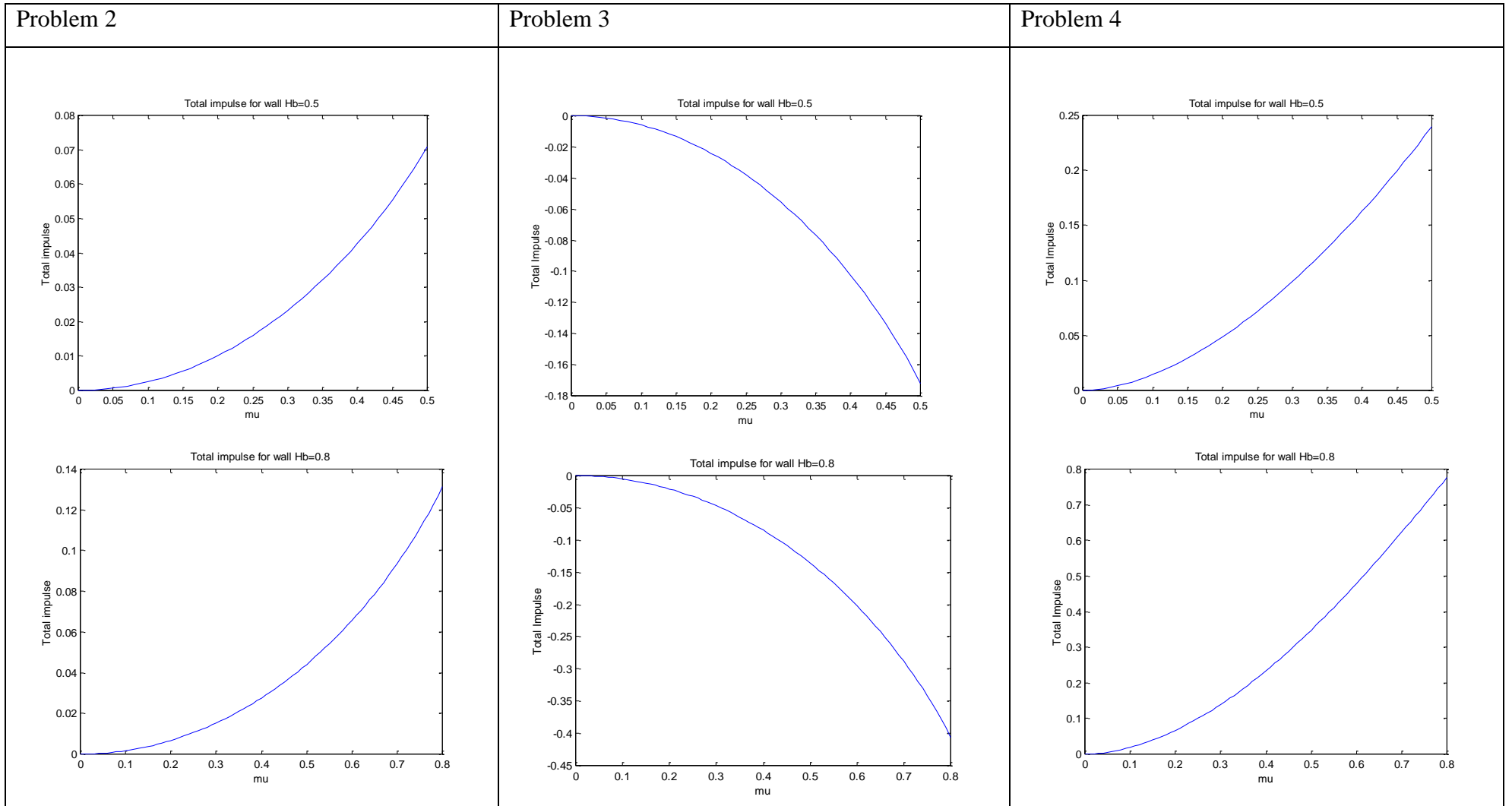
Figure 7.5.10: Total impulse on wall for $H_b = 0.5$ and $H_b = 0.8$

7.5.4 Total impulse on the deck

Total impulse on the deck, I_d for problem 3 is given by the integral of $P_1(x,0)$ from $x = b_1$ to $x = 0$:

$$I_d = -\int_{b_1}^{0} P_1(x,0)dx$$

The total impulse on deck for $H_b = 0.5$ and $H_b = 0.8$ is given in figure 7.5.11 and figure 7.5.12 respectively. When the length of baffle increases the total impulse on the deck increases.
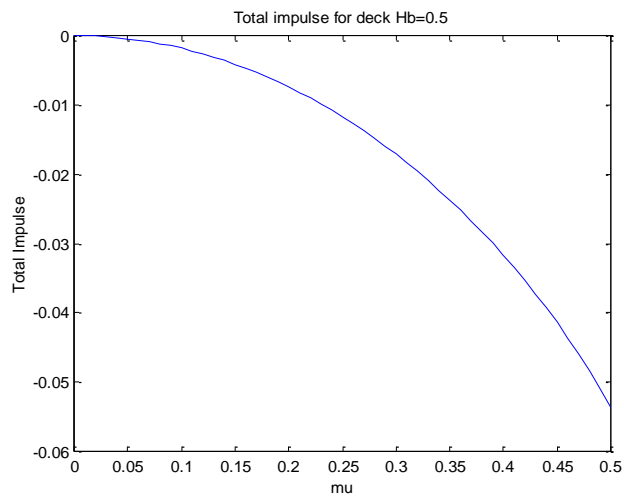
Figure 7.5.11: Total impulse on deck for $H_b = 0.5$
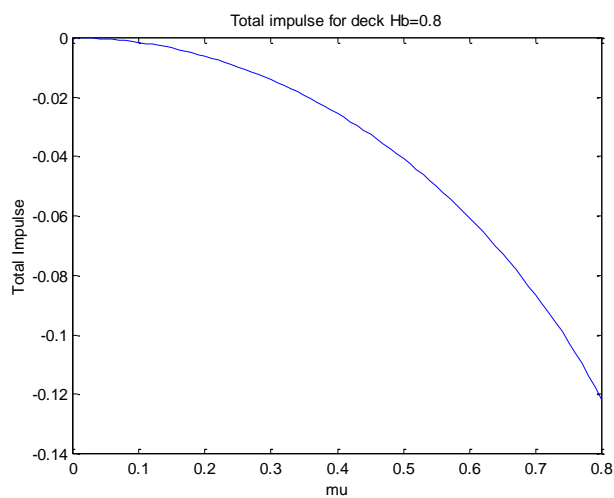
Figure 7.5.12: Total impulse on deck for $H_b = 0.8$

7.6 Moment Impulse

In this section we will calculate the moment impulse on the baffle, M_b on the wall, M_w on the seabed, M_s and on the deck, M_d for each problem. We take the clockwise direction sense about the foot (●) of the wall as positive moment.
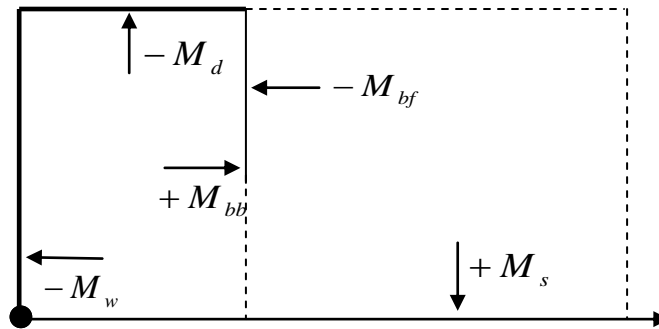
Figure 7.6.1: The direction of the moment impulses.

7.6.1 Moment impulse on the baffle

The moment impulse on the baffle, M_b is given by adding the moment impulse on back of the baffle, M_{bb} and moment impulse on the front of baffle, M_{bf} and its positive for moment impulses directed in a clockwise sense about the foot of the wall.

$$M_b = \int_{-H_b}^{0} (y + H_b) P_1(x, y) dy - \int_{-H_b}^{0} (y + H_b) P_2(x, y) dy$$

The moment impulse on the baffle for each problem we can see as below:

      i)   Moment impulse on baffle for problem 1

      ii)   Moment impulse on baffle for problem 2

      iii)   Moment impulse on baffle for problem 3

      iv)   Moment impulse on baffle for problem 4

Figure 7.6.2 and figure 7.6.3 show the moment impulse for the whole structure with a baffle for each problem. We can see that the moment impulse for problem 3 is the opposite direction and quite a bit higher than problem 1, 2 and 4. The moment impulses for problem 1, 2 and 4 are almost same except the shape of the graph for problem 4 is quite different.

Problem 1	Problem 2
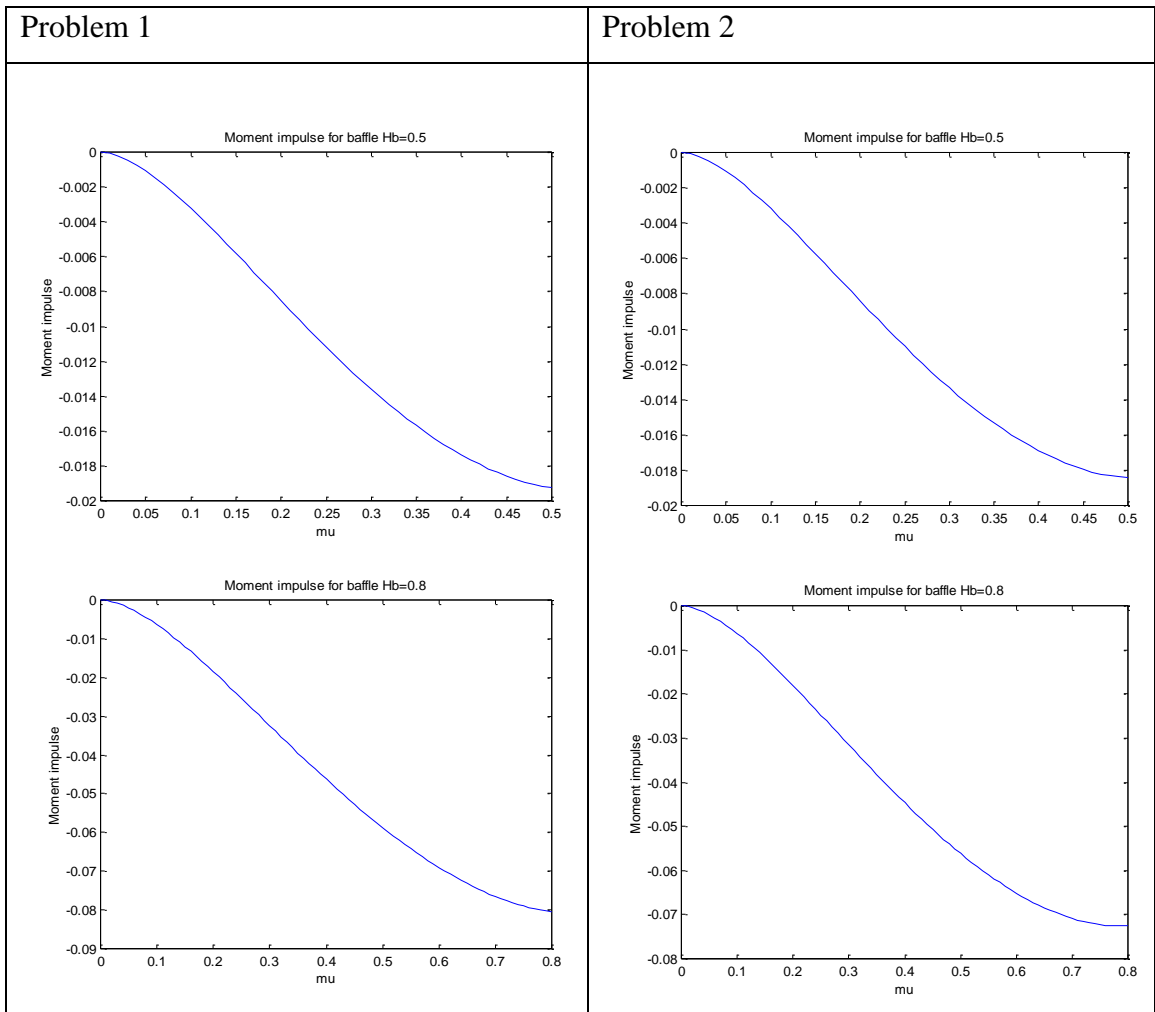
Figure 7.6.2 : Moment impulse on baffle for $H_b = 0.5$ and $H_b = 0.8$.
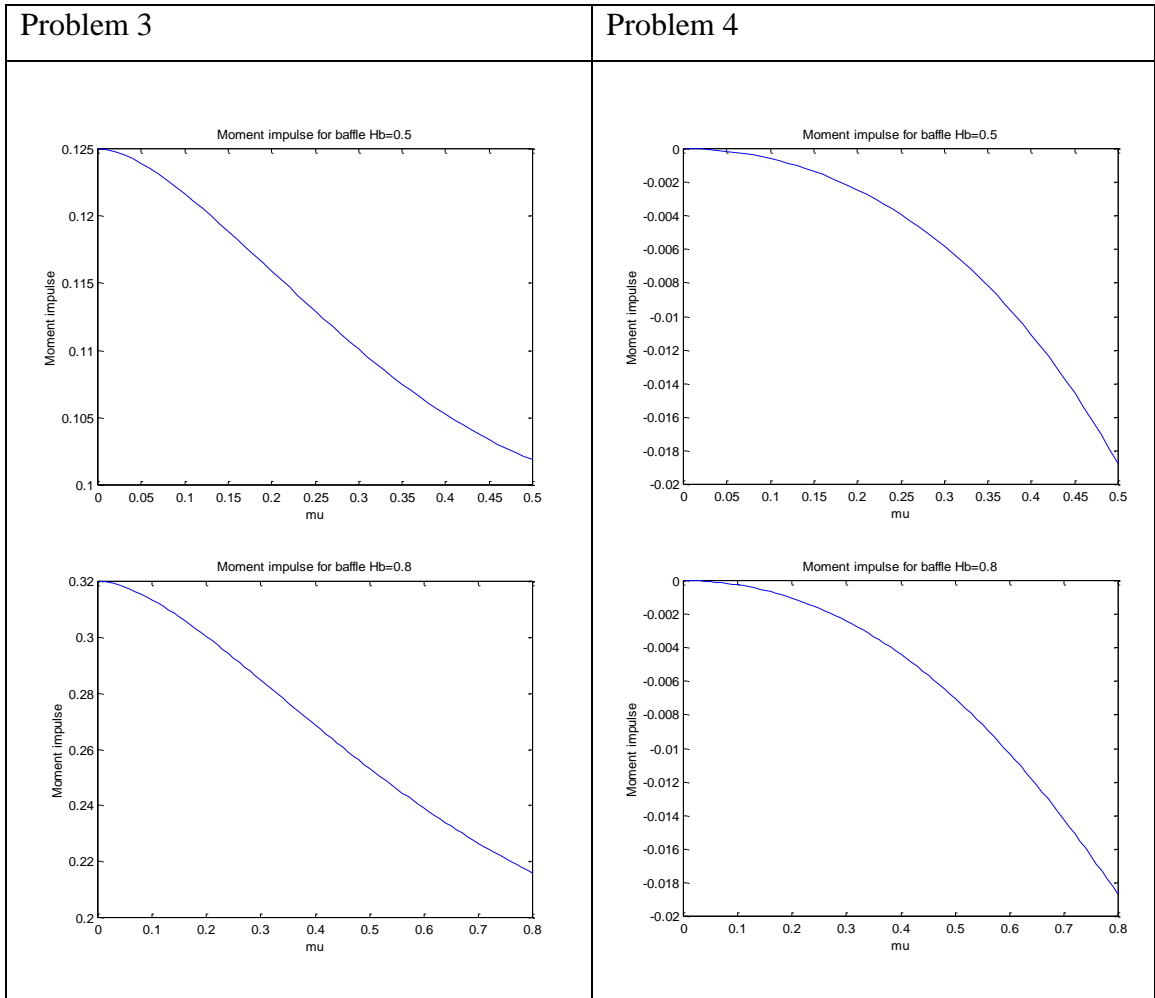
Problem 3	Problem 4

Figure 7.6.3: Moment impulse on baffle for $H_b = 0.5$ and $H_b = 0.8$

7.6.2 Moment impulse on the seabed

The moment impulse on the seabed about the foot of the wall is

$$M_s = \int_{b_1}^{0} xP_1(x, y)dx + \int_{0}^{b_2} xP_2(x, y)dx$$

The moment impulse on the seabed for each problem is shown in figures 7.6.4 and 7.6.5. We can see that the highest moment impulse on the seabed is in problem 3 followed by problem 4. Problems 1 and 2 are almost the same. Moment impulses for all problems increase when the length of the baffle increases. The moment impulse for problem 1 is higher than problem 2. Problem 3 remains the highest and problem 4 is the lowest.

7.6.3 Moment impulse on the wall

The moment impulse on the wall, about an axis at its bottom, due to the pressure impulse on the wall is

$$M_w = -\int_{-1}^{0} (y+1)P_1(x,y)dy$$

and the results we can see in figure 7.6.6. We can see that the moment impulse on the wall for problem 3 is in the seaward direction and it has the highest moment impulse compared to problems 2 and 3.
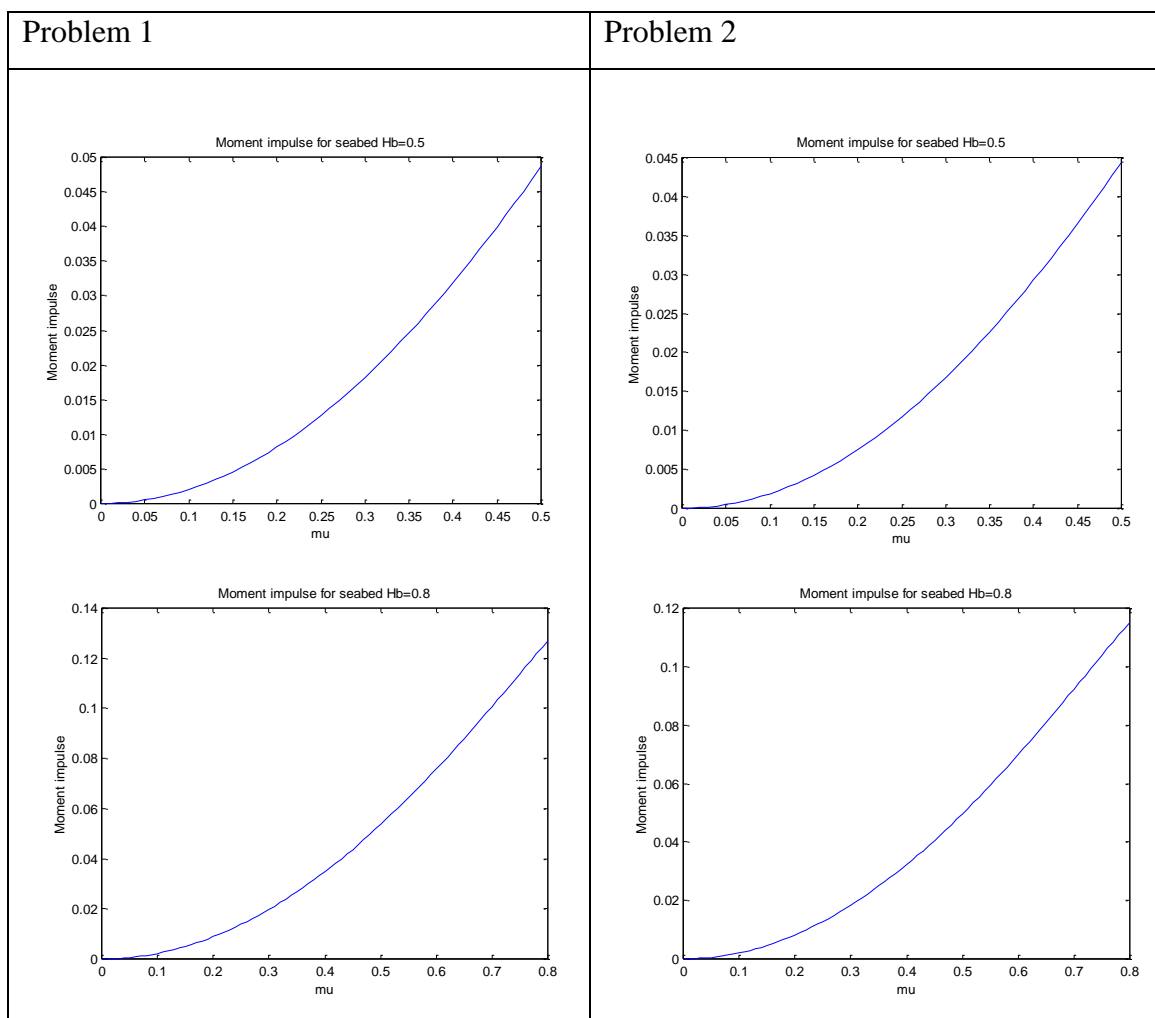
Figure 7.6.4: Moment impulse on seabed for $H_b = 0.5$ and $H_b = 0.8$

Problem 3	Problem 4
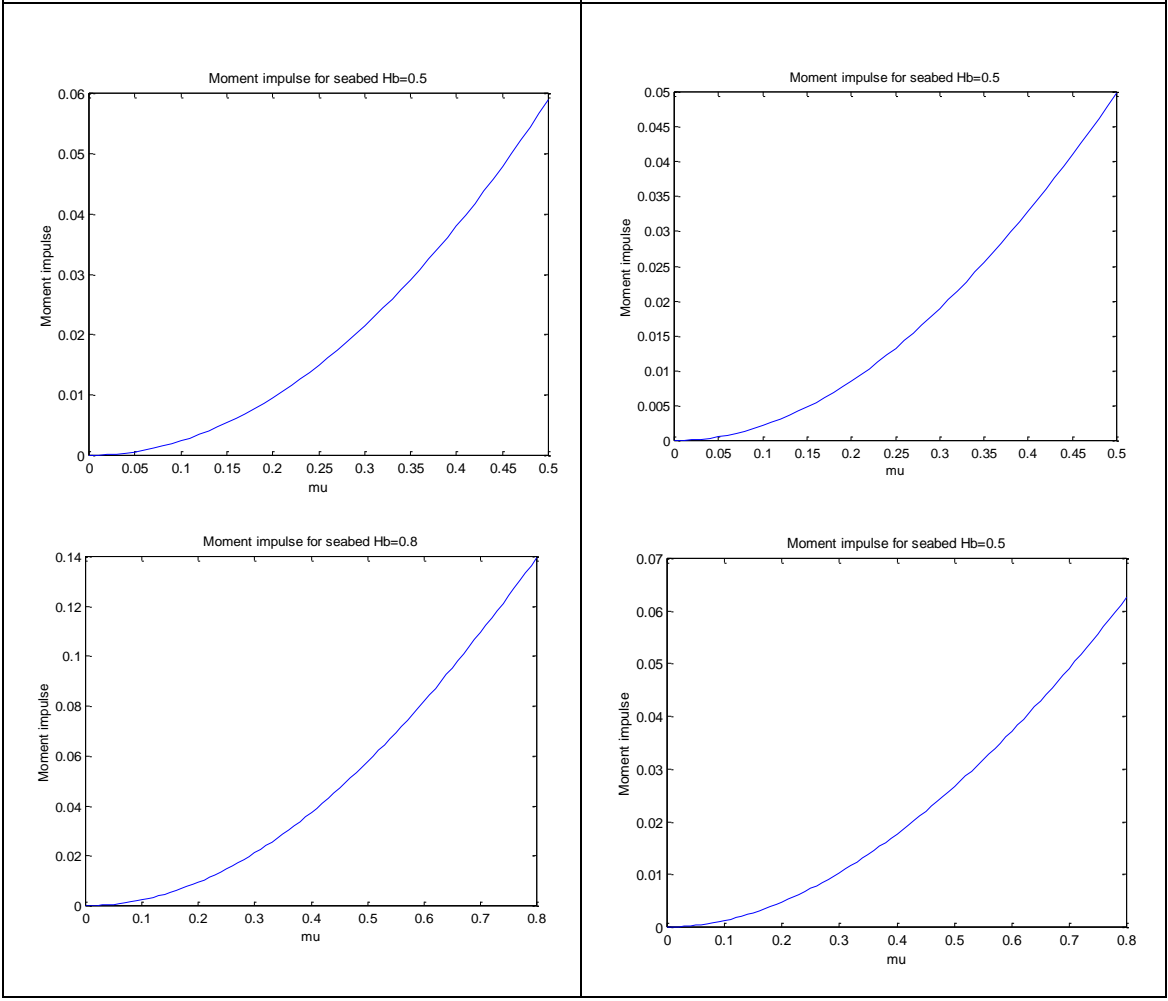
Figure 7.6.5: Moment impulse on seabed for $H_b = 0.5$ and $H_b = 0.8$.

Problem 2	Problem 3	Problem 4
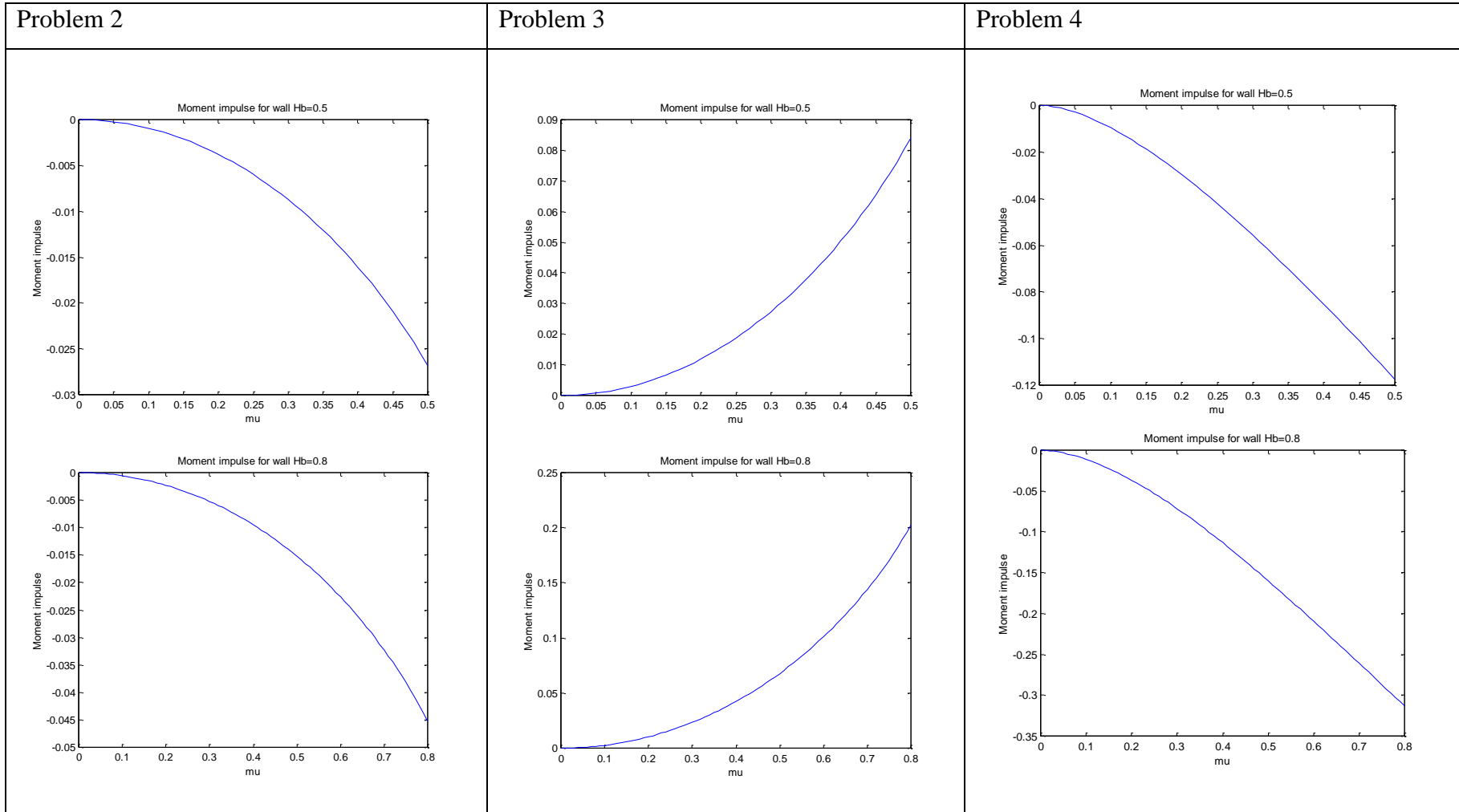
Figure 7.6.6: Moment impulse on the wall for $H_b = 0.5$ and $H_b = 0.8$

7.6.4 Moment impulse on the deck

The moment impulse on the deck about the foot of the wall is

$$M_d = -\int_{b_1}^{0} xP_1(x, y)dx$$

The moment impulse on the deck for problem 3 is given in figures 7.6.7 and 7.6.8. The moment impulse increases when the length of baffle increases.
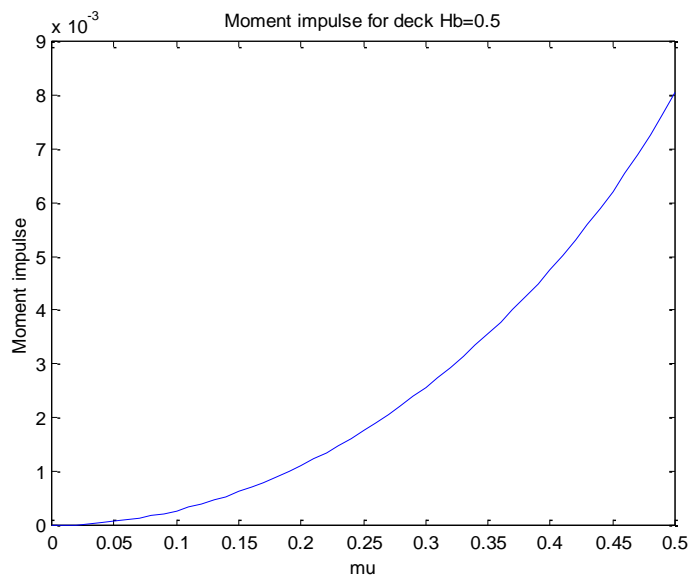
Figure 7.6.7: Moment impulse on deck for $H_b = 0.5$
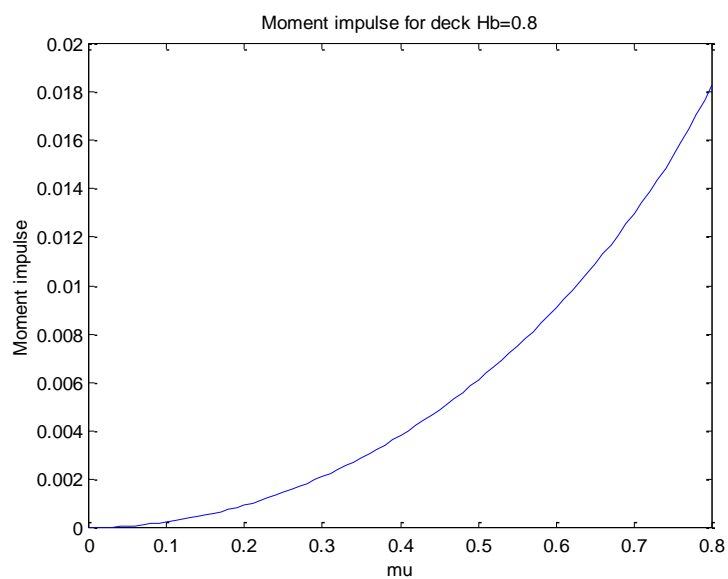
Figure 7.6.8: Moment impulse on deck for $H_b = 0.8$

7.7 Conclusion

We can see different impact pressure impulse distributions for different cases of baffle. We note that pressure impulse on the baffles is almost the same for cases 1, 2 and 3 for different length of baffles with same size of impact. However the pressure impulse behind the baffles decreases when the length of baffle increases for problem 2 and 3.

For problem 4, the pressure impulse on the wall and behind the baffles increases when the length of baffle on the seabed increases.

The total impulse in front of baffles is greater than those on the back of baffle for problems 1 and 2. In contrast, for problem 3 the total impulse behind the baffle is greater than total impulse in front of the baffle.

The total impulse on the seabed for problem 3 is the highest compared to the other problems.

Problem 4 has the highest total impulse on the wall. The total impulse on the wall for problem 3 is higher than problem 2 and in the seaward direction. This somewhat counter-intuitive result arises from high pressure impulses behind the baffle being trapped beneath a rigid top surface.

CHAPTER 8

CONCLUSIONS

8.1   Conclusions

In this thesis we have explored various mathematical models of wave impact on rectangular structures. By solving Laplace's equation for the pressure impulse, *P*, we model a wave breaking against vertical structures. We have been particularly interested in the pressure impulse that is generated, due to the damage that they it can cause to structures.

Chapter 2 reviewed the literature concerning the modelling of wave breaking against coastal structures, and then derived the Pressure Impulse theory.

In Chapter 3 we considered a two-dimensional model of the berm and ditch problems. We compared the berm and ditch results with a vertical wall. When comparing the worst cases i.e. those for the largest possible impact region, the seawall with a ditch has a largest maximum pressure impulse which is $1.400\rho U_0 H$, with $\mu = 1.2$, the basic seawall (Cooker's model) has pressure impulse $0.742\rho U_0 H$, with $\mu = 1.0$, and the seawall with a berm has the smallest maximum pressure impulse which is $0.570\rho U_0 H$, with $\mu = 0.8$.

From table 3.8.1, we can see that total impulse on the wall with a ditch is the greatest followed by the plain seawall and then the berm as expected. This is partly because a seawall with a ditch has the largest area of impact while the area of impact of a seawall with a berm is smaller than for the plain seawall. The same trend occurs for total impulse for the seabed as defined in figure 3.5.1

Table 3.8.2, shows the moment impulse for wall and seabed for the vertical wall, berm and ditch problems. We can see that a seawall with a ditch has the largest value of moment impulse on the wall and on the seabed. As expected, the moment impulse for a seawall with a berm has the smallest value compared to the other two problems.

We can conclude that a seawall with a berm has a beneficial effect on reducing pressure impulse while a seawall with a ditch can be very detrimental. This means that scour at the base of a seawall is likely to be extremely dangerous. For the maximum impact region, a seawall with a berm has a beneficial effect on reducing pressure impulse by almost 23% (compared with Cooker's model) while a seawall with a ditch makes the impact almost double. This confirmed the work of Greenhow (1996).

Figure 3.7.2 shows the overtopping discharge for a seawall with a berm and a ditch. We can see that the discharge of the overtopping for both cases is comparable for corresponding freeboard values. Having said that, the freeboard values for the berm are substantially higher than for the ditch, meaning that the berm's jet will reach far higher in the air.

Further results show that the ditch overtopping is largely insensitive to the ditch width (as expected because the ditch pressure is almost constant). More surprisingly, the berm overtopping is also quite insensitive to the berm size if the berm is submerged to at least half the water depth. On the other hand if the berm's top is near the bottom of the impact region then there is typically an increase of about 20% to 30% compared with a deeply submerged berm, for any given freeboard.

In Chapter 4, a structure with a missing block, we divide the structure into two regions, where the inner region is for the missing block. The results show no noticeable decrease in pressure impulse in the missing block region. This agrees with Wolters and Müller

(2004) who also concluded that partially-filled cracks are more dangerous for the integrity of the structure than fully-filled cracks.

From the comparison results for different widths ($B_1 = 0.1, 0.2, 0.3$) of block with same depth ($H_2 - H_1 = 0.1$) of the missing block for varying μ **,** we can conclude that the pressure impulse decreases when the width of missing block increases. The pressure in the missing block region looks almost constant. As μ increases, the pressure impulse in this region also increases.

The comparison of results for different depths ($H_2 - H_1 = 0.1, 0.2, 0.3$) of block with the same width ($B_1 = 0.2$) for varying μ show that the pressure impulse for different depths gives no significant difference, except for the pressure impulse in the missing block region, which shows slight decrease when the depth is increased. We can conclude that the thinner the missing block, the greater the pressure impulse on the walls of the missing block region. For the pressure impulse on the wall in the outer region, we get an increase when μ increases.

We also found that the total impulse on the wall for the missing block problem is greater when the location of the missing block is close to the seabed, but it is still smaller than the total impulse on the wall for Cooker's model. The same trend happens to the total impulse on the seabed.

The results for the total impulse on seawall, the total impulse on the inner region (top and bottom of the block) and on the seabed can be seen in figure 4.5.2 to 4.5.5. Figure 4.5.2, figure 4.5.3 and figure 4.5.4 show the total impulse on the wall and on the top and bottom of the missing block, with different location of the missing block but the same width and depth. We can see that when the location of the missing block is closer to the seabed, the total impulse for each face increases. For instance, for total impulse on the wall, the first location which near to the free surface $(H_1 = 0.2, H_2 = 0.3)$ has a total impulse of 0.0425 $\rho U H^2$, the second location $(H_1 = 0.5, H_2 = 0.6)$ has a total impulse of 0.190 $\rho U H^2$ and the location near to the seabed $(H_1 = 0.8, H_2 = 0.9)$ has a total impulse of 0.380 $\rho U H^2$.

We also can see there is a total impulse on the vertical wall at the inner region but it is small compared to vertical wall at the outer region. However, it can be larger than the total impulse at the bottom of the vertical wall of the outer region when the location of the missing block is near to the seabed. The total impulse on the top and bottom of the inner region largely cancel each other. Given the almost constancy of the pressure in the missing block region, this is expected. These impulses do not move the wall vertically but may tend to open cracks in the missing block region.

We can see that the total impulse increases when the location of the missing block moves down to the seabed, see figure 4.5.5. The total impulse on the wall is larger than the impulse on the seabed in all cases.

Figures 4.6.2 to 4.6.4 show the moment impulses for different locations of the missing block. We can see that the deeper the location of the missing block, the bigger the overturning moment impulse. We also can see that the moment impulse on the seabed for each case is lower than the total moment impulse on the wall.

The moment impulse on the wall and the seabed for the missing block problem is greater when the location of the missing block is close to the seabed. Compared to the Cooker model, the moment impulse on the wall for the missing block is greater than moment impulse on the wall for Cooker's model. However for the moment impulse on the seabed, the missing block problem has a much smaller value than Cooker's model.

Since region 2 is largely unaffected by the missing block, the overtopping calculations will be almost the same as for the simple seawall.

The work of Chapter 5 and Chapter 6 studied the effect of having a deck projecting from a seawall. To do this it was useful to consider the impact of a wave from different directions.

Chapter 5 considered a wave impacting the seawall. It is found that pressure impulse on the wall is greater when the length of the deck is bigger. For the same length of deck, the pressure impulse is greater when the impact region is larger.

We notice that the value of pressure impulse increases when the value of μ increases for each length of the deck. If we compare the results between the different lengths of deck, we can see the pressure impulse also increases when the length of the deck increases. The largest value of pressure impulse is when $\mu = 1.0$ which is 0.7546 $\rho U_0 H$ and 0.9909 $\rho U_0 H$ for $b_1 = 0.1$ and $b_1 = 0.5$ respectively for depth 1 below the free surface. The first shows the good agreement with Cooker and Peregrine (1995) who discovered the maximum value of pressure impulse is 0.742 $\rho U_0 H$ when $\mu = 1.0$ for depth 1 below the free surface.

A good agreement is also shown with Cooker and Peregrine (1995), in which the different impact lengths give very similar pressure impulse distributions near the impact wall.

We see that having a deck on the top of the wall can dramatically increase the pressure impulse on the wall. The position of the maximum P can move to the corner between the vertical wall and the deck, see figures 5.4.9 and 5.4.10. Hence we can conclude that having a deck on the top of the seawall increases the value of the maximum pressure impulse and the extent down the seawall of a high pressure impulse region. These results show a good agreement with those of Oumeraci (1994), which gave a high pressure impulse on the breakwater resulting from wave impact on the deck.

The highest values for pressure impulse occur at the wall and the region beneath the deck. As μ increases towards 1 the maximum value increases, as expected, the pressure impulse also increases as the length of the deck increases.

Figures 5.4.13 and 5.4.14 show the distribution of pressure impulse in the water beneath the deck for different values of μ and b_1. The highest value of pressure impulse occurs at the landward end and it increases as μ increases toward 1. The values of pressure impulse for $b_1 = 0.5$ are more than 50% greater than those for $b_1 = 0.1$ for each value of μ. Overall we can see that pressure impulse beneath the deck is greater than pressure impulse along the seabed.

The total impulse for a seawall with a deck is greater than the total impulse for Cooker's model. When the length of deck increases, the total impulse increases. The total impulse on the seabed for a seawall with a deck is greater than the total impulse for Cooker's model. When the length of deck increases, the total impulse increases. The total impulse beneath the deck is greater when the length of the deck is bigger.

The moment impulse on the wall for a seawall with a deck is almost double the moment impulse for Cooker's model. It increases when the length of the deck increases. The moment impulse on the seabed also increases when the length of the deck increases. The moment impulse beneath the deck becomes larger when the length of the deck is bigger. The presence of a deck increases the overtopping.

Chapter 6 considered a wave impacting upwards underneath a deck. We confirmed that increasing the length of the deck increases the pressure impulse and total impulse for the both cases. Similar results for the case in Chapter 6 are given in Wood and Peregrine (1997). The moment impulse beneath the deck, becomes larger when the length of the deck is bigger.

We found that the pressure impulse on the deck increases when the length of deck increases. There is a strong pressure gradient beneath the deck near the seaward edge. Similar results were found in Wood and Peregrine (1997) who studied the pressure impulse beneath the deck for different depths of water for the same length of deck. We also agreed that the maximum pressure impulse is at the landward end of the impact zone.

We can conclude that when the deck's length to depth ratio is increased, the pressure impulse will increase. The same trend was described by Wood and Peregrine (1996).

Finally, in Chapter 7 we studied pressure impulse for different cases of baffle. We can see different impact pressure impulses for different cases of baffle. We note that pressure impulse on the baffles is almost the same for cases 1, 2 and 3 for different length of baffles with the same size of impact. However the pressure impulse behind the baffles decreases when the length of baffle increases for problem 2 and 3.

For problem 4, the pressure impulse on the wall and behind the baffles increases when the length of baffle on the seabed increases.

As we can see that for problem 1 in figures 7.4.1 and 7.4.2 the pressure impulse on the baffle increases when μ increases. For small μ, the pressure impulse is almost same for different lengths of baffle but when μ is greater, the pressure impulse is higher the greater the length of the baffle.

For problem 2, the pressure behind the baffle increases when μ increases but it decreases when the length of baffle increases.

For a closed surface between the wall and baffle (problem 3), we can see there is a high pressure behind the baffle. For the same size of impact, let say $\mu = 0.5$, the pressure impulse behind the baffle is greater when the length of baffle increases.

We have a different case for problem 4 which the baffle is located on the seabed in front of the wall. We can see that pressure impulse on the wall is greater when μ increases and the pressure impulse behind the baffle increases for higher lengths of baffle for the same impact.

From the comparison between the four problems for the same baffle length and μ, we can see that the pressure on the baffle for problem 1 to 3 are almost the same and they have a small increase when the length of baffle increases. For problem 2, the pressure impulse behind the baffle at the bottom is high and it decreases when length of baffle increases. For problem 3, the pressure impulse behind the baffle under the closed region is higher when the length of the baffle is smaller. This contrasts with problem 4, where the pressure impulse on the wall is greater than on the baffle for problem 1, 2 and 3 and the pressure impulse behind the baffle is greater when the baffle is higher.

The total impulse in front of the baffle for problem 1 and 2 is higher than the total impulse behind the baffle. The total impulse on the front of the baffle and behind the baffle for problem 2 is higher than problem 1 respectively. However the total impulse (obtained by adding the total impulse on the front and on the back of the baffle) shows

problem 1 is only slightly higher. The total impulse for both problems increases when the length of the baffle increases.

For problem 3, the total impulse on the front of the baffle is higher than the total impulse behind the baffle. However we can see that when the length of baffle increases, the total impulse at the back is slightly higher than at the front. The total impulse after adding the total impulse at the back and in front of baffle is smaller than problems 1 and 2. For a greater μ, the total impulse at the back for problem 3 is higher than total impulse on the front of baffle, so it will push the baffle seaward. This somewhat counter-intuitive result arises from high pressure impulses behind the baffle being trapped beneath a rigid top surface.

The lowest total impulse on the wall is in problem 2. The highest is in problem 4 as expected because the baffle is located on the seabed. The total impulse on the wall for problem 3 is higher than problem 2, and in the seaward direction. For problem 4 we can see that the total impulse at the back is greater than at the front of the baffle.

Experimental comparison may be time consuming due to the many parameters involved. The present study will hopefully inform experimenters as to the likely effect of varying these parameters and suggest which experiments would be most useful to do.

8.2 Method used in the thesis

We use two methods to solve the problems in this thesis. For problem in Chapter 3, Chapter 5 and Chapter 6 we used hybrid collocation method and for Chapter 4 and Chapter 7 we used a basis function method. In contrast to the simple seawall case of Cooker (1990), the basis functions are not orthogonal over the integration range and hence we do not get the unknown coefficients explicitly, as in equation (2.4.15). Instead this procedure gives a matrix system, which is truncated and solved in MATLAB. This can cause numerical problems in some cases.

We initially wanted to use the basis function method to solve all the problems in this thesis, but the method failed for the Fourier series in Chapter 5 and Chapter 6. Then we introduced collocation method and used it first to solve the problems in Chapter 3, the berm and ditch problems which were solved by Greenhow (2006) using a basis function method. After it worked for berm and ditch, this method was applied to solve the problems in Chapter 5 and Chapter 6 where the basis function method fails.

8.2.1 The difference between basis function method and hybrid collocation method

After we have a formulation which satisfies all the boundary conditions in the problems except on the impact region, both methods use an integral method on the seawall which gives us a forcing term on the right hand side of the resulting matrix system. The difference between these two methods is at the matching interface, see Chapter 3-6. For basis function method, we multiply by basis functions and integrate over the depth for both sides of equations and its derivatives. In contrast, for hybrid collocation method, we matched the equations and its derivatives by the collocation points distributed over the depth. We explored and compared both methods in Chapter 3 and Chapter 4. Comparisons were made between both methods for the simple seawall, in order to establish the collocation method for a known case.

8.2.2 The reasons basis function method fails for the Fourier series in Chapter 5 and Chapter 6

The reason why the basis function method failed in Chapter 5 and Chapter 6 is not fully understood, analytically. The hyperbolic terms such as $\dfrac{\cosh(\gamma_n(x-B_1))}{\cosh(\gamma_n B_1)}$ in both chapters require MATLAB to evaluate very large numbers which may lead to overflow problems. More importantly the hyperbolic terms in Chapter 4 result in terms such as

214

$$\frac{\cosh\left(\dfrac{2\gamma_n x}{H_2 - H_1}\right)}{\cosh\left(\dfrac{\gamma_n B_1}{H_2 - H_1}\right)}$$ which grow exponentially large for finite x and their evaluation is

needed at the matching boundary. However the method still works in Chapter 7 which has the same hyperbolic term as in Chapter 5 and Chapter 6. So we conclude that the basis function method fails for the Fourier series numerically, not mathematically, in Chapter 5 and Chapter 6. On the other hand the collocation method does not require multiplication by basis function, so the 2 in the above cosh term is missing and the exponential growth is less rapid. This postpones the problem so that most cases of practical interest, with moderate values of x at the matching interface, can be calculated. We showed that in cases where both methods work, the collocation method is, in fact, preferable anyway.

8.3   Poorly-conditioned matrix

Sometimes, in Chapter 5 for example, we will get a non-sensical graph and warning from MATLAB as in figure 2.9.1. The poor conditioning means the solution $\underset{\sim}{x}$ is sensitive to numerical errors in the RHS $\underline{b}$ of $A\underline{x} = \underline{b}$. A square matrix A also can become poor-conditioned if it is invertible but can become singular when some of its entries are changed very slightly. Figure 8.1 shows an example of a poorly conditioned matrix which happened when the value of b, was slightly changed.

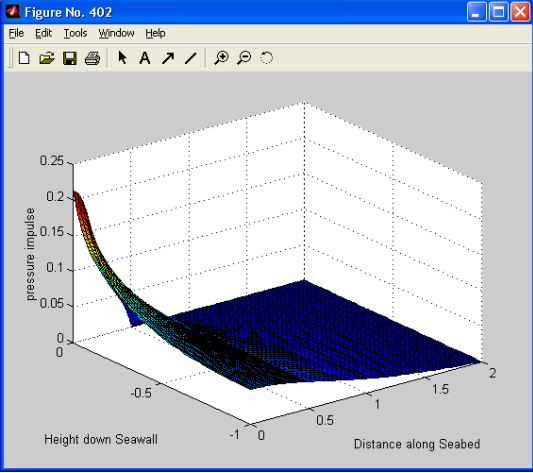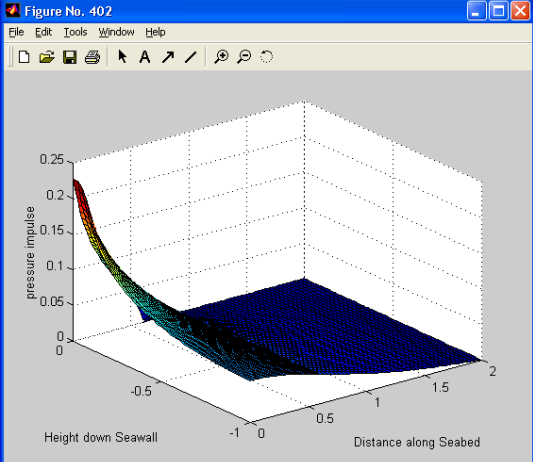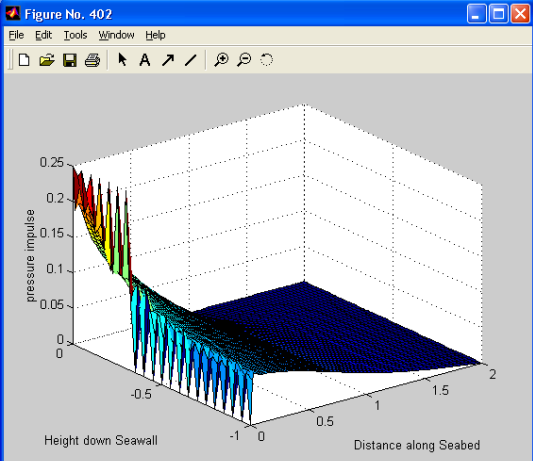| Length of deck	Results
$b_1 = 0.5$	
$b_1 = 0.6$	Warning: Matrix is close to singular or badly scaled. Results may be inaccurate. RCOND = 4.028648e-017.
$b_1 = 0.7$	Warning: Matrix is close to singular or badly scaled. Results may be inaccurate. RCOND = 4.028648e-017.

Figure 8.3.1: Poorly-conditioned matrix

8.4   Possible extension to VLFS

i.   Very large floating structure (VLFS) problem

A very large floating structure (VLFS) is a floating structure with very large length-to-draft and width-to-draft ratios relative to the largest existing ships (Jiao, 2011). This problem has studied by Jiao for floating airports, where wave impact on the seaward edge of the structure was solved using advanced numerical solvers. In principle we could apply pressure impulse theory to solve this problem.

The problem needs to be divided into three regions.
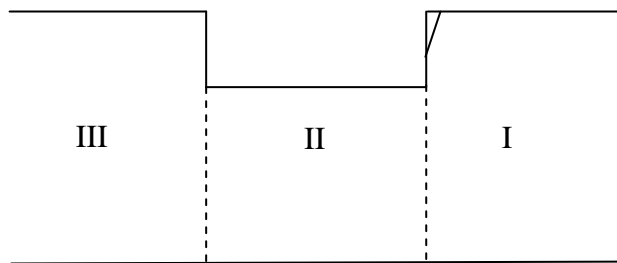
Figure 8.4.1: VLFS sketch model, wave impact on the seaward edge.

The impact region indicated here is on the front of the VLFS.   Jiao and Linlin considered impact on the bottom of a structure of very small draft which might be modelled as:
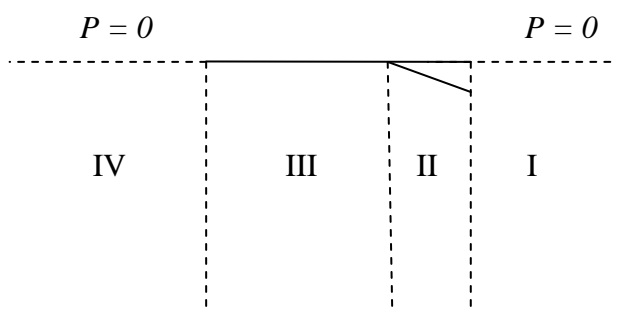
Figure 8.4.2: VLFS sketch model, wave impact on the front of the VLFS.

Here there would be four regions to consider, or perhaps three if the VLFS length is considered to be infinite. The specification of the eigenfunction expansions under the impact region (II) cannot exploit the boundary conditions (as has been done throughout this thesis) and would need special care.

APPENDIX

Chapter 2

A.2.1 Convergence and divergence check for the overtopping formula.

Since the initial upwards velocity (before impact) is zero, the velocity afterwards is simply given by Cooker's model as

$$v_y = \frac{\partial P}{\partial y} = \sum_{n=1}^{\infty} a_n \lambda_n \cos(\lambda_n y) \frac{\sinh(\lambda_n(x-b))}{\cosh(\lambda_n b)} \tag{A.2.1}$$

So that the initial velocity upward when $y = 0$ is

$$v_y = \sum_{n=1}^{\infty} a_n \lambda_n \frac{\sinh(\lambda_n(x-b))}{\cosh(\lambda_n b)} \tag{A.2.2}$$

Equations (A.2.2) diverges at $x = 0$, which can be proved by a comparison test. From (A.2.2) we have

$$v_y = \sum_{n=1}^{\infty} \frac{(1-\cos(\mu\lambda_n))}{\lambda_n} \tanh(\lambda_n b) \ , \tag{A.2.3}$$

where $\lambda_n = \left(n - \frac{1}{2}\right)\pi$ at $x = 0$.

Since $\tanh(x)$ is a monotonic increasing function of x, we have

$$v_y > \sum_{n=1}^{\infty} \frac{(1-\cos(\mu\lambda_n))}{\left(n+\frac{1}{2}\right)\pi} C \tag{A.2.4}$$

where $C = \tanh(\lambda_1 b) > 0$.

219

Now $1 - \cos(\mu\lambda_n) \geq 0$ where we have equality if $\mu\lambda_k = 2k\pi$ with $k \in \mathbb{Z}$.

$$\text{i.e. } \mu\left(n - \frac{1}{2}\right) = 2k$$

$$\text{i.e. } \frac{2k}{\mu} = n - \frac{1}{2}$$

if μ is irrational then this equation cannot hold. If μ is rational then $\mu = \dfrac{p}{q}$, $p, q \in \mathbb{Z}$

and p and q have no common factors. Hence $2kq = pn + \dfrac{p}{2}$ which also cannot hold if p is odd, since the LHS is an integer but the RHS is not.

If p is even and of the form $p = 2r$ with r odd then we have $2kq = 2rn - r$ which cannot hold since the LHS is even but the RHS is odd. More generally we have $p = 2^s r$ where $s \geq 2$ and r is odd. Then $\mu = \dfrac{2^s r}{q}$ having cancelled any common factors so that q and r have no common factors. Observe also that since p is even, q is odd.

Suppose we have a solution k_1 for $n = n_1$. Then $k_1 q = 2^{s-2} r(2n - r)$. Now suppose there is a solution k_2 for $n = n_1 + 1$. Then $k_2 q = 2^{s-2} r(2n - r + 2)$. Subtracting gives $k_2 - k_1 = 2^{s-1} \dfrac{r}{q}$.

The LHS must be an integer but the RHS cannot be since r and q have no common factors. Alternatively observe that the numerator is even but the denominator is odd.

Hence any term in the series for v_y with zero coefficients must be followed by a term with non-zero coefficient. So at most only every other coefficients in the series can be zero. Moreover the first term has non-zero coefficient.

Hence

$$\sum_{n=1}^{\infty} \frac{\left(1 - \cos(\mu\lambda_n)\right)}{\left(n - \frac{1}{2}\right)\pi} C \geq \sum_{n=1}^{\infty} \frac{\left(1 - \cos(\mu\lambda_{2n-1})\right)}{\left(2n - \frac{3}{2}\right)\pi} C \qquad \text{(A.2.5)}$$

220

So we then have the result

$$1 - \cos(\mu\lambda_m) \geq D > 0 \tag{A.2.6}$$

where D is the minimum value of $1 - \cos(\mu\lambda_m)$ for any m in the case when all the coefficients are non-zero (p odd or $p = 2r$ with r odd) or for any odd value of m (in the above case when $p = 2^s r$, $s \geq 2$ and r odd).

Hence:

$$v_y > \sum_{n=1}^{\infty} \frac{E}{n+1} \quad \text{where} \quad E = \frac{CD}{\pi} > 0$$

$$= \sum_{n=2}^{\infty} \frac{E}{n} \to \infty \quad \text{by the Integral Test.} \tag{A.2.7}$$

i.e. v_y is bounded below by a divergent series and hence diverges.

For $0 < x < b$ we have

$$v_y = \sum_{n=1}^{\infty} \frac{(1 - \cos(\mu\lambda_n))}{\lambda_n} \frac{\sinh(\lambda_n(x-b))}{\cosh(\lambda_n b)}$$

$$\leq \sum_{n=1}^{\infty} \frac{(1 - \cos(\mu\lambda_n))}{\lambda_n} \frac{e^{-\lambda_n x} e^{\lambda_n b}}{e^{\lambda_n b}} \tag{A.2.8}$$

By the ratio test, $\lim_{n\to\infty} \left| \frac{a_{n+1}}{a_n} \right|$, gives

$$\lim_{n\to\infty} \left| \frac{e^{-\left(n+1+\frac{1}{2}\right)\pi x} \left(n+\frac{1}{2}\right)\pi}{\left(n+1+\frac{1}{2}\right)\pi \quad e^{-\left(n+\frac{1}{2}\right)\pi x}} \right| = e^{-\pi x} < 1 \tag{A.2.9}$$

so the series converges.

REFERENCES

Akyildiz, H. and Ünal, E. (2005). Experimental investigation of pressure distribution on a rectangular tank due to the liquid sloshing. *Ocean Engineering.* 32:1503-1516.

Allsop, W., Bruce, T., Pearson, J. and Besley, P. (2005). Wave overtopping at vertical and steep seawalls. Proceedings of the Institution of Civil Engineers. *Maritime Engineering.*158: 103-114.

Allsop, W., Vicinanza, D., and McKenna, J.E. (1995). Wave forces on vertical and composite breakwaters. *HR Wallingford.*

Armenio, V., and Rocca, M.L. (1996). On the analysis of sloshing of water in rectangular containers: Numerical study and experimental validation. *Ocean Engineering.* 23(8):705-739.

Bagnold, R.A. (1939). Interim report on wave-pressure research. *Journal of the Institute of Civil Engineers.* 12: 202-206.

Blackmore, P.A and Hewson, P.J. (1984). Experiments on full-scale wave impact pressures. *Coastal Eng*. 8:331-346.

Besley, P. (1999). Overtopping of seawalls-Design and assessment manual. *R&D Technical Report W 178. Environment Agency, Bristol.*

Bullock, G.N., Crawford, A.R., Hewson, P.J., Walkden, M.J.A. and Bird, P.A.D. (2001). The influence of air and scale on wave impact pressures. *Coastal Eng*. 42: 291-312.

Bullock, G.N., Obhrai, C., Peregrine, D.H. and Bredmose, H. (2007). Violent breaking wave impacts. Part 1: Results from large-scale regular wave test on vertical and sloping walls. *Coastal Eng*. 54: 602-617.

Chan, E.S. (1994). Mechanics of deep water plunging-wave impacts on vertical structures. *Coastal Eng*. 22: 115-133.

Chan, E.S. and Melville, W.K. (1988). Deep-water plunging wave pressures on a vertical plane wall. *Proc. R. Soc. Lon.*. 417: 95-131.

Cooker, M.J. (1990). The interaction between steep water waves and costal structures. *Ph.D Thesis* University of Bristol.

Cooker, M.J. and Peregrine, D.H. (1990). A model for breaking wave impact pressures. *Proc. 22nd Intl. Conf. Coastal Eng*.: 1473-1486.

Cooker, M.J. and Peregrine, D.H. (1992). Wave impact pressure and its effect upon bodies lying on the sea bed. *Coastal Engineering.* 18: 205-229.

Cooker, M.J. and Peregrine, D.H. (1995). Pressure-impulse theory for liquid impact problems. *J. Fluid Mech.* 297: 193-214.

Cooker, M.J. (2010). The flip-through of a plane inviscid jet with a free surface. *Journal Eng Math.* 67:137-152.

Cox, S.J. and Cooker, M.J. (2001). The pressure impulse in a fluid saturated crack in a sea wall. *Coastal Engineering*. 42:241-256.

Cox, S.J and Cooker, M.J. (1999). The motion of a rigid body impelled by sea-wave impact. *Applied Ocean Research*. 21:113-125.

Crest Level Assessment of Coastal Structures By Full Scale Monitoring, Neural Network Prediction and Hazard Analysis on Permissible Wave Overtopping, website http://www.clash-eu.org. (accessed March 2011)

Cuomo, G., Allsop, W., Bruce, T. and Pearson, J. (2010) Breaking wave loads at vertical seawalls and breakwaters. *Coastal Eng*. 57: 424-439.

Cuomo, G., Piscopia, R. and Allsop, W. (2011). Evaluation of wave impact loads on caisson breakwaters based on joint probability of impact maxima and rise times. *Coastal Eng*. 58: 9-27.

Eswaran, M., Saha, U.K. and Maity, D. (2009). Effects of baffles on a partially filled cubic tank: Numerical simulation and experimental validation. *Computers and Structures*. 87: 198-205.

European Coast, website http://www.kennisbank-waterbouw.nl/EC/CLM01060002.html (accessed July 2012)

Faltinsen, O.M. and Timokha, A.N. (2009). Sloshing. *Cambridge University Press*.

Franco, L., de Gerloni, M. and van der Meer, J.W.(1994). Wave overtopping on vertical and composite breakwaters. *Proc 24th Int Conf. Coastal End., Kobe, ASCE*. 1030-1045.

Frey P. (2008). Partial Differential Equations, website http://www.ann.jussieu.fr/~frey/cours/UdC/ma691/ma691_ch3.pdf (accessed July 2012)

Geeraerts, J., Troch, P., De Rouck, J., Verhaeghe, H. and Bouma, J.J. (2007*). Wave overtopping at coasatal structures: prediction tools and related hazard analysis. *Journal of Cleaner Production*.15: 1514-1521.

Greenhow, M. (1989). A probability distribution of breaking wave crest height based on a crest-acceleration threshold method. *Ocean Engineering*. 16: 537-544.

Greenhow, M. (2006). Wave impact on seawalls of various geometries. *CoastalLabs06 Proceedings*. 517-524.

Hattori, M., Arami, A. and Yui, T.(1994). Wave impact pressure on vertical walls under breaking waves of various types. *Coastal Eng*. 22: 79-114.

Hofland, B., Kaminski, M.L., and Wolters, G. (2010). Large scale wave impacts on a vertical wall. *Coastal Engineering.* 1-15.

Jervis, M. and Peregrine, D.H. (1996). Overtopping of waves at a wall: a theoretical approach. *Proc. Intl. Conf. on Coastal Engineering.*2192-2205.

Jiao, L. (2011). Wave-induced nonlinear effects on a pontoon-type Very Large Floating Structures (VLFS), *PhD Thesis* Norwegian University of Science and Tecnology.

Kirkgöz, M. S. (1982). Shock pressures of breaking waves on vertical walls. *Proceeding of American Society of Civil Engineers.* 108: 81-95.

Kirkgöz, M. S. (1991). Impact pressure of breaking waves on vertical and sloping walls. *Ocean Engineering.* 18: 45-59.

Kirkgöz, M. S. and Mamak, M. (2004). Impulse modelling of wave impact pressures on vertical wall. *Ocean Engineering.* 31: 343-352.

Liu, D. and Lin, P. (2009). Three-dimensional liquid sloshing in a tank with baffles. *Ocean Engineering.* 36:202-212.

Lundgren, H.(1969). Wave shock forces: An analysis of deformation and forces in the wave and in the foundation. *Proc. Symp. On Wave Action, Delft Hydraulics Laboratory, Delft, The Netherlands.*153-174.

Masselink, G. and Russell, P. Coastal erosion and coastal geomorphology. *Marine Climate Change Impacts Partnership (MCCIP) Annual Report Card 2007-2008 Scientific Review.*

Müller, G. (1997). Wave impact pressure propagation into cracks. *Proc. Inst. Civil Eng. Water Marit.& Energy.* 124:79-85

Offord, P. (2011). Islanders' worry at sight of crumbling seawall.

Website, http://www.echo-news.co.uk/news/local_news/8792437.Islanders____worry_at_sight_of__crumbling_seawall/ (accessed March 2011)

Okamura, M. (1993). Impulsive pressure due to wave impact on an inclined plane wall. *Fluid Dynamics Research*. 12: 215-228.

Oumeraci, H. (1994). Review and analysis of vertical breakwater failures-lesson learned. *Coastal Engineering*. 22:3-29.

Partenscky, H.W. and Tounsi, K.(1989). Theoretical analysis of shock pressures caused by waves breaking at vertical structures. *Intl. Assoc. for Hydraulic Research XXIII Congress, Ottawa.*C-113-C-118.

Pearson, J., Bruce,T., Allsop, W.and Gironella, X. (2002) Violent wave overtopping-measurement at large and small scale. *Coastal Engineering*.2227-2238.

Peregrine, D.H. (2003). Water-wave impact on walls. *Annual Review Fluid Mech*.35:23-43.

Pullen, T., Allsop,W., Bruce, T. and Geeraerts, J. (2004). Violent wave overtopping: CLASH field measurements at Samphire Hoe. *Proceedings of Conference Coastal Structures (ASCE).*

Srokosz, M. A. (1986). On the probability of wave breaking in deep water. *Journal of Physical Oceanography.* 16: 382-385.

Stewart, J. (2009). Calculus. *Brooks Cole*.

Takahashi, S. (1996). Design of vertical breakwaters; *Reference Document No.34, Port and Harbour Research Institute, Japan.*

Topliss, M.E. (1994). Water wave impact on structures. *PhD Thesis* University of Bristol.

Violent Overtopping of Waves at Seawalls, website http://www.vows.ac.uk/
(accessed April 2011)

Wave Overtopping, website http://www.overtopping-manual.com/
(accessed April 2011)

Weggel, J.R. and Maxwell, W.H.C. (1970). Numerical model for wave pressure distributions. *Journal of the Waterways, Harbors and Coastal Engineering Division, ASCE.* 623-642.

Wolters, G. and Müller, G. (2004). The propagation of wave impact induced pressures into craks and fissures. *Geological Society, London, Engineering Geology Special Publications.* 20:121-130.

Wood, D.J. & Peregrine, D.H. (1998). Two and three-dimensional pressure-impulse models of wave impact on structures. *Coastal Engineering.*1502-1515.

Wood, D.J. and Peregrine, D.H. (1996). Wave impact beneath a horizontal surface. *Intl. Conf. on Coastal Eng*. 3:2573-2583.

Wood, D.J. and Peregrine, D.H. (2000). Wave impact on a wall using pressure-impulse theory. II: Porous berm. *Journal of Waterway, Port, Coastal, and Ocean Engineering.*191-195.

Wood, D.J. (1997). Pressure-impulse impact problems and plunging wave jet impact. *PhD Thesis* University of Bristol.

Wright A. (2002). Uniqueness theorem, website http://www-solar.mcs.st-and.ac.uk/~andy/LectureNotes/Fundamentals1/node52.html (accessed July 2012)

Zauderer, E. (1989). Partial Differential Equations of Applied Mathematics. *Wiley,* 2nd Ed.